AEROSOL-DEPOSITED MULTICALORIC THICK FILMS

Victor Regis de Moraes

Doctoral Dissertation
Jožef Stefan International Postgraduate School
Ljubljana, Slovenia

Supervisor: Assoc. Prof. Dr. Hana Uršič Nemevšek, Jožef Stefan Institute, Ljubljana, Slovenia

Evaluation Board:
Prof. Dr. Vid Bobnar, Chair, Jožef Stefan Institute, Ljubljana, Slovenia
Assoc. Prof. Dr. Joško Valentinčič, Member, University of Ljubljana, Ljubljana, Slovenia
Prof. Dr. Brahim Dkhil, Member, Université Paris-Saclay, Paris, France

MEDNARODNA PODIPLOMSKA ŠOLA JOŽEFA STEFANA
JOŽEF STEFAN INTERNATIONAL POSTGRADUATE SCHOOL



Victor Regis de Moraes

AEROSOL-DEPOSITED MULTICALORIC THICK FILMS

Doctoral Dissertation

VEČKALORIČNE DEBELE PLASTI, PRIPRAVLJENE Z METODO NANOSA V AEROSOLU

Doktorska disertacija

Supervisor: Assoc. Prof. Dr. Hana Uršič Nemevšek

Ljubljana, Slovenia, June 2026

To my parents, who raised me

To my Aunt Mônica, who is no longer with us

To my younger self, who dreamed

E àqueles que ainda perseveram

Acknowledgments

This work was only possible due to the professional and personal collaboration of many people who helped me over the years.

My sincerest gratitude goes to my supervisor, Assoc. Prof. Dr. Hana Uršič Nemevšek, who saw potential in me 12.000 km away. I would like to thank her for all the discussions, ideas and support throughout this almost five years. In particular, for all the patience particularly when I was still getting accommodated to this new life. I also take this opportunity to express my gratitude to the Slovenian Research and Innovation Agency for the funding (N2-0212, P2-0105 and J2-60035) and the JSI Director's fund 2017-ULTRACOOL which funded the Ultracool laboratory, where most of the work was performed.

I would like to thank Matej Šadl, whose work was the starting point of my research, for sharing his knowledge and assisting me in so many daily laboratory tasks. I highly appreciate Brigita Kmet and Jena Cilenšek and colleagues from the Electronic Ceramics Department, who helped me with several additional experiments. Also, my sincere appreciation goes to Urban Tomc who helped so much in the magnetocaloric and simulations parts, without him this work would not be possible. My gratitude also goes to all co-authors and former colleagues who also partook in my research in any capacity.

The collaborators from abroad, who helped me with insights, discussions are also deeply appreciated. In particular, Enric Stern-Taulats, Klara Lünser and Lluís Mañosa who hosted me at the university of Barcelona and assisted the research with the most important measurement needed for this thesis. This collaboration would not have happened, if not for the always-helpful Jožef Stefan Postgraduate school, who supported me and funded my Erasmus+ visit to Spain.

I deeply thank my parents, back in Brazil, who always incentivized me to study, to break my limits and go beyond. Also, I would like to acknowledge my cousin João and my friend from college Velasco for participating in my life for all these years. I would also like to thank all the friends that I've made since arriving to Ljubljana and all the great experiences we've had over the years. In particular, my closest friends *the Ivans* (Alnilan, Katy, Layrton, Ivan, Katja, Antea and Martin), Adri, Oana and Katarina who made this entire experience so much better.

Finally, my deepest and most intense appreciation goes to Meryem, who has accompanied me in many ways during these years. Without her I would be nowhere near where I am today.

Abstract

Solid-state cooling technologies have received increased attention as suitable alternatives to conventional vapor-compression systems. In recent years, significant research has been done on caloric materials. In the pursuit of improved room-temperature caloric responses, with potential for multifunctionality, multicalorics have also been the focus of research, as these exhibit distinctive caloric responses under different external stimuli. However, thus far, there are no reports on the preparation and characterization of room-temperature electrocaloric-magnetocaloric (EC-MC) composites. Because of this, the main focus of this thesis is the preparation and characterization of the caloric properties of $0.9Pb(Mg_{1/3}Nb_{2/3})O_3$–$0.1PbTiO_3$/LaFeSiCo (PMN–10PT/LFSC) composite thick films prepared via the aerosol deposition (AD) method.

We started our work with a preliminary study on non-caloric ceramic-metal films to better understand their inherent properties. By combining Al_2O_3 with different vol% of Al, a wide range of composite films were prepared via AD. While Al_2O_3 exhibited a permittivity of ∼12, composites reached values as large as ∼800, at 27 vol %, albeit with large dielectric losses. However, up to 15 vol% of Al, an enhancement in permittivity was observed with no significant increase in losses. Our results show that, even at low vol% of metal, improved electrical properties can be achieved when preparing the AD composites.

Moreover, reports that utilize direct characterization techniques of caloric responses, such as thermistor-in-calorimeter and the infrared (IR) camera method, mostly focus on bulk samples. In the case of films, the influence of heat losses to the substrate and to the black coating layer, necessary for the IR camera method, remain unaddressed. In light of this, we have numerically investigated the criterion required to achieve maximized measurements response. First, the substrate should exhibit a thermal effusivity $\leq$3 kW $s^{1/2}$ m^{-2} K^{-1} or a thermal conductivity $\leq$1 W m^{-1} K^{-1}, both of which are satisfied in the case of polyimide. Thus, polyimide was chosen as the substrate for the multicaloric thick films. In addition, in order to achieve maximized measurement response during IR camera characterizations, the simulations indicated that the caloric films should exhibit a thickness $\geq$5 µm, while the black paint coatings should not exceed this value. In light of this, we have also developed the airbrush method, which is a novel and affordable black paint coating method, and can prepare coatings as thin as ∼3 µm.

Lastly, by combining the PMN–10PT EC ceramic with 2 wt% of LFSC MC alloy, the aerosol-deposited composite thick films were successfully prepared on polyimide substrates. Due to the embedded MC metallic particles, the composites exhibited enhanced electrical properties, when compared to the PMN–10PT films. In particular, the room-temperature EC response of composites was ∼0.45 K, at 250 kV cm^{-1}, whereas for PMN–10PT films the value was ∼0.35 K. In other words, a 32 % enhancement in EC response was achieved. The room-temperature MC response of composite films was also directly characterized, achieving a MC response ∼1.4 K at 2 T, after corrections. In this way, for the first time, we demonstrate that it is possible to prepare multicaloric composites with both caloric properties at room-temperature. Our results offer novel insights and perspectives on the development of alternative cooling technologies

Povzetek

Tehnologije hlajenja v trdnem stanju so deležne vse večje pozornosti kot primerne alternative običajnim hladilnim sistemom na osnovi parne kompresije. V zadnjih letih je bil dosežen pomemben raziskovalni napredek na področju trdnih kaloričnih materialov za bodoče hladilne sisteme. V iskanju izboljšanih kaloričnih odzivov pri sobni temperaturi so v središču raziskav tudi večkalorični materiali. Doslej še ni bilo poročano o elektrokaloričnomagnetokaloričnih kompozitih, ki bi pri sobni temperaturi izkazovali oba pojava. Zato je osrednji del disertacije namenjen prav tej temi, in sicer razvoju in karakterizaciji debeloplastnih kompozitov $0{,}9Pb(Mg_{1/3}Nb_{2/3})O_3$–$0{,}1PbTiO_3$/LaFeSiCo (PMN–10PT/LFSC), pripravljenih z metodo nanosa v aerosolu (AD).

Za boljše razumevanje lastnosti kompozitov, pripravljenih z AD, smo delo pričeli s študijo nekaloričnih keramično-kovinskih plasti. Pripravljene so bile kompozitne plasti z različnimi volumenskimi deleži aluminija. Dielektričnost debele plasti Al_2O_3 je znašala približno 12, medtem ko so kompozitne plasti s 27 vol. % aluminija dosegle vrednosti do približno 800. Do 15 vol. % aluminija je bilo opaženo povečanje dielektričnosti brez znatnega povečanja izgub. Naši rezultati kažejo, da je mogoče pripraviti kompozite z izboljšanimi električnimi lastnostmi že pri nizki vsebnosti kovinske faze.

Dosedanja literatura o uporabi tehnik direktne karakterizacije kaloričnih odzivov, vključno z meritvami s termistorjem v kalorimetru in metodo infrardeče kamere, se večinoma osredotoča na volumenske vzorce. Pri plasteh vpliv toplotnih izgub v podlago in vpliv črne prevleke, ki je potrebna za meritve s toplotno kamero, ostaja precej neraziskan. Zato smo z numeričnim modeliranjem določili kriterije za doseganje maksimalnega merilnega odziva. Kot osnovni pogoj se je izkazalo, da mora biti toplotna efuzivnost podlage ≤ 3 kW $s^{1/2}$ m^{-2} K^{-1} oziroma njena toplotna prevodnost ≤ 1 W m^{-1} K^{-1}. Na podlagi opredeljenih kriterijev je bil poliimid izbran kot primerna podlaga za pripravo večkaloričnih debelih plasti. Nadalje so simulacije pokazale, da mora biti debelina kalorične plasti najmanj 5 µm. Tako se namreč doseže maksimalni merilni odziv pri karakterizaciji z infrardečo kamero. Nasprotno pa debelina črne prevleke ne sme presegati te vrednosti. Zato smo razvili metodo nanašanja črne prevleke z zračnim čopičem (ang. airbrush), ki je cenovno ugodna metoda in omogoča tanek nanos debeline do ~3 µm.

V zadnjem delu raziskave smo na poliimidne podlage z metodo AD uspešno nanesli kompozitne debele plasti PMN–10PT/LFSC. Plasti so bile sestavljene iz elektrokalorične faze PMN–10PT in 2 mas. % magnetokalorične zlitine LFSC. Pri sobni temperaturi je elektrokalorični odziv kompozitov znašal 0,45 K pri električnem polju 250 kV cm^{-1}, medtem ko je bil za plasti PMN–10PT odziv le 0,35 K. Zaradi vsebnosti kovinskih delcev se je torej elektrokalorični odziv kompozitnih plasti izboljšal za 32 %. Pri sobni temperaturi smo neposredno izmerili tudi magnetokalorični odziv kompozitnih plasti. Po upoštevanju ustreznih popravkov je bil dosežen magnetokalorični odziv ~1,4 K pri 2 T. S tem smo pokazali, da je mogoče pripraviti večkalorične kompozite, ki pri sobni temperaturi izkazujejo oba kalorična odziva. Rezultati prinašajo nove vpoglede v razvoj večkaloričnih kompozitnih sistemov in odpirajo nove možnosti za razvoj alternativnih tehnologij hlajenja.

Contents

List of Figures **xv**

List of Tables **xvii**

Abbreviations **xix**

Symbols **xxi**

1 Introduction **1**
1.1 Definition of the Problem 1
1.2 Caloric Effects 2
1.2.1 Electrocaloric Effect 3
1.2.2 Magnetocaloric Effect 5
1.2.3 Multicaloric Effect 8
1.3 Powder Aerosol Deposition Method 11
1.3.1 Powder Requirements 12
1.3.2 Aerosol-Deposited Thick Films 14
1.4 Characterization Methods of Caloric Materials 15
1.4.1 Thermistor-in-Calorimeter Method 16
1.4.2 Infrared Camera Method 17
1.5 Objectives and Hypotheses 18

2 Investigation of Structural and Electrical Properties of Al_2O_3/Al Composites prepared by Aerosol Co-Deposition **21**

3 Roadmap for Electrocaloric Films Characterization **39**

4 Airbrushing: A Novel Method for Preparation of High-Emissivity Black Coating for Infrared Measurements **55**

5 Direct Observation of Room-Temperature Electrocaloric and Magnetocaloric Responses in Multicaloric Composite Films **71**

6 Summary and Conclusions **91**

References **95**

Bibliography **101**

Biography **105**

List of Figures

Figure 1.1: Schematic representation of the heating segment of different caloric effects. After the application of the external stimulus, the samples exhibit an increase in temperature by ΔT. In the MC diagram, the "S" and "N" symbols correspond to the south and north poles of the magnet, respectively. 2
Figure 1.2: Schematic representation of the EC cycle. 3
Figure 1.3: Polarization hysteresis loops of a) dielectrics, b) ferroelectrics and c) relaxors. P_{max} indicates the maximum polarization value at the maximum applied field, E_{max} 5
Figure 1.4: Schematic representation of the MC cycle....6
Figure 1.5: Schematic representation of a typical diamagnetic and ferromagnetic responses to an external magnetic field. 7
Figure 1.6: Schematic representation of single-phase and composite multicalorics.....8
Figure 1.7: Electrocaloric and magnetocaloric responses of a PFN-based composition. Notice the different temperature range....9
Figure 1.8: Schematic representation of a) ferromagnetism in elemental Ni and b) ferroelectricity in the perovskite unit cell. 9
Figure 1.9: Schematic representation of a) multilayered and b) particulate composites. The different colors represent distinctive materials. 10
Figure 1.10: a) Micrograph of the multicaloric composite. The small particles with lighter contrast (indicated by black arrows) correspond to the EC phase. Notice the cracking (red arrows) in the grains of the MC phase. b) Caloric measurements of EC and MC responses of the PT-LPM composite....11
Figure 1.11: Schematic representation of an AD device. 12
Figure 1.12: Schematic representation of the influence of ceramic particle size on the deposition process.... 13
Figure 1.13: Photographs, line profile of as-deposited PMN–10PT films, and cross-sectional micrographs showing the influence of powder processing on the film deposition. All the films were prepared under the same conditions. 13
Figure 1.14: Influence of annealing on the microstrain and ferroelectric properties of aerosol-deposited PMN–10PT films. 14
Figure 1.15: Schematic representation of a) the AD process for composite powders and b) the composite thick-film microstructure. 15
Figure 1.16: Directly measured EC response of a ceramic thick film obtained via indirect and direct methods.... 16
Figure 1.17: Photograph of a film prepared for the TiC method. The Pt1000 is the environment temperature sensor....16
Figure 1.18: Schematic representation of the IR camera set up. The sample emits IR radiation which is captured and processed by the IR camera, resulting on a thermographic map....17

List of Tables

Table 6.1 Comparison between the properties of PMN–10PT and PMN–10PT/LFSC composite thick films..... .92
Table 6.2 Comparison of caloric measurement conditions from the previous literature and from this work.....93

Abbreviations

AD	... aerosol deposition
BC	... barocaloric
EC	... electrocaloric
eC	... elastocaloric
HM30	... heat-treated and milled (30 min) powder
HM60	... heat-treated and milled (60 min) powder
HT	... heat-treated powder
IR	... infrared
LFSC	... LaFeSiCo
LPM	... $La_{0.7}Pb_{0.3}MnO_3$
MC	... magnetocaloric
NT	... non-treated powder
PFN	... $Pb(Fe_{0.5}Nb_{0.5})O_3$
PMN–10PT	... $0.9Pb(Mg_{1/3}Nb_{2/3})TiO_3$–$PbTiO_3$
PST	... $Pb(Sc_{0.5}Ta_{0.5})O_3$
PT	... $PbTiO_3$
RF	... relaxor-ferroelectric
TiC	... thermistor-in-calorimeter

Symbols

c_{E}	... specific heat capacity at constant electric field
c_{H}	... specific heat capacity at constant magnetic field
E	... electric field
H	... magnetic field
k	... correction factor
M	... magnetization
P	... polarization
$P\mathrm{r}$	... remnant polarization
S	... entropy
T	... temperature
T_0	... initial temperature
$T\mathrm{c}$	... Curie temperature
ΔT	... adiabatic temperature change
ΔT_{EC}	... electrocaloric temperature change
ΔT_{MC}	... magnetocaloric temperature change
ΔT_{M}	... measured temperature change
μ_0	... magnetic permeability of vacuum
ρ	... density

Chapter 1

Introduction

In this chapter, an overview of the relevant topics for the thesis will be introduced. The chapter starts with the definition of the problem and the scientific motivation for this work. In the following sections, the caloric effects will be defined and additional theoretical background will be provided for electrocalorics, magnetocalorics and multicalorics. Then, the aerosol deposition method will be discussed, covering its working principle and fundamentals. Lastly, a description of different characterization methods of caloric materials will be given. At the end, the objectives and hypotheses of the dissertation are presented.

1.1 Definition of the Problem

Vapor compression technology has been the preferred method for cooling systems for over 200 years. However, a conventional vapor refrigerator has at most 50 % of Carnot efficiency, wasting half of the input energy used [1], [2], [3]. Such refrigerators also rely on chlorofluorocarbons and hydrochlorofluorocarbons, which are detrimental to the ozone layer. Although they have been banned since 2019, the gas-based alternatives are still harmful to the environment [3]. From this point of view, vapor-compression technologies are neither efficient nor environmentally friendly, thus the interest in alternative cooling technologies has increased.

Among the alternatives, solid-state cooling devices based on caloric effects are one of the most promising. These have an expected efficiency of at least 60 % [2], [4] and can be environmentally friendly and inexpensive. Their operating principle is based on the caloric effects, i.e., the temperature change of a material as a result of an external stimulus. For example, the electrocaloric effect is the temperature change associated with an applied electric field, whereas the magnetocaloric effect is related to an external magnetic field. Moreover, the combination of different caloric effects, namely the multicaloric effects, may result in larger caloric output, improving the performance of the material [5], [6]. In light of this, research has been done on combining and exploring multicaloric materials and their underlying mechanisms.

The literature of multicaloric systems is still, however, mostly unexplored. In particular, in composites, where the caloric phases are physically separated. Thus far, there are no reports of a multicaloric sample which exhibited both electrocaloric and magnetocaloric effects at room temperature. Therefore, the focus of this thesis is to prepare, using the aerosol deposition method, a thick film multicaloric composite and directly characterize the electrocaloric and magnetocaloric properties. Attention is also given to the different characterization methods and further optimizations were achieved.

1.2 Caloric Effects

In the pursuit of more efficient and environment-friendly cooling technologies, caloric-based systems have received increased attention in recent years. A caloric effect is defined as an adiabatic and reversible temperature change of a material as response to an external stimulus. The nature of the caloric effect is inherently associated with the applied stimulus. An external electric field, magnetic field, hydrostatic pressure or uniaxial stress results in the electrocaloric (EC), magnetocaloric (MC), barocaloric (BC) or elastocaloric (eC), respectively [7], [8]. A schematic representation of the different caloric effects is shown in Figure 1.1.

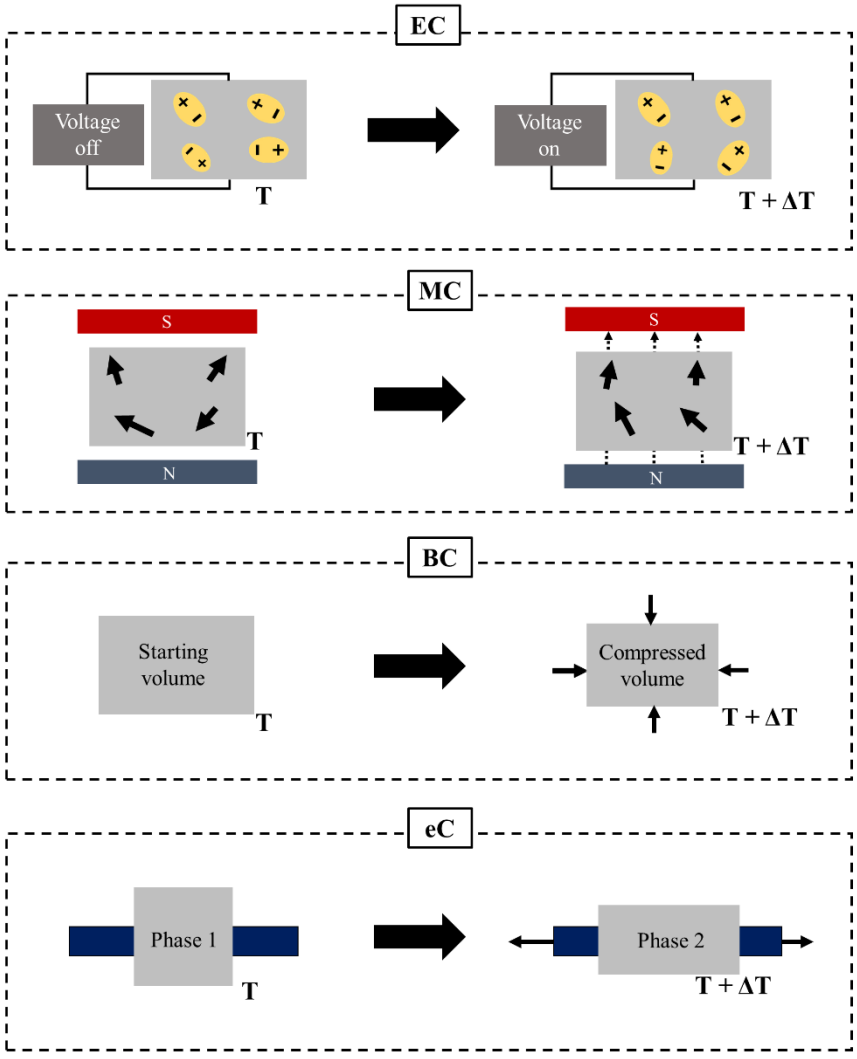


Figure 1.1: Schematic representation of the heating segment of different caloric effects. After the application of the external stimulus, the samples exhibit an increase in temperature by ΔT (after [7]). In the MC diagram, the "S" and "N" symbols correspond to the south and north poles of the magnet, respectively.

In addition to their efficiency, one of the advantages of caloric-based systems is the wide range potential applications, as many materials can exhibit caloric properties. For example, metallic compounds can exhibit excellent caloric performance, if a sufficiently large magnetic field is applied. Albeit, the same class of material may exhibit BC or eC effects, depending on composition [9], [10], [11], [12], [13]. If biocompatibility or flexibility

is needed, caloric polymers may be used as the coolant material, as these have been reported to exhibit eC, BC or EC effect [14], [15], [16], [17]. For integration on microelectronics or exposure to harsh environments, oxides are a suitable class of materials and have been reported to exhibit MC, BC or the EC effect [18], [19], [20], [21], [22], [23]. Because of this broad range of materials and associated effects, caloric-based cooling technologies are the most promising solid-state cooling alternatives to conventional vapor-compression.

The main focus of this thesis is the investigation of EC and MC effects in thick films, related to oxide and metallic compounds, respectively. In light of this, these two effects and associated materials will be described in further details in the following sections. It is worth emphasizing that the BC and eC effects will be only discussed as part of the literature review.

1.2.1 Electrocaloric Effect

From its definition, the EC effect is the adiabatic temperature change associated with an external applied/removed electric field (E). Due to this fact, EC materials are promising for integrated micro-cooling systems, as its stimulus is already present in all electronic devices. The EC cycle is analogous to conventional vapor-compression, in other words, it works by exchanging heat from a heat load through a coolant material, which is subjected to a thermodynamic cycle [18]. The heating/cooling EC cycle (Figure 1.2) is as follows:

(a) Dipole moments are disordered within the material. There is no external electric field and the material is at temperature T_0.

(b) The application of the electric field leads to a partial alignment of the electric dipoles, increasing the net polarization (P) in the material resulting in a decreased entropy (S) in the dipolar subsystems. Under adiabatic conditions (no thermal exchange between the material and the heat sink) the total entropy is constant; thus, the dipolar entropy loss must be compensated elsewhere. The lattice vibrations therefore increase, which leads to an increase in the temperature of the material by ΔT.

(c) The electric field is still applied on the material, but the excess heat is transferred to a heat sink, cooling the material back to T_0.

(d) The electric field is turned off and the dipoles return to the disordered state, increasing the entropy and decreasing the temperature by ΔT, which is defined as EC temperature change, ΔT_{EC}.

(e) The EC material absorbs heat from the heat source, returning to the same state as in (a).

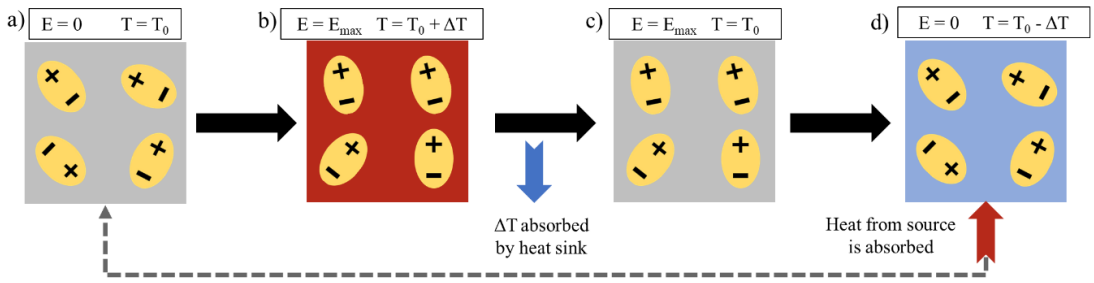


Figure 1.2: Schematic representation of the EC cycle (after [8]).

As evidenced by the EC cycle, the main mechanism of the EC effect is the change in entropy in the polar subsystems [1], [2]. The entropy can be expressed as a function of the applied field and temperature ($S \rightarrow S(E,T)$), in differential form:

$$dS = \left(\frac{\partial S}{\partial E}\right)_{\mathrm{T}} dE + \left(\frac{\partial S}{\partial T}\right)_{\mathrm{E}} dT. \tag{1.1}$$

The second term can be promptly associated with the specific heat capacity of the material at constant field E (c_{E}):

$$c_{\mathrm{E}} = \frac{T}{\rho}\left(\frac{\partial S}{\partial T}\right)_{\mathrm{E}}, \tag{1.2}$$

where ρ is the density of the material. The first term in (1.1) can be derived from the first law of thermodynamics:

$$dU = TdS + EdP, \tag{1.3}$$

where U is the total internal energy of the system. The Gibbs free energy (G) is then expressed as:

$$dG = -SdT - PdE. \tag{1.4}$$

From the second derivatives, we obtain the Maxwell relation:

$$\left(\frac{\partial S}{\partial E}\right)_{\mathrm{T}} = \left(\frac{\partial P}{\partial T}\right)_{\mathrm{E}}. \tag{1.5}$$

Inserting this relation into equation (1.1), we then obtain:

$$dS = \left(\frac{\partial P}{\partial T}\right)_{\mathrm{E}} dE + \rho\frac{c_{\mathrm{E}}}{T}\, dT, \tag{1.6}$$

Under adiabatic conditions ($dS = 0$), the temperature change can be calculated. Mathematically:

$$\Delta T_{\mathrm{EC}} = -\int_{E_i}^{E_f} \frac{T}{\rho c_{\mathrm{E}}}\left(\frac{\partial P}{\partial T}\right)_{\mathrm{E}} dE, \tag{1.7}$$

where E_{i} and E_{f} are the initial and final applied fields, respectively. Moreover, to maximize the EC output, generally $E_{\mathrm{i}} = 0$ and E_{f} can be as large as several hundreds of kV cm^{-1}. Thus, a promising EC material should withstand large electric fields and convert most of the applied energy into the EC response, with minimal losses due to electrical conductivity. In other words, it must be an electrically insulating material. In addition, although the EC effect is an intrinsic effect of polar materials, noticeable values can only be achieved if the material also exhibits a large polarization change as function of temperature, shown in equation (1.7). A class of materials that satisfies both conditions are ferroelectrics, discussed below.

Ferroelectric Materials

In this section, key electrical properties of insulating materials are briefly introduced, with emphasis on ferroelectricity, as it is a fundamental property for the most promising EC materials.

In general, electrically insulating materials are dielectrics, i.e., upon the application of an external electric field these will exhibit a non-zero polarization. However, this polarization is not retained after the field is removed (Figure 1.3a). Under certain symmetry conditions, dielectric materials can exhibit an electromechanical coupling, the piezoelectric effect. Some of which, may exhibit pyroelectricity, namely a temperature-dependent spontaneous polarization even in the absence of an applied field. Furthermore, some

pyroelectric materials also exhibit a spontaneous polarization with two or more equilibrium states, which can be switched by an applied external field. This property is called ferroelectricity [24], [25].

In addition, at a critical temperature called the Curie temperature (Tc) ferroelectrics undergo a phase transition from a high-temperature paraelectric (with no spontaneous polarization) into a low-temperature ferroelectric phase. At the vicinity of Tc, the temperature-dependent polarization change is maximized and therefore the largest EC response can be achieved. However, another typical characteristic of ferroelectric materials is the long-range ordering between the electric dipoles, forming regions of uniformly oriented polarization, known as ferroelectric domains. After field removal, these domains partially preserve their polarization orientation, leading to a non-zero remnant polarization (Pr) at zero field. Due to the presence of domains, ferroelectric materials exhibit a broad non-linear polarization hysteresis loop, as schematically shown in Figure 1.3b. In contrast to conventional ferroelectrics, relaxor-ferroelectrics (RFs) are chemically/compositionally disordered at the nanoscale, resulting in a short-range ordering between the electric dipoles [26], [27], [28]. Hence, RFs exhibit nano-sized regions of uniform polarization, called polar nano-regions. Due to this, RFs are less likely to preserve the dipolar orientation after removing the applied field, i.e., slim polarization hysteresis loop (Figure 1.3c), while still achieving large polarization values. Therefore, RFs were investigated as promising EC materials.

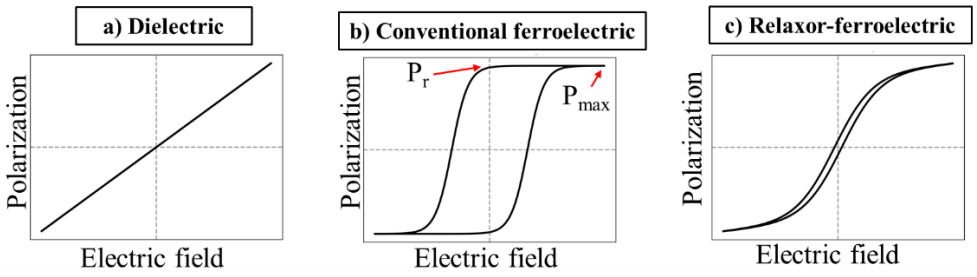


Figure 1.3: Polarization hysteresis loops of a) dielectrics, b) ferroelectrics and c) relaxors. P_{max} indicates the maximum polarization value at the maximum applied field, E_{max} (after [24]).

The most prolific materials for EC applications are oxide-based ceramics, such as $0.9Pb(Mg_{1/3}Nb_{2/3})O_3$–$0.1PbTiO_3$ (PMN–10PT) and $Pb(Sc_{1/2}Ta_{1/2})O_3$ (PST) [21], [29], [30]. In particular, PMN–10PT has been extensively characterized in bulk ceramic form and as thin and thick films. It shows excellent EC properties, with ΔT_{EC} as large as ~2.5 K, in thick film form [23]. Due to its properties and rich literature, in this thesis, PMN–10PT was selected as the EC material. It is worth emphasizing that the preparation of oxide-based EC materials require high-energy processes and elevated sintering temperatures, commonly in oxygen-rich atmospheres, for densification and optimal functional properties [31].

1.2.2 Magnetocaloric Effect

The MC effect is the adiabatic and reversible temperature change of a material associated to a change of the magnetic field H [4]. The heating/cooling cycle (Figure 1.4) is as follows:

(a) Magnetic moments are disordered throughout the material. There is no external magnetic field and the material is at temperature T_0.

(b) The application of an external magnetic field leads to a partial alignment of the magnetic moments, increasing the magnetization (M) of the system, and decreasing the

entropy of the magnetic subsystems. Under adiabatic conditions the total entropy is constant, hence the entropy loss is compensated by lattice vibrations therefore increasing the temperature
of the material by ΔT.

(c) The magnetic field is still applied on the material and the excess heat is transferred to a heat sink, cooling the material back to T_0.

(d) The magnetic field is turned off and the magnetic moments return to the disordered state, increasing the entropy and decreasing the temperature by ΔT, which is defined as the MC temperature change, ΔT_{MC}.

(e) The MC material absorbs heat from the heat source, returning to the same state as in (a).

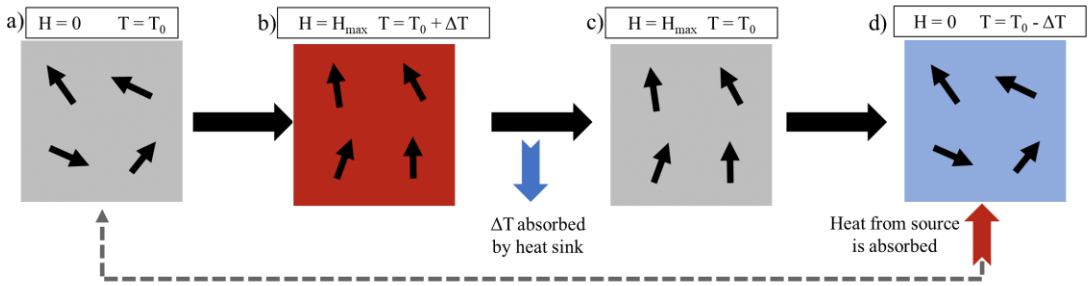


Figure 1.4: Schematic representation of the MC cycle (after [8]).

Similar to the EC effect, the MC effect can be mathematically derived from changes in entropy in the magnetic moment subsystem [4]:

$$dS = \left(\frac{\partial S}{\partial H}\right)_{\mathrm{T}} dH + \left(\frac{\partial S}{\partial T}\right)_{\mathrm{H}} dT. \tag{1.8}$$

The second term is associated to the specific heat capacity of the material at constant field H (c_{H}):

$$c_{\mathrm{H}} = \frac{T}{\rho}\left(\frac{\partial S}{\partial T}\right)_{\mathrm{H}}, \tag{1.9}$$

where ρ is the density of the material. The first term in (1.8) can be derived from the first law of thermodynamics:

$$dU = TdS + \mu_0\ HdM, \tag{1.10}$$

where U is the total internal energy of the system. The Gibbs free energy (G) is then expressed as:

$$dG = \ -SdT - \mu_0 MdH. \tag{1.11}$$

From the second derivatives, we obtain the Maxwell relation:

$$\left(\frac{\partial S}{\partial H}\right)_{\mathrm{T}} = \mu_0 \left(\frac{\partial M}{\partial T}\right)_{\mathrm{H}}. \tag{1.12}$$

Inserting this relation into equation (1.8), we then obtain:

$$dS = \mu_0 \left(\frac{\partial M}{\partial T}\right)_{\mathrm{H}}\ dH + \rho \frac{c_{\mathrm{H}}}{T}\ dT, \tag{1.13}$$

Under adiabatic conditions, the temperature change can be calculated as:

$$\Delta T_{\mathrm{MC}} = -\mu_0 \int_{H_\mathrm{i}}^{H_\mathrm{f}} \frac{T}{\rho c_\mathrm{H}} \left(\frac{\partial M}{\partial T}\right)_\mathrm{H} dH. \tag{1.14}$$

Suitable materials for MC applications must exhibit a significant magnetization change as a function of temperature. The materials that satisfy this condition are the ferromagnets, described further in the following section.

Ferromagnetic Materials

This section focuses on the ferromagnetic properties of materials, while also providing an overview of general magnetic properties. Typical ferromagnetic materials relevant to MC applications are presented and discussed.

All materials exhibit some form of magnetic response to an external magnetic field. The most commonly observed is diamagnetism, a negatively induced magnetization linearly proportional to the external field H [32], schematically shown in Figure 1.5. Similar to dielectrics, upon the removal of the applied field, the magnetization returns to zero. Some diamagnets can also exhibit a magneto-mechanical coupling, called piezomagnetism, if certain symmetry conditions are met. Moreover, some piezomagnets will exhibit a temperature-dependent spontaneous magnetization, known as the pyromagnetic effect. Lastly, if the spontaneous magnetization shows multiple equilibrium states, which can be switched by an external magnetic field, then the material is a ferromagnet. As shown in Figure 1.5, ferromagnetic loops are analogous to the ferroelectric polarization loops, and generally exhibit similar characteristics.

In addition, at some critical temperature, also called the Curie temperature (Tc), ferromagnetic materials will undergo a transition from a high-temperature phase with no spontaneous magnetization into a low-temperature phase with a spontaneous magnetization. Analogous to the ferroelectric case, in the vicinity of Tc a large temperature-dependent magnetization change can be achieved, resulting in maximized ΔT_{MC}.

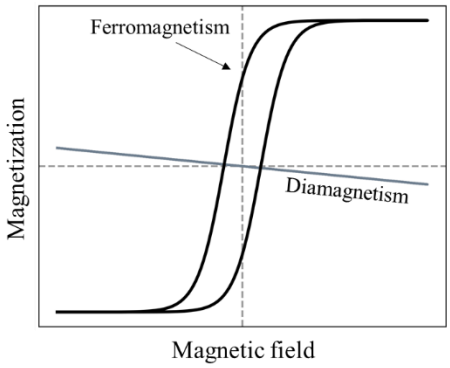


Figure 1.5: Schematic representation of a typical diamagnetic and ferromagnetic responses to an external magnetic field (after [4]).

The MC effect can be observed on a wide range of materials including pure metals, alloys and oxides. The benchmark MC materials are Gd, with ΔT_{MC} as large as ~5 K at 2 T [33], [34], and FeRh which exhibits values up to ΔT_{MC} ~9 K at 2 T [9]. However, metallic Gd and Rh are expensive, limiting their potential applicability and hindering investigations. An alternative is La-Fe-Si-Co-based (LFSC) alloys, which can exhibit ΔT_{MC} ~3.4 K at 2 T and room temperature conditions. This family of alloys are commercially

available and have been investigated under a wide range of experimental conditions [35]. Thus, LFSC has been chosen as the MC phase for the investigations in this thesis. It is worth emphasizing that the aforementioned materials are generally synthesized in oxygen-poor atmospheres to prevent oxidization and degeneration of the MC phase [34], [35], [36], [37], [38].

1.2.3 Multicaloric Effect

The caloric effects are not limited to a single stimulus, some materials exhibit responses to different external stimuli, called the multicaloric materials [6], [7]. It has been shown that the caloric performance of such materials may benefit from the coupling between the caloric phases [5], [39]. In addition, multicalorics can be single-phase, where the same material exhibits different caloric phases simultaneously, or composite, where the caloric phases are physically separated and may interact via interfacial coupling. Schematic representations of single-phase and composite multicalorics are shown in Figure 1.6.

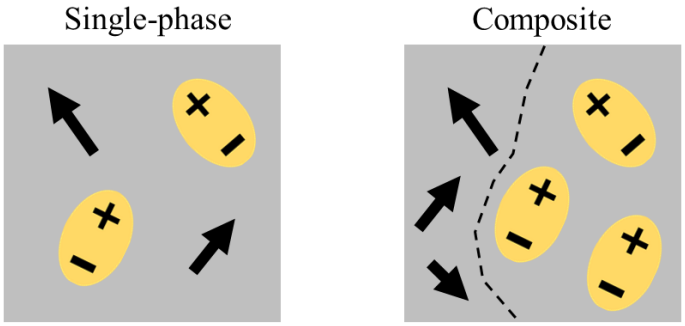


Figure 1.6: Schematic representation of single-phase and composite multicalorics.

In the following two sections, single-phase and composite room-temperature multicalorics will be discussed. Reports on EC and MC multicalorics will be addressed in further detail, with focus on the challenges and limitations therein.

Single-phase Multicalorics

Most of the literature on room-temperature multicalorics are investigations on single-phase materials and their properties [7]. For example, the combination of MC and eC has been investigated on a wide range of metallic alloys [10], [40], [41], [42], while the PST ceramics have been reported to exhibit both EC and BC properties [20]. However, the EC-MC combination has been shown to be challenging to achieve near room temperature caloric responses. Prah et al. investigated the multicaloric properties of $Pb(Fe_{1/2}Nb_{1/2})O_3$-based (PFN) ceramics. In their work, the authors reported a ΔT_{EC} up to ~1.1 K at room temperature, whereas the reported ΔT_{MC} of ~3.6 K was achieved only at cryogenic temperatures [43], shown in Figure 1.7.

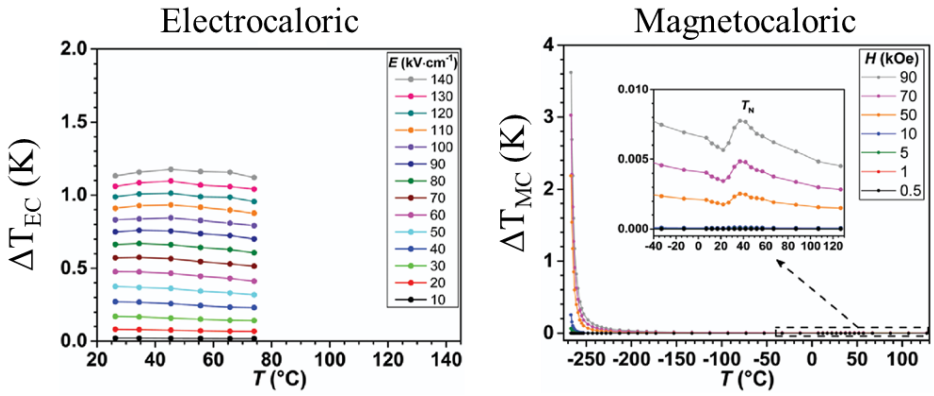


Figure 1.7: Electrocaloric and magnetocaloric responses of a PFN-based composition. Notice the different temperature range (after [43]).

This large difference between the caloric maxima is due to the conflicting nature of ferromagnetism and ferroelectricity, which makes the preparation of single-phase EC-MC multicalorics difficult, particularly with both properties at room temperature conditions [44]. At a fundamental level, ferromagnetism in a material requires its Fermi level to lie in the region where the 3d and 4s bands overlap. This condition, as well as unpaired d-shell electrons, leads valence electrons to partially occupy both 3d and 4s bands, effectively resulting in an asymmetric spin occupation, thereby giving rise to a spontaneous magnetization, shown in Figure 1.8a. On the other hand, ferroelectricity arises in materials from an off-center displacement of an ion, which results in a non-zero dipolar moment (Figure 1.8b). Such behavior is commonly observed on materials with a perovskite structure, such as PMN–10PT, in which the displacement occurs on the B-site at the center of the oxygen octahedron. However, the B-site materials are, for the most part, elements which exhibit an effectively complete d-shell, such as Ti and Nb, conflicting with the key requirement for ferromagnetism.

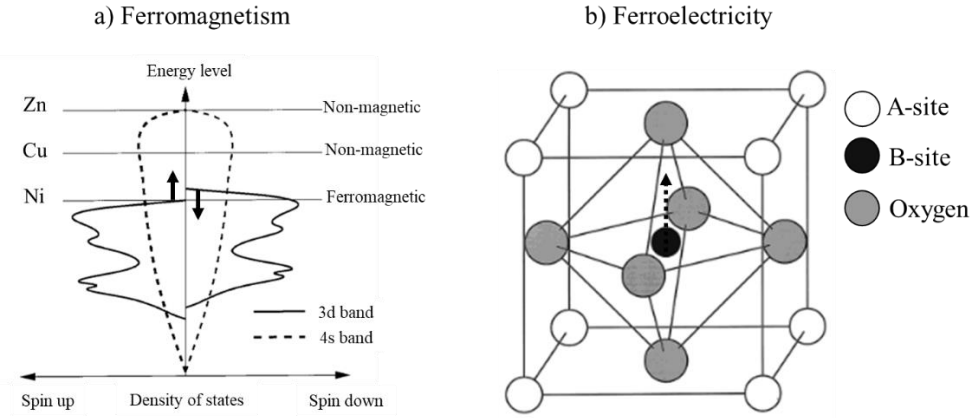


Figure 1.8: Schematic representation of a) ferromagnetism in elemental Ni and b) ferroelectricity in the perovskite unit cell (after [44]).

While materials with partially filled d-bands may be used in perovskites at the B-site, effects such as Jahn-Teller distortions decrease the likelihood of off-center displacements, limiting ferroelectric behavior [44]. Over the last decades, research has been done on overcoming such challenges, with no report of single-phase multicalorics with significant response near room temperature conditions. One approach to achieving simultaneous

ferroelectricity and ferromagnetism at room temperature is the preparation of multiferroic composites, where the distinct ferroic phases are physically separated.

Composite Multicalorics

Composite materials can be prepared on a wide range of configurations, such as multilayers or particulate composites [7], [45], schematically shown in Figure 1.9. In the former, the layers are stacked atop each other, and the caloric phases interact via interfacial coupling. Similar structure has been successfully prepared for EC-only multilayer capacitors, which exhibited a large caloric output [22]. However, due to the large heat losses between the caloric layers, there is no report on the direct characterization of the caloric effects of EC-MC multilayered composites and the literature is mostly limited to investigating the coupling between the ferroic phases [46].

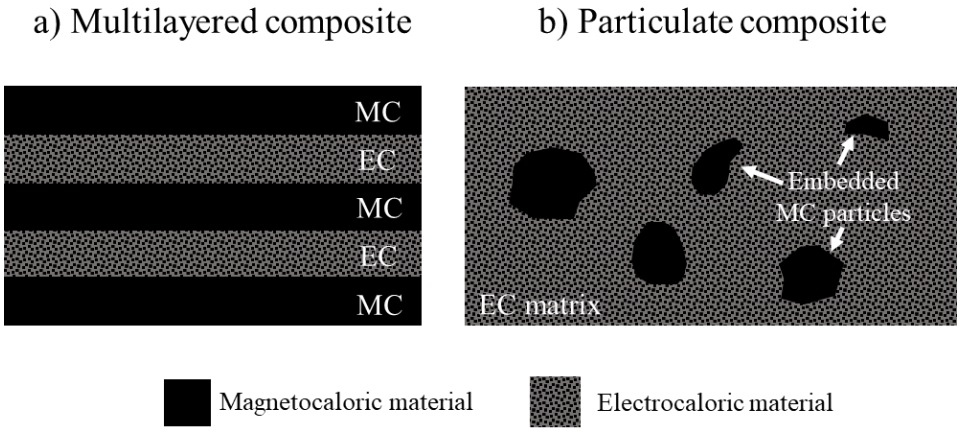


Figure 1.9: Schematic representation of a) multilayered and b) particulate composites. The different colors represent distinctive materials.

On the other hand, composites may also be prepared as an EC ceramic matrix with MC particles embedded into it. In this case, composites may benefit from properties of both phases, for example EC and MC responses, as well as the interaction between them, such as via the Maxwell-Wagner polarization effect [47], [48], [49]. However, to date, there is only one report of such composite, with limited success. Mikhaleva et al. prepared a particulate composite by combining the ferroelectric $PbTiO_3$ (PT) with 15 vol% of the ferromagnetic $La_{0.7}Pb_{0.3}MnO_3$ (LPM) [50]. The prepared composite pellets were conventionally sintered at 900 °C in air. Although no chemical reaction between the phases was reported, the microstructure exhibited cracking due to the different thermal expansion coefficients, shown in Figure 1.10a, which is deleterious to the overall properties of the samples. The authors reported a ΔT_{MC} of ~0.06 K at magnetic field of 0.5 T and a ΔT_{EC} of ~2.3 K at 4.5 kV cm^{-1}, as shown in Figure 1.10b. However, the MC and EC responses were measured at 57 °C and 493 °C, respectively, far from room temperature conditions.

Furthermore, only ΔT_{MC} was measured directly, and the magnetic hysteresis loops were not reported. It is worth emphasizing, that the ΔT_{EC} was estimated via specific heat measurements and constitutive equations. The authors were likely unable to directly measure neither the EC effect nor the ferroelectric hysteresis loops, as the microstructural damage in the samples may have resulted in a high electrical conductivity.

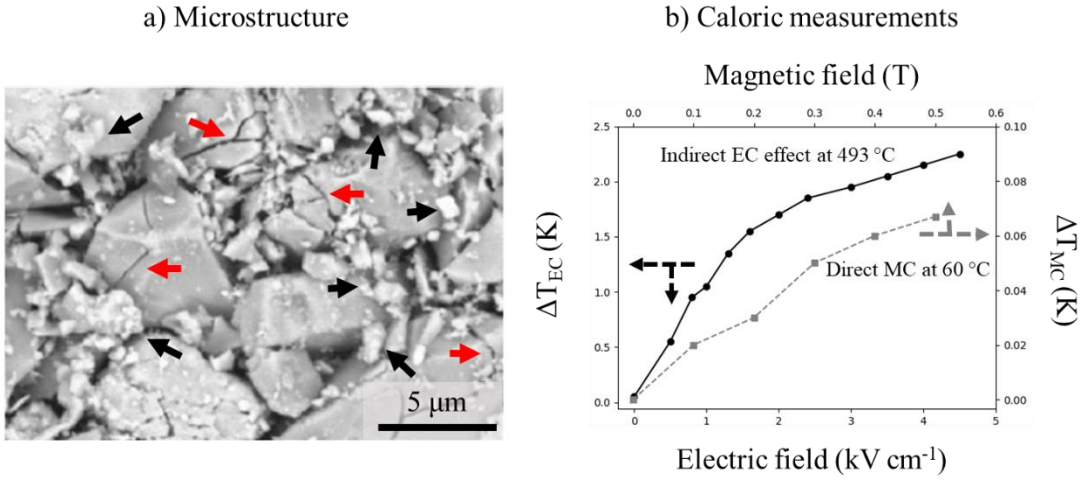


Figure 1.10: a) Micrograph of the multicaloric composite. The small particles with lighter contrast (indicated by black arrows) correspond to the EC phase. Notice the cracking (red arrows) in the grains of the MC phase. b) Caloric measurements of EC and MC responses of the PT-LPM composite (after [50]).

The current literature of EC-MC multicaloric composites is still mostly unexplored, particularly at near room temperature conditions. Moreover, as previously discussed, EC-based structures are promising alternatives for cooling at the micro-scale. Therefore, the multicaloric composite should be prepared as a µm-thick sample, as well as be suitable for integration onto electronic devices. In light of this, in the scope of my PhD, I prepared and investigated EC-MC multicaloric composite thick films. For characterization purposes, it is essential to prepare the multicaloric films on a thermally insulating substrate.

The investigated materials were PMN–10PT EC ceramics and LFSC MC intermetallic alloy, since these materials exhibit caloric properties near room temperature conditions. However, the preparation conditions of PMN–10PT and LFSC are conflicting. While the EC material conventionally requires high temperatures (≥1000 °C) in oxygen-rich atmospheres for densification, the MC material should be thermally treated at temperatures below 1000 °C in oxygen-poor atmospheres to avoid oxidation and decomposition of the MC phase [34], [35], [36], [37], [38]. In addition, the work of Mikhaleva et al. indicates that materials with incompatible thermal expansion coefficients will result in significant microstructural damage. In other words, a room-temperature film preparation method is needed.

1.3 Powder Aerosol Deposition Method

One of the most prominent low-temperature film preparation technique is the aerosol deposition (AD) method, also known as powder aerosol deposition. A schematic representation of the system is shown in Figure 1.11. The deposition process is based on the collision of fine particles with high kinetic energy onto a substrate [51], [52], onto which they fragment and rebond, thus forming dense thick films entirely at room temperature.

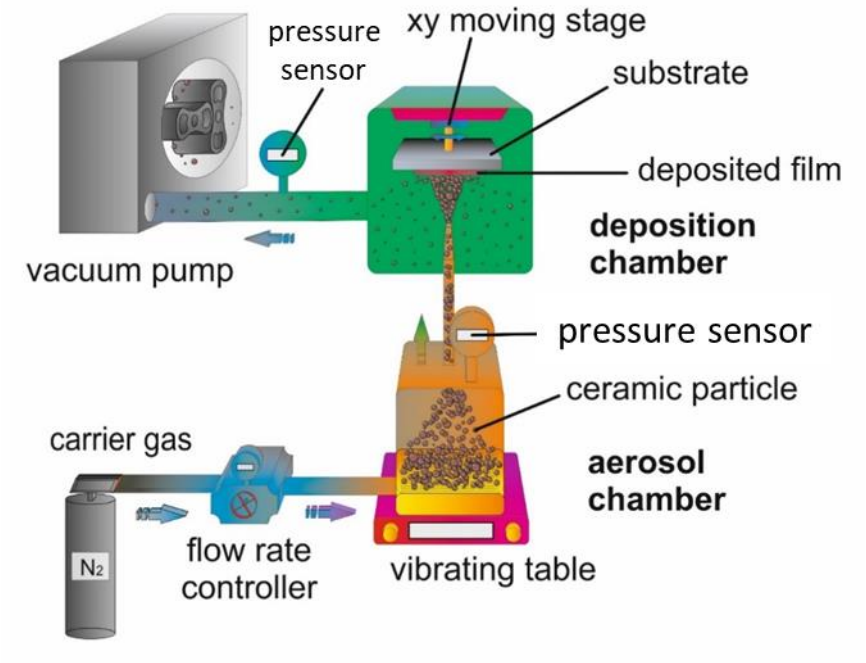


Figure 1.11: Schematic representation of an AD device (after [53]).

The starting powder is placed in the aerosol chamber, which is connected to the deposition chamber through a pipe and nozzle. The deposition chamber is then evacuated to a pressure $p_0 \leq 0.5$ mbar. To form the aerosol, the vibrating table is turned on and the carrier gas injected into the aerosol chamber. Due to the pressure difference the aerosolized fine particles are carried towards deposition chamber at high velocities, generally 200 m s^{-1} – 600 m s^{-1} [54], [55]. Upon colliding with the substrate, the moving particles fragment and rebond, thereby forming the film. The substrate is moved along the programmed length several times, gradually increasing the film thickness until the desired value is reached. Generally, the key process parameters that can be adjusted in AD are the carrier gas (N_2, He, Ar), carrier gas flow rate (0.5 L min^{-1}–20 L min^{-1}), number of scans (1–50), scan velocity (1 mm s^{-1}–10 mm s^{-1}) and nozzle geometry [53].

1.3.1 Powder Requirements

For a successful deposition, the starting powder also needs to be optimized [56], [57]. If the particle size is smaller than 0.1 µm, then the particles do not have enough mass and, therefore not enough kinetic energy to fragment and rebond with the substrate. The small particles will bounce off the substrate without forming the film.

Particles from 0.1 µm to 10 µm are within the optimal deposition range. These particles can achieve enough kinetic energy to fracture and rebond onto the substrate. It is worth mentioning that different powders will exhibit different optimal distributions [53], [58]. While ceramic-based powders are commonly from 0.2 µm to under 1 µm, metal-based powders tend to be at 2 µm–5 µm range. In addition, within an optimal particle size range for a material, further optimizations of other deposition parameters are likely needed.

Lastly, if the particle size is much larger than 10 µm, the particles will have excessive kinetic energy and cause abrasive blasting on the substrate, damaging it without adhering, or partially forming a film with significant defects and mechanical instability [51], [57]. A schematic representation of the influence of particle size on the deposition process is shown in Figure 1.12.

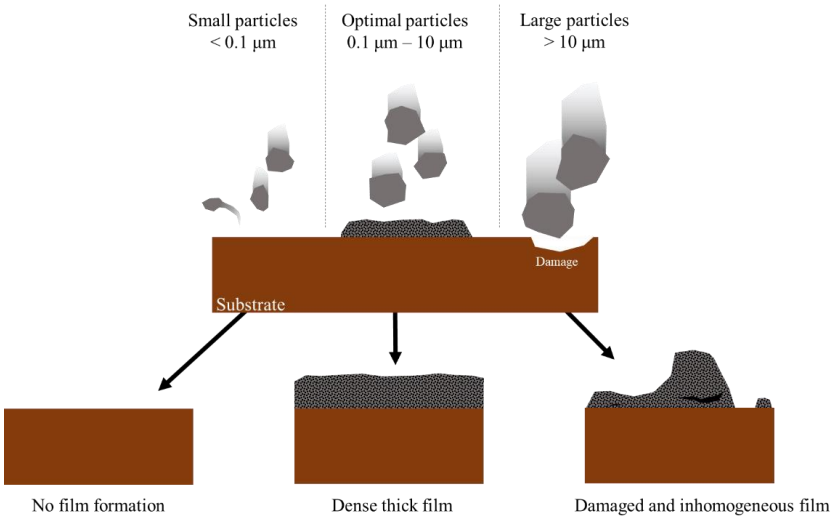


Figure 1.12: Schematic representation of the influence of ceramic particle size on the deposition process (after [51]).

In addition, it has been shown that heating the PMN–10PT powder prior to the deposition is essential to achieving a successful deposition. As shown in Figure 1.13 a non-treated (NT) PMN–10PT powder does not adhere to the substrate, while a heat-treated (HT) powder forms a dense thick film. After the heat treatment, the starting powder achieves a suitable crystallinity which results on better fracturing and plastic deformation during the deposition process. Furthermore, after the heat treatment, the PMN–10PT powders were additionally milled for 30 minutes (HM30) and 60 minutes (HM60). Under the same preparation conditions for all powders, the authors observed an increase in film thickness from the HM30 powder, indicating that the additional milling step was necessary in order to achieve the optimized particle size. However, the films prepared from the HM60 powder, exhibited significantly inhomogeneous thickness, evidencing that excessive milling is detrimental to the deposition efficiency [56], [57].

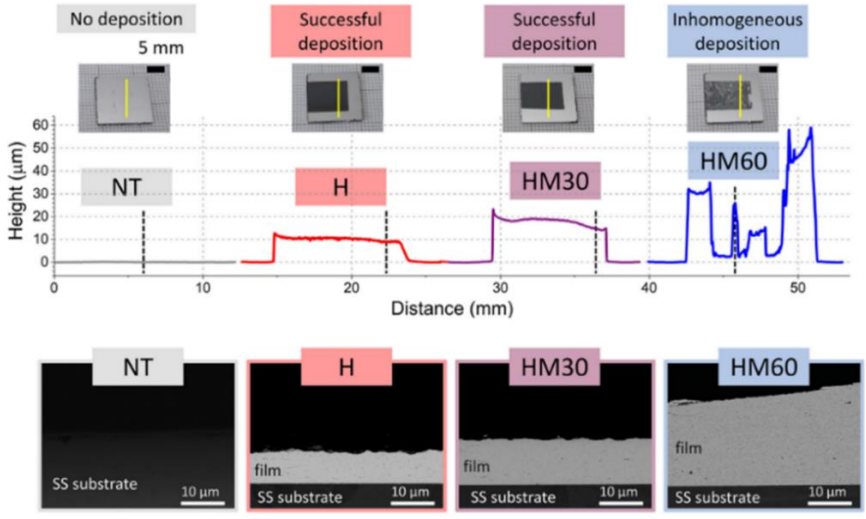


Figure 1.13: Photographs, line profile of as-deposited PMN–10PT films, and cross-sectional micrographs showing the influence of powder processing on the film deposition. All the films were prepared under the same conditions (after [56]).

1.3.2 Aerosol-Deposited Thick Films

Due to the high kinetic energy during the deposition process, typical as-deposited ceramic films tend to exhibit characteristics such as high density (over 95 % of theoretical density), nano-sized pores and strong adhesion to the substrate. However, the fracturing nature of the method also has drawbacks, with as-deposited films exhibiting residual internal stresses from hundreds of MPa to GPa [59], [60], which significantly affect the functional properties, such as the polarization hysteresis loops. Therefore, aerosol-deposited films generally undergo a post-annealing process to partially release such stresses. The annealing temperature can range from 400 °C to 800 °C, depending on the substrate material [23], [56], [61], [62]. A comparison between the microstructural and electrical properties of a PMN–10PT ceramic film deposited on stainless-steel before and after annealing at 500 °C in air, is shown in Figure 1.14.

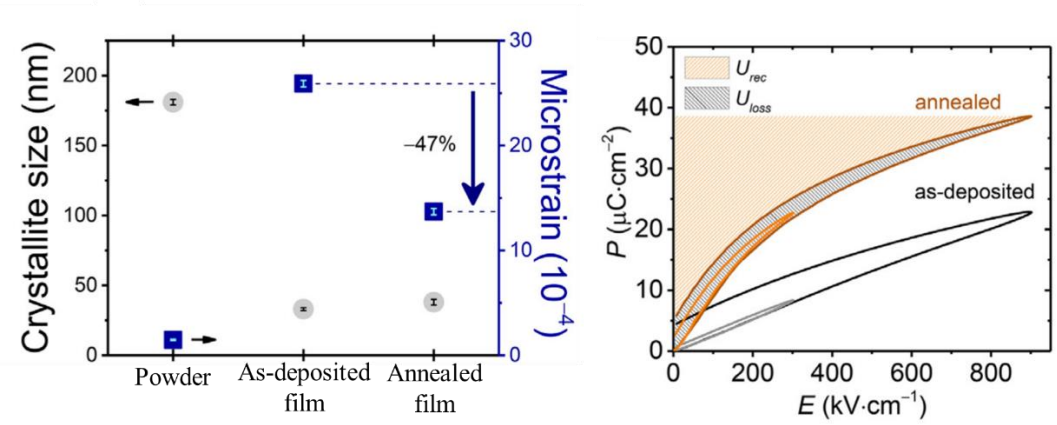


Figure 1.14: Influence of annealing on the microstrain and ferroelectric properties of aerosol-deposited PMN–10PT films (after [56]).

The literature of aerosol-deposited thick films is mainly based on ceramic materials including PMN–10PT [23], [56], $BaTiO_3$ [63] and Al_2O_3 [53], [60] and $Pb(Zr,Ti)O_3$ [64], [65]. In particular, using this method, PMN–10PT EC films were successfully prepared on thermally-insulating polymer substrates, and have been shown to achieve a ΔT_{EC} as large as 1.5 K at room temperature [27]. Since neither elevated temperatures nor an oxygen-rich atmosphere are required in AD, metallic materials have also been successfully prepared, such as Al [53], [58] and Ag [66]. Therefore, AD is a suitable option for the preparation of ceramic-metal composites [51]. As shown in Figure 1.15, different phases can be homogenized together and subsequently co-deposited.

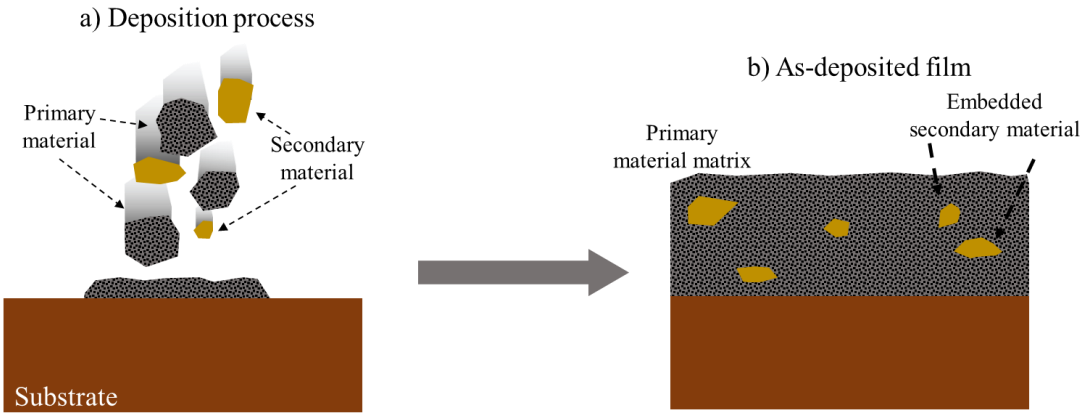


Figure 1.15: Schematic representation of a) the AD process for composite powders and b) the composite thick-film microstructure.

It is worth emphasizing that the literature on AD-prepared ceramic-metal composites has mostly focused on scratching resistance and enhanced mechanical properties [67], [68]. Thus far, there are no reports on the preparation of EC-MC ceramic metal composites via the AD method.

1.4 Characterization Methods of Caloric Materials

In this section, the characterization of caloric properties will be discussed. In particular, the thermistor-in-calorimeter (TiC) and infrared (IR) camera methods will be addressed in detail, as these are the techniques used for the caloric investigations in this thesis. The characterization of caloric materials can be classified as either indirect, where the caloric response is calculated via a mathematical approach or direct, where the time-dependent temperature change of the sample is directly obtained [69], [70].

In the case of indirect methods, the caloric temperature change can be obtained by measuring the polarization/magnetization hysteresis loops over a wide temperature range and then calculated via equation (1.7)/equation (1.14); This method offers a benchmark value for the caloric output of the investigated material. However, it is not fully accurate as it does not account for Joule heating and heat losses to the substrate. In addition, the indirect method assumes an ideal chemical, polar and thermodynamic equilibrium at all times, which may not be true in all cases [23], [69].

Direct characterization methods, such as the TiC and the IR camera methods, provide a more precise understanding of the caloric material and its performance. Figure 1.16 shows a comparison of the EC response of a ceramic PMN–10PT thick film obtained via the indirect, TiC and IR camera methods. Notice that the direct methods are in great agreement with each other, whereas the indirect method underestimates the ΔT_{EC} value.

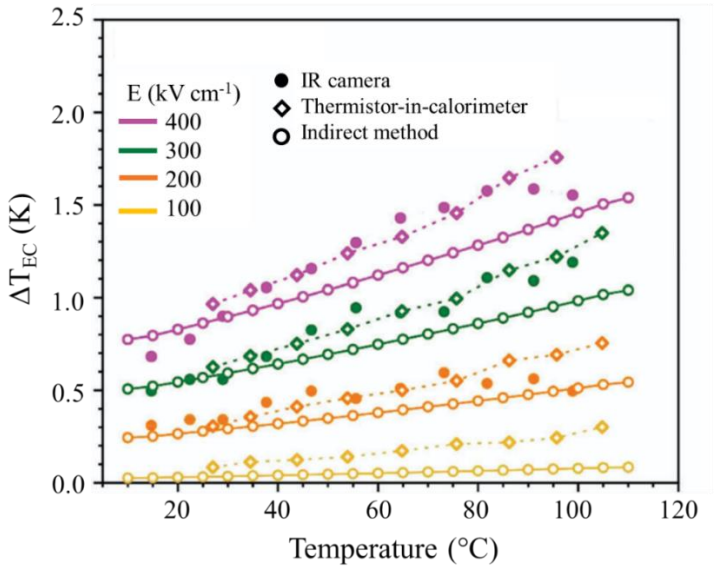


Figure 1.16: Directly measured EC response of a ceramic thick film obtained via indirect and direct methods (after [23]).

However, the main drawback of direct methods are systematic heat losses. The measured temperature change (ΔT_{M}) is a fraction of the intrinsic ΔT of the material. The relationship between those values is described as [23], [69]:

$$\Delta T = k\ \Delta T_{\mathrm{M}}, \tag{1.15}$$

where k is called the correction factor, which is related to the passive thermal mass in the system and quantifies the systematic heat losses. Thus, significant research has been done on minimizing the values of k by optimizing the characterization methods, and searching for more suitable substrate materials, as these correspond to more than 80% of the correction factor [23].

1.4.1 Thermistor-in-Calorimeter Method

The thermistor-in-calorimeter method is a direct characterization technique of EC properties, and can achieve excellent thermal stability, thereby being suitable for the characterization of both bulk and film samples [23], [29], [69]. For the measurements, the sample requires a glass-bead thermistor and wires to be attached to the sample with adhesives, shown in Figure 1.17.

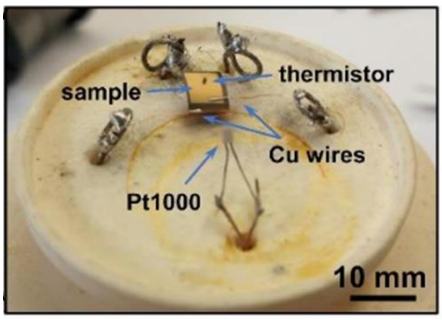


Figure 1.17: Photograph of a film prepared for the TiC method. The Pt1000 is the environment temperature sensor (after [23]).

Since the TiC method operates at the 1 s time scale, k can be obtained by calculating the ratio of the active heat capacity ($C_{\mathrm{p}}^{\mathrm{active}}$), corresponding to the film under electrode, and the total heat capacity ($C_{\mathrm{p}}^{\mathrm{total}}$), considering the entire system. In the case of the TiC method, k can be mathematically represented as [69]:

$$k = \frac{C_{\mathrm{p}}^{\mathrm{total}}}{C_{\mathrm{p}}^{\mathrm{active}}}. \tag{1.16}$$

In the case of EC ceramic thick films, k can range from 30 to 60, depending on film thickness, electrode area, mass of the adhesives and substrate material.

1.4.2 Infrared Camera Method

Another commonly used direct characterization technique is the IR camera method [14], [23], [41], [71], schematically shown in Figure 1.18. It has been widely used for the characterization of caloric effects in various materials, particularly for MC and eC effects of bulk materials [33], [41], [72], [73]. In contrast to the TiC method, the IR camera measurements only require an additional high-emissivity black paint coating. In addition, the temporal resolution of this method is inherent the IR camera acquisition rate which may reach values as small as ~1 ms. Due to this, the correction factor for the IR camera method is calculated using finite-element modelling, and can be significantly lower values when compared to TiC, with k as low as ~3 [23].

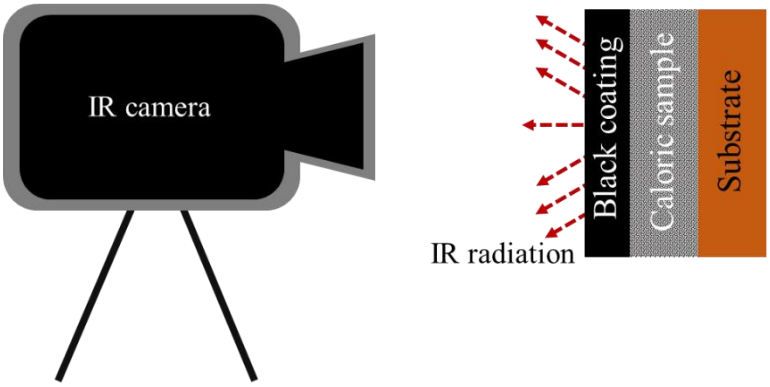


Figure 1.18: Schematic representation of the IR camera set up. The sample emits IR radiation which is captured and processed by the IR camera, resulting on a thermographic map.

However, in most reports neither the coating thickness nor the coating technique are reported in sufficient detail [73], [74], [75], [76], [77]. The reported black coating techniques are spray coating and ink printing. The former can be performed with commercially available spray paint. While it is suitable for large bulk samples, it lacks thickness control. The prepared black coatings can reach values as large as ~100 µm, hindering its applications on µm-thick films [78], [79]. To circumvent this the ink printing technique can be used. This method allows for the preparation of black paint coatings as thin as 3.5 µm [23], which is appropriate for flexible films. However, it requires the sample to be processed through an office printer mechanism, which curves and bends therefore being unsuitable for larger or brittle samples. In light of this, a coating method which allows for the preparation of µm-thick black paint coatings, with precise thickness control that can be used on samples regardless of size and geometry is highly desired. Furthermore, the limits of the IR camera method are not yet fully understood. The influence of the substrate

material, coating thickness and film thickness on the measured values remain mostly unaddressed.

1.5 Objectives and Hypotheses

The main focus of this thesis is the preparation and characterization of aerosol-deposited multicaloric composite thick films. However, the overall literature on the topic is scarce and mostly unexplored. For example, although there are investigations of ceramic-metal particulate composites prepared via AD [80], none study the influence of the metallic content on the overall dielectric properties of the films. In light of this, prior to the preparation of the PMN–10PT/LFSC multicalorics, we have aerosol-deposited ceramic-metal composites with non-caloric properties. Starting from fully ceramics and gradually increasing metallic content, this preliminary work focused on investigating and understanding the effects of the metallic content on the electrical properties of the films. Aluminum oxide (Al_2O_3) and metallic Al were used as the ceramic and metallic phases, respectively, as these are affordable materials which have been previously prepared as thick films via the AD method [53], [57], [60]. It is worth emphasizing that these materials do not exhibit caloric properties, ensuring that the observed effects are inherent to ceramic-metal composites.

Moreover, the literature of the direct characterization of caloric films is limited. Thus far, there is no report discussing the influence of the substrate on the caloric measurements, which is particularly relevant for films. In addition, for characterizations via the IR camera method, a high-emissivity black paint coating is essential. In this case, most studies only report case-specific parameters, if at all [14], [23], [73], [74]. In light of this, investigations and optimizations targeting maximized caloric response related to the direct characterization methods were also performed. We have numerically investigated how the thermal properties of the substrate affect the measurement response. The optimal thicknesses of the caloric film and black paint coating was also considered, aiming for maximized caloric measurements via the IR camera method. In light of these results, we have developed and optimized a novel black coating preparation method.

These investigations established the foundation necessary for achieving the primary objective of this thesis. Then, by combining the LFSC MC alloy with the PMN–10PT EC ceramic, multicaloric composites were successfully prepared via the AD method and directly characterized.

The objectives of this doctoral dissertation are the following:

1. To perform the feasibility study on how to prepare the ceramic-metal composite using the AD method, prior to the preparation and investigation of multicaloric composites. Inexpensive, inert ceramic alumina (Al_2O_3) powder and metal aluminum powder are used for this purpose.
2. To benchmark thermal parameters which minimize substrate influence on EC measurements, particularly via the IR camera method.
3. To develop a novel black-coating method which allows for maximized direct characterization of caloric responses via the IR camera method.
4. To prepare a ceramic-metal multicaloric composite thick films via the AD method, by combining PMN–10PT and LFSC intermetallic alloy and integrate the films onto gold-sputtered polyimide substrates.

5. To characterize the electrical and magnetic properties of composite films, including EC and MC performances using direct characterization methods.
6. To investigate the influence of the metallic particles on the functional properties of thick films.

This doctoral dissertation has the following hypotheses:

1. Al_2O_3/Al composite films can be prepared using the AD method, with homogeneous distribution of Al particles in the Al_2O_3 matrix. Influence of the Al content can be observed in the dielectric properties of prepared composite thick films.
2. To minimize the substrate influence on the EC performance of thick films, the substrate material needs to exhibit low thermal conductivity, such as polymers, thereby increasing measurement response.
3. For the IR camera measurements of caloric response, optimized measurements can be achieved by fine-tuning the thickness ratio between the functional layer and the black coating. The airbrush method is suitable for preparing the required black coating layers.
4. PMN–10PT and LFSC powders, with appropriate processing can achieve the suitable particle for efficient AD of the composite thick films, while preserving the caloric phases. With appropriate processing of PMN–10PT and LFSC powders, the composite thick films can be prepared by AD onto gold-sputtered polymer substrates with a homogenous distribution of MC particles across the EC matrix.
5. The presence of metallic particles will enhance the dielectric and EC responses of the prepared films.
6. After the AD process, the metallic particles preserve the MC phase. The AD composites exhibit ferromagnetic behavior and MC response at room temperature.

Chapter 2

Investigation of Structural and Electrical Properties of Al_2O_3/Al Composites prepared by Aerosol Co-Deposition

The literature of aerosol-deposited ceramic-metal composite films does not address the influence of the metallic phase on the electrical properties of the composite films [53], [80]. In light of this, prior to the preparation of the multicaloric samples, we have combined Al_2O_3 and Al as the ceramic and metallic phases, respectively. The materials were selected as these are affordable and have previously been prepared via the AD method. In addition, since neither of the materials exhibit caloric properties, the findings in this work could be understood as inherent of ceramic-metal composites.

In this work, the ceramic and metal starting powders were homogenized at a wide range of Al vol%, namely from 0 vol% Al to 100 vol% Al. The composite films exhibited enhanced dielectric permittivity when compared to Al_2O_3 films. This is due to the Maxwell-Wagner polarization, which is an effective increase in the permittivity induced by the metallic particles. In the case of Al_2O_3/Al composites, the samples exhibit electrically conductive behavior starting at 29 vol % Al. However, up to 15 vol% Al, the composite films exhibited an enhanced dielectric permittivity with no significant change in dielectric losses. In other words, improved dielectric properties can be achieved in ceramic-metal composites even at low concentrations of metallic content.

This chapter addresses thesis objectives: 1

Published in: V. Regis, M. Sadl, G. Brennecka, A. Bradesko, U. Tomc and H. Ursic, "Investigation of Structural and Electrical Properties of Al_2O_3/Al Composites Prepared by Aerosol Co-Deposition," Crystals, vol. 13, p. 850, 2023 (IF = 2.4, 2023)

My contribution: I processed the Al_2O_3 powders with heating and milling steps, as well as performed the homogenization process for the composite powders. I prepared the films via the AD method. In addition, I performed the following measurements: profilometry, permittivity, powder granulometry, numerical simulations and quantification of the embedded metallic phase. In collaboration with colleagues, I participated in the following experiments: x-ray diffraction, scanning electron microscopy and conductive atomic force

microscopy. I elaborated the concept of the manuscript and wrote the paper, with assistance of the co-authors.

crystals

MDPI

Article

Investigation of Structural and Electrical Properties of Al_2O_3/Al Composites Prepared by Aerosol Co-Deposition

Victor Regis [1,2], Matej Šadl [1], Geoff Brennecka [3], Andraž Bradeško [1], Urban Tomc [4] and Hana Uršič [1,2,*]

[1] Electronic Ceramics Department, Jožef Stefan Institute, Jamova Cesta 39, 1000 Ljubljana, Slovenia
[2] Jožef Stefan International Postgraduate School, Jamova cesta 39, 1000 Ljubljana, Slovenia
[3] Colorado School of Mines, 1500 Illinois Ave., Golden, CO 80401, USA
[4] Laboratory for Refrigeration and District Energy, Faculty of Mechanical Engineering, University of Ljubljana, Aškerceva Cesta 6, 1000 Ljubljana, Slovenia
* Correspondence: hana.ursic@ijs.si

Abstract: As the microelectronic industry develops, components that can perform several different tasks receive increasingly more attention, resulting in multifunctional materials being highly sought after. Al_2O_3 is widely present in electronic applications as a protective coating or as an electrical and thermal insulator due to its mechanical and thermal stabilities and chemical inertness. Al_2O_3 is also an important dielectric material, with high resistivity and stable permittivity over a wide range of temperatures and electric fields, but its modest permittivity necessitates large effective areas or extremely thin layers when a large capacitance is desired. Composites consisting of discrete conducting phases within an insulating matrix can produce large capacitance via Maxwell–Wagner polarization. In this work, Al_2O_3/Al composite thick films with different volume ratios of Al were prepared using the aerosol deposition method. A relative dielectric permittivity (ε_r') of 800 at 1 MHz was achieved at 27 vol% of Al, a sixty-sevenfold enhancement compared to Al_2O_3. On the other hand, dielectric losses, tan(δ), at 1 MHz increased from 0.01 for Al_2O_3 up to 0.58 for the composite with 27 vol% of Al. A finite-element model of the composites was implemented, supporting the nonlinear electrical behavior of the composites as function of vol% of Al. Our results show novel possibilities for the applications of Al_2O_3-based materials in the microelectronic industry, especially for temperature-sensitive applications, for which the integration strengths of aerosol deposition are valuable.

Keywords: alumina; aluminum; multifunctional materials; thick films; aerosol deposition

check for updates

Citation: Regis, V.; Šadl, M.; Brennecka, G.; Bradeško, A.; Tomc, U.; Uršič, H. Investigation of Structural and Electrical Properties of Al_2O_3/Al Composites Prepared by Aerosol Co-Deposition. *Crystals* **2023**, *13*, 850. https://doi.org/10.3390/cryst13050850

Academic Editor: Dah-Shyang Tsai

Received: 24 April 2023
Revised: 12 May 2023
Accepted: 19 May 2023
Published: 21 May 2023

Copyright: © 2023 by the authors. Licensee MDPI, Basel, Switzerland. This article is an open access article distributed under the terms and conditions of the Creative Commons Attribution (CC BY) license (https://creativecommons.org/licenses/by/4.0/).

1. Introduction

In recent decades, the electronics industry has sought increasingly small high-performance components that can perform multiple functions at the same time, resulting in more intense research on multifunctional low-cost materials [1]. For example, Al_2O_3, or namely alumina, is already used in electronic devices as a protective layer due to its high mechanical stability, chemical inertness, and electrical insulating properties [2–4] and therefore is a promising candidate for multifunctional applications. In light of this, it is highly desirable to expand the functionalities of Al_2O_3-based layers, for example for complementary metal-oxide semiconductor (CMOS) or embedded capacitor applications [5,6]. However, in such cases a large dielectric permittivity ε_r' is needed [7,8], usually ∼30 for CMOS applications and over several hundred for embedded capacitors. Therefore, the low relative dielectric permittivity of Al_2O_3, which is ∼10 at 1 kHz [9], is a limiting factor.

Ceramic–metal composite materials can exhibit a significantly larger dielectric permittivity when compared to that of pure ceramics, in our case Al_2O_3. When an external electric field is applied, the free electrons from the embedded metal particles move to the metal/insulator interfaces, acting as additional electric dipoles, therefore increasing the total dielectric permittivity. This is known as Maxwell–Wagner polarization [10–12]. By

increasing the metallic content within the matrix, ε_r' also increases. However, at a critical concentration the metallic material will form a conductive percolative path across the insulating matrix, which will undergo an insulator-conductor transition. In addition, there is a sharp increase in ε_r' at a critical concentration, also called the percolation threshold [13–15]. The enhancement of ε_r' for ceramic–metal composites at the percolation threshold is typically for a factor of a few tens. However, the tan(δ), also referred to as dielectric losses, also tends to increase by a similar amount [16–18]. For example, for $BaTiO_3/(Ni_{0.3}Zn_{0.7})Fe_{2.1}O_4$ composites, both the ε_r' and dielectric losses, tan(δ), were reported to have increased by a factor of 10 [19].

The preparation of ceramic–metal composite films can be difficult, as conventional ceramic-based film preparation methods usually rely on high sintering temperatures (above 900 °C) which leads to undesired effects such as interdiffusion and oxidization of the metallic filler [2,20,21]. To overcome this issue, aerosol deposition (AD) can be used. The AD method is a spray-coating process that allows for the preparation of dense films at room temperature. The ceramic–metal composite powder is mixed with a carrier gas to form an aerosol which is ejected towards the substrate with high kinetic energy due to pressure difference. Upon impact, the particles fragment and rebond to the substrate forming the film [22,23]. The AD method allows parameters such as carrier gas, gas flow rate, and number of scans to be controlled.

Investigations of Al_2O_3 films prepared via AD have been previously reported [2,24,25], as well as Al_2O_3-based composite films with metallic, such as silver [26] and copper [27], and polymer fillers [9]. However, the research on Al_2O_3-based composites has been focused on mechanical and optical properties, while the influence of the metallic filler on the dielectric permittivity of the composite was not studied. In addition, Al as a metallic filler in the ceramic matrix has not yet been reported. In light of this, we prepared Al_2O_3/Al composite films using the AD method and investigated the effects of the Al filler on the structure and on the dielectric properties of the samples. We used Al as the metallic filler since it is an affordable, abundant material that was shown to have a high AD rate [2]. The ceramic–metal composite powders were prepared with different Al vol%, ranging from Al_2O_3 (0 vol%) to Al (100 vol%). A 67-fold enhancement of the dielectric permittivity of Al_2O_3 was achieved for the first time, expanding the possibilities for Al_2O_3-based electronic components.

2. Materials and Methods

For the preparation of composites, raw Al (99.96%, 2 HPC, Toyal Europe, Accous, France) and Al_2O_3 (99.8%, A 16 SG, Almatis, Ludwigshafen, Germany) powders were used. The Al_2O_3 was thermally treated in a chamber furnace (Custom-made, Terna, Ljubljana, Slovenia) at 1150 °C for 1 h with heating and cooling rates of 5 K × min^{-1} and additionally milled in a planetary ball mill (PM400, Retsch, Haan, Germany) at 200 min^{-1} for 4 h using an Al_2O_3 milling jar and yttrium-stabilized zirconia milling balls with diameters of 3 mm in iso-propanol as a liquid medium. The treatment of the Al_2O_3 powder was necessary to achieve a particle size distribution suitable for the AD method [21]. The as-received Al powder was already within the optimal particle size range, and therefore no additional processing was required. To prepare the composites, Al_2O_3 and Al powders were dry mixed in different Al volume ratios (0 vol%, 3 vol%, 7 vol%, 13 vol%, 15 vol%, 21 vol%, 23 vol%, 27 vol%, 33 vol%, 60 vol%, and 100 vol%) and homogenized in a roll-mill at 50 min^{-1} for 48 h with yttrium-stabilized zirconia balls with 10 mm diameters. Prior to the AD, the powders were sieved through an 80-micrometer mesh and vacuum-dried for 12 h at 80 °C and at 10 mbar. The particle size analyses of the powders were performed using a light-scattering laser granulometer (S3500, Microtrac, York, PA, USA), and isopropanol was used as the medium. The particle size distribution of the powders (Supplementary Material: Figure S1) shows that all compositions are within 0.2 µm–5 µm optimal range for AD [20].

The AD apparatus was provided by InVerTec e.V., Bayreuth, Germany. Detailed information of the AD method can be found elsewhere [21]. Stainless steel (SS, no. 304, American Iron and Steel Institute, Washington, DC, USA) squares with dimensions 15 mm × 15 mm × 0.8 mm were used as substrates, and all depositions were performed with the process parameters shown in Table 1. The number of scans was adjusted to achieve 4 µm–5 µm thickness in all films.

Table 1. Parameters used during AD.

AD Parameters	
Carrier gas species	N_2
Nozzle geometry (slit size)	(0.5×10) mm^2
Nozzle-to-substrate distance	5 mm
Sweep speed	5 mm × s^{-1}
Gas flow rate	4 L × min^{-1}
Pressure in the deposition chamber	0.2 mbar

The powders and the as-deposited films were investigated using X-ray diffraction (XRD) analysis with a high-resolution diffractometer (X'Pert PRO, PANalytical, Almelo, The Netherlands) with Cu–$K_{\alpha 1}$ radiation. Diffraction patterns were recorded in the Bragg-Brentano geometry with a 100-channel X'Celerator detector in a 2θ range 10–70° with a step of 0.034° and an integration time of 100 s per step.

For the microstructural analyses of the films in cross-sectional form, the samples were cut, mounted in epoxy resin, and fine-polished with a colloidal silica suspension. Analyses were performed using scanning electron microscopy (SEM) and energy dispersive spectroscopy (EDS) using a field-emission scanning electron microscope (FE-SEM, JSM-7600F, JEOL, Tokyo, Japan) equipped with a backscattered electron detector and an energy dispersive X-ray spectrometer (Inca Oxford 350 EDS SSD, Oxford Instruments, Abingdon, UK). Prior to the SEM analyses, all samples were coated with a 10-nanometer-thick carbon layer by carbon evaporation (Bal-Tec Sputter-coater SCD 050, Bal-Tec, Pfäffikon, Switzerland).

The Al volume fraction in the thick films was estimated from a combined analysis of the SEM images and EDS mappings, using the ImageJ tool [28]. The Al volume fraction was estimated as the ratio between the sum of the areas of the embedded Al particles and the total cross-sectional area of the film. To minimize errors, the values were calculated from three different regions and averaged.

The topography of the samples was characterized using atomic force microscopy (AFM) and conductive atomic force microscopy (CAFM). Both types of measurements were performed using Asylum Research MFP-3D (Oxford Instruments, Abingdon, UK) microscope and titanium-iridium-coated silicon tips (Asylec-01-R2, Oxford Instruments, Abingdon, UK). For surface characterization, the images were scanned in 20 µm × 20 µm areas from which the surface roughness (root mean-square roughness, R_q) was calculated. The CAFM measurements were performed in 10 µm × 10 µm areas and DC voltage of 10 V.

Prior to dielectric measurements, gold electrodes of 1.0 mm diameter were deposited through a shadow mask onto the surface of the samples by magneton sputtering (Cinquepascal SRL, Milan, Italy). The dielectric properties were measured using a Precision LCR meter (HP 4284A, Santa Rosa, CA, USA) within the 1 kHz–1 MHz frequency range.

The percolative behavior of the prepared composite films was simulated using a simple, 2-dimensional finite-element model. By using COMSOL Multiphysics® Version 5.5 [29] in combination with Matlab LiveLink, we simulated the ac electrical conductivity of Al_2O_3/Al composites. The simulations were performed using the Frequency Domain solver; the frequency range spanned from 1 kHz to 1 MHz, and the DC voltage was set to 1 V. The boundary conditions of the system geometry were as follows: the left and right edges were electrically insulating; the top and bottom edges were set as the electrodes: bias

and ground, respectively. The relative permittivity of Al and Al_2O_3 were both assumed to be independent of frequency and were set to 10^4 and 10, respectively. Similarly, the dc conductivity (σ) values were set to 0 for Al_2O_3 and 3.7×10^7 S/m for Al. It is worth mentioning that, in our case, the electrical response of a particular composite structure should vary little with the precise values used the conductivity of either phase, since such quantities differ by several orders of magnitude. The physical properties of the materials used in the simulation are collected in Table 2.

Table 2. Physical properties of Al and Al_2O_3 used for the simulations [2,30].

Physical Property	Al	Al_2O_3
σ (S/m)	3.7×10^7	0
ε_r' (/)	10^4	10
Density (g/cm^3)	2.70	3.97

The Al_2O_3 matrix was generated as a rectangle of 4.5 μm × 27 μm, and the Al particles were generated as spheres within this matrix. Their center positions were generated according to a uniform distribution, while a gaussian distribution was used for the radius of the particles. The gaussian parameters were evaluated as follows: from SEM images, the mean diameter and standard deviation of the Al particles within the Al_2O_3 matrix were estimated. From the percolation theory perspective [13,31], the two axes of an embedded particle play distinctive roles. The horizontal axis connects different particles forming larger clusters. On the other hand, the vertical axis contributes to the formation of clusters, similar to the horizontal axis, but it is also the direction that directly connects the top and bottom electrodes, resulting in a percolation path throughout the film. In light of this, to approximate the asymmetric Al particles into spheres, the vertical axis was used as the reference to generate the radius of the particles. It is worth emphasizing that the estimated particle diameters from SEM were used as reference values for the radius of the simulated spheres. This was conducted in order to compensate for the pronounced asymmetry between horizontal and vertical axes of the Al particles. The simulated composite film structures were represented in a circuit model as an ideal capacitor in parallel with a simple resistor, enabling direct comparison of calculated admittance and conductivity with measured complex permittivity [32].

3. Results and Discussion

The X-ray patterns of the prepared composite films are shown in Figure 1a, while the particle size distributions, X-ray patterns, and SEM images of the precursor powders are shown in Supplementary Material: Figures S1, S2, and S3, respectively. As expected, with increasing Al content in the compositions, the Al peaks become more intense (Figure 1b). Compared to the Al peaks, the Al_2O_3 peaks are broader (Figure 1c), which is most likely due to the brittleness of the ceramic material that leads to fracturing of the crystallites during aerosol deposition [2,3,21]. In contrast, Al shows narrower peaks, which is consistent with the fact that it is ductile and therefore tends to not fragment as much as Al_2O_3. In agreement with this, from Figure 2 and Supplementary Material: Figure S4 it can be promptly observed that, in the deposited films, the Al particles are much larger than the Al_2O_3 particles.

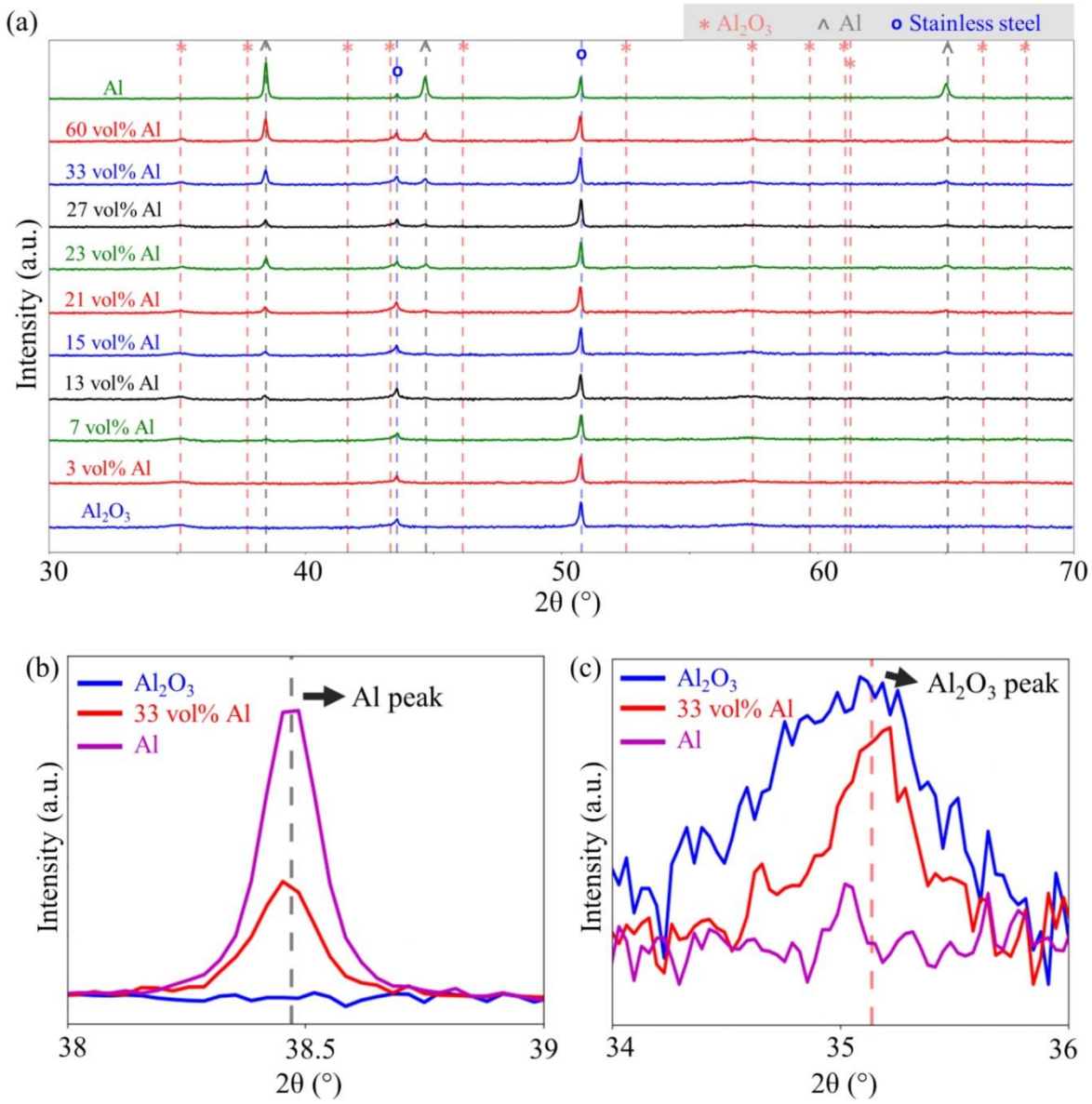


Figure 1. (**a**) XRD patterns of the composite films. (**b**) Enlarged view of the most intense peak of (**b**) Al and (**c**) Al_2O_3.

Figure 2 shows the SEM and EDS analyses for the Al_2O_3 film and composite films in cross-section with 3 vol% Al, 23 vol% Al, 27 vol% Al, and 33 vol% Al. The SEM images reveal highly dense films with no visible pores and excellent adhesion to the substrates. The EDS analyses show a homogeneous distribution of Al in Al_2O_3 matrix. In the composite films, the brighter regions in the Al mappings and dark regions in the oxygen mappings represent the Al phase inside the Al_2O_3 matrix. It is evident that the Al_2O_3 films have the least rough profile compared to other films, suggesting that the Al content plays a significant role in the surface roughness. The SEM images of all prepared thick-film samples can be found in Supplementary Material: Figure S4. To investigate whether the vol% of Al in the composite films differs from the nominal vol% of Al from the composite powders, the vol% Al in films was estimated from SEM/EDS images. From the estimates, the Al contents embedded in the Al_2O_3 matrix were in good agreement with their respective

nominal values. The comparison between the values is shown in Supplementary Material: Figure S5.

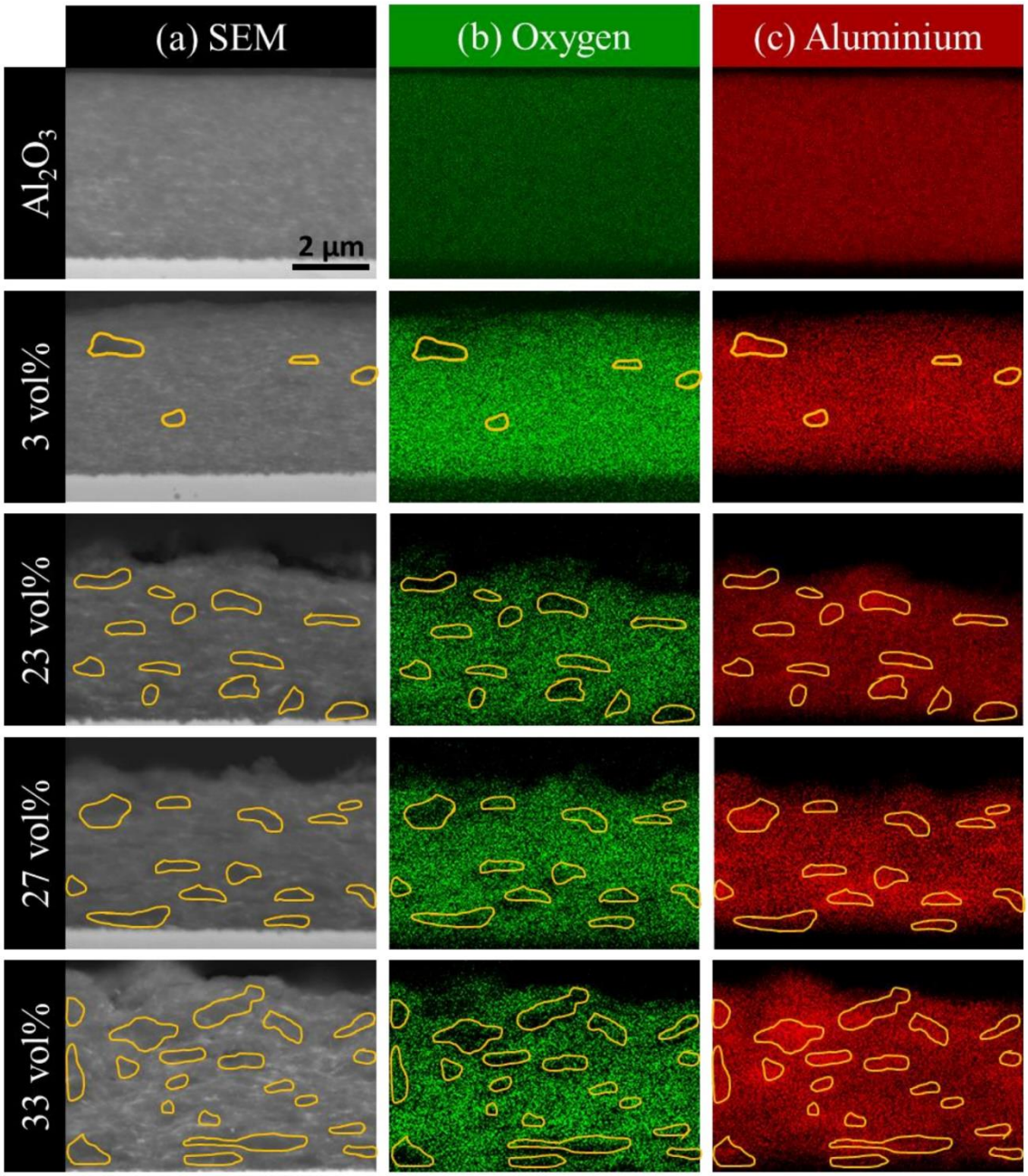


Figure 2. SEM images using a backscattered electron detector (**a**) and EDS mapping of oxygen (**b**) and Al (**c**) for Al_2O_3 film and composite films with 3 vol%, 23 vol%, 27 vol%, and 33 vol% of Al content. The regions highlighted in yellow indicate the Al phase within the Al_2O_3 matrix. Yellow lines are guides to the eye.

To better characterize the influence of the Al content within the Al_2O_3 matrix, the surface topography of the films was investigated using AFM, shown in Figure 3a. The roughness factors of the prepared samples, i.e., the ratio of the surface roughness (R_q) to film thickness (t), were calculated [33,34] and are shown in Figure 3b. It can be seen that

the Al_2O_3 films have the lowest roughness factor of 15×10^{-3}, while Al films show the highest roughness factor of 80×10^{-3}. In composites up to 21 vol% of Al, the roughness factors do not exceed 40×10^{-3}. However, an increase in roughness factor appears in films with ≥23 vol% of Al content, where the factors increase to over 50×10^{-3}. This sharp increase suggests that Al is playing a more significant role in the structure of the films with ≥23 vol% of Al content.

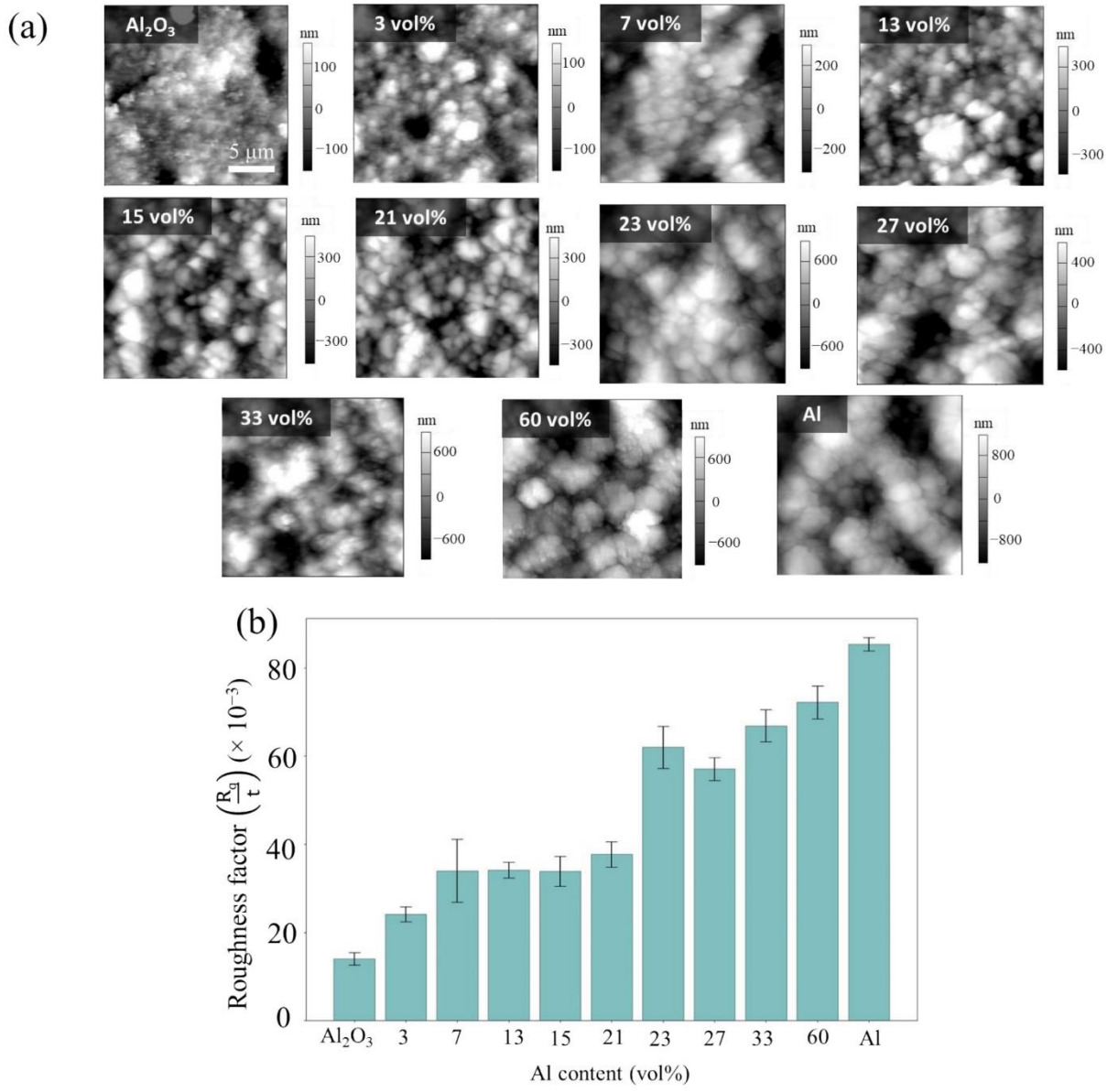


Figure 3. (**a**) AFM topography images of the thick-film surfaces. (**b**) Roughness factor versus Al content. The roughness factor was calculated by averaging the R_q values of five areas per composition.

The dielectric permittivity of ceramic–metal composites is enhanced by increasing the metal content within the ceramic matrix, especially near the percolation threshold, which is the transition point from electrically insulating to conducting. The enhanced ε_r' at this

critical point can be mathematically expressed according to percolation theory as the power law [12,15,31,35], in our case as:

$$\varepsilon_r'(f_{Al}) = \varepsilon'_r(Al_2O_3)\left|\frac{f_c - f_{Al}}{f_c}\right|^{-q} \quad (1)$$

where f_c is the percolation threshold in vol%, f_{Al} is the Al volume fraction, and q is the critical exponent. Due to the nonlinearity of the phenomenon, it is expected to observe a swift change in the electric properties of the films, especially near f_c.

In order to identify percolative paths in the films, CAFM measurements were performed, as these measure the local electrical current flowing through the films (Figure 4a). The CAFM results for the Al_2O_3 film and composite films with 3 vol%, 23 vol%, 27 vol%, and 33 vol% content of Al are shown in Figure 4b,c. In Al_2O_3 films, the local electric currents flowing through the sample were below the detection threshold (0.5 pA [36]) of the measuring device; thus, the films exhibit good electrically insulating properties. This trend is maintained up to an Al content of 21 vol%. At 23 vol%, the material starts to conduct locally, but only minor regions of local electrical current up to 1.3 pA are observed. At an Al content of 27 vol%, a few areas of enhanced local electric currents of ~80 pA are observed, which is around 80 times higher than in the previous composition. This trend may be an indicator that this composition is close to the percolation threshold. At 33 vol%, the sample locally conducts in many regions across the surface, indicating that this composition is above the percolation threshold. The local electrical currents that flow through the sample can reach 140 pA.

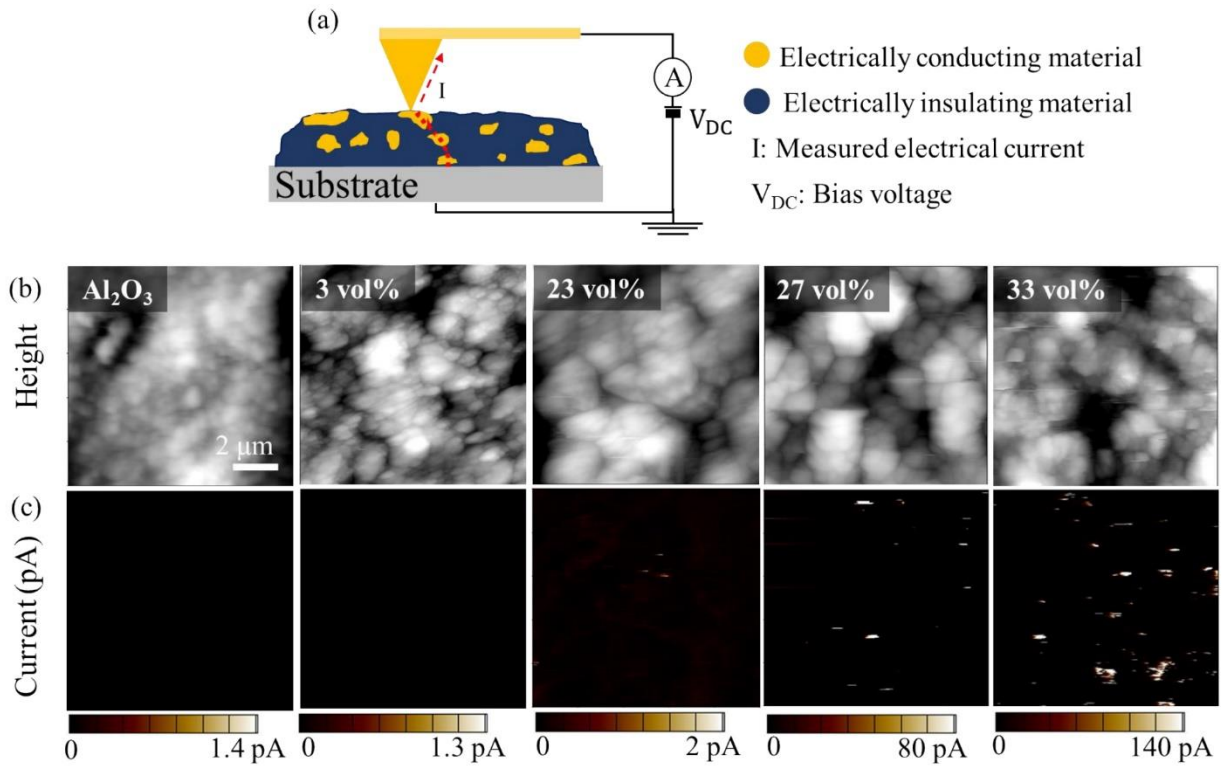


Figure 4. (**a**) Schematic representation of the CAFM setup. The stainless-steel substrates were used as bottom electrodes. (**b**) AFM topography height images and (**c**) CAFM current images of the Al_2O_3 and composite films.

The ε_r' of the composite films as a function of frequency is shown in Figure 5a. Films with compositions ≥ 33 vol% of Al were not measured as they were electrically conductive films; therefore, the Cp-D model would be unsuitable for interpretation and beyond the scope of this work. In addition, it is worth mentioning that in the case of tan(δ) ≫ 0.1, the quantitative uncertainty is significantly increased [37]. Note that for up to 21 vol% of Al content there is no significant change in the ε_r' of composite films compared to Al_2O_3 films. However, the ε_r' increases for compositions ≥ 21 vol% of Al, especially at 27 vol% of Al, which exhibits a significantly large enhancement. This trend is in good agreement with previous CAFM electric current mappings, which showed more areas of higher intensity electric current across the surface at 27 vol% of Al; hence, this concentration must be close to the percolation threshold. At 1 MHz, the Al_2O_3 films show ε_r' of 12, while the composite films with 27 vol% of Al show a value of 800, a sixty-sevenfold increase.

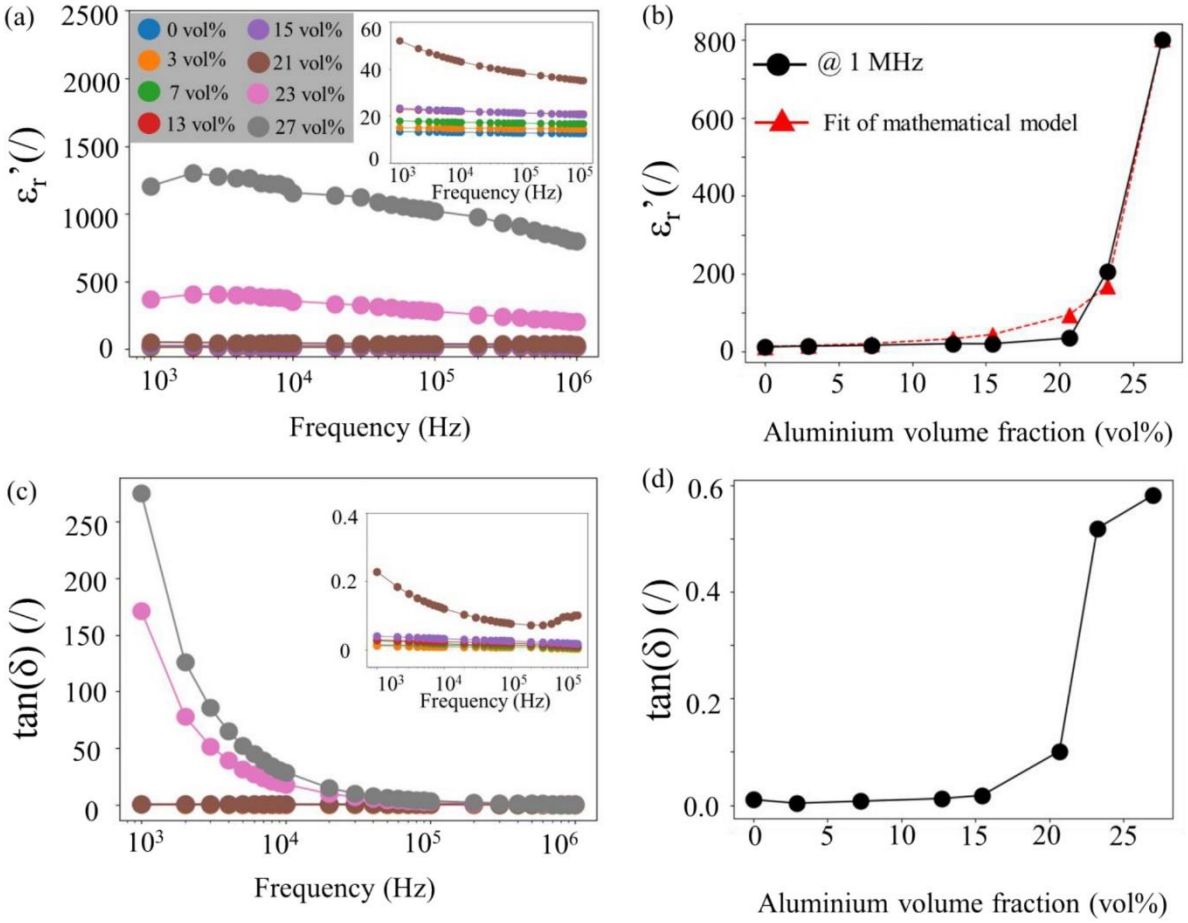


Figure 5. (**a**) ε_r' of the composites as function of frequency, the inset shows ε_r' up to 60. (**b**) ε_r' at 1 MHz as function of Al content. (**c**) The tan(δ) as function of frequency, the inset shows tan(δ) up to 0.4. (**d**) tan(δ) at 1 MHz as function of Al content.

At 1 MHz, the best fit for the power law (Equation (1)) results in q = 1.6 and f_c = 29 vol%. The dielectric permittivity values at 1 MHz as function of Al content and the best fit are shown in Figure 5b. With increasing Al content, the tan(δ) values also increase, especially at frequencies lower than 10 kHz, shown in Figure 5c. As the frequency increases, the tan(δ) decreases, and at 1 MHz, the films with 27 vol% of Al exhibit tan(δ) of 0.58 which is higher than that of Al_2O_3 films, i.e., tan(δ) ∼ 0.01, as shown in Figure 5d. Although the

mathematical model (Equation (1)) results in f_c = 29 vol%, it is evident from the CAFM measurements that at 27 vol% the compositions are bordering the percolation threshold.

Furthermore, we simulated the percolative trends of the compositions using a simple finite-element model. The center coordinates of the Al particles were generated according to estimates from SEM images, as described in the experimental section. In this manner, we obtained 0.385 µm and 0.117 µm for the mean diameter and standard deviation, respectively. The gaussian distribution and histogram from SEM data are shown in Figure 6a. From the simulations, we observe a sudden increase in electrical conductivity at 27 vol% of Al, indicating that this composition is at the percolation threshold. The electrical conductivity for different compositions at 1 kHz and 1 MHz is shown in Figure 6b. Our percolation threshold obtained from the simulations, 27 vol%, is in excellent agreement with the experimental results shown above. Figure 6c shows the voltage and polarization distributions at 1 MHz for the 27 vol% composition. Notice in the polarization panel, that the largest values are located at the metallic-insulating interfaces, as expected from the Maxwell–Wagner effect [13].

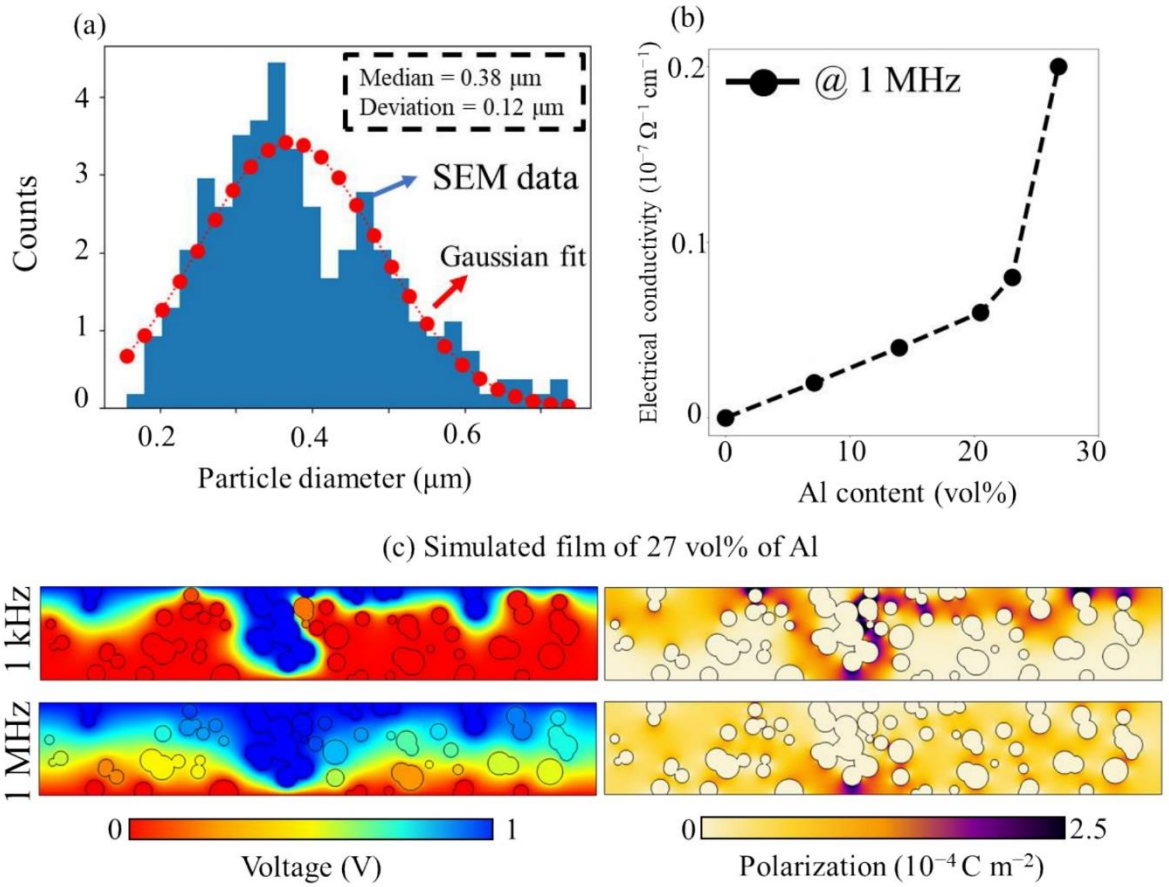


Figure 6. (**a**) Histogram of the diameter of embedded Al particles estimated from SEM images and the gaussian distribution used to generate the radius of the particles. (**b**) Electrical conductivity as function of compositions at 1 MHz, for different simulated compositions. (**c**) Simulation of a 27 vol% of Al film at 1 MHz. The voltage and polarization distributions are shown in the upper and lower panels, respectively.

4. Conclusions

In conclusion, Al_2O_3/Al thick films were prepared for the first time via AD. Successful depositions of composite powders with different vol% of Al were achieved. The films

exhibited dense structure with no pores and homogenous distribution of Al throughout the Al_2O_3 matrix. At 27 vol% of Al, a sharp increase in the dielectric permittivity of the films was achieved. At 1 MHz, the Al_2O_3 films show ε_r' of 12, while the composite films with 27 vol% of Al exhibit a value of 800. On the other hand, the tan(δ) of Al_2O_3 films is 0.01 and increases to 0.58 for the composite films with 27 vol% of Al. By combining dielectric measurements and CAFM electrical current mappings, we were able to determine the percolation threshold at ∼27 vol% of Al. Our experimental results were further confirmed by a simple finite-element model of the composite films. From the simulations, the percolation threshold was obtained at 27 vol% of Al, in excellent agreement with the experimental data. To conclude, our results broaden the possibilities of use Al_2O_3-based ceramic-metal composites in the microelectronics industry.

Supplementary Materials: The following supporting information can be downloaded at: https://www.mdpi.com/article/10.3390/cryst13050850/s1, Figure S1: Particle size distribution of all compositions; Figure S2: X-ray patterns of the composite powders; Figure S3: SEM images of the precursor powder of all compositions; Figure S4: SEM images (left) and EDS mapping of oxygen (middle) and aluminum (right) for 7 vol%, 13 vol%, 15 vol%, 21 vol%, 60 vol%, and Al films; Figure S5: Comparison between the estimated Al volume fraction in the composite films and the nominal Al volume fraction in the powder mixtures prior to AD.

Author Contributions: Conceptualization, V.R., U.T. and H.U.; methodology, V.R., M.Š., G.B. and H.U.; Investigation, V.R., M.Š. and H.U.; resources, V.R., M.Š. and H.U.; data curation, V.R., G.B., A.B. and H.U.; software, V.R., U.T. and A.B.; supervision, H.U.; visualization, V.R.; writing—original draft preparation, V.R. and H.U.; writing—review and editing, V.R., M.Š., U.T., A.B., G.B. and H.U. All authors have read and agreed to the published version of the manuscript.

Funding: This work is funded by the Slovenian Research Agency (research project N2-0212, research core funding P2-0105, bilateral project BI-US/22-24-039) and M.ERA-NET project COOLBATMAN. GLB gratefully acknowledges financial support for this research by the Fulbright U.S. Scholar Program, which is sponsored by the U.S. Department of State.

Data Availability Statement: The data presented in this study are available upon request from the corresponding author.

Acknowledgments: The authors thank Nikola Tutić, Val Fišinger, Jena Cilenšek, and Brigita Kmet for help in the laboratory. JSI Director's fund 2017-ULTRACOOL is also acknowledged.

Conflicts of Interest: The authors declare no conflict of interest.

References

1. Salonitis, K.; Pandremenos, J.; Paralikas, J.; Chryssolouris, G. Multifunctional materials: Engineering applications and processing challenges. *Int. J. Adv. Manuf. Technol.* **2010**, *49*, 803–826. [CrossRef]
2. Sadl, M.; Tomc, U.; Ursic, H. Investigating the Feasibility of Preparing Metal–Ceramic Multi-Layered Composites Using Only the Aerosol-Deposition Technique. *Materials* **2021**, *14*, 4548. [CrossRef] [PubMed]
3. Sadl, M.; Tomc, U.; Prah, U.; Ursic, H. Protective Alumina Coatings Prepared by Aerosol Deposition on Magnetocaloric Gadolinium Elements. *J. Microelectron. Electron. Compon. Mater.* **2019**, *49*, 177–182.
4. Seto, N.; Endo, K.; Sakamoto, N.; Hirose, S.; Akedo, J. Hard α-Al_2O_3 Film Coating on Industrial Roller Using Aerosol Deposition Method. *J. Therm. Spray Technol.* **2014**, *23*, 1373–1381. [CrossRef]
5. Lu, J.; Wong, C.P. Recent Advances in High-k Nanocomposite materials for embedded capacitor applications. *IEEE Trans. Dielectr. Electr. Insul* **2008**, *15*, 1322–1328.
6. Robertson, J. High dielectric constant oxides. *Eur. Phys. J. Appl. Phys.* **2004**, *28*, 265–291. [CrossRef]
7. Hubbard, K.J.; Schlom, D.G. Thermodynamic stability of binary oxides in contact with silicon. *Int. J. Mater. Res.* **1996**, *11*, 2757–2776. [CrossRef]
8. Misra, D.; Iwai, H.; Wong, H. High-k Gate Dielectrics. *Electrochem. Soc. Interface* **2005**, *14*, 30–34. [CrossRef]
9. Kim, H.; Yoon, Y.; Kim, J.; Nam, S. Application of Al_2O_3-based polyimide composite thick films to integrated substrates using aerosol deposition method. *Mater. Sci. Eng. B* **2009**, *161*, 104–108. [CrossRef]
10. Wilkinson, D.; Langer, J.S.; Sen, P.N. Enhancement of the dielectric constant near a percolation threshold. *Phys. Rev. B Condens. Matter.* **1983**, *28*, 1081–1087. [CrossRef]
11. Pecharromán, C.; Esteban-Betegón, F.; Bartolomé, J.; López-Esteban, S.; Moya, J. New Percolative $BaTiO_3$-Ni Composites with a High and Frequency-Independent Dielectric Constant. *Adv. Mater.* **2001**, *13*, 1541–1544. [CrossRef]

12. Bobnar, V.; Hrovat, M.; Holc, J.; Kosec, M. All ceramic lead-free percolative composite with a colossal dielectric response. *J. Eur. Ceram. Soc.* **2008**, *29*, 725–729. [CrossRef]
13. Kirkpatrick, S. Percolation and conduction. *Rev. Mod. Phys.* **1973**, *45*, 574–587. [CrossRef]
14. Bergman, D.J.; Imry, Y. Critical Behavior of the Complex Dielectric Constant near the Percolation Threshold of a Heterogeneous Material. *Phys. Rev. Lett.* **1977**, *39*, 1222–1225. [CrossRef]
15. Stauffer, D.; Aharony, A. *Introduction to Percolation Theory*; Taylor & Francis: London, UK, 1992.
16. Kim, J.J.; Kim, H.-K.; Lee, S.-H.; Lee, S.-G.; Kim, J.-S.; KIm, J.-S.; Lee, Y.-H. Dielectric properties of percolative $BaTiO_3$/Ni composite film fabricated by aerosol deposition process. *J. Mater. Sci. Mater. Electron.* **2016**, *27*, 8567–8572. [CrossRef]
17. Xiang, P.-H.; Dong, X.-L.; Feng, C.-D.; Liang, R.-H.; Wang, Y.-L. Dielectric behavior of lead zirconate titanate/silver composites. *Mater. Chem. Phys.* **2004**, *97*, 410–414. [CrossRef]
18. Lee, J.H.; Kim, H.-K.; Lee, S.-H.; Choi, K.; Lee, Y.-H. Effect of Zn filler for percolative $BaTiO_3$/Zn composite films fabricated by aerosol deposition. *Ceram. Int.* **2015**, *41*, 12153–23257.
19. Yu, Z.; Ang, C. Maxwell-Wagner polarization in ceramic composites $BaTiO_3$-$(Ni_{0.3}Zn_{0.7})Fe_{2.1}O_4$. *J. Appl. Phys.* **2002**, *91*, 794–797. [CrossRef]
20. Khansur, N.H.; Eckstein, U.; Li, Y.; Hall, D.A.; Kashta, J.; Webber, K.G. Revealing the effects on aerosol deposition on the substrate-film interface using NaCl coating. *J. Am. Ceram. Soc.* **2019**, *102*, 5763–5771. [CrossRef]
21. Hanft, D.; Exner, J.; Schubert, M.; Stocker, T.; Fuierer, P.A.; Moos, R. An Overview of the Aerosol Deposition Method: Process Fundamentals and New Trends in Materials Applications. *J. Ceram. Sci. Technol.* **2015**, *6*, 147–182.
22. Schubert, M.; Hanft, D.; Nazarenus, T.; Exner, J.; Schubert, M.; Nieke, P.; Glosse, P.; Leupold, N.; Kita, J.; Moos, R. Powder aerosol deposition method—Novel applications in the field of sensing and energy technology. *Funct. Mater. Lett.* **2019**, *12*, 1930005. [CrossRef]
23. Akedo, J. Room Temperature Impact Consolidation (RTIC) of Fine Ceramic Powder by Aerosol Deposition Method and Applications to Microdevices. *J. Therm. Spray Technol.* **2008**, *17*, 181–198. [CrossRef]
24. Schubert, M.; Leupold, N.; Exner, J.; Kita, J.; Moos, R. High-Temperature Electrical Insulation Behavior of Alumina Films Prepared at Room Temperature by Aerosol Deposition and Influence of Annealing Process and Powder Impurities. *J. Therm. Spray Technol.* **2018**, *27*, 870–879. [CrossRef]
25. Leupold, N.; Schubert, M.; Kita, J.; Moos, R. Influence of high temperature annealing on the dielectric properties of alumina films prepared by the aerosol deposition method. *Funct. Mater. Lett.* **2018**, *11*, 1850022. [CrossRef]
26. Lee, C.; Cho, M.-Y.; Kim, M.; Jang, J.; Oh, Y.; Oh, K.; Kim, S.; Park, B.; Kim, B.; Koo, S.-M.; et al. Applicability of Aerosol Deposition Process for flexible electronic device and determining the Film Formation Mechanism with Cushioning Effects. *Sci. Rep.* **2019**, *9*, 2166. [CrossRef]
27. Cho, M.-Y.; Lee, D.-W.; Ko, P.-J.; Koo, S.-M.; Kim, J.; Coi, Y.-K.; Oh, J.-M. Adhesive Mechanism of Al_2O_3/Cu Composite Film via Aerosol Deposition Process for Application of Film Resistor. *Eletron. Mater. Lett.* **2019**, *15*, 227–237. [CrossRef]
28. Schneider, C.A.; Rasband, W.S.; Eliceiri, K.W. NIH Image to ImageJ: 25 years of image analysis. *Nat. Methods* **2012**, *9*, 671–675. [CrossRef]
29. COMSOL Multiphysics®, Version 5.5, Stockholm, Sweden. Available online: comsol.com (accessed on 11 November 2022).
30. Haynes, W.M. *CRC Handbook of Chemistry and Physics*; Taylor & Francis: Boca Raton, FL, USA, 2015.
31. Lunkenheimer, P.; Bobnar, V.; Pronin, A.V.; Ritus, A.I.; Volkov, A.A.; Loidl, A. Origin of apparent colossal dielectric constants. *Phys. Rev. B Condens. Matter* **2002**, *66*, 052105. [CrossRef]
32. Moulson, A.J. *Electroceramics: Materials, Properties, Applications*; Wiley: Hoboken, NJ, USA, 2003.
33. Henon, J.; Piechowiak, M.A.; Durand-Panteix, O.; Etchgoyen, G.; Masson, O.; Dublanche-Tixier, C.; Marchet, P.; Lucas, B.; Rossignol, F. Dense and highly textured coatings obtained by aerosol deposition method from Ti_3SiC_2 powder: Comparison to a dense material sintered by Spark Plasma Sintering. *J. Eur. Ceram. Soc.* **2015**, *35*, 1179–1189. [CrossRef]
34. Khansur, N.H.; Eckstein, U.; Benker, L.; Deisinger, U.; Merle, B.; Webber, K.G. Room temperature deposition of functional ceramic films on low-cost metal substrate. *Ceram. Int.* **2018**, *44*, 16295–16301. [CrossRef]
35. Bobnar, V.; Levstik, A.; Huang, C.; Zhang, Q. Enhanced dielectric response in all-organic polyaniline-poly(vinylidene fluoride-trifluorothylenechlorotrifluoroethylene) composite. *J. Non-Cryst. Solids* **2007**, *353*, 205–209. [CrossRef]
36. Asylum Research, ORCATM—Conductive AFM. Available online: https://afm.oxinst.com/assets/uploads/products/asylum/documents/ORCA%E2%84%A2-%E2%80%93-Conductive-AFM-Imaging-Using-the-MFP-3D%E2%84%A2-AFM.pdf (accessed on 4 March 2023).
37. HP 4284A Precision LCR Meter Operation Manual. Available online: https://wiki.epfl.ch/carplat/documents/hp4284a_lcr_manual.pdf (accessed on 10 November 2022).

Disclaimer/Publisher's Note: The statements, opinions and data contained in all publications are solely those of the individual author(s) and contributor(s) and not of MDPI and/or the editor(s). MDPI and/or the editor(s) disclaim responsibility for any injury to people or property resulting from any ideas, methods, instructions or products referred to in the content.

crystals

MDPI

Supplementary Material

Investigation of structural and electrical properties of Al_2O_3/Al composites prepared by aerosol co-deposition

Victor Regis[1,2], Matej Šadl[1,2], Geoff Brennecka[3], Andraž Bradeško[1], Urban Tomc[4] and Hana Uršič[1,2,*]

[1] Electronic Ceramics Department, Jožef Stefan Institute, Jamova Cesta 39, 1000 Ljubljana, Slovenia
[2] Jožef Stefan International Postgraduate School, Jamova cesta 39, 1000 Ljubljana, Slovenia
[3] Colorado School of Mines, 1500 Illinois Ave., Golden, CO 80401, USA
[4] Laboratory for Refrigeration and District Energy, Faculty of Mechanical Engineering, University of Ljubljana, Aškerceva Cesta 6, 1000 Ljubljana, Slovenia
* Correspondence: hana.ursic@ijs.si

S1: Particle size distribution

To ensure that the composite powder particles were within the optimal range for AD, within 0.2 μm – 5 μm [21], the particle size distribution of all the compositions was measured (Figure S1). Notice the continuous shift from the Al_2O_3 peak at 0.4 μm to the Al peak at 1.5 μm.

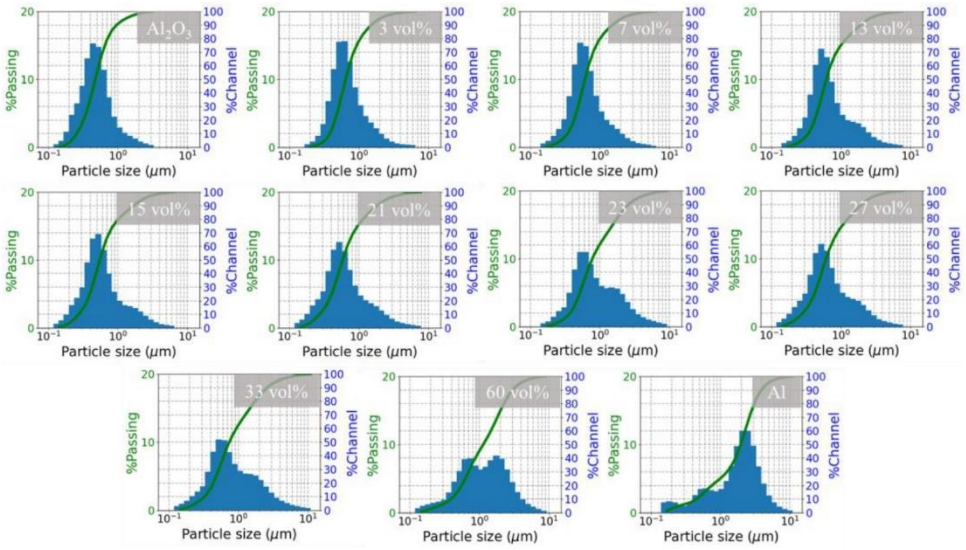


Figure S1: Particle size distribution of all compositions.

S2: X-ray patterns of composite powders

Before the depositions, X-ray patterns of the powders were measured, as shown in **Error! Reference source not found.**S2. Distinctive Al_2O_3 and Al peaks can be observed, with no peak shifts from the peak positions of Al_2O_3 (reference code: 01-071-1123) or Al (reference code: 01-089-2837), indicating no reacting between Al_2O_3 and Al. As expected, with

Citation: Regis, V.; Šadl, M.; Brennecka, G.; Bradeško, A.; Tomc, U.; Uršič, H. Investigation of Structural and Electrical Properties of Al_2O_3/Al Composites Prepared by Aerosol Co-Deposition. *Crystals* **2023**, *13*, x. https://doi.org/10.3390/cryst1305085

Academic Editor: Dah-Shyang Tsai

Received: 24 April 2023
Revised: 12 May 2023
Accepted: 19 May 2023
Published: 21 May 2023

Copyright: © 2023 by the authors. Submitted for possible open access publication under the terms and conditions of the Creative Commons Attribution (CC BY) license (https://creativecommons.org/licenses/by/4.0/).

increasing Al content in the compositions, the Al_2O_3 peaks become less intense, whereas Al peaks become more intense.

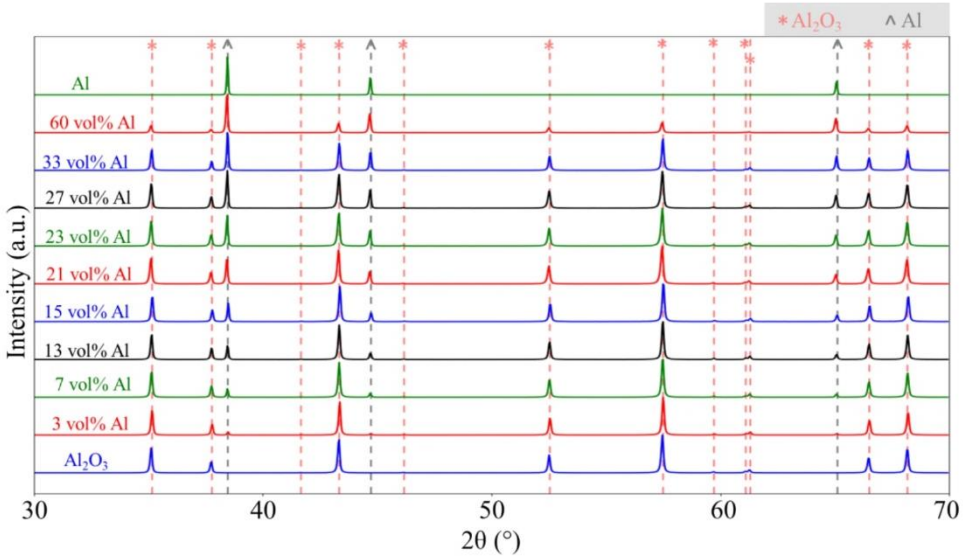


Figure S2. X-ray patterns of the composite powders.

S3: SEM images of composite powders

To analyze the morphology of the precursor powders, the powders were investigated using scanning electron microscopy (Prisma E, Thermo Fisher Scientific, Massachusetts, USA). Prior to the SEM analysis, the powders were deposited on carbon tape and coated with a 10-nanometre-thick carbon layer by carbon evaporation (Bal-Tec Sputter-coater SCD 050, Bal-Tec, Pfäffikon, Switzerland). From the SEM images, it can be seen that the Al particles have a typical mostly spherical shape, while the Al_2O_3 particles are smaller and have irregular shapes. In the composite precursor powders, as expected, the Al particles become increasingly more evident with larger Al vol% (some examples are marked by red arrows until the composition 33 vol% of Al).

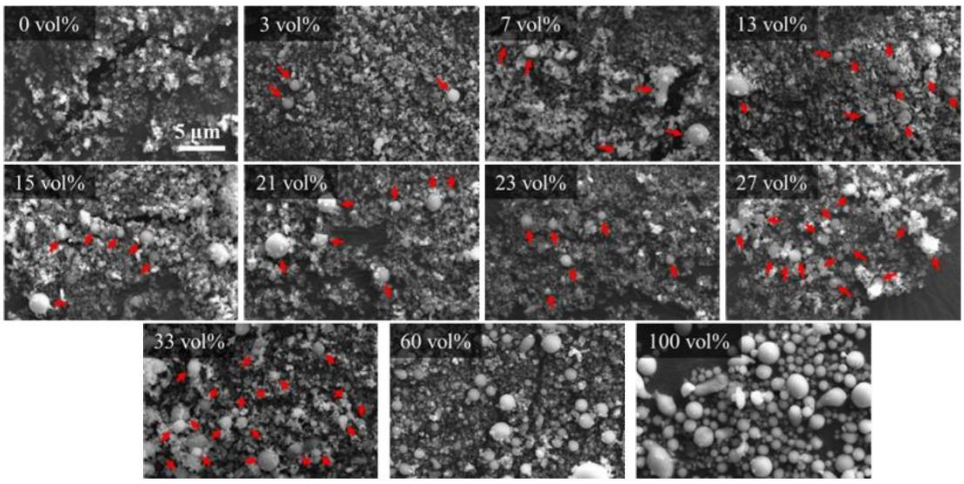


Figure S3. SEM images of the precursor powder of all compositions. The red arrows indicate some of the Al particles within the Al_2O_3 matrix for Al_2O_3-rich compositions. For visual clarity, the Al particles in the 60 vol% composition are not indicated by red arrows because the Al content predominates.

S4: Additional SEM and EDS analyses of the composites

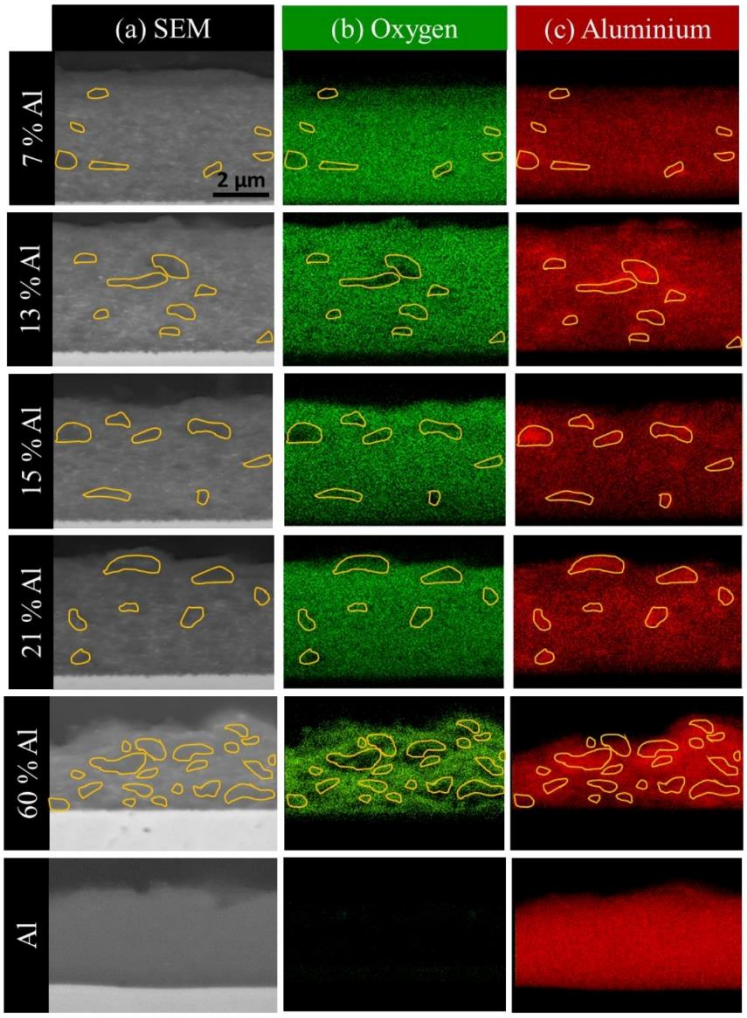


Figure S4. SEM images (**a**) and EDS mapping of oxygen (**b**) and aluminium (**c**) for 7 vol%, 13 vol%, 15 vol%, 21 vol%, 60 vol%, and Al films. The regions highlighted in yellow indicate the aluminium phase within the alumina matrix. Yellow lines are guides to the eye.

S5: Quantitative analysis of the Al vol% within the Al_2O_3 matrix

Using a combination of SEM images and EDS mappings, the Al volume fraction in the thick films was estimated and compared to the nominal Al volume fraction in the powder mixtures (see Figure S5). The estimated Al volume fraction in the thick films was defined as the ratio between the sum of the surface areas of the Al particles and the total cross-sectional area of the thick film in a SEM / EDS image. The procedure was performed on three different areas (three SEM/EDS images of the thick film cross-section with a magnification of 15000 times), and the compositions 3 vol%, 23 vol%, 27 vol%, and 33 vol% were selected as representative cases. From the estimates, the average experimental Al volume percentage value in the thick films is comparable to the nominal value of the powder mixture before AD, so both quantities can be considered equivalent.

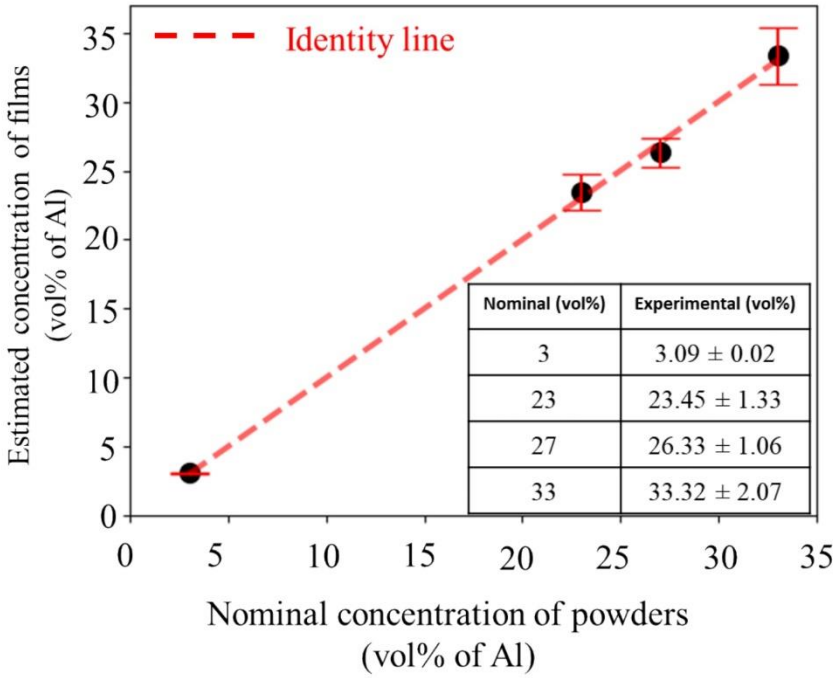


Figure S5. Comparison between the estimated Al volume fraction in the composite films and the nominal Al volume fraction in the powder mixtures prior to AD. The red dashed line represents the ideal case in which both quantities are identically equivalent. The table shows the nominal vol% Al in the powder mixture and mean estimated values of vol% Al in thick films and their respective standard deviations.

Chapter 3

Roadmap for Electrocaloric Films Characterization

Direct characterization methods of caloric effects have received increased attention in recent years, as these allow for an accurate quantification of the caloric output of materials. As the primary objective of this thesis is to directly characterize multicaloric films, it is essential to maximize the measurement response. However, most studies report direct measurements of caloric effects on bulk samples. Investigations of the caloric properties of films, in contrast, are largely unexplored. It is known that the substrate and the black paint coating (in the case of the IR camera) are the main contributors to systematic heat losses in films, reducing the caloric response during measurements. Nonetheless, to which extent remain unaddressed.

In light of this, targeting minimizing systematic heat losses, we have numerically investigated the influence of the substrate material and the black paint thickness on the caloric response of films for characterization purposes. First, the influence of the thermal properties of the substrate was considered. For the investigations, PMN–10PT was selected as a reference material, albeit a wider range of active caloric materials was also discussed, with similar conclusions. Our results indicate that substrates which exhibit a thermal effusivity lower than 3 kW $s^{1/2}$ m^{-2} K^{-1} are optimal for caloric characterizations. In addition, if the substrate exhibits low thermal conductivity ($\leq$1 W m^{-1} K^{-1}), it will be suitable for direct characterizations, regardless of the other thermal parameters. Our results showed that polyimide is amongst the most suitable materials for direct characterization purposes. For this reason, it was chosen later during my PhD work as the substrate for the multicaloric composites.

Furthermore, in this work, the influence of the caloric layer and black paint coating thicknesses on IR camera measurements was also numerically investigated. The simulations suggest that the caloric film should exhibit a thickness of $\geq$5 µm, in order to achieve a maximized response. Overall, the thickness of the black paint coating should be as thin as a few µm, and not exceed that of the caloric films.

This chapter addresses thesis objectives: 2,3,4

Published in: V. Regis, U. Tomc, A. Kitanovski and H. Ursic, “Roadmap for electrocaloric films characterization,” iScience, vol. 29, p. 115965, 2026. (IF = 4.1, 2026)

My contribution: I performed the numerical modelling and simulations. I measured the specific heat of the black paint, necessary for the simulations. I conceptualized the manuscript and, together with the co-authors, wrote the paper.

iScience

CellPress
OPEN ACCESS

Article

Roadmap for electrocaloric films characterization

Victor Regis,[1,2] Urban Tomc,[3] Andrej Kitanovski,[3] and Hana Uršič[1,2,4,*]
[1]Electronic Ceramics Department, Jožef Stefan Institute, Jamova cesta 39, 1000 Ljubljana, Slovenia
[2]Jožef Stefan International Postgraduate School, Jamova cesta 39, 1000 Ljubljana, Slovenia
[3]Faculty of Mechanical Engineering, University of Ljubljana, Aškerceva cesta 6, 1000 Ljubljana, Slovenia
[4]Lead contact
*Correspondence: hana.ursic@ijs.si
https://doi.org/10.1016/j.isci.2026.115965

SUMMARY

The development of electrocaloric (EC) elements for cooling technologies has progressed by integrating the EC layers onto various substrates. However, a precise understanding of heat losses on direct characterization methods is still lacking, particularly in the infrared (IR) camera method. In this work, we perform numerical simulations on EC film structures to benchmark the substrate influence on the cooling output of the structure for characterization purposes. Substrates with low thermal effusivity ($\leq$3 kW $s^{1/2}$ m^{-2} K^{-1}) exhibit minimal influence on the output of films. Simulations were also performed to investigate the impact of EC film and black-paint coating thicknesses on the correction factor for IR characterization methods. A single-digit correction factor can be achieved if the EC film is thicker than the coating. Our results offer a roadmap for designing EC structures for cooling at the micro-to-nano scales.

INTRODUCTION

Vapor compression cooling technologies, although widespread and well-established, have a limited Carnot efficiency and do not offer a viable way to be miniaturized at micro or nano scales. In the last few decades, research on cooling alternatives has intensified, particularly on the materials that exhibit caloric effects, which are the adiabatic and reversible temperature change (ΔT_{AD}) as a response to external stimuli. Such materials are categorized into electrocalorics (ECs), magnetocalorics, or mechanocalorics, which are responsive to electric field, magnetic field, or mechanical load, respectively.[1–4] Particularly, ECs show a promising future for miniaturized cooling devices, as these only require the material layers, electrodes, and the voltage supply, all of which are already present in electronic devices.[4] The most prominent ECs are Pb-based oxides, such as $Pb(Mg_{1/3}Nb_{2/3})O_3$-$xPbTiO_3$ and $Pb(Sc_{0.5}Ta_{0.5})O_3$.[5–13] In particular, $0.9Pb(Mg_{1/3}Nb_{2/3})O_3$-$0.1PbTiO_3$ (PMN-10PT) has been extensively studied for its thermal properties as well as its excellent EC performance in film[8] and ceramic[13–16] forms.

EC films are promising for micro-cooling applications as they have been shown to achieve large ΔT_{AD},[4–8] and can be integrated onto a variety of substrates: polymers,[7–9] metals,[17–20] glasses,[19–21] and ceramics.[21–23] Caloric-based prototypes require excellent thermal properties in order to achieve optimal performance.[24–28] However, for characterization purposes, low thermal transport properties are required, otherwise the substrate will absorb all the caloric output, hindering the measurement. In other words, for a reliable quantification and understanding of the intrinsic properties of caloric materials, it is necessary to minimize systematic heat losses, therefore maximizing the measurement response.[8,29] In light of this, in recent years, research has focused on finding and optimizing substrates that allow for maximized measurement responses. Despite that, most reports which discuss heat sink effects for characterization purposes consider only case-specific parameters and, to the authors' knowledge, there is no study on the impact of substrate thermal parameters, such as heat capacity (c_p), thermal conductivity (λ), and density (ρ), on the effective cooling output of caloric film structures, particularly for characterization purposes.

Characterization methods of the caloric response of materials are generally classified as either direct or indirect. The indirect approach offers a benchmark ΔT_{AD} value, however it does not take into consideration effects such as Joule heating and heat losses to the substrate, resulting in potentially inaccurate values.[8] To circumvent such an issue, direct characterization methods can be performed. A common drawback of direct methods is the heat losses related to the measurement setup; in other words, the intrinsic ΔT_{AD} is proportional to the measured temperature change (ΔT_M) by a constant k, called the correction factor. Mathematically, it can be described as $\Delta T_{AD} = k\,\Delta T_M$, where k can be determined by assessing method-specific experimental parameters. For example, the thermistor-in-calorimeter method requires wiring, a bead-thermistor, glue and has an acquisition time of $\sim$1 s, which leads to a factor of 30–50.[8,9] The correction factor can be significantly reduced by means of a non-contact infrared (IR) characterization method, which has been typically used for magnetocaloric and elastocaloric characterizations.[30–37] Using the IR method, only a thin layer of a high-emissivity coating, generally black paint, is required, and the acquisition time may be as fast as $\sim$1 ms.[29–31] It has been shown that the IR characterization method can also be used in EC thick films. With the method, single-digit k-values have been achieved on µm-thick EC films prepared on polymer substrates.[7,8,29]

This is an open access article under the CC BY license (http://creativecommons.org/licenses/by/4.0/).

CellPress
OPEN ACCESS

iScience
Article

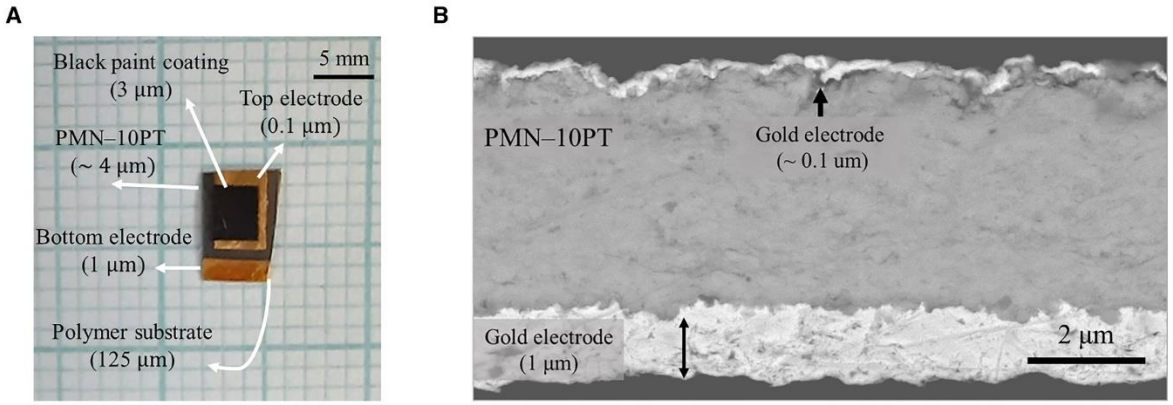


Figure 1. Photograph and microstructure images of the reference sample

(A) Photograph of PMN-10PT thick film on gold-sputtered polymer substrate covered with gold top electrode and coated with black paint layer for IR characterization. The scale bar represents 5 mm.

(B) SEM image of a sample in cross-sectional view. The scale bar represents 2 μm. Note the large thickness difference between the top and bottom electrodes.

In recent years, the IR method has become more widespread, with a wide range of samples being characterized. However, most studies do not report the thickness of the paint, and many do not consider the influence of the black coating on the measurements, likely assuming that the correction factor is negligible.[38–40] In other studies, targeting the direct characterization of EC μm-thick films, the EC film thickness (d_{EC}) and black paint coating (d_{BP}) are both considered and simulated, albeit only using case-specific parameters.[8,29] Although the literature reports consistent and accurate results, the influence of d_{EC} and d_{BP} on the correction factor remains unaddressed.

In light of this, in this work, using a finite-element model, we numerically investigate the influence of the substrate thermal parameters on the cooling performance of a caloric film structure, aiming to optimize measurement response. Due to its excellent properties, PMN-10PT was chosen as the reference EC material. For the IR method, the impact of the d_{EC}, as well as black coating thicknesses, d_{BP}, on the correction factor k was investigated. This work aims to establish a preliminary assessment on substrate material as well as benchmark sample-to-coating optimization for the IR characterization method of caloric samples.

RESULTS AND DISCUSSION

Numerical model of electrocaloric structures

A typical EC thick-film sample, prepared via the aerosol deposition method, coated for IR characterizations[7,8] is shown in Figure 1A. Generally, for EC measurements, it is desired to have electrodes as thin as possible to minimize substrate influence. However, in the case of aerosol-deposited samples, due to processing constraints, the bottom electrode must be at least 1 μm-thick to ensure proper film adhesion.[8,22] Such a structure was used as a reference geometry for the simulations. A scanning electron microscopy image of a sample in a cross-sectional view is shown in Figure 1B.

The investigations were performed via a 2-dimensional finite-element model using COMSOL multiphysics within the interval 0 s to 50 ms at 10 μs steps. The simulations were then split into two segments: minimizing the influence of the substrate and minimizing the correction factor for IR camera measurements. For the former, d_{EC} was fixed at 5 μm, and different values of ρ, cp, and λ were investigated. For the latter, an additional d_{BP} atop of the previous structure was implemented, and polyimide was set as the substrate material. Structures with different combinations of d_{EC} and d_{BP} were simulated, with both values within 0.5 μm and 50 μm. The simulated structures are schematically shown in Figure 2. The EC effect was implemented through the power density, P_{EC}, described as follows[8,29]:

$$P_{EC} = \begin{cases} 0, t < 10\ \mu s \\ \frac{\rho C_p \Delta T_{AD}}{\tau}, 10\ \mu s \leq t \leq \tau \\ 0, t > \tau_{pul} \end{cases} \quad \text{(Equation 1)}$$

where τ is the duration of the caloric pulse, and it was set to 1 ms to simulate a fast thermal exchange rate.

It should be noted that the intrinsic ΔT_{AD} is proportional to the ΔT_s, which reaches the surface layer of the system. For the substrate optimization, the proportionality constant, δ, quantifies only the losses to the substrate, henceforth called the heat sink coefficient, defined as:

$$\Delta T_{AD} = \delta \Delta T_S \quad \text{(Equation 2)}$$

For IR camera optimizations, the black paint further contributes to the losses. In this case, the intrinsic ΔT_{AD} is proportional to the measured ΔT_M by a constant k, which is an experimental parameter conventionally called the correction factor, mathematically described as:

$$\Delta T_{AD} = k \Delta T_M \quad \text{(Equation 3)}$$

For the simulations, PMN-10PT was used as the reference material due to its excellent ΔT_{AD}[8,16] as well as moderate thermal properties.[14] To accurately represent the influence of the black

iScience
Article

CellPress
OPEN ACCESS

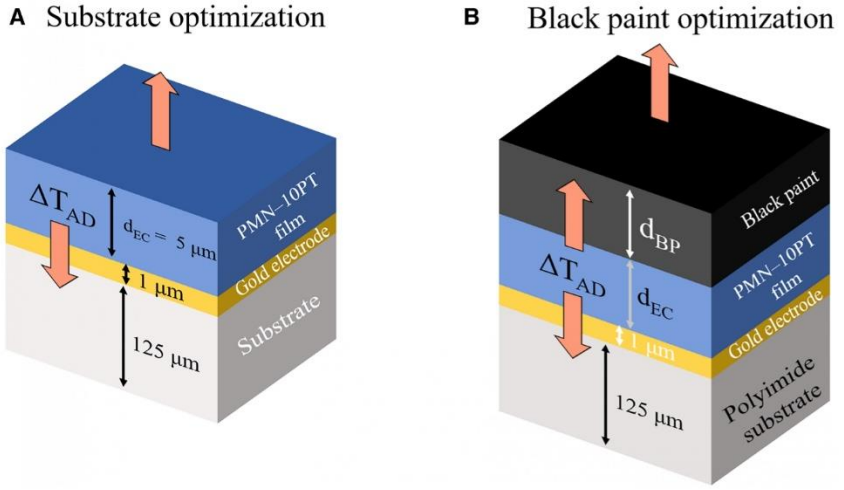


Figure 2. Simulated structures for substrate material and black paint optimizations

Schematic representation of simulated structures for (A) substrate optimization and (B) correction factor optimization. The arrows indicate the heat flow direction after the EC pulse is active.

paint, coatings were prepared using the airbrush method[41] and the black paint c_p was characterized, a value of 1350 J kg^{-1} K^{-1} was measured at room temperature, shown in supplemental information S1. The numerical values of the physical parameters of PMN-10PT, gold, and black paint used in the simulations are shown in Table 1.

Verification of the numerical model

The EC structure model was verified for its numerical consistency by checking the sufficiency of spatial and temporal discretization. For the validation, the structure for IR characterization was selected; in other words, the substrate was set to polyimide, and the black paint layer was considered. In particular, d_{EC} and d_{BP} were set to 5 μm. As shown in Figure 3A, a number of elements larger than 5 $\times 10^4$ is needed for the simulations to converge. Figure 3B shows k values as a function of different temporal resolutions, with 100 μs being the largest convergent value. Hence, to ensure convergence across all cases, in this work, 7.5 $\times 10^4$ elements were used and a time resolution of 10 μs was implemented. In addition, the calculated Knudsen number of the system was much smaller than 0.01, indicating that the system is in the continuum regime, therefore within converging limits, satisfying the conditions for the heat flow model.[43–46]

Minimizing the heat sink contribution from the substrate

The heat sink coefficient, δ, quantifies the thermal influence of the substrate material on the cooling performance of the caloric structure, as defined in Equation 2. If there is no heat transfer between the caloric film and the substrate, δ achieves its minimum value of 1. Therefore, the substrate materials that lead to δ as close to 1 as possible are the most suitable. In other words, to evaluate the influence of a substrate material on δ, it is necessary to quantify the ability of the substrate to transfer heat to its surroundings, namely, its thermal effusivity (r_T), mathematically described as[42,47]:

$$r_T = \sqrt{c_p \lambda \rho} \qquad \text{(Equation 4)}$$

In the simulations, a wide range of materials was implemented as substrates, namely polymers, metals, silica glass and ceramic Al_2O_3. As shown Figure 4, substrate materials that exhibit effusivity $r_T \leq 3$ kW $s^{1/2}$ m^{-2} K^{-1}, such as polyimide, polytetrafluoroethylene (PTFE) and silica glass, are the most suitable as such structures can achieve the lowest single-digit δ due to overall poor thermal exchange properties of the substrates. Whereas materials such as Gd, stainless steel, and Al_2O_3, exhibit $9 < \delta < 15$, in other words, these materials are potentially suitable for the substrates, depending on specific physical parameters of the system and experimental conditions. Among the simulated materials, brass exhibits the largest value of δ ~18. The c_p, λ, ρ, r_T of the substrate materials and the corresponding δ of the simulated EC structures are collected in Table 2.

To further assess the substrate influence, the individual contributions of c_p, λ, and ρ of the substrate on the δ values of the systems were also investigated. Using a simulated structure shown in Figure 1A, multiple combinations of the thermal parameter values were investigated. The selected c_p, λ, and ρ values were chosen to represent a wide range of materials for substrates, including polymers, ceramics, and metals.

In the first numerical analysis, c_p of the substrate was set to 450 J kg^{-1} K^{-1} (Figure 5, upper panel). These values approximately correspond to various metals and ceramics. Albeit at low λ, a comparatively low δ can be obtained, metals tend to exhibit larger density compared to ceramics and polymers and large λ, resulting in larger heat sink effects, reaching δ ~20. Then, c_p was set to 900 J kg^{-1} K^{-1}, representing ceramics and polymers, shown in the middle panel of Figure 5. Particularly, polyimide with λ = 0.2 W m^{-1} K^{-1} and ρ = 1420 kg m^{-3} results in δ = 2. In contrast, Al_2O_3 shows a larger thermal conductivity, λ = 30 W m^{-1} K^{-1} and larger density ρ = 3990 kg m^{-3}, leading to δ ~15. Lastly, materials with large c_p (2500 J kg^{-1} K^{-1}) were also simulated, shown in the bottom panel of Figure 5. At large ρ and λ, the coefficient δ can reach values as large as 30.

Table 1. Physical parameters of materials used in the simulations

Parameter	Electrocaloric PMN-10PT[8,14]	Gold electrode[8,29]	Black paint[8,42]
c_p (J kg^{-1} K^{-1})	349	129	1350[S1]
ρ (kg m^{-3})	8120	19300	1160
λ (W m^{-1} K^{-1})	1.3	318	0.2
ΔT_{AD}	1 K	–	–
τ	1 ms	–	–

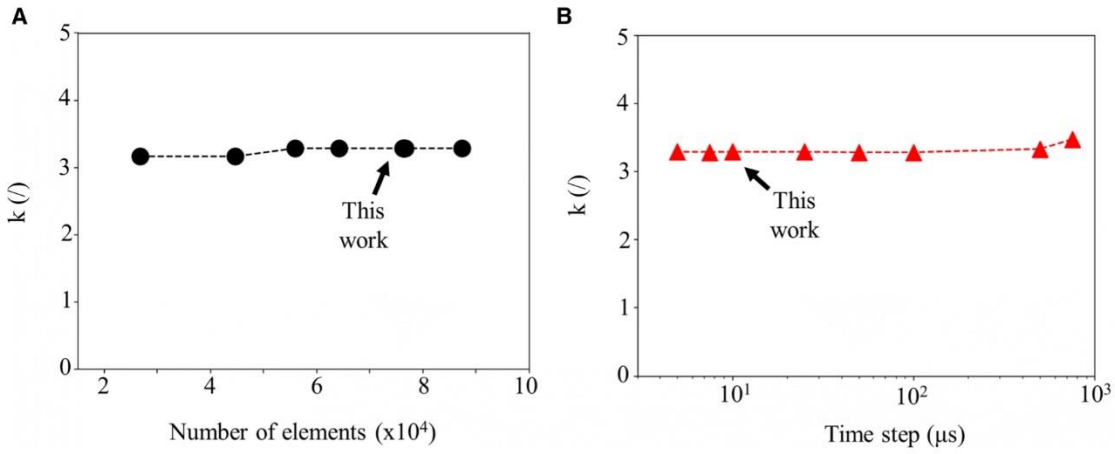


Figure 3. Proof of convergence of simulations
Dependence of the correction factor on (A) the number of elements and (B) the time resolution.

However, at low ρ and λ, for example, in the case of polyethylene that exhibits low density ($\rho < 1420$ kg m^{-3}) and low thermal conductivity ($\lambda < 0.5$ W m^{-1} K^{-1}),[42,60] the heat sink coefficient results in $\delta < 4$. Notice that in all panels, single-digit δ can be achieved regardless of c_p and ρ, if $\lambda \leq 1$ W m^{-1} K^{-1}. In other words, a low thermal conductivity of the substrate is a sufficient condition to minimize thermal losses.

Minimizing the correction factor in IR characterizations

The influence of the d_{EC} and the d_{BP} thickness on the correction factor in IR characterizations was investigated. Polyimide ($\rho = 1420$ kg m^{-3}, $c_p = 904$ J kg^{-1} K^{-1}, $\lambda = 0.2$ W m^{-1} K^{-1})[8] was used as a substrate material due to its minimal δ contribution. Simulations were performed with different d_{EC} and d_{BP} combinations, from sub-micron sizes up to 50 μm, as shown in Figure 2B. The values of k as a function of both d_{EC} and d_{BP} are shown in Figure 6A. Notice that regions of $k \leq 10$ (blue regions) are more predominant than regions of $k \geq 20$ (red regions), suggesting that increasing d_{EC} plays a more important role in minimizing k than decreasing d_{BP}. Particularly, most of $k \leq 10$ is found above the threshold $d_{EC} \geq 5$ μm, suggesting that k is strongly dependent on d_{EC}.

Figures 6B and 6C show k as a function of d_{EC} and d_{BP}, respectively. Notice that while k decreases nonlinearly with d_{EC}, it increases linearly with d_{BP}. It should be emphasized that d_{BP} can be as thin as a few μm, while larger thicknesses can be prepared with additional coatings.[41] Assuming $d_{BP} \leq 40$ μm, in order to achieve single-digit k values, at least one of the following conditions must be satisfied: $d_{EC} \geq d_{BP}$ or $d_{EC} \geq 5$ μm. In bulk materials, $d_{EC} \gg d_{BP}$, as the samples are millimeter-thick, while coatings do not exceed the micrometer-range, leading to a negligible correction factor. Thin films, however, generally have $d_{EC} \leq 0.5$ μm, and the expected correction factor should be considerably large, $k \gg 30$, hindering the IR characterization method as a viable option. In the case of thick-film characterizations, both d_{EC} and d_{BP} are a few micrometers thick, requiring case-specific optimizations in order to obtain $k \leq 10$. In addition, the case of free-standing films is discussed in supplemental information S2. Our results are in good agreement with the literature, where

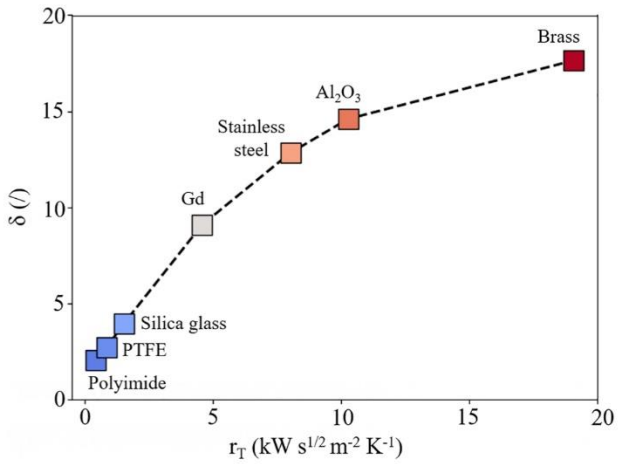


Figure 4. Heat sink coefficient as a function of thermal effusivity
Heat sink coefficient δ as a function of r_T for different materials. Blue markers represent low δ, while red markers represent higher δ values.

Table 2. c_p, λ, and ρ for different substrate materials at 300 K

Material	c_p (J kg^{-1} K^{-1})	λ (W m^{-1} K^{-1})	ρ (kg m^{-3})	rT (kW s$^{1/2}$ m^{-2} K^{-1})	δ (/)
Polyimide[8,42]	904	0.1	1420	0.36	2.0
PTFE[48–50]	1100	0.3	2200	0.85	2.7
Glass[51,52]	750	1.4	2200	1.51	3.9
Gd[53,54]	300	8.8	7900	4.57	9.1
Stainless steel[42]	500	16.2	7930	8.01	12.8
Al_2O_3[55–57]	880	30	3990	10.26	14.6
Brass[42,58,59]	380	111	8600	19.05	17.7

The simulated r_T and δ are also shown.

iScience
Article

CellPress
OPEN ACCESS

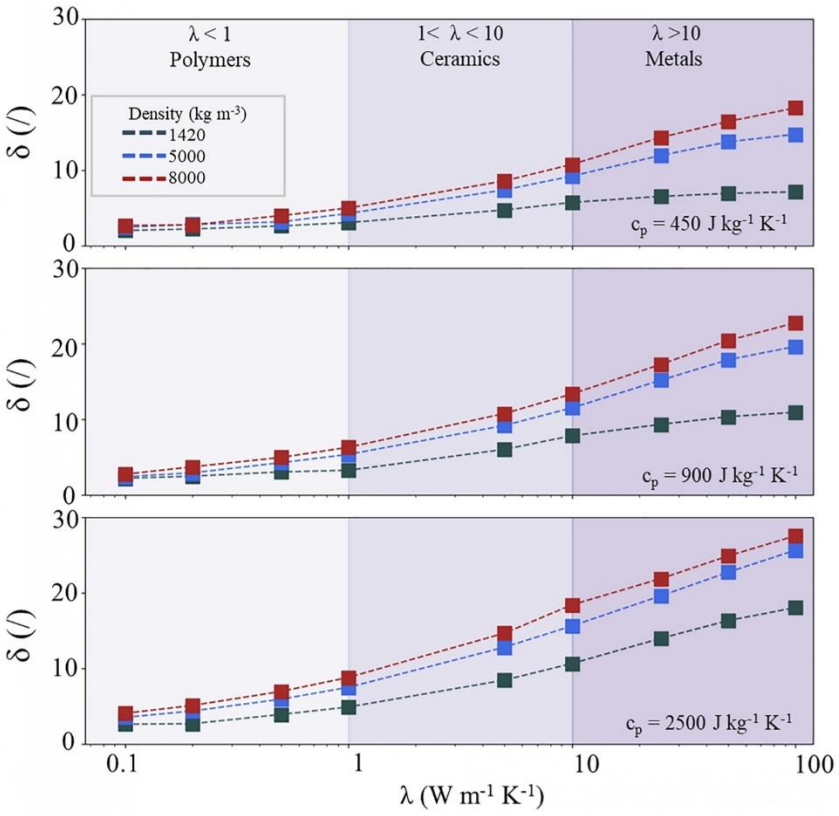


Figure 5. Heat sink coefficient as a function of different thermal parameters

Heat sink coefficient δ as a function of thermal conductivity at different substrate c_p values: 450 J kg^{-1} K^{-1} (upper panel), 900 J kg^{-1} K^{-1} (middle panel), 2500 J kg^{-1} K^{-1} (lower panel). The colored regions within the panels represent the thermal conductivity range of polymers ($\lambda < 1$ W m^{-1} K^{-1}), ceramics (1 W m^{-1} $K^{-1} \leq \lambda \leq$ 10 W m^{-1} K^{-1}), and metals ($\lambda > 10$ W m^{-1} K^{-1}). The marker colors represent different densities. The dashed lines are a guide to the eyes.

a 3-μm-thick PMN-10PT sample with a 3.5-μm-thick coating was estimated to have a k∼3.4 on a polyimide substrate.[8] In our simulations, under similar conditions, k ∼3.8 can be obtained. The difference between the values is attributed to the different thermal parameters of the black paints.

It is worth mentioning that in most practical applications, heat loss effects are expected to be larger than those calculated here, as the simulations were performed assuming ideal conditions (thermally insulated, no electrical contacts, low acquisition time), therefore, our values of δ and k represent lower-bound estimates. In other words, structures that exhibit large δ values according to our work will likely exhibit large values in real-world applications. In addition, this work is based on PMN-10PT as the active material, and, evidently, distinctive materials will interact differently and should be considered on a case-by-case basis. Further discussion on the influence of different materials, IR camera frame rate, and systematic contributions can be found in supplemental information S3.

In conclusion, using numerical simulation, we have investigated the substrate influence on the EC cooling output of PMN-10PT thick-film structures. Our results indicate that substrate materials with thermal effusivity $r_T \leq 3$ kW $s^{1/2}$ m^{-2} K^{-1} lead to minimal heat losses. Particularly, the condition $\lambda_{substrate} \leq 1$ W m^{-1} K^{-1}, regardless of c_p and ρ, is sufficient to achieve the heat sink coefficient $\delta \leq 10$, while further minimization can be achieved with substrate materials with lower overall r_T. In this manner, we have benchmarked the values for the thermal properties of substrates in the EC thick-film structures targeting optimized caloric performance.

In addition, the influence of the EC layer thickness and d_{BP} thickness on the correction factor for the IR characterization

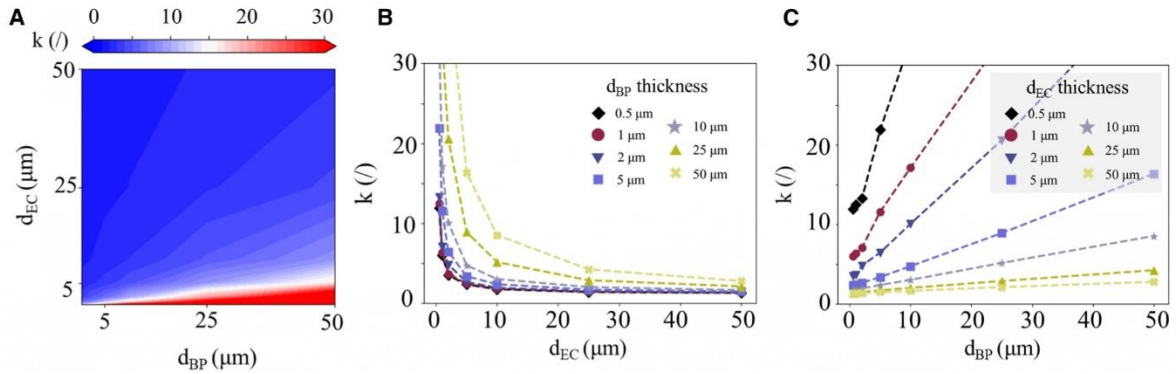


Figure 6. Correction factor as a function of electrocaloric film thickness and black paint thickness

(A) 2D mapping of the correction factor as a function of d_{EC} and d_{BP}. Correction factor k as a function of (B) d_{EC}, and (C) d_{BP}.

method was investigated. Our simulations show that single-digit k can be achieved if at least one of the following conditions is met: if the $d_{EC} \geq 5$ μm, assuming $d_{BP} \leq 40$ μm; or $d_{EC} \geq d_{BP}$, with layers thicker than 1 μm. Both conditions are satisfied in the case of bulk materials, while fine-tuning is required for the characterization of thick films. Our results confirm that coating methods that can achieve d_{BP} as thin as possible, such as printing and airbrushing, are highly desirable for IR-based characterization techniques.

This work provides a framework for preliminary assessment on substrate materials as well as sample-to-black coating optimization for the IR characterization method, and offers a roadmap for designing and characterizing caloric film structures for cooling at the micro-to-nano scales.

Limitations of the study

The main limitation of the work is the ideal case assumption, which results in lower estimates for the heat sink coefficient and correction factor. While it was briefly discussed in the supplemental information, further adjustments and considerations should be made on a case-by-case basis to ensure an accurate estimate of the parameters. In addition, this work focuses on the reference material PMN-10PT, which shows generally intermediate thermal properties. However, caloric effects can be observed on a diverse range of materials, including polymers (thermal insulators) and metals (thermal conductors). In other words, different thermal behaviors can be expected for different caloric materials and should be taken into consideration accordingly.

RESOURCE AVAILABILITY

Lead contact

Further information and requests for resources should be directed to and will be fulfilled by the lead contact, Prof. Dr. Hana Uršič (hana.ursic@ijs.si).

Materials availability

This study did not generate new unique materials.

Data and code availability

- The data that support the findings of this study are openly available in Zenodo at https://doi.org/10.5281/zenodo.18233562, reference number.[61]
- This study generated no custom code.
- Any additional information required to analyze the data reported in this study is available from the lead contact upon request.

ACKNOWLEDGMENTS

The authors acknowledge the financial support of the Slovenian Research and Innovation Agency (projects no. J2-60035, program no. P2-0105, and young researcher project) and the transnational consortium M-ERA.NET for the project Cool BatMan: Battery Thermal Management System Based on High Power Density Digital Microfluidic Magnetocaloric Cooling (no. 9400, Slovenian part of the project is financed by Ministry of Higher Education, Science and Innovation, Slovenia).

AUTHOR CONTRIBUTIONS

Conceptualization: H.U. and V.R.; data curation: V.R.; formal analysis: V.R.; funding acquisition: H.U. and U.T.; investigation: H.U., V.R., U.T., and A.K.; methodology: U.T. and V.R.; resources: H.U.; software: H.U. and V.R.; supervision: H.U., U.T., and A.K.; validation: H.U., U.T., and V.R.; writing – original draft: H.U. and V.R.; writing – review and editing: H.U., V.R., U.T., and A.K.

DECLARATION OF INTERESTS

A. Kitanovski is a member of iScience's Advisory Board and one of the co-guest editors of the special issue "Advanced thermal control: Fundamentals and applications."

STAR★METHODS

Detailed methods are provided in the online version of this paper and include the following:

- KEY RESOURCES TABLE
- METHOD DETAILS
  - Scanning electron microscopy
  - Numerical modelling
- QUANTIFICATION AND STATISTICAL ANALYSIS

SUPPLEMENTAL INFORMATION

Supplemental information can be found online at https://doi.org/10.1016/j.isci.2026.115965.

Received: January 5, 2026
Revised: March 11, 2026
Accepted: April 28, 2026

REFERENCES

1. Shi, J., Han, D., Li, Z., Yang, L., Lu, S.G., Zhong, Z., Chen, J., Zhang, Q.M., and Qian, X. (2019). Electrocaloric Cooling Materials and Devices for Zero-Global-Warming-Potential, High-Efficiency Refrigeration. Joule *3*, 1200–1225. https://doi.org/10.1016/j.joule.2019.03.021.
2. Moya, X., Kar-Narayan, S., and Mathur, N.D. (2014). Caloric materials near ferroic phase transitions. Nat. Mater. *13*, 439–450. https://doi.org/10.1038/nmat3951.
3. Klinar, K., Law, J.Y., Franco, V., Moya, X., and Kitanovski, A. (2024). Perspectives and Energy Applications of Magnetocaloric, Pyromagnetic, Electrocaloric, and Pyroelectric Materials. Adv. Energy Mater. *14*, 2401739. https://doi.org/10.1002/aenm.202401739.
4. T. Correia and Q. Zhang, eds. (2014). Electrocaloric Materials: New Generation of Coolers (Springer).
5. Zhang, T., Li, W., Cao, W., Hou, Y., Yu, Y., and Fei, W. (2016). Giant electrocaloric effect in PZT bilayer thin films by utilizing the electric field engineering. Appl. Phys. Lett. *108*, 162902. https://doi.org/10.1063/1.4947446.
6. Correia, T.M., Kar-Narayan, S., Young, J.S., Scott, J.F., Mathur, N.D., Whatmore, R.W., and Zhang, Q. (2011). PST thin films for electrocaloric coolers. J. Phys. D Appl. Phys. *44*, 165407. https://doi.org/10.1088/0022-3727/44/16/165407.
7. Sadl, M., Prah, U., Kovacova, V., Defay, E., Rojac, T., Lebar, A., Valentinčič, J., and Ursic, H. (2023). Multifunctional flexible ferroelectric thick-film structures with energy storage, piezoelectric and electrocaloric performance. J. Mater. Chem. C *11*, 10058–10068. https://doi.org/10.1039/D3TC01555F.
8. Prah, U., Sadl, M., Torello, A., Lheritier, P., Kovacova, V., Ursic, H., and Defay, E. (2023). Direct Electrocaloric Characterization of Ceramic Films. Small Methods *7*, 2300212. https://doi.org/10.1002/smtd.202300212.
9. Sadl, M., Lebar, A., Valentincic, J., and Ursic, H. (2022). Flexible Energy-Storage Ceramic Thick-Film Structures with High Flexural Fatigue Endurance. ACS Appl. Energy Mater. *5*, 6896–6902. https://doi.org/10.1021/acsaem.2c00518.

10. Pérez-Martín, Y., Peláiz-Barranco, A., García-Zaldívar, O., Calderón-Piñar, F., Yang, T., Paiva, P.M., Silva, A.C., and Guerra, J.D.S. (2023). Electrocaloric effect, pyroelectric response and energy storage performance of lanthanum-modified PZT relaxor ferroelectric ceramic. Phys. B Condens. Matter *671*, 415420. https://doi.org/10.1016/j.physb.2023.415420.

11. Li, J., Torelló, A., Kovacova, V., Prah, U., Aravindhan, A., Granzow, T., Usui, T., Hirose, S., and Defay, E. (2023). High cooling performance in a double-loop electrocaloric heat pump. Science *382*, 801–805. https://doi.org/10.1126/science.adi5477.

12. Sarkar, A., Šadl, M., Jazbec, A., Snoj, L., Drnovšek, S., Rojac, T., Brennecka, G.L., Uršič, H., and Malič, B. (2023). Influence of neutron and gamma irradiation on the electrocaloric properties of Mn-doped $0.9Pb(Mg_{1/3}Nb_{2/3})O_3$–$0.1PbTiO_3$ ceramics. JPhys Energy *5*, 045006. https://doi.org/10.1088/2515-7655/acf61b.

13. Uršič, H., Vrabelj, M., Otoničar, M., Fulanović, L., Rožič, B., Kutnjak, Z., Bobnar, V., and Malič, B. (2021). Influence of synthesis-related microstructural features on the electrocaloric effect for $0.9Pb(Mg_{1/3}Nb_{2/3})O_3$–$0.1PbTiO_3$ ceramics. Crystals *11*, 372. https://doi.org/10.3390/cryst11040372.

14. Vrabelj, M., Fulanovič, L., Bradeško, A., Drnovšek, S., and Malič, B. (2015). Specific Heat Capacity and Thermal Conductivity of the Electrocaloric $(1-x)Pb(Mg_{1/3}Nb_{2/3})O_3$–$xPbTiO_3$ Ceramics Between Room Temperature and 300 °C. Inf. MIDEM *45*, 260–265.

15. Uršič, H., Prah, U., Rojac, T., Jazbec, A., Snoj, L., Drnovšek, S., Bradeško, A., Mirjanić, A., Vrabelj, M., and Malič, B. (2022). High radiation tolerance of electrocaloric $(1-x)Pb(Mg_{1/3}Nb_{2/3})O_3$–$xPbTiO_3$. J. Eur. Ceram. Soc. *42*, 5575–5583. https://doi.org/10.1016/j.jeurceramsoc.2022.05.051.

16. Vrabelj, M., Uršič, H., Kutnjak, Z., Rožič, B., Drnovšek, S., Benčan, A., Bobnar, V., Fulanović, L., and Malič, B. (2016). Large electrocaloric effect in grain-size-engineered $0.9Pb(Mg_{1/3}Nb_{2/3})O_3$-$0.1PbTiO_3$. J. Eur. Ceram. Soc. *36*, 75–80. https://doi.org/10.1016/j.jeurceramsoc.2015.09.031.

17. Regis, V., Šadl, M., Brennecka, G., Bradeško, A., Tomc, U., and Uršič, H. (2023). Investigation of Structural and Electrical Properties of Al_2O_3/Al Composites Prepared by Aerosol Co-Deposition. Crystals *13*, 850. https://doi.org/10.3390/cryst13050850.

18. Sadl, M., Condurache, O., Bencan, A., Dragomir, M., Prah, U., Malic, B., Deluca, M., Eckstein, U., Hausmann, D., Khansur, N.H., et al. (2021). Energy-storage-efficient $0.9Pb(Mg_{1/3}Nb_{2/3})O_3$–$0.1PbTiO_3$ thick films integrated directly onto stainless steel. Acta Mater. *221*, 117403. https://doi.org/10.1016/j.actamat.2021.117403.

19. Tan, W.K., Shigeta, Y., Yokoi, A., Kawamura, G., Matsuda, A., and Muto, H. (2019). Investigation of the anchor layer formation on different substrates and its feasibility for optical properties control by aerosol deposition. Appl. Surf. Sci. *483*, 212–218. https://doi.org/10.1016/j.apsusc.2019.03.278.

20. Exner, J., Hahn, M., Schubert, M., Hanft, D., Fuierer, P., and Moos, R. (2015). Powder requirements for aerosol deposition of alumina films. Adv. Powder Technol. *26*, 1143–1151. https://doi.org/10.1016/j.apt.2015.05.016.

21. Exner, J., Linz, M., Kita, J., and Moos, R. (2021). Making powder aerosol deposition accessible for small amounts: A novel and modular approach to produce dense ceramic films. Int. J. Appl. Ceram. Technol. *18*, 2178–2196. https://doi.org/10.1111/ijac.13841.

22. Hatono, H., Ito, T., Iwata, K., and Akedo, J. (2006). Multilayer Construction with Various Ceramic Films for Electronic Devices Fabricated by Aerosol Deposition. Int. J. Appl. Ceram. Technol. *3*, 419–427. https://doi.org/10.1111/j.1744-7402.2006.02109.x.

23. Sadl, M., Tomc, U., Prah, U., and Ursic, H. (2019). Protective alumina coatings prepared by aerosol deposition on magnetocaloric gadolinium elements. Inf. MIDEM *49*, 177–182. https://doi.org/10.33180/infmidem2019.306.

24. Maiorino, A., Del Duca, M.G., Tomc, U., Tušek, J., Kitanovski, A., and Aprea, C. (2021). A numerical modelling of a multi-layer LaFeCoSi Active magnetic regenerator by using Artificial Neural Networks. Appl. Therm. Eng. *197*, 117375. https://doi.org/10.1016/j.applthermaleng.2021.117375.

25. Peixer, G.F., Tomc, U., Kitanovski, A., Lozano, J.A., and Barbosa, J.R. (2025). AI-driven Monte Carlo uncertainty analysis of Curie temperature effects on active magnetic regenerator performance. Int. J. Refrig. *180*, 518–527. https://doi.org/10.1016/j.ijrefrig.2025.09.011.

26. Petelin, N., Pečar, B., Vrtačnik, D., Perne, J., Tomc, U., and Kitanovski, A. (2024). Oscillating thermal switch using electrostatic forces. J. Phys., Conf. Ser. *2766*, 012204. https://doi.org/10.1088/1742-6596/2766/1/012204.

27. Nielsen, K.K., Tusek, J., Engelbrecht, K., Schopfer, S., Kitanovski, A., Bahl, C.R.H., Smith, A., Pryds, N., and Poredos, A. (2011). Review on numerical modeling of active magnetic regenerators for room temperature applications. Int. J. Refrig. *34*, 603–616. https://doi.org/10.1016/j.ijrefrig.2010.12.026.

28. Tomc, U., Peixer, G.F., Bahl, C.R.H., Nielsen, K.K., Lozano, J.A., Barbosa, J.R., and Kitanovski, A. (2025). Influence of Layering and Curie Temperature Uncertainty on the Performance of Multilayer Active Magnetic Regenerators. Adv. Funct. Mater. *35*, e24282. https://doi.org/10.1002/adfm.202424282.

29. Aravindhan, A., Lheritier, P., Torelló, A., Prah, U., Nouchokgwe, Y., El Moul, A., Chevalier, X., Domingues Dos Santos, F., Defay, E., and Kovacova, V. (2023). Direct measurement of electrocaloric effect in P(VDF-TrFE-CFE) film using infrared imaging. J. Materiomics *9*, 256–260. https://doi.org/10.1016/j.jmat.2022.10.009.

30. Vives, E., Burrows, S., Edwards, R.S., Dixon, S., Mañosa, L., Planes, A., and Romero, R. (2011). Temperature contour maps at the strain-induced martensitic transition of a Cu–Zn–Al shape-memory single crystal. Appl. Phys. Lett. *98*, 011902. https://doi.org/10.1063/1.3533403.

31. Mañosa, L., and Planes, A. (2017). Materials with Giant Mechanocaloric Effects: Cooling by Strength. Adv. Mater. *29*, 1603607. https://doi.org/10.1002/adma.201603607.

32. Gràcia-Condal, A., Planes, A., Mañosa, L., Wei, Z., Guo, J., Soto-Parra, D., and Liu, J. (2022). Magnetic and structural entropy contributions to the multicaloric effects in Ni-Mn-Ga-Cu. Phys. Rev. Mater. *6*, 084403. https://doi.org/10.1103/PhysRevMaterials.6.084403.

33. Lünser, K., Kavak, E., Gürpinar, K., Emre, B., Atakol, O., Stern-Taulats, E., Porta, M., Planes, A., Lloveras, P., Tamarit, J.-L., and Mañosa, L. (2024). Elastocaloric, barocaloric and magnetocaloric effects in spin crossover polymer composite films. Nat. Commun. *15*, 6171. https://doi.org/10.1038/s41467-024-50373-2.

34. Valdés, E., Stern-Taulats, E., Candau, N., Mañosa, L., and Vives, E. (2024). Enhancement of the Elastocaloric Performance of Natural Rubber by Forced Air Convection. Polymers *16*, 3078. https://doi.org/10.3390/polym16213078.

35. Wei, Z.Y., Sun, W., Shen, Q., Shen, Y., Zhang, Y.F., Liu, E.K., and Liu, J. (2019). Elastocaloric effect of all-*d*-metal Heusler NiMnTi(Co) magnetic shape memory alloys by digital image correlation and infrared thermography. Appl. Phys. Lett. *114*, 101903. https://doi.org/10.1063/1.5077076.

36. Pereira, M.J., Santos, T., Correia, R., Amaral, J.S., Amaral, V.S., Fabbrici, S., and Albertini, F. (2023). Mapping the magnetocaloric effect at the microscale on a ferromagnetic shape memory alloy with infrared thermography. JPhys Mater. *6*, 024002. https://doi.org/10.1088/2515-7639/acc13b.

37. Tušek, J., Engelbrecht, K., and Pryds, N. (2016). Elastocaloric effect of a Ni-Ti plate to be applied in a regenerator-based cooling device. Sci. Technol. Built Environ. *22*, 489–499. https://doi.org/10.1080/23744731.2016.1176809.

38. Ianniciello, L., Romanini, M., Mañosa, L., Planes, A., Engelbrecht, K., and Vives, E. (2020). Tracking the dynamics of power sources and sinks during the martensitic transformation of a Cu–Al–Ni single crystal. Appl. Phys. Lett. *116*, 183901. https://doi.org/10.1063/5.0006859.

39. Ossmer, H., Lambrecht, F., Gültig, M., Chluba, C., Quandt, E., and Kohl, M. (2014). Evolution of temperature profiles in TiNi films for elastocaloric

cooling. Acta Mater. *81*, 9–20. https://doi.org/10.1016/j.actamat.2014.08.006.

40. Hirai, T., Iguchi, R., Miura, A., and Uchida, K. (2022). Elastocaloric Kirigami Temperature Modulator. Adv. Funct. Mater. *32*, 2201116. https://doi.org/10.1002/adfm.202201116.

41. Regis, V., Brennecka, G., Tomc, U., Kitanovski, A., Cerar, J., Tušek, J., Jerman, I., Stern-Taulats, E., Lünser, K., Mañosa, L., and Uršič, H. (2025). Airbrushing: A Novel Method for Preparation of High-Emissivity Black Coating for Infrared Measurements. Adv. Mater. Interfac. *12*, e00467. https://doi.org/10.1002/admi.202500467.

42. Blaine, R.L. (2018). In search of thermal effusivity reference materials. J. Therm. Anal. Calorim. *132*, 1419–1422. https://doi.org/10.1007/s10973-018-7020-6.

43. Ziambaras, E., and Hyldgaard, P. (2006). Phonon Knudsen flow in nanostructured semiconductor systems. J. Appl. Phys. *99*, 054303. https://doi.org/10.1063/1.2175474.

44. Moffett, M.B., Robinson, H.C., Powers, J.M., and Baird, P.D. (2007). Single-crystal lead magnesium niobate-lead titanate (PMN/PT) as a broadband high power transduction material. J. Acoust. Soc. Am. *121*, 2591–2599. https://doi.org/10.1121/1.2717496.

45. Poletkin, K.V., Gurzadyan, G.G., Shang, J., and Kulish, V. (2012). Ultrafast heat transfer on nanoscale in thin gold films. Appl. Phys. B *107*, 137–143. https://doi.org/10.1007/s00340-011-4862-z.

46. Huber, R.C., Dattelbaum, D.M., Lang, J.M., Coe, J.D., Peterson, J.H., Bartram, B., and Gibson, L.L. (2023). Polyimide dynamically compressed to decomposition pressures: Two-wave structures captured by velocimetry and modeling. J. Appl. Phys. *133*, 035106. https://doi.org/10.1063/5.0128515.

47. Cottrill, A.L., Liu, A.T., Kunai, Y., Koman, V.B., Kaplan, A., Mahajan, S.G., Liu, P., Toland, A.R., and Strano, M.S. (2018). Ultra-high thermal effusivity materials for resonant ambient thermal energy harvesting. Nat. Commun. *9*, 664. https://doi.org/10.1038/s41467-018-03029-x.

48. Walters, R.N., and Lyon, R.E. (2003). Molar group contributions to polymer flammability. J. Appl. Polym. Sci. *87*, 548–563. https://doi.org/10.1002/app.11466.

49. Hsu, K.-L., Kline, D.E., and Tomlinson, J.N. (1965). Thermal conductivity of polytetrafluoroethylene. J. Appl. Polym. Sci. *9*, 3567–3574. https://doi.org/10.1002/app.1965.070091106.

50. Fai Lau, S., Suzuki, H., and Wunderlich, B. (1984). The thermodynamic properties of polytetrafluoroethylene. J. Polym. Sci. Polym. Phys. Ed. *22*, 379–405. https://doi.org/10.1002/pol.1984.180220305.

51. Wu, M., Liang, Y., Jiang, J.-Z., and Tse, J.S. (2012). Structure and Properties of Dense Silica Glass. Sci. Rep. *2*, 398. https://doi.org/10.1038/srep00398.

52. Andersson, S., and Dzhavadov, L. (1992). Thermal conductivity and heat capacity of amorphous SiO_2 : pressure and volume dependence. J. Phys. Condens. Matter *4*, 6209–6216. https://doi.org/10.1088/0953-8984/4/29/005.

53. Dan'kov, S.Y., Tishin, A.M., Pecharsky, V.K., and Gschneidner, K.A. (1998). Magnetic phase transitions and the magnetothermal properties of gadolinium. Phys. Rev. B *57*, 3478–3490. https://doi.org/10.1103/PhysRevB.57.3478.

54. Jacobsson, P., and Sundqvist, B. (1989). Thermal conductivity and electrical resistivity of gadolinium as functions of pressure and temperature. Phys. Rev. B *40*, 9541–9551. https://doi.org/10.1103/PhysRevB.40.9541.

55. Hu, Y., Du, G., and Chen, N. (2016). A novel approach for Al_2O_3/epoxy composites with high strength and thermal conductivity. Compos. Sci. Technol. *124*, 36–43. https://doi.org/10.1016/j.compscitech.2016.01.010.

56. Galusek, D., and Galusková, D. (2015). Alumina Matrix Composites with Non-Oxide Nanoparticle Addition and Enhanced Functionalities. Nanomaterials *5*, 115–143. https://doi.org/10.3390/nano5010115.

57. Yao, Y., Zeng, X., Guo, K., Sun, R., and Xu, J.b. (2015). The effect of interfacial state on the thermal conductivity of functionalized Al_2O_3 filled glass fibers reinforced polymer composites. Composites Part A *69*, 49–55. https://doi.org/10.1016/j.compositesa.2014.10.027.

58. Gustavsson, M., Karawacki, E., and Gustafsson, S.E. (1994). Thermal conductivity, thermal diffusivity, and specific heat of thin samples from transient measurements with hot disk sensors. Rev. Sci. Instrum. *65*, 3856–3859. https://doi.org/10.1063/1.1145178.

59. Chang, Y.A., and Hultgren, R. (1965). The Dilation Contribution to the Heat Capacity of Copper and α-Brass at Elevated Temperatures[1]. J. Phys. Chem. *69*, 4162–4165. https://doi.org/10.1021/j100782a017.

60. Mathot, V.B.F., and Pijpers, M.F.J. (1983). Heat capacity, enthalpy and crystallinity for a linear polyethylene obtained by DSC. J. Therm. Anal. *28*, 349–358. https://doi.org/10.1007/BF01983270.

61. Regis, V., and Uršič, H. (2026). Roadmap for Electrocaloric Films Characterization: A Numerical Study (Zenodo). https://doi.org/10.5281/ZENODO.18233561.

iScience
Article

CellPress
OPEN ACCESS

STAR★METHODS

KEY RESOURCES TABLE

REAGENT or RESOURCE	SOURCE	IDENTIFIER
Deposited data		
Raw data	This paper	https://doi.org/10.5281/zenodo.18245578
Software and algorithms		
COMSOL Multiphysics	COMSOL AB	comsol.com
Python 3	Python Software Foundation	python.org
Other		
SEM Verios HP 4G	Thermo Fisher Scientific	thermofisher.com
Acryllic black paint	Vallejo	70.602
DSC 204 F1	Netzsch Group	netzsch.com

METHOD DETAILS

Scanning electron microscopy

The cross-section of the reference sample was analyzed using a scanning electron microscope (SEM; Verios HP 4G, ThermoFisher, USA). Prior to the imaging, the sample was prepared into an epoxy resin matrix and fine polished.

Numerical modelling

The heat flow dynamics of the caloric system was simulated via a 2-dimensional finite-element model (COMSOL® Multiphysics version 6.2) using the thermal management module and time-dependent solver, within the interval 0 s to 50 ms at 10 μs steps. In all cases, the substrate had a fixed thickness of 125 μm, and a 1 μm-thick gold bottom electrode, the width of all layers was set to 5 mm. It is worth emphasizing that in the case of aerosol-deposited films, considered the reference structure, the thickness of the top electrode is at most ∼0.1 μm and, therefore, it was not implemented in the simulations. The influence of contacts for voltage application was assumed to be negligible, and all surrounding edges of the system were considered thermally insulated.

QUANTIFICATION AND STATISTICAL ANALYSIS

The simulation data is produced by COMSOL Multiphysics. Figures shown in the main text were produced in Python and Microsoft PowerPoint.

Supplemental Information

S1. Heat capacity characterization of black paint

To characterize the heat capacity of the black paint (Vallejo Primer Black, Vallejo, Barcelona, Spain), a black paint layers were deposited via the airbrush method (Filmotool DG-30, Filmotool, Ljubljana, Slovenia) on 76 mm x 26 mm glass substrates (Hirschmann Labogeräte, Eberstadt, Germany) and subsequently removed using a conventional laboratory spatula. The temperature dependence of the C_p was determined with a differential scanning calorimeter (DSC, Netzsch DSC 204 F1, Germany). Measurements were performed on disc-shaped plates (2r ~6 mm, d = 0.125 mm) placed in a Pt crucible with a lid. To exclude possible thermal effects related to evaporation of water and desorption of gasses from the surface of the sample, two heating and cooling cycles were performed. In the first cycle, the samples were heated from 25 °C to 120 °C and then cooled to 0 °C with liquid nitrogen. Subsequently, the samples were heated again to 120 °C and cooled to 25 °C. Heating and cooling rates of 5 K min^{-1} were used for all measurements. Sapphire (Netzsch, 2r = 5.2 mm, d = 0.25 mm) was used as the standard material to determine the C_p of the sample. The Cp measurement is shown in Figure S1.

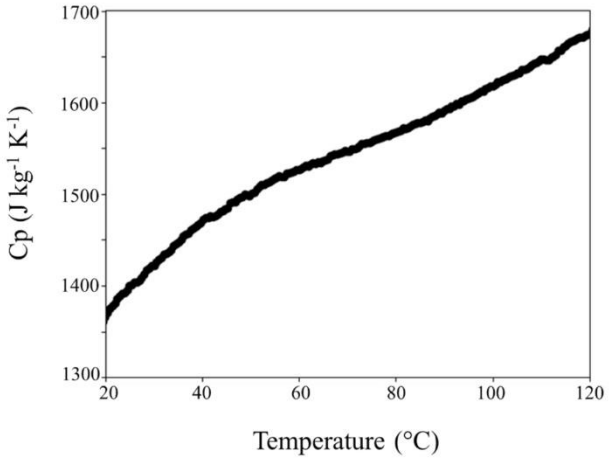


Figure S1: Heat capacity of acrylic-based black paint. Related to Table 1.

S2. Thickness dependence of the correction factor k for free-standing PMN–10PT films

The correction factor k in the case of free-standing films was also considered. The simulations were performed with different thicknesses of free-standing PMN–10PT films. The thickness of the black paint d_{BP} was 5 μm in all cases. As shown in Figure S2, when the thickness of a free-standing PMN–10PT film is 5 μm, a correction factor of ~2 can be obtained. As the thickness of the free-standing PMN–10PT film exceeds that of the black coating, the correction factor converges to

unity, reaching ~1.3 at 50 μm. It is worth mentioning that bulk samples are generally thicker than 200 μm, further decreasing the influence of the black paint.

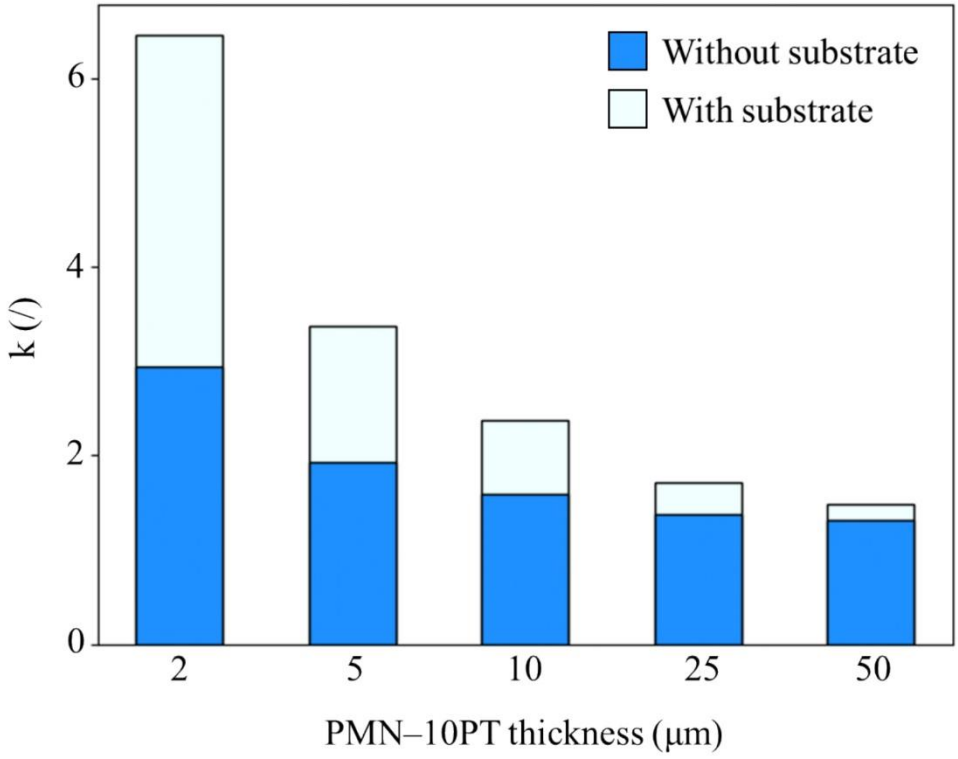


Figure S2: Correction factor as a function of free-standing PMN–10PT thickness. The case considering a polyimide substrate was included for reference. Related to Figure 5.

S3. Parameter dependence of the correction factor k: active material, substrate, and measurement acquisition time

In the main text, we discussed the correction factor on caloric film structures assuming PMN–10PT as the active layer and ideal conditions (thermally insulated, no electrical contacts, low acquisition time), with no additional influence beyond the layers. When assessing different substrates and optimizing the coatings, this approach promptly offers a lower bound estimate for the correction factor. However, real-world infrared-based measurements can be done on a wide range of materials and other parameters may also differ between experimental equipment. In light of this, in this section, the influence of key experimental conditions on the correction factor will be discussed.

First, the impact of different materials as active films was investigated. The simulated materials represent a wide range of thermal properties: P(VDF-TrFE-CFE) is a highly insulating EC polymer (r_T ~0.8 kW $s^{1/2}$ m^{-2} K^{-1})[1], $BaTiO_3$ (BTO) is an EC ceramic material with r_T ~2.6 kW $s^{1/2}$ m^{-2} K^{-1} ,[2]

and Gd is a magnetocaloric (MC) material with comparatively large effusivity, showing r_Γ ~4.6 kW $s^{1/2}$ m^{-2} K^{-1}.[3,4] Similar criteria on the broad range of thermal properties (as explained in the main text) were used to select the simulated substrate materials: polyimide, glass, and Al_2O_3 substrates. The simulations were performed with the same parameters as the simulations in the main text (Figure 2b). In all the simulations, the thicknesses of films and black paint coatings were set to 5 µm, while the thickness of the substrates was set to 125 µm.

The P(VDF-TrFE-CFE) polymer material exhibits a low thermal effusivity value, and therefore, the P(VDF-TrFE-CFE) films on all three substrates achieve a single-digit correction factor (Figure S3, left group of bars). The ceramic material BTO exhibits single-digit correction factors on polyimide and glass substrates, however, k ~ 20 in the case of Al_2O_3 substrate. Gd also exhibited single-digit correction factors on polyimide and glass substrates, while on Al_2O_3 substrate, k ~ 22.

It is worth emphasizing that thick-film structures for all simulated active materials exhibited comparable k values on both polyimide and glass substrates (orange bars and blue bars in Figure S3). However, this is not the case for Al_2O_3 substrates (grey bars), where the k value changes for different active materials. This is because the Al_2O_3 substrates have the highest thermal effusivity among all three simulated substrates, which imposes significant variance on k values (from 6 to 22). In other words, for Al_2O_3 substrates, a low-effusivity active thick-film material is recommended. The thermal properties of the simulated active materials are collected in Table S1.

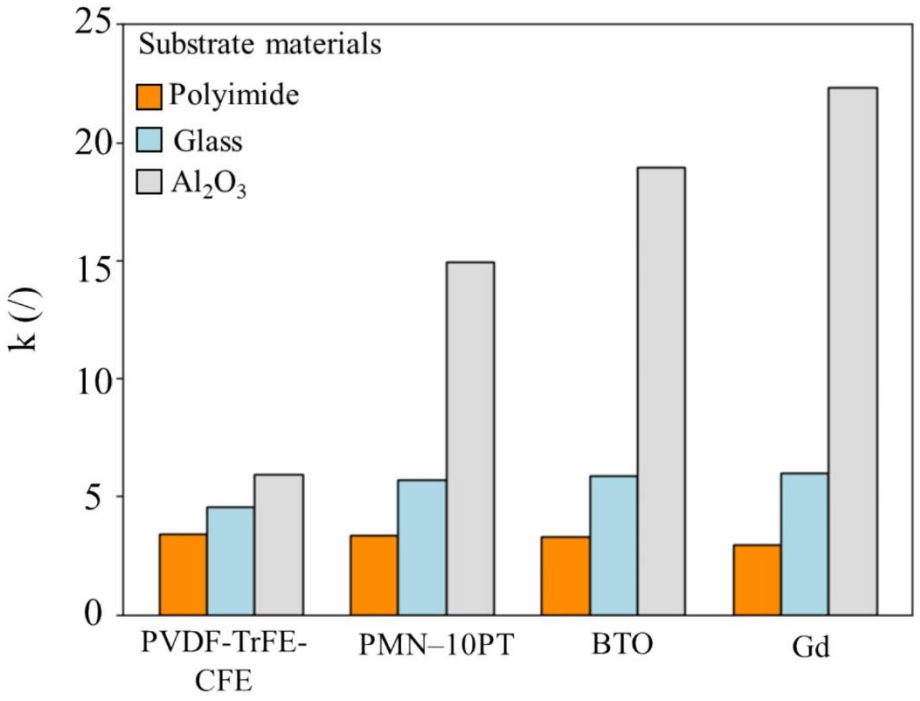


Figure S3: Correction factor, k, of different active thick-film materials on three different substrates. A bottom electrode was not simulated in the case of Gd thick-film structure, as it is not required for MC applications. As a reference, PMN–10PT was also included. Related to Figure 5.

Table S1: Physical parameters of different active materials. Related to Figure 5.

Material	c_p ($J\ kg^{-1}\ K^{-1}$)	λ ($W\ m^{-1}\ K^{-1}$)	ρ ($kg\ m^{-3}$)	r_T ($kW\ s^{1/2}\ m^{-2}\ K^{-1}$)
P(VDF-TrFE-CFE)[1]	1780	0.2	1800	0.8
$BaTiO_3$[2]	434	2.7	5900	2.6
Gd[3,4]	300	8.8	7900	4.6
PMN–10PT[5,6]	349	1.3	8120	1.9

Moreover, the acquisition time (inverse of frame rate) of the measurement system plays a significant role in the value of the correction factor. To investigate this influence, simulations were performed with different frame rates, from 10 Hz to 1000 Hz. The simulated structure was the same in all cases, with both the thickness of black paint coating and PMN–10PT layer set to 5 μm, and the thickness of the polyimide substrate set to 125 μm. As shown in Figure S4, at a frame rate of 10 Hz, the correction factor k can reach a value as large as ~ 12.1, which strongly decreases with the frame rate. At 100 Hz, the correction factor k is halved (k ~ 6.2), ultimately decreasing to k ~ 3.4 at 1 kHz.

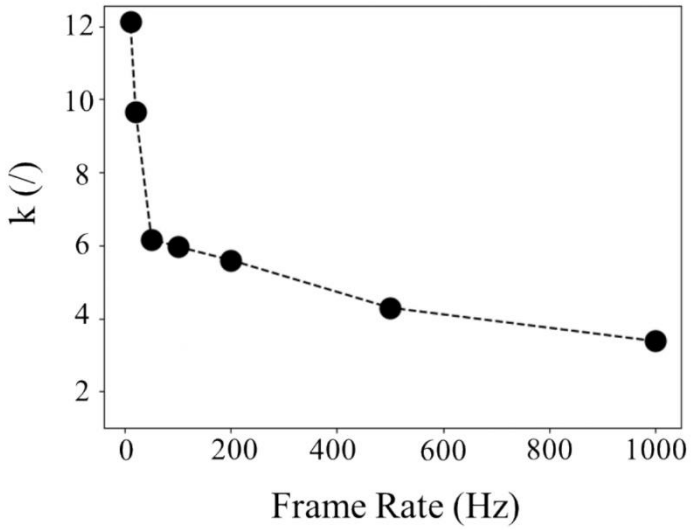


Figure S4: Correction factor, k, as a function of frame rate. Related to Figure 5.

At lower frame rates, there is enough time for the heat to dissipate further into the measurement setup, and, therefore, other systematic contributions should be considered when calculating the correction factor. At such a time scale, the correction can also be obtained via:[6–9]

$$k = \frac{C_p^A}{C_p^T}, \tag{1}$$

where Cp^A and Cp^T are the heat capacity of the active area (under the electrodes) and the total heat capacity of the system, respectively.

While the IR-camera method only requires coating the sample with a black paint layer and can be operated over a wide range of frame rates, the thermistor-in-calorimeter (TiC) method is limited to 1 Hz and additionally requires wiring, a thermistor, and adhesive materials [6–9]. Due to the larger passive thermal masses of the wires, the thermistor, and glues, and the large time scale (~1 s) of the TiC method, we conclude that $k_{TiC} > k_{IR}$. Within this scope, calculating k_{TiC} offers an upper limit to the systematic contributions of k_{IR}. For the TiC method, a correction factor of ~27 is obtained for 5-µm-thick PMN–10PT film on a polyimide substrate. In this case, the polyimide substrate contributes with 85 % of this k value, while wiring, glues, and thermistor correspond to the additional 15 % of k value. Since the systematic contributions of the TiC method are always larger than those of the IR camera method, a variance in k_{IR} is in the range of 15 % can be estimated. This value is expected to decrease at larger frame rates, as indicated in Figure S4.

References

1. Aravindhan, A., Lheritier, P., Torelló, A., Prah, U., Nouchokgwe, Y., El Moul, A., Chevalier, X., Domingues Dos Santos, F., Defay, E., and Kovacova, V. (2023). Direct measurement of electrocaloric effect in P(VDF-TrFE-CFE) film using infrared imaging. J. Materiomics *9*, 256–260. https://doi.org/10.1016/j.jmat.2022.10.009.

2. He, Y. (2004). Heat capacity, thermal conductivity, and thermal expansion of barium titanate-based ceramics. Thermochim. Acta *419*, 135–141. https://doi.org/10.1016/j.tca.2004.02.008.

3. Dan'kov, S.Yu., Tishin, A.M., Pecharsky, V.K., and Gschneidner, K.A. (1998). Magnetic phase transitions and the magnetothermal properties of gadolinium. Phys. Rev. B *57*, 3478–3490. https://doi.org/10.1103/PhysRevB.57.3478.

4. Jacobsson, P., and Sundqvist, B. (1989). Thermal conductivity and electrical resistivity of gadolinium as functions of pressure and temperature. Phys. Rev. B *40*, 9541–9551. https://doi.org/10.1103/PhysRevB.40.9541.

5. M. Vrabelj, L. Fulanovič, A. Bradeško, S. Drnovšek, B. Malič, H.U. (2015). Specific Heat Capacity and Thermal Conductivity of the Electrocaloric (1-x)$Pb(Mg_{1/3}Nb_{2/3})O_3$–x$PbTiO_3$ Ceramics Between Room Temperature and 300 °C. Informacije MIDEM 45, 260–265.

6. Prah, U., Sadl, M., Torello, A., Lheritier, P., Kovacova, V., Ursic, H., and Defay, E. (2023). Direct Electrocaloric Characterization of Ceramic Films. Small Methods *7*, 202300212. https://doi.org/10.1002/smtd.202300212.

7. Kutnjak, Z., Rožič, B., and Pirc, R. (2015). Electrocaloric Effect: Theory, Measurements, and Applications. In Wiley Encyclopedia of Electrical and Electronics Engineering, J. G. Webster, ed. (Wiley). https://doi.org/10.1002/047134608X.W8244.

8. Rožič, B., Malič, B., Uršič, H., Holc, J., Kosec, M., Neese, B., Zhang, Q.M., and Kutnjak, Z. (2010). Direct Measurements of the Giant Electrocaloric Effect in Soft and Solid Ferroelectric Materials. Ferroelectrics *405*, 26–31. https://doi.org/10.1080/00150193.2010.482884.

9. Correia, T. (ed.), and Zhang, Q. (ed.) (2014). Electrocaloric Materials: New Generation of Coolers (Springer).

Chapter 4

Airbrushing: A Novel Method for Preparation of High-Emissivity Black Coating for Infrared Measurements

Direct characterization methods of caloric effects have become widespread in recent years, as these techniques allow for an accurate quantification of the intrinsic caloric properties of materials. In particular, the IR camera method has received significant attention due to its low systematic heat losses, when compared to other direct methods. For the characterization via the IR method, only a layer of high-emissivity coating is needed, which is generally a black paint layer. From our previous results, in order to achieve maximized response during caloric measurements of films, we have concluded that the thickness of the coating should be in the range of a few µm and not exceed the thickness of the caloric film. Therefore, a controllable method which can satisfy this condition is highly desirable.

However, most of the literature does not report the black paint coating method or thickness. While in the case of bulk materials, the black paint may only marginally influence the measured values, it significantly affects measurements of µm-thick films, as some black paint coating methods lack fine thickness control and the paint may exceed the thickness of the film itself by an order of magnitude. A potential solution is the ink printing technique, where a 3.5 µm-thick paint was achieved. This technique, however, can only be employed on small flexible samples as it is limited by the geometry of the printing device.

In light of this, we have developed a novel black coating preparation method, using the low-cost airbrush tool. This technique is easy to use, portable and allows for the preparation of black paint coatings on surfaces of any geometry. The method exhibited fine thickness control starting at ∼3 µm, at a single layer, and gradually increasing with additional layers. At 35 layers, a thickness of ∼30 µm was achieved. In addition, the emissivity of the black coating was measured and a value of ∼0.95 was obtained. Furthermore, a commercially available magnetocaloric sample was coated and characterized via the IR method and the measurements of the room-temperature magnetocaloric response were in excellent agreement with the supplier's datasheet for this material. In this way, we bring forth a novel black coating preparation method, which can be applied onto a wide range of samples for IR caloric measurements.

This chapter addresses thesis objectives: 2,3

Published in: V. Regis, G. Brennecka, U. Tomc, A. Kitanovski, J. Cerar, J. Tusek, I. Jerman, E. Stern-Taulats, K. Lunser, L. Mañosa and H. Ursic, "Airbrushing: A Novel

Method for Preparation of High-Emissivity Black Coating for Infrared Measurements," Adv. Mater. Interfaces, vol. 12, p. e00467, 2025. (IF = 4.4, 2025)

My contribution: I prepared the black paint coatings and optimized the parameters for the airbrushing technique. I performed the profilometric thickness measurements, analyzed the samples under an optical microscope and electron microscope. In collaboration with colleagues I performed the magnetocaloric measurement on the reference sample and measured the emissivity of the samples. I elaborated the concept of the manuscript and wrote the paper, together with the co-authors.

Check for upda

RESEARCH ARTICLE

ADVANCED MATERIALS INTERFACES Open Access

www.advmatinterfaces.de

Airbrushing: A Novel Method for Preparation of High-Emissivity Black Coating for Infrared Measurements

*Victor Regis, Geoff Brennecka, Urban Tomc, Andrej Kitanovski, Jan Cerar, Jaka Tušek, Ivan Jerman, Enric Stern-Taulats, Klara Lünser, Lluís Mañosa, and Hana Uršič**

The reliability of infrared (IR) imaging is strongly dependent on the surface emissivity of the investigated object. Achieving near-unity emissivity is essential to IR measurement accuracy. To meet this requirement, black paint coatings are commonly applied onto the studied samples. However, there is a lack of a systematic study of the coating preparation for IR measurements. In this work, a new procedure is developed for the preparation of black paint coatings using the cost-effective airbrush tool. With this novel method, it can achieve black paint coatings as thin as ≈3 µm or thicker, depending on the number of layers. The coatings are homogeneous and with excellent adhesion to the substrate. Furthermore, the coatings can be entirely removed from the substrate using conventional laboratory solutions. The coatings exhibited an average emissivity of ≈0.95 within the 0.5–2.5 µm wavelength range. The quality of the coatings is validated by directly measuring the magnetocaloric response of a commercially available material, which is in excellent agreement with the supplier's datasheet. In this way, a novel affordable black coating method is showcased, which can be applied on a wide variety of samples for IR measurements, broadening the possibilities for IR characterizations.

1. Introduction

Any material whose temperature is above absolute zero radiates energy through a process called black-body emission, which, according to Planck's law, encompasses the entire electromagnetic spectrum. In nature, the temperatures of objects vary significantly, for example, in astronomy, objects of interest, such as stars, can exceed 5000 Kelvin,[1] whereas in biology and materials science, relevant properties are typically studied at temperatures a few hundred degrees below or above room temperature (near room temperature conditions).[2,3] At these conditions, most of the emitted radiation will exhibit a wavelength between 750 nm and ≈50 µm, within the infrared (IR) spectrum.[2] In light of this, the IR camera method of imaging was developed allowing for real-time heat maps, or thermographs, of a wide variety of objects and has been used in several research fields.[4–7] In biology, for example, IR imaging is used to investigate the heat dissipation mechanisms in different species of plants and animals,[8–10] and in human medicine, as an early-stage indication of illness.[11–13] In the research of inorganic materials, IR thermal camera imaging has been used to investigate the structural, microstructural, electrical or magnetic properties.[14–18] A key parameter to ensure the reliability and accuracy of IR imaging is emissivity, which is defined as the effectiveness of a surface in emitting thermal radiation. The closer it is to unity, the more the surface behaves as an ideal black-body.[5–7] In organic tissues, the emissivity was shown to be between 0.7 and 0.95,[8–13] while metals can exhibit emissivities as low as 0.02 or as high as 0.6, depending on the material, surface conditions, and preparation methods.[19–25] Generally, low-emissivity surfaces, such as metals

V. Regis, H. Uršič
Electronic Ceramics Department
Jožef Stefan Institute
Jamova cesta 39, Ljubljana 1000, Slovenia
E-mail: hana.ursic@ijs.si
V. Regis, H. Uršič
Jožef Stefan International Postgraduate School
Jamova cesta 39, Ljubljana 1000, Slovenia

The ORCID identification number(s) for the author(s) of this article can be found under https://doi.org/10.1002/admi.202500467

© 2025 The Author(s). Advanced Materials Interfaces published by Wiley-VCH GmbH. This is an open access article under the terms of the Creative Commons Attribution License, which permits use, distribution and reproduction in any medium, provided the original work is properly cited.

DOI: 10.1002/admi.202500467

G. Brennecka
Colorado School of Mines
1500 Illinois Ave., Golden, CO 80401, USA
U. Tomc, A. Kitanovski, J. Cerar, J. Tušek
Faculty of Mechanical Engineering
University of Ljubljana
Aškerceva cesta 6, Ljubljana 1000, Slovenia
I. Jerman
Laboratory for Coating Development
Department of Materials Chemistry
National Institute of Chemistry
Hajdrihova 19, Ljubljana 1000, Slovenia
E. Stern-Taulats, K. Lünser, L. Mañosa
Departament de Física de la Matèria Condensada
Facultat de Física
Martí i Franquès 1
Universitat de Barcelona
Barcelona 08028, Catalonia, Spain

ADVANCED SCIENCE NEWS
www.advancedsciencenews.com

ADVANCED MATERIALS INTERFACES
Open Access
www.advmatinterfaces.de

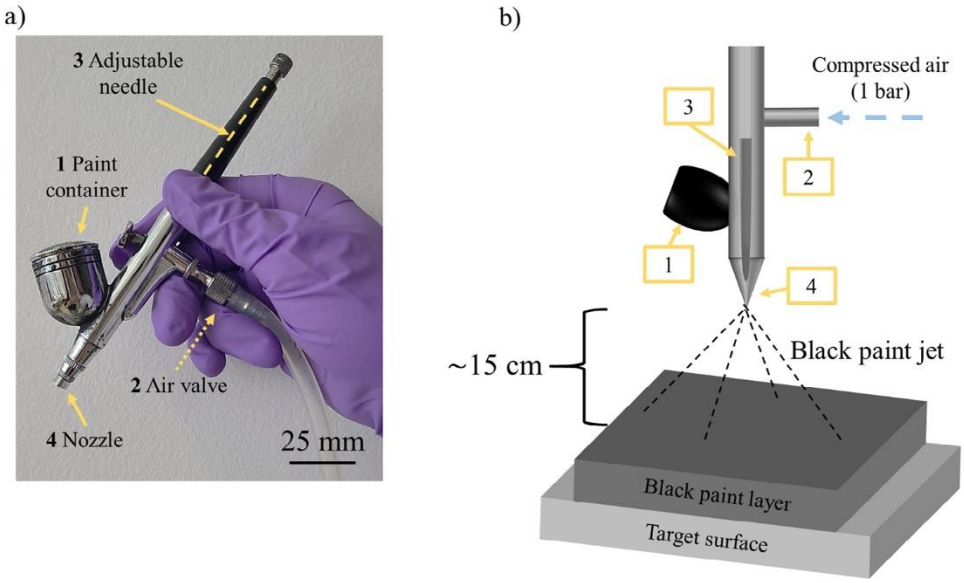


Figure 1. a) Photograph of the airbrush used in this work. b) Schematic representation of coating procedure. The numbered labels indicate the same components of the airbrush.

and ceramics, will be coated with black paint to ensure a high emissivity during the IR thermal camera investigations.[14–19,26–31]

In recent years, there has been an increase in studies on materials that exhibit an adiabatic and reversible temperature change as a response to an electric field, magnetic field, uniaxial stress or hydrostatic pressure, namely the electrocaloric, magnetocaloric, elastocaloric or barocaloric effect, respectively.[32–38] In the case of conventional caloric materials, when an external stimulus is applied, in isothermal conditions, the entropy in the material will decrease, which, in adiabatic conditions, will lead to an increase in temperature. After thermal relaxation, the material will return to ambient temperature, and the removal of the stimulus will result in a decrease in temperature, which can potentially be used to cool down the target object. Caloric technology is a cleaner and potentially more energy-efficient alternative to traditional vapor-compression cooling and is often integrated into active regenerators to enhance performance and minimize thermal losses.[33,34] However, despite their promising properties, current prototypes cannot yet compete with commercial cooling systems due to various limitations. Incorporating thermal control devices, such as thermal diodes and switches, can further reduce these drawbacks and improve the efficiency of caloric-based systems.[39,40] In the search for better caloric materials, the IR method has been widely used to characterize the thermal output of materials,[16–18,29,41] as this method is contactless and therefore minimizes thermal losses during the measurements. However, most magnetocaloric and elastocaloric materials are metals or alloys, in addition electrocaloric materials require metal electrodes for applications of electric fields, producing surfaces with very low emissivity. To circumvent such issue, prior to the IR measurements, the surface of the materials is coated with a high emissivity coating, usually black paint. However, in most research articles, the coating procedure is often not detailed.[42–47] To the authors' knowledge, researchers typically use spray painting techniques with commercially available paints to produce the black coatings. This method lacks control over the thickness, homogeneity and roughness of the coating. As a result, the coating can be as thick as ≈100 μm.[48,49] Evidently, this method is unsuitable for samples with a thickness lower than 100 μm, as the paint will act as a significant heat sink, which significantly affects the temperature measurements in the caloric system. Recently, there were two reports[16,17] on IR imaging of 3-μm-thick electrocaloric films, where the authors systematically produced ≈3.5 μm coatings of conventional black printer ink using a commercial office printer. Although the method is suitable for flexible films, the setup limits the geometry and dimension of the samples, as they must have a flat surface with no curvature or bending, and it is detrimental to brittle samples such as ceramic pellets. In light of this, a sample-geometry independent coating preparation method that can achieve controlled thickness and high emissivity is required for advanced IR thermal camera characterization.

In this work, black paint coatings were prepared using an inexpensive, easy-to-use airbrush method. This method has been previously used to prepare ceramic layers,[50,51] but it has not yet been considered as a black coating technique for IR measurements. We propose using the airbrush method for the preparation of dense black paint coatings with ≈3 μm thickness and an average emissivity of 0.95, which can be easily removed without damaging the target surfaces. In this way, we have developed a reliable, novel method for black coatings that can be used for IR camera measurements on a wide range of samples, regardless of their material, shape or size.

2. Experimental Section

The black coatings were prepared using a Filmotool Airbrush DG-30 (Filmotool, Ljubljana, Slovenia). The airbrush paint container was filled with the black-paint solution prepared from 15 mL of commercial black paint (Vallejo Primer Black, Vallejo, Barcelona, Spain) and 3 mL of paint thinner (Vallejo Airbrush

© 2025 The Author(s). Advanced Materials Interfaces published by Wiley-VCH GmbH

21967350, 0, Downloaded from https://advanced.onlinelibrary.wiley.com/doi/10.1002/admi.202500467 by Hana Ursic - Institut Jozef Stefan , Wiley Online Library on [29/08/2025]. See the Terms and Conditions (https://onlinelibrary.wiley.com/terms-and-conditions) on Wiley Online Library for rules of use; OA articles are governed by the applicable Creative Commons License

ADVANCED SCIENCE NEWS
www.advancedsciencenews.com

ADVANCED MATERIALS INTERFACES
Open Access
www.advmatinterfaces.de

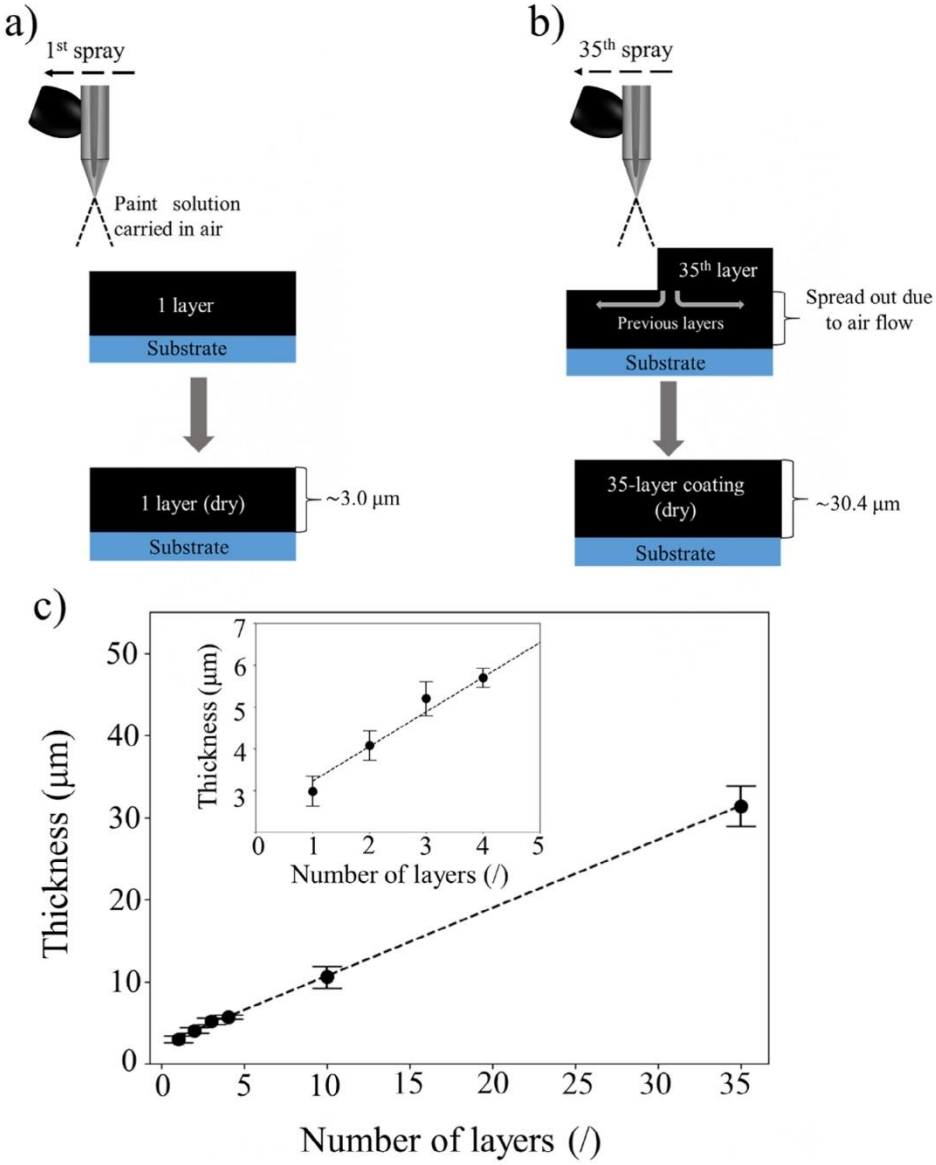


Figure 2. Schematic representation of the coating procedure for a) 1 layer and b) 35 layers. c) Average total coating thickness as a function of number of layers. The black dashed line is a guide to the eyes. The inset shows the average thickness of coatings with up to four layers.

Thinner, Vallejo, Barcelona, Spain). The airbrush can operate with a pressured difference within 0.5 and 2 bar. In this work, the compressed air was injected through the air valve at a constant pressure difference of 1 bar and regulated with the adjustable needle, as shown in **Figure** 1a. During the coating procedure, the airbrush nozzle was positioned 15 cm away from the target surface (Figure 1b). For the systematic investigation of the prepared coatings, 76 mm × 26 mm glass substrates (Hirschmann Labogeräte, Eberstadt, Germany) were used, which were fixed in place with conventional tape, exposing an area of ≈5 mm × 15 mm. To study the influence of the number of layers on the total thickness of the painted coatings, the substrates were painted with 1, 2, 3, 4, 10 or 35 layers of black paint. To ensure consistency, each individual layer was prepared within a time interval of ≈1 s. To reduce the influence of systematic variations between preparations, five samples were prepared for each set.

Using a contact stylus profilometer (DektakXT, Bruker, Karlsruhe, Germany) the coating thickness was measured and mean-square-root roughness (R_q) was calculated along a millimeter-long line scan. To minimize errors, the thickness and R_q measurements for each set of layers were calculated as the average of five samples. The surface and cross-section of the coatings were investigated using an optical microscope (Axio Imager M2m, Zeiss, Jena, Germany). The surface of the coatings was further investigated by atomic force microscopy (AFM; MFP-3D, Asylum Research, Santa Barbara, California, USA). Regions with the size of 80 µm x 80 µm, and 20 µm x 20 µm were scanned using titanium-iridium-coated silicon tips (Asylec-01-R2, Oxford Instruments, Abingdon, UK). The cross-sections of the samples

© 2025 The Author(s). Advanced Materials Interfaces published by Wiley-VCH GmbH

21967350, 0, Downloaded from https://advanced.onlinelibrary.wiley.com/doi/10.1002/admi.202500467 by Hana Ursic - Institut Jozef Stefan , Wiley Online Library on [29/08/2025]. See the Terms and Conditions (https://onlinelibrary.wiley.com/terms-and-conditions) on Wiley Online Library for rules of use; OA articles are governed by the applicable Creative Commons License

ADVANCED SCIENCE NEWS
www.advancedsciencenews.com

ADVANCED MATERIALS INTERFACES
Open Access
www.advmatinterfaces.de

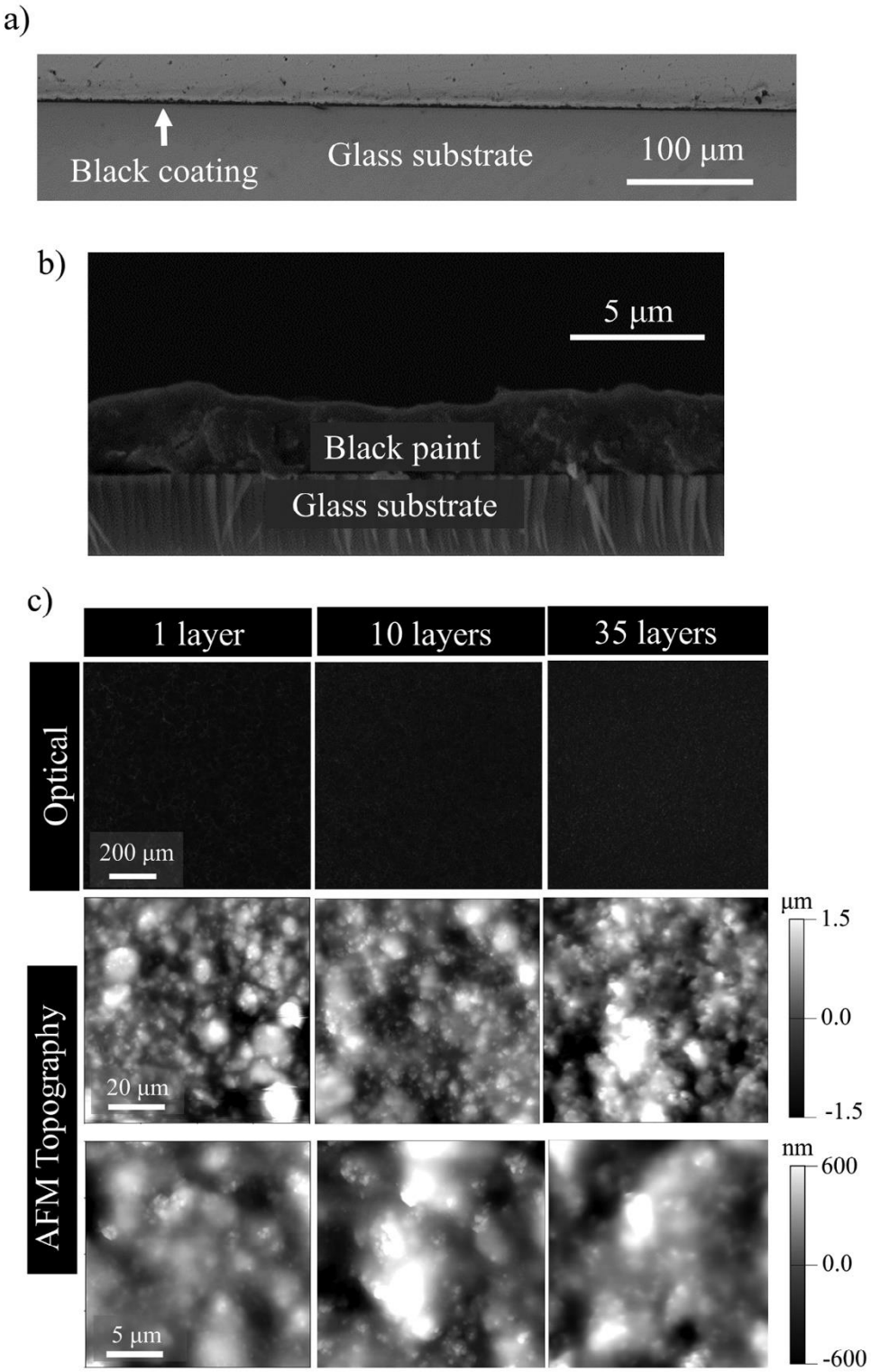


Figure 3. a) Optical microscope, and b) SEM image of single-layer coating in cross-section view. c) Optical microscope and AFM topography height images of the surface of the coatings with 1, 10, and 35 sprayed layers.

© 2025 The Author(s). Advanced Materials Interfaces published by Wiley-VCH GmbH

21967350, 0, Downloaded from https://advanced.onlinelibrary.wiley.com/doi/10.1002/admi.202500467 by Hana Ursic - Institut Jozef Stefan , Wiley Online Library on [29/08/2025]. See the Terms and Conditions (https://onlinelibrary.wiley.com/terms-and-conditions) on Wiley Online Library for rules of use; OA articles are governed by the applicable Creative Commons License

ADVANCED SCIENCE NEWS
www.advancedsciencenews.com

ADVANCED MATERIALS INTERFACES
Open Access
www.advmatinterfaces.de

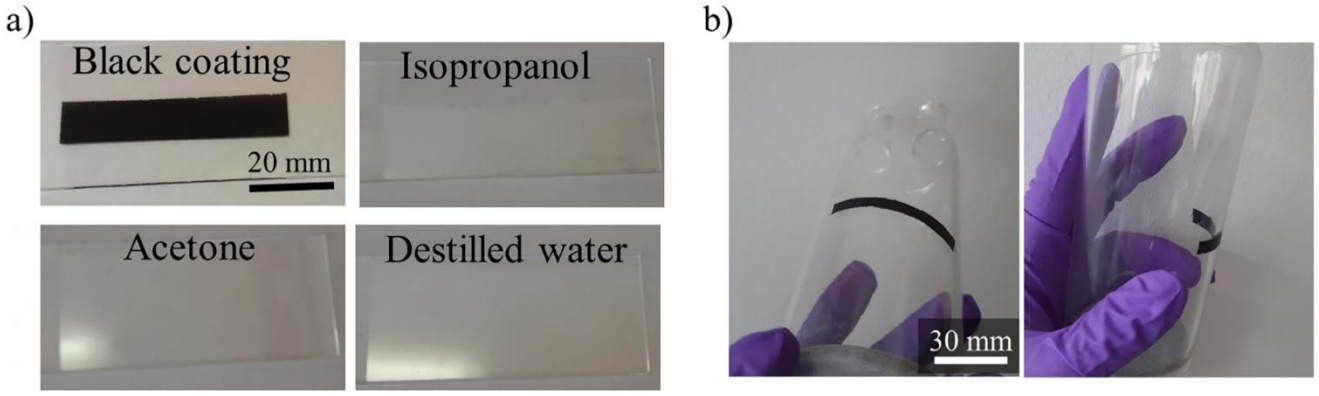


Figure 4. a) Photographs of as-prepared black coating and substrates after removal of coating using isopropanol, acetone, and distilled water. b) Photographs of single-layer on a cylindrical glass flask. Notice the pronounced curvature of the coating on the second panel.

were also investigated by scanning electron microscope (SEM; Prisma-E, Thermo Fisher, Massachusetts, USA).

For emissivity measurements, five 26 mm × 40 mm samples were coated with a single layer of black paint. The surface emissivity was characterized with the Lambda 950 spectrophotometer (Perkin Elmer, Waltham, USA), with wavelengths from 0.5 to 2.5 µm in steps of 5 nm.

For magnetocaloric measurements, 17 mm × 11 mm × 0.3 mm $La_{1.0}Fe_{10.79}Si_{1.12}Co_{1.09}$ plates (Calorivac C 292, Vacuumschmelze GmbH & Co. KG, Hanau, Germany) were used. Prior to the coating, to remove surface contaminants, the plates were thermally treated in a chamber furnace (Custom-made, Terna, Ljubljana, Slovenia) in Argon inert atmosphere at 400 °C for 1 h with heating and cooling rates of 2 K min^{-1}. The plates were coated with a single layer under the same conditions as the glass substrates. A constant magnetic field of 1.1 T was applied using a custom-made electro-permanent magnet with a magnetization time of 10 ms.[52,53] The measurements were done with a magnetic cycle of 50 s. Detailed information about the magnet system is provided elsewhere.[52,53] The magnetocaloric output was characterized using an IR camera (FLIR A6750sc MWIR, FLIR, Oregon, USA) at room temperature and with the frame rate of 100 Hz. The spectral range of the IR camera is 1 –5 µm.

3. Results

During the coating process, the paint is ejected onto the target surface with air as the carrier medium. After drying, a single-layer coating achieves an average thickness of 3.0 µm schematically shown in **Figure 2**a. The single-layer coating is suitable for caloric characterizations, particularly of µm-thick films. However, on a general case, if the substrate roughness is large (Rq >> 1 µm), in order to obtain reliable IR measurements, thicker coatings might be necessary. Therefore, multi-layer coatings were also prepared. As additional layers are sprayed, the incoming airflow affects the previous wet layer underneath, causing it to spread, effectively thinning the layer, while simultaneously adding more coating solution. As a result, a *N*-layered coating does not achieve an average thickness of *3N* µm. For example, a two-layer coating has an average thickness of 4.2 µm, which is lower than the expected 6.0 µm, i.e., double the single-layer thickness. At 35 layers, the average thickness reaches 30.4 µm, shown schematically in Figure 2b. It is worth emphasizing that the ratio

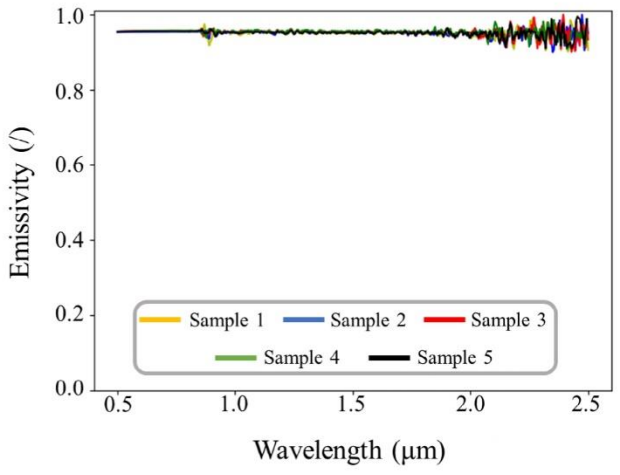


Figure 5. Emissivity of five single-layer black coatings on glass substrates. The noise at larger wavelengths can be attributed to a lower sensitivity of the detector with increasing wavelength.

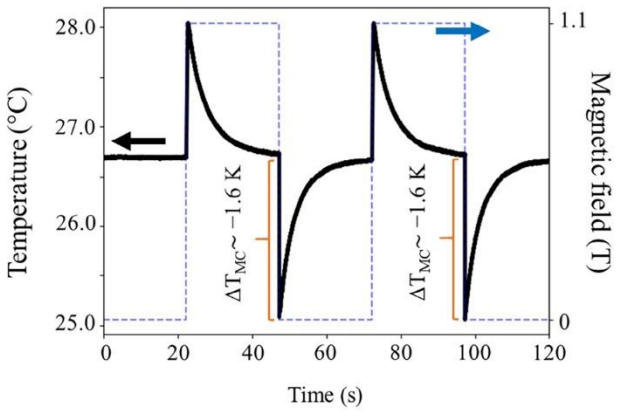


Figure 6. Temperature profile of a coated magnetocaloric plate under a cycling applied field of 1.1 T. The slight difference between heating and cooling peaks can be attributed to the difference in heat capacities of this material at zero and non-zero magnetic fields, as shown in ref. [55].

© 2025 The Author(s). Advanced Materials Interfaces published by Wiley-VCH GmbH

21967350, 0, Downloaded from https://advanced.onlinelibrary.wiley.com/doi/10.1002/admi.202500467 by Hana Ursic - Institut Jozef Stefan , Wiley Online Library on [29/08/2025]. See the Terms and Conditions (https://onlinelibrary.wiley.com/terms-and-conditions) on Wiley Online Library for rules of use; OA articles are governed by the applicable Creative Commons License

ADVANCED SCIENCE NEWS
www.advancedsciencenews.com

ADVANCED MATERIALS INTERFACES Open Access
www.advmatinterfaces.de

Table 1. Summary of conventional coating methods and their respective properties.

Method	Conventional spray painting[42–47]	Printing[16–18]	Airbrush (This work)
Thickness	Unreported	3.5 µm – 4.5 µm	≥3 µm
Samples with thickness ≥100 µm	✔	✗	✔
Sample with thickness <100 µm	✗	✔	✔
Curved samples	✔	✗	✔

between the standard deviation to the average thickness in all cases is ≈9%. In addition, regardless of coating thickness, the samples exhibited comparable surface roughness within the 600 – 700 nm range, shown in Supplementary Material S1. The average total thickness as function of number of layers is shown in Figure 2c.

Single-layer coatings were investigated using optical and electron microscopes in cross-section views, as shown in **Figure 3**a,b. A uniform continuous coating was observed along the substrate length in both cases. Furthermore, using optical and atomic force microscopes, the surface of coatings with 1, 10, and 35 layers was investigated as shown in Figure 3c. The surface of coatings is uniform, with no visible defects, for example, porosity or pinholes, regardless of thickness.

Furthermore, the coatings are not permanent and can be easily removed from the substrates. By wiping with acetone, isopropanol or distilled water, the coatings can be completely removed without leaving any residue or damaging the substrates, shown in **Figure 4**a. Notably, the black paint is soluble in isopropanol and acetone, allowing for its complete removal by immersing the coated sample in the solvent. A single coating was successfully applied to a large curved glass flask, demonstrating that this method can also be applied to non-flat surfaces (Figure 4b). In addition, black paint layers can be successfully prepared on various substrates of different materials as shown in S2 (Supporting Information).

The emissivity of five single-layer coatings was characterized over the wavelength range from 0.5 to 2.5 µm, as shown in **Figure 5**. The coatings exhibited an average emissivity of 0.95 with a standard deviation of 0.01. Our measurements are in excellent agreement with the reported emissivity of various black paints, which are 0.92 or larger.[16–19,28] Additional details on the emissivity measurements and the histogram distribution of the data of individual samples are provided in S3 and S4 (Supporting Information), respectively.

To investigate the suitability of the coating for IR camera measurements, the magnetocaloric plates were coated with a single layer. The IR camera used in this work covers the spectral range 1–5 µm, partially overlapping with the range (0.5–2.5 µm) of the Lambda 950 spectrophotometer used for emissivity measurements of the black coatings (more details in S5, Supporting Information). **Figure 6** shows the magnetocaloric temperature change (ΔT_{MC}) of − 1.60 K immediately after the field switch-off, and the same value was obtained after a second magnetic field cycle. The measurements of the magnetocaloric cooling are in accordance with the datasheet of the provider, namely − 1.60 K at 1.1 T and room temperature,[54] which confirms that the prepared black coatings are appropriate for the IR camera measurement method. It is worth mentioning, that the value from the datasheet was obtained indirectly by measuring the magnetization at different magnetic fields and temperatures during cooling and subsequently ΔT_{MC} was calculated via the Maxwell relations.[55] Since the black paint exhibits a very large emissivity with no significant variations within the measurement range, and the ΔT_{MC} IR measurements are in excellent agreement with the supplier's datasheet, a high emissivity can also be expected at wavelengths larger than 2.5 µm.

4. Conclusion

In this work, we investigated a non-destructive, easy-to-use coating technique for the preparation of black-paint coating for thermal camera imaging using an affordable airbrush method. The influence of the number of layers on the coating thickness was investigated, and a linearly increasing trend was observed, from an average of ≈3.0 µm at a single layer up to ≈30.4 µm at thirty-five painted layers. The coatings were homogeneous, with no visible defects and adhered well to the substrates. The surface roughness remained within 600 – 700 nm, regardless of the number of layers. The coatings were removed from the glass substrates using conventional laboratory solutions such as isopropanol, acetone and distilled water.

To demonstrate the suitability of the airbrush coating method for IR thermal camera imaging, the emissivity of the coatings was determined to be ≈0.95 on average. In addition, a commercially available magnetocaloric material was airbrush coated with black paint and examined using the IR imaging method under a magnetic field of 1.1 T. The measured magnetocaloric response was in excellent agreement with the literature.

In conclusion, our method enables the deposition of high-emissivity black paint coatings with thicknesses of a few microns on samples of any geometry, and combines the benefits of established techniques, such as conventional spray painting and printing as summarized in **Table 1**.

We propose to use the airbrush method for IR thermal imaging camera characterization of caloric bulk materials, micrometer-thick films and extend its application to other research disciplines requiring IR camera measurements.

Supporting Information

Supporting Information is available from the Wiley Online Library or from the author.

© 2025 The Author(s). Advanced Materials Interfaces published by Wiley-VCH GmbH

21967350, 0, Downloaded from https://advanced.onlinelibrary.wiley.com/doi/10.1002/admi.202500467 by Hana Ursic - Institut Jozef Stefan , Wiley Online Library on [29/08/2025]. See the Terms and Conditions (https://onlinelibrary.wiley.com/terms-and-conditions) on Wiley Online Library for rules of use; OA articles are governed by the applicable Creative Commons License

ADVANCED SCIENCE NEWS
www.advancedsciencenews.com

ADVANCED MATERIALS INTERFACES
Open Access
www.advmatinterfaces.de

Acknowledgements

The authors acknowledge the financial support of the Slovenian Research and Innovation Agency (projects no. N2-0212 and J2-60035, program no. P2-0105, bilateral cooperation BI-US/22-24-039, BI-US/24-26-094 and young researcher project) and the transnational consortium M-ERA.NET for the project Cool BatMan: Battery Thermal Management System Based on High Power Density Digital Microfluidic Magnetocaloric Cooling (No. 9400, Slovenian part of the project was financed by the Ministry of Higher Education, Science and Innovation. Spanish part financed by MCIN/AEI/10.13039/501100011033, project No. PCI2022-132957). The Erasmus+ program is greatly acknowledged by Victor Regis. The authors also acknowledge Jena Cilenšek, Alan Selin, Val Fišinger, and Brigita Kmet for help in the laboratory, and Alexander Barcza from Vacuuschmelze GmbH, Germany, for providing the magnetocaloric samples.

Conflict of Interest

The authors declare no conflict of interest.

Data Availability Statement

The data that support the findings of this study are openly available in Zenodo at doi.org/10.5281/zenodo.15681995, reference number.[56]

Keywords

airbrush, black paint, caloric, infrared thermal camera, IR imaging

Received: June 17, 2025
Revised: August 2, 2025
Published online:

[1] E. Bohm-Vitense, *Ann. Rev. Astron. Astrophys.* **1981**, *19*, 295.
[2] C. Meola, G. Carlomagno, *Meas. Sci. Technol.* **2004**, *15*, R27.
[3] (Ed: H. Czichos), *Handbook of Technical Diagnostics: Fundamentals and Application to Structures and Systems*, Springer Berlin, Heidelberg, Germany, **2013**.
[4] G. Gaussorgues, *Infrared Thermography*, Springer, Dordrecht, Netherlands **1994**.
[5] L. Ibos, M. Marchetti, A. Boudenne, S. Datcu, Y. Candau, J. Livet, *Meas. Sci. Technol.* **2006**, *17*, 2950.
[6] J. Speakman, S. Ward, *Zoology* **1998**, *101*, 224.
[7] E. Sest, G. Drazic, B. Genorio, I. Jerman, *Sol. Energy Mater. Sol. Cells* **2018**, *176*, 19.
[8] M. Jarrap, S. Rands, *Plant Methods* **2021**, *1*, 17.
[9] N. Playa-Montmanny, G. Tattersall, *Methods Ecol. Evol.* **2020**, *12*, 828.
[10] B. B. Lahiri, S. Bagavathiappan, T. Jayakumar, J. Philip, *Infrared Phys. Technol.* **2012**, *55*, 221.
[11] A. Astasio-Picadoa, E. E. Martinez, A. M. Nova, R. S. Rodriguez, B. Gomez-Martin, *Infrared Phys. Technol.* **2018**, *93*, 59.
[12] G. Kastberger, R. Stachl, *Behav. Res. Methods* **2003**, *3*, 429.
[13] M. Soroko, K. Howell, *J. Equine Vet. Sci.* **2018**, *60*, 90.
[14] Q. Badosa, L. Manosa, E. Vives, A. Planes, B. Weise, L. Beyer, E. Stern-Taulats, *J. Appl. Phys.* **2023**, *134*, 113902.
[15] C. A. Balaras, A. A. Argiriou, *Energy Build.* **2002**, *34*, 171.
[16] U. Prah, M. Sadl, A. Torello, P. Lheritier, V. Kovacova, H. Urisc, E. Defay, *Small Methods* **2023**, *7*, 2300212.
[17] M. Sadl, U. Prah, V. Kovacova, E. Defay, T. Rojac, A. Lebar, J. Valentincic, H. Ursic, *J. Mater. Chem. C* **2023**, *11*, 10058.
[18] A. Aravindhan, P. Lheritier, A. Torello, U. Prah, Y. Nouchokgwe, A. E. Moul, X. Chevalier, F. D. D. Santos, E. Defay, V. Kovacova, *J. Materiomics* **2023**, *9*, 256.
[19] E. Barreira, R. Almeida, M. Simoes, *Sensors* **2021**, *21*, 1961.
[20] H. Jo, J. L. King, K. Blomstrand, K. Sridharan, *Int. J. Heat Mass Transfer* **2017**, *115*, 1065.
[21] N. Avdelidis, A. Moropoulou, *Energy Build.* **2002**, *35*, 663.
[22] S. Woods, T. Jung, D. Sears, J. Yu, *Cryogenics* **2014**, *60*, 44.
[23] W. Sabuga, R. Todtenhaupt, *High Temp.-High Pressures* **2001**, *33*, 261.
[24] M. G. D. Duca, J. Tusek, A. Maiorino, L. Fulanovic, A. Bradesko, U. Plaznik, B. Malic, C. Aprea, A. Kitanovski, *J. Appl. Phys.* **2020**, *128*, 104102.
[25] P. Wang, Z. Xie, H. Meng, Z. Hu, In *27th Chinese Control and Decision Conf.*, IEEE, Qingdao, China **2015**, pp. 6197–6200.
[26] Z. Ahcin, S. Dall'Olio, A. Zerovnik, U. Z. Baskovic, L. Porenta, P. Kabirifar, J. Cerar, S. Zupan, M. Brojan, J. Klemenc, J. Tusek, *Joule* **2022**, *6*, 2338.
[27] J. Chen, Y. Zhou, Q. Nan, Y. Sun, Z. Ye, Z. Wang, *Appl. Surf. Sci.* **2007**, *253*, 9154.
[28] Y. Gao, G. Y. Tian, *Sens. Actuators, A* **2018**, *270*, 8.
[29] E. Vives, S. Burrows, R. Edwards, S. Dixon, L. Manosa, A. Planes, R. Romero, *Appl. Phys. Lett.* **2011**, *98*, 011902.
[30] R. Faye, T. Usui, A. Torello, B. Dkhil, X. Moya, N. D. Mathur, S. Hirose, E. Defay, *J. Alloys Compd.* **2020**, *834*, 155042.
[31] K. Xie, J. Housseini, P. M. Resende, F. L. Goupil, J.-D. Isasa, S. Tence-Girault, G. Fleury, H. Kellay, G. Hadziionnou, *Adv. Funct. Matter.* **2024**, *34*, 2411397.
[32] A. Kitanovski, *Adv. Energy Mater.* **2020**, *10*, 1903741.
[33] (Eds: T. Correia, Q. Zhang), *Electrocaloric Materials*, Springer Berlin, Heidelberg, Germany **2014**.
[34] A. Kitanovski, J. Tusek, U. Tomc, U. Plaznik, M. Ozbolt, A. Poredos, *Magnetocaloric Energy Conversion*, Springer Cham, Cham, Switzerland, **2015**, https://doi.org/10.1007/978-3-319-08741-2.
[35] J. Y. Law, L. M. Moreno-Ramirez, A. Diaz-Garcia, V. Franco, *J. Appl. Phys.* **2023**, *133*, 040909.
[36] V. Franco, J. S. Blasquez, J. J. Ipus, J. Y. Law, L. M. Moreno-Ramirez, A. Conde, *Prog. Mater. Sci.* **2018**, *93*, 112.
[37] N. Zeggai, B. Dkhil, M. LoBlue, M. Almanza, *Appl. Phys. Lett.* **2023**, *122*, 081903.
[38] F. L. Goupil, A. Berenov, A.-K. Azelsson, M. Valant, N. M. Alford, *J. Appl. Phys.* **2012**, *111*, 124109.
[39] K. Klinar, A. Kitanovski, *Renew. Sustain. Energy Rev.* **2020**, *118*, 109571.
[40] T. Swoboda, K. Klinar, A. S. Yalamarthy, A. Kitanovski, M. M. Rojo, *Adv. Electron. Mater.* **2021**, *7*, 2000625.
[41] L. Manosa, A. Planes, *Adv. Mater.* **2017**, *29*, 1603607.
[42] M. J. Pereira, T. Santos, R. Corriea, J. S. Amaral, V. S. Amaral, S. Fabbrici, F. Albertini, *J. Phys. Mater.* **2023**, *6*, 024002.
[43] K. Wang, Y. Ouyang, Y. Shen, Y. Zhang, M. Zhang, J. Liu, *J. Mater. Sci.* **2021**, *56*, 2332.
[44] M. Sanilialp, V. V. Shvartsman, R. Faye, M. O. Karabasov, C. Molin, S. Gebhardt, E. Defay, D. C. Lupascu, *Rev. Sci. Instrum.* **2018**, *89*, 034903.
[45] H. Ossmer, F. Lambrecht, M. Gultig, C. Chluba, E. Quandt, M. Kohl, *Acta Mater.* **2014**, *81*, 9.
[46] T. Hirai, R. Iguchi, A. Miura, K.-i. Uchida, *Adv. Funct. Mater.* **2022**, *32*, 2201116.
[47] L. Ianniciello, M. Romanini, L. Manosa, A. Planes, K. Engelbrecht, E. Vives, *Appl. Phys. Lett.* **2020**, *116*, 1839011.
[48] M. A. S. Arikan, T. Balkan, *J. Rob. Syst.* **2000**, *17*, 479.
[49] S. Krimi, J. Klier, J. Jonuscheit, G. v. Freymann, R. Urbansky, R. Beigang, *Appl. Phys. Lett.* **2016**, *109*, 021105.

© 2025 The Author(s). Advanced Materials Interfaces published by Wiley-VCH GmbH

[50] I. Mendoza, D. Drury, S. Koumlis, J. Ivy, G. Brennecka, L. Lamberson, *J. Am. Ceram. Soc.* **2022**, *105*, 3116.
[51] I. Mendoza, D. Drury, A. Matejunas, J. Ivy, S. Koumlis, P. Jewell, G. Brennecka, L. Lamberson, *Eng. Fract. Mech.* **2021**, *247*, 107669.
[52] U. Tomc, S. Nosa, K. Klinar, A. Kitanovski, *J. Adv. Res.* **2023**, *45*, 157.
[53] K. Klinar, U. Tomc, B. Jelenc, S. Nosa, A. Kitanovski, *Appl. Energy* **2019**, *236*, 1062.
[54] Vacuumshmelze, Magnetocaloric Materials Calorivac, https://vacuumschmelze.com/products/advanced-technologies/magnetocaloric-material-calorivac.
[55] M. Katter, V. Zellmann, G. W. Reppel, K. Uestuener, *IEEE Trans. Magn.* **2008**, *44*, 3044.
[56] V. Regis, H. Uršič, *Zenodo* **2025**, https://doi.org/10.5281/zenodo.15681995.

© 2025 The Author(s). Advanced Materials Interfaces published by Wiley-VCH GmbH

21967350, 0, Downloaded from https://advanced.onlinelibrary.wiley.com/doi/10.1002/admi.202500467 by Hana Ursic - Institut Jozef Stefan , Wiley Online Library on [29/08/2025]. See the Terms and Conditions (https://onlinelibrary.wiley.com/terms-and-conditions) on Wiley Online Library for rules of use; OA articles are governed by the applicable Creative Commons Lic

Supplementary Information

Airbrushing: a novel method for preparation of high-emissivity black coating for infrared measurements

Victor Regis[1,2], Geoff Brennecka[3], Urban Tomc[4], Andrej Kitanovski[4], Jan Cerar[4], Jaka Tušek[4], Ivan Jerman[5], Enric Stern-Taulats[6], Klara Lünser[6], Lluís Mañosa[6] and Hana Uršič[1,2,*]

[1] Electronic Ceramics Department, Jožef Stefan Institute, Jamova cesta 39, 1000 Ljubljana, Slovenia

[2] Jožef Stefan International Postgraduate School, Jamova cesta 39, 1000 Ljubljana, Slovenia

[3] Colorado School of Mines, 1500 Illinois Ave., Golden, 80401Colorado, USA

[4] Faculty of Mechanical Engineering, University of Ljubljana, Aškerceva cesta 6, 1000 Ljubljana, Slovenia

[5] Laboratory for Coating Development, Department of Materials Chemistry, National Institute of Chemistry, Hajdrihova 19, 1000 Ljubljana, Slovenia

[6] Departament de Física de la Matèria Condensada, Facultat de Física, Martí i Franquès 1, Universitat de Barcelona, 08028 Barcelona, Catalonia

*Correspondence: hana.ursic@ijs.si

S1. Average surface roughness of coatings

The surface roughness as function of number of layers is shown in Figure S1. Notice that all samples exhibit roughness within the 600 nm to 700 nm range.

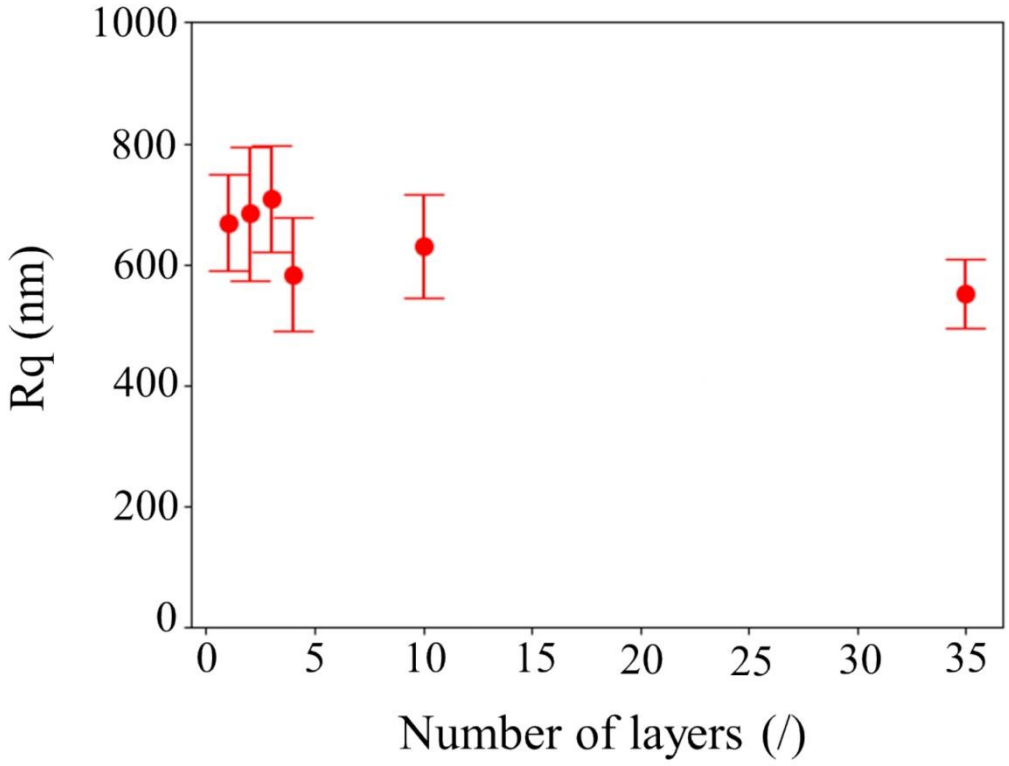


Figure S1: Average surface roughness as a function of the number of painted layers.

S2. Coating on different substrates

To showcase the versatility of the airbrush coating method, a single layer of black paint was sprayed onto 125-µm thick polyimide (Kapton® HN, Dupont, Wilmington, USA),75-µm thick Cu67/Zn43 brass foils (GoodFellow, Huntingdon, UK), and 75-µm thick stainless-steel 301 foils (MecaFlash, Magny-les-Hameaux, France). For the sake of comparison, the data of glass substrate coated with a single layer is also presented in this section. For each substrate, the thickness and roughness were calculated by averaging five different samples. As shown in Fig. S2, the black coated layers on glass, polyimide, brass and steel substrates exhibit comparable average thicknesses of 3.6 µm, 3.6 µm, 3.8 µm and 3.7 µm, respectively. Similarly, the roughness Rq values of the black coatings on all substrates are comparable with averages of 727 nm, 659 nm, 631 nm and 755 nm, respectively.

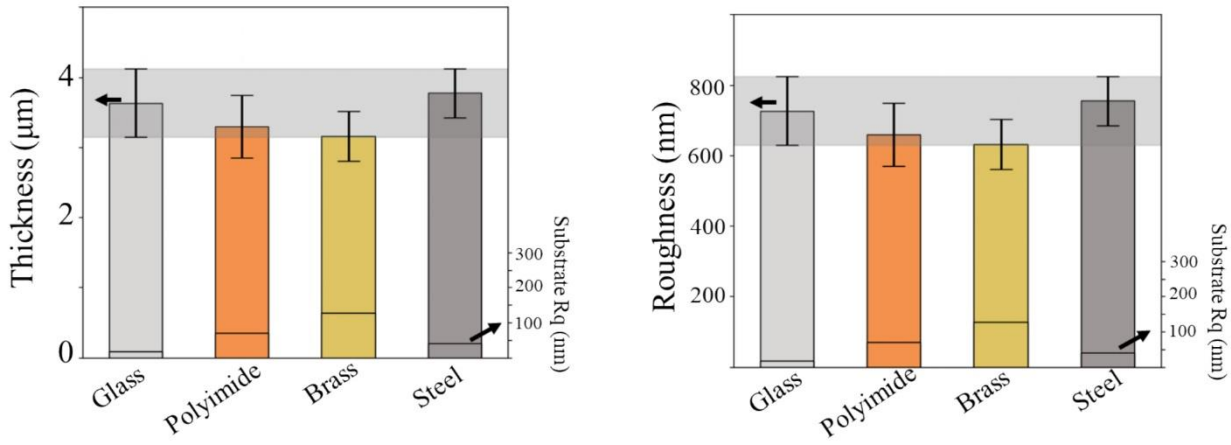


Figure S2: Average coating thickness (left) and average Rq values (right) for a single-layer coating on glass, polyimide, brass and steel substrates. The gray regions indicate the values for the glass substrates. The lower bars correspond to the Rq value of the respective pristine substrate (scale on the right side of the diagrams).

S3. Black paint coatings on various substrates

The emissivity values were calculated from reflectivity (R) measurements, mathematically,

$$1 - R = E_{BP} + T,$$

where E_{BP} is the emissivity of the black paint and T is the contribution transmitted through the black paint. Since all light which reaches the substrate must travel through the black paint, T depends on the black paint transmissivity (T_{BP}) and on the optical properties of the substrate. [1] Figure S3 shows the 1-R measurements of single-layer coatings on glass, polyimide, stainless steel and brass substrates. Because the thickness of the black paint coating is comparable for all samples, the transmissivity of the coating is also comparable. Therefore, any variation in the total transmitted contribution can be attributed to the differences in substrate optical properties. Notice that the measurements are in excellent agreement with each other and no significant influence of the substrates was observed. The average 1-R within the 0.5 µm – 2.5 µm range was comparable in all cases, namely 0.95, 0.95, 0.94 and 0.94 for glass, polyimide, stainless steel and brass substrates, respectively, which can be written as:

$$(1\text{-}R)_{glass} \sim (1\text{-}R)_{polyimide} \sim (1\text{-}R)_{steel} \sim (1\text{-}R)_{brass} \sim 0.95.$$

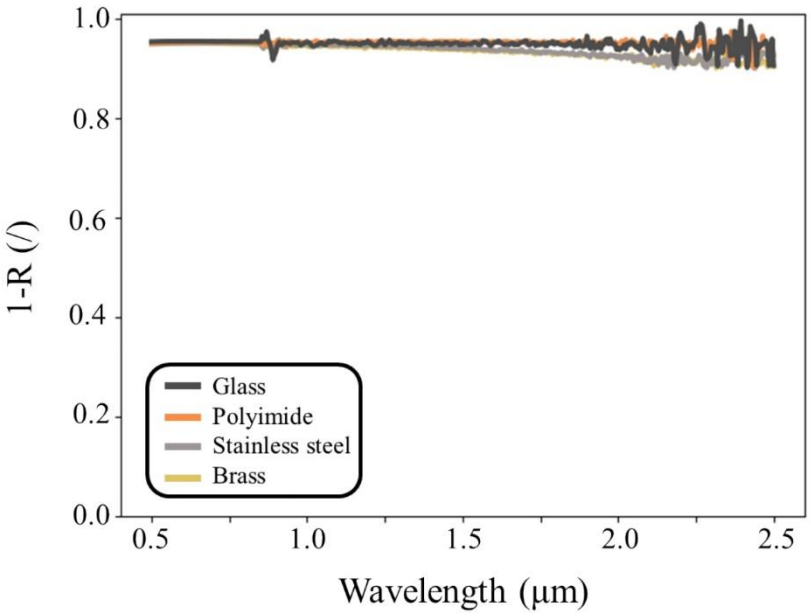


Figure S3: 1-R versus wavelength of single-layer coatings prepared onto different substrates.

Because the (1-R) measurements can only differ from each other through T, and (1-R) as well as E_{BP} are constant for all samples, then either all substrates (glass, polyimide, stainless steel and brass substrates) interact with light in the same manner, or $T_{BP} << 1$. Since the substrates span a wide range of materials with different surface conditions and different optical properties, we can conclude that the transmissivity contribution is negligible within the scope of this work. Therefore, $E_{BP} \sim (1\text{-}R)$.

S4. Emissivity data

In Figure S4, the emissivity data for each individual single-layer coated sample are collected. Notice that all samples exhibit similar behavior, with an average emissivity of 0.95 and a standard deviation of 0.01 throughout the entire measurement range.

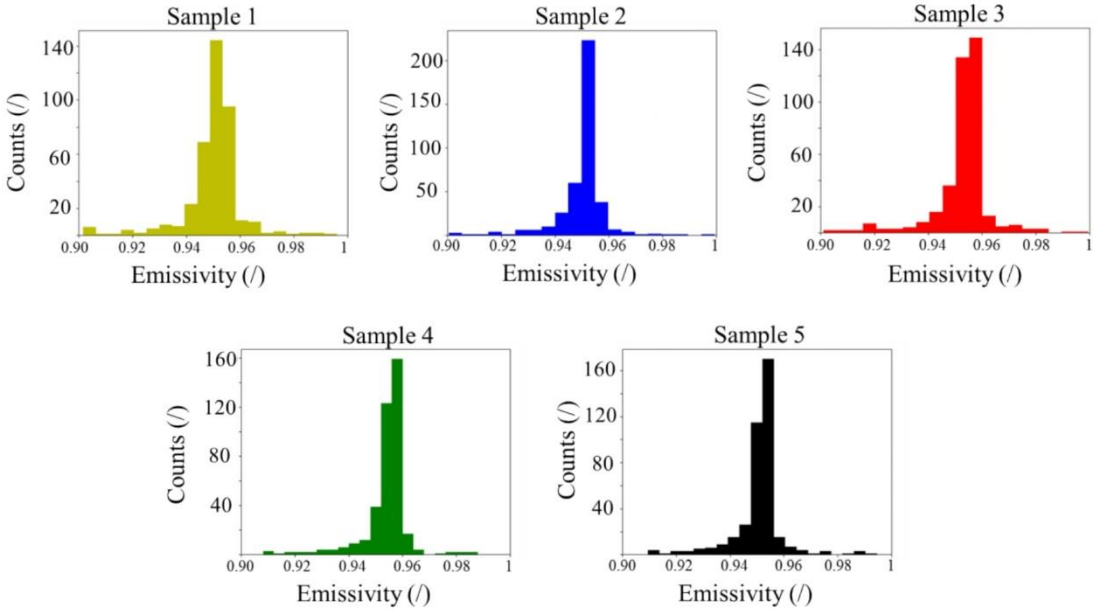


Figure S4: Emissivity data of single-layer samples.

S5. Spectral ranges of IR camera measurements

The IR spectral range of cameras used in caloric characterizations can span different segments of IR spectrum[1–4], with some models starting at wavelengths as low as 0.9 µm. As shown in Figure S4, the reported emissivity measurements of the black coatings were performed within the 0.5 µm – 2.5 µm wavelength range, which partially overlaps with the spectral ranges of several IR camera models used in caloric research, [1-4] as well as the one used in this work. It is worth emphasizing that the black paint coating exhibits a very high emissivity without significant variations throughout the entire measurement range and that the magnetocaloric material was successfully characterized at room temperature, which suggests that a high emissivity (≥ 0.5) can also be expected beyond 2.5 µm.

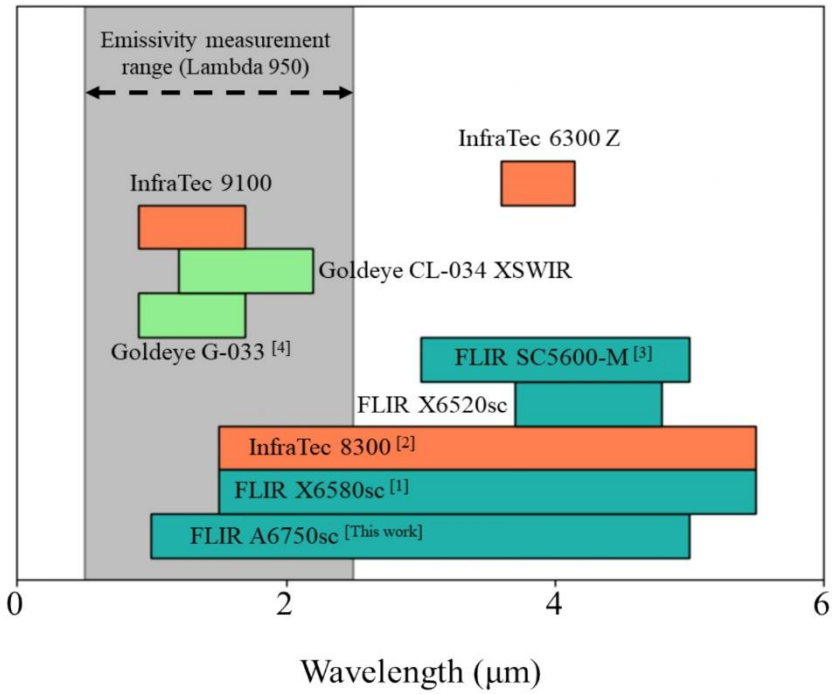


Figure S3: Spectral range of IR cameras of different brands commonly used in caloric characterizations[1–4]. Notice that models with no reports on caloric characterizations are also shown. FLIR[5] cameras are shown in blue, InfraTec[6] in orange, and Goldeye[7] in green.

Bibliography

[1] U. Prah, M. Sadl, A. Torello, P. Lheritier, V. Kovacova, H. Ursic, E. Defay, "Direct Electrocaloric Characterization of Ceramic Films", *Small Methods. vol.* 7, pp. 2300212 1-8, 2023.

[2] Q. Badosa, L. Manosa, E. Vives, A. Planes, B. Weise, L. Beyer and E. Stern-Taulats, "Demagnetizing field-induced magnetocaloric effect in Gd," *J. Appl. Phys.,* vol. 134, pp. 113902 1-6, 2023.

[3] M. J. Pereira, T. Santos, R. Corriea, J. S. Amaral, V. S. Amaral, S. Fabbrici and F. Albertini, "Mapping the magnetocaloric effect at the microscale on a ferromagnetic shape memory alloy with infrared thermography," *J. Phys. Mater.,* vol. 6, pp. 024002 1-16, 2023.

[4] T. A. Nguyen, N. Kakuta, K. Uchida, H. Nagano, "Near-infrared imaging of heat transfer behavior between gadolinium and fluid during magnetization/demagnetization process of magnetocaloric effect", *J. Appl. Phys.*, vol. 135, pp. 193904 1-13, 2024.

[5] FLIR, FLIR homepage, 2025. [Online] flir.com (Accessed: June 05, 2025).

[6] InfraTec, InfraTec homepage, 2025. [Online] infratec.eu/thermography (Accessed: June 05, 2025).

[7] Alliedvision, Goldeye SWIR homepage, 2025. [Online] alliedvision.com/en/products/camera-series/goldeye-swir (Accessed: June 05, 2025).

Chapter 5

Direct Observation of Room-Temperature Electrocaloric and Magnetocaloric Responses in Multicaloric Composite Films

This chapter addresses the main focus of this thesis, using the works from the previous chapters as starting points. Here, for the first time, an EC-MC composite film is prepared and its room-temperature caloric properties directly characterized.

In this work, we combined the room-temperature EC relaxor-ferroelectric PMN–10PT with 2 wt% of the magnetocaloric LFSC intermetallic alloy and prepared multicaloric thick films onto gold-sputtered polyimide substrates via the AD method. Prior to the deposition, the LFSC as-received powder was milled, to ensure a suitable particle size. The magnetocaloric phase was preserved after the milling process. The prepared films were annealed at 400 °C in argon atmosphere. Due to its inert nature, the atmosphere did not oxidize the embedded LFSC metallic particles within the PMN–10PT matrix.

The composite samples exhibited increased permittivity and maximum polarization values when compared to PMN–10PT films. In addition, composite films showed a ferromagnetic hysteresis loop, evidencing the presence of magnetically active particles. Moreover, the room-temperature ΔT_{EC} of the samples were characterized using the thermistor-in-calorimeter method. The composites, at 250 kV cm^{-1}, exhibited a ΔT_{EC} ~0.45 K, while PMN–10PT exhibits ~0.35 K under the same conditions. This 32 % enhancement is attributed to the embedded metallic particles which increases the overall electrical properties of the composites, namely the Maxwell-Wagner polarization effect. Lastly, the room-temperature ΔT_{MC} of composite sample was investigated using the IR camera method. The samples exhibited ΔT_{MC} ~1.4 K at 2 T, after corrections. This work demonstrates that it is possible to prepare EC-MC composites with room-temperature caloric properties.

This chapter addresses thesis objectives: 4,5,6

Published in: V. Regis, I. Gorican, M. Sadl, A. Bencan, G. Drazic, S. Gyergyek, U. Tomc, A. Kitanovski, L. Beyer, E. Stern-Taulats, K. Lunser, L. Mañosa, H. Ursic, "Direct observation of room-temperature electrocaloric and magnetocaloric responses in multicaloric composite films," J. Eur. Ceram. Soc., vol. 46, p. 118584, 2026. (IF = 6.2, 2026)

My contribution: I synthesized the PMN–10PT powder via mechanochemical synthesis, and performed the necessary milling steps for the LFSC powder. I also performed the following measurements on the powders: granulometry, electron microscopy, XRD acquisition (in collaboration with colleagues). I prepared the thick films via the AD method, as well as the annealing in argon atmosphere. I also performed the following measurements: dielectric permittivity, polarization and magnetization hysteresis loops, electrocaloric measurements. In collaboration with coworker, I have also done: XRD measurements on films, Rietveld refinement, electron microscopy of cross-section of films and the associated energy dispersive spectroscopy, conductive atomic force microscopy at the surface of the films, and room-temperature magnetocaloric measurements. I conceptualized the manuscript and, with the co-authors, I wrote the paper.

Journal of the European Ceramic Society 46 (2026) 118584

Contents lists available at ScienceDirect

Journal of the European Ceramic Society

journal homepage: www.elsevier.com/locate/jeurceramsoc

Direct observation of room-temperature electrocaloric and magnetocaloric responses in multicaloric composite films

Victor Regis [a,b], Ivana Goričan [a,b], Matej Šadl [a,b], Andreja Benčan [a,b], Goran Dražić [a,b,c], Sašo Gyergyek [d], Urban Tomc [e], Andrej Kitanovski [e], Lukas Beyer [f,g], Enric Stern-Taulats [h], Klara Lünser [h,i,j], Lluís Mañosa [h], Hana Uršič [a,b,*]

[a] Electronic Ceramics Department, Jožef Stefan Institute, Jamova cesta 39, Ljubljana 1000, Slovenia
[b] Jožef Stefan International Postgraduate School, Jamova cesta 39, Ljubljana 1000, Slovenia
[c] Department of Materials Chemistry, National Institute of Chemistry, Hajdrova ulica 19, Ljubljana 1000, Slovenia
[d] Department of Synthesis of Materials, Jožef Stefan Institute, Jamova cesta 39, Ljubljana 1000, Slovenia
[e] Faculty of Mechanical Engineering, University of Ljubljana, Aškerčeva cesta 6, Ljubljana 1000, Slovenia
[f] Leibniz Institute for Solid State and Materials Research Dresden, Helmholtzstr. 20, Dresden 01069, Germany
[g] Institute of Materials Science, Technische Universität Bergakademie Freiberg, Gustav-Zeuner-Str. 5, Freiberg 09599, Germany
[h] Departament de Física de la Matèria Condensada, Facultat de Física, Martí i Franquès 1, Universitat de Barcelona, Barcelona, Catalonia 08028, Spain
[i] Institute for Energy and Materials Processes – Applied Quantum Materials, University Duisburg-Essen, Duisburg 47057, Germany
[j] Research Center Future Energy Materials and Systems (RC FEMS), Research Alliance Ruhr, Bochum, Germany

ARTICLE INFO

Keywords:
Electrocaloric
Magnetocaloric
Multicaloric
Powder aerosol deposition
Thick films

ABSTRACT

For the first time, room-temperature electrocaloric (EC) and magnetocaloric (MC) effects were observed in multicaloric composites using direct characterization methods. By combining the EC ceramic $0.9Pb(Mg_{1/3}Nb_{2/3})O_3$–$0.1PbTiO_3$ (PMN–10PT) with the MC La-Fe-Si-Co (LFSC) alloy, the multicaloric films were prepared. The PMN–10PT films exhibited a dielectric permittivity of ~600, while composites exhibited improved values at ~700. The room-temperature EC response of composites was ~0.45 K at 250 kV cm^{-1}, a 32% enhancement when compared to PMN–10PT films. This enhancement in composite films is attributed to Maxwell-Wagner-type polarization effects, induced by the embedded LFSC MC particles. The room-temperature MC response of composite films was directly characterized, achieving a MC response ~1.4 K at 2 T, after corrections. Our results bring novel insights on the feasibility of preparing multicaloric composites with enhanced caloric properties for room-temperature micro-cooling technologies.

1. Introduction

Solid-state cooling technologies have received increased attention in recent years as alternatives to vapor-compression technologies. Particularly, research has focused on materials that show an adiabatic and reversible temperature change in response to an external stimulus, namely materials that exhibit caloric effects. If the stimulus is an electric field, magnetic field, uniaxial stress or hydrostatic pressure, the corresponding effect is the electrocaloric (EC), magnetocaloric (MC), elastocaloric (eC) or barocaloric (BC) effect, respectively [1–6]. Caloric effects can be observed on a wide range of materials such as ceramics, polymers, metals, and alloys [7–18], and state-of-the-art prototypes show promising properties for next-generation cooling devices, including flexible cooling applications [19–27].

Caloric effects are not limited to one type of external stimulus. Certain materials can exhibit responses to two or more stimuli, leading to a multicaloric effect [28–38]. Such materials are generally categorized as either single-phase multicalorics or composite multicalorics. Single-phase multicalorics are materials that exhibit different caloric effects simultaneously. For example, MC and eC responses have been observed on different families of alloys [28–30]. In ceramics, both EC and BC effects were observed on $Pb(Sc_{0.5}Ta_{0.5})O_3$ (PST) pellets [31]. In addition, research has been done on single-phase materials which exhibit both MC and EC effects, albeit with limited success at near room temperature conditions. $Pb(Fe_{0.5}Nb_{0.5})O_3$-based single-phase ceramics were shown to have an electrocaloric temperature change (ΔT_{EC}) of

* Corresponding author at: Electronic Ceramics Department, Jožef Stefan Institute, Jamova cesta 39, Ljubljana 1000, Slovenia.
E-mail address: hana.ursic@ijs.si (H. Uršič).

https://doi.org/10.1016/j.jeurceramsoc.2026.118584
Received 18 February 2026; Received in revised form 6 May 2026; Accepted 3 June 2026
Available online 4 June 2026
0955-2219/© 2026 The Author(s). Published by Elsevier Ltd. This is an open access article under the CC BY license (http://creativecommons.org/licenses/by/4.0/).

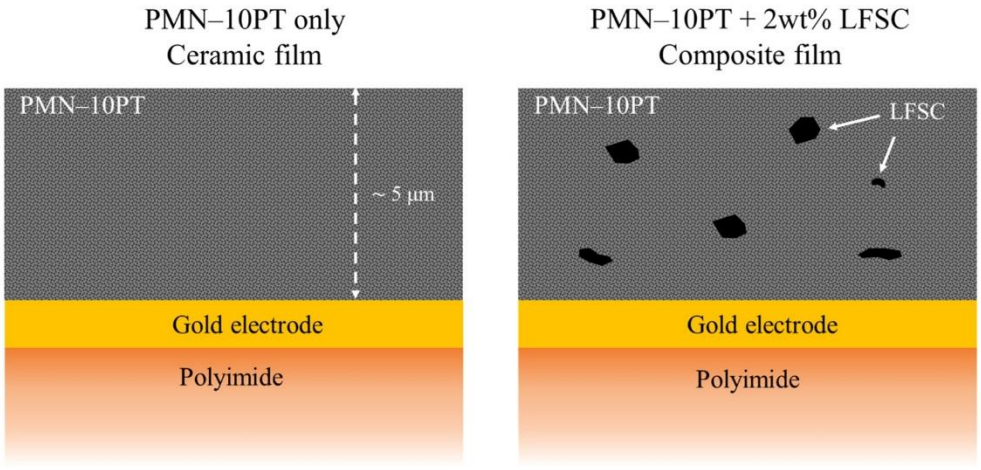


Fig. 1. Schematic representation of prepared PMN–10PT and PMN–10PT/LFSC thick-film structures.

~1.2 K at 140 kV cm^{-1} at room temperature, and a magnetocaloric temperature change (ΔT_{MC}) of ~3.6 K at 0.5 T under cryogenic temperatures [32,33]. The conflicting nature of ferroelectricity and ferromagnetism results in single-phase multiferroics being scarce, particularly materials that exhibit both caloric properties near room temperature [39–43].

One approach to achieving simultaneous ferroelectricity and ferromagnetism at room temperature is the preparation of multiferroic composites, where the distinct ferroic phases are physically separated and interact through interfacial coupling, which has been shown to play a significant role in the interplay between the ferroic phases [44,45]. In multilayer structures, albeit exhibiting interesting coupled properties between the ferroic phases, one of the layers will act as a heat sink, effectively decreasing the caloric output, which limits their applications as novel cooling devices. Composites may also be prepared as an EC ceramic matrix with MC particles embedded into it. Mikhaleva et al., characterized the multicaloric responses of $PbTiO_3$–$La_{0.7}Pb_{0.3}MnO_3$ ceramic composite pellets prepared via conventional sintering. The authors reported a ΔT_{MC} of ~0.06 K at magnetic field of 0.5 T and a ΔT_{EC} of ~2.5 K at 4.5 kV cm^{-1} [46]. However, the MC and EC responses were measured at 57 °C and 493 °C, respectively, far from room temperature conditions. In addition, only ΔT_{MC} was measured via a direct method. The ΔT_{EC} was estimated via specific heat measurements and, through constitutive equations, the electrocaloric response was calculated. Therefore, a direct characterization of both MC and EC room-temperature responses in composites has not yet been reported.

The most commonly reported EC materials are ceramics, which conventionally require high temperatures (≥ 1000 °C) in oxygen-rich atmospheres for densification, with most prolific materials being Pb-based oxides such as $0.9Pb(Mg_{1/3}Nb_{2/3})O_3$–$0.1PbTiO_3$ (PMN–10PT) and PST [14–16]. In contrast, the benchmark MC materials [27], such as Gd, La-based alloys, Mn-based alloys and FeRh, are generally thermally treated at temperatures below 1000 °C in oxygen-poor atmospheres to avoid oxidation and decomposition of the MC phase [47–53]. Therefore, the EC-MC composite is difficult to prepare due to the different conditions required for the thermal treatment of both materials. In other words, the preparation of such ceramic-metal alloy composites is a challenging task, still mostly unaddressed. In light of this, there has been significant development of low-temperature sample preparation techniques which allow for the synthesis of ceramic-metal composites. One of the most prominent method is the aerosol deposition (AD) method, also known as powder aerosol deposition method, which allows for the preparation of dense thick films entirely at room temperature. The method is based on the ejection of the powder particles at high velocities towards the surface of the substrate. Upon collision, the particles fragment and rebond, forming the film [54]. AD has been a prolific method for the preparation of functional ceramic films, with a wide range of reported materials including $Pb(Zr,Ti)O_3$ [55,56], Al_2O_3 [57,58], $BaTiO_3$ [59,60], and a variety of composites [61,62]. Previously, PMN–10PT has been successfully aerosol-deposited on thermally-insulating substrates for EC characterizations. The authors reported a ΔT_{EC} as large as 1.5 K at room temperature [15]. In addition, ceramic-metal composites have also been prepared targeting scratch-resistance and mechanical toughening [62,63]. However, the preparation of thick films via the AD method for EC-MC composites remains unexplored.

In light of this, we prepared, via the AD method, a room-temperature multicaloric composite by combining the excellent EC ceramic PMN–10PT and a commercially available La-Fe-Si-Co (LFSC) MC alloy. Our results show that 2 wt% of the MC phase leads to an enhancement on the overall EC properties of the film. In addition to the EC effect, the MC response was also observed in prepared composite films at room temperature. In this way, for the first time, room-temperature EC-MC composite films have been successfully prepared and directly characterized.

2. Experimental

Before the preparation of thick films, PMN–10PT ceramic powder was prepared from oxides via the mechanochemical synthesis route. Pre-synthesised PT and PMN were mixed in stoichiometric molar ratio and homogenized via wet milling at 200 rpm and 2 h on a planetary ball mill (PM400, Retsch, Germany). The mechanochemical preparation of PMN–10PT is described in further detail in [64]. Subsequently, in the same planetary mill, the mixture was dry-milled at 300 rpm for 36 h. The reacted powder was annealed at 900 °C for 1 h in air, and milled at 200 rpm for 2 h.

Before the preparation of the composite films, the MC alloy $La_{1.0}Fe_{10.79}Si_{1.12}Co_{1.09}$ (Calorivac C, Vacuumschmelze, Germany), was milled at 100 rpm for 4 h. The composite powder was prepared by mixing 2 wt% of LFSC powder with a 98 wt% of PMN–10PT powder. The powder mixture was homogenized in a roll-mill under dry conditions at 50 rpm for 48 h. Particle size analysis was performed using a light-scattering laser granulometer (S3500, Microtrac, USA). Prior to the analysis, the powder was suspended in isopropanol.

The thick films were prepared via the AD method (InVerTec, Germany) at room temperature. The substrates were polyimide foils with 125 µm thickness (Kapton® HN, DuPont, USA) sputtered with 1 µm-thick Au layer by a RF-magnetron sputtering equipment (5Pascal, Italy). Prior to the AD deposition, the powder mixture was sieved and dried at

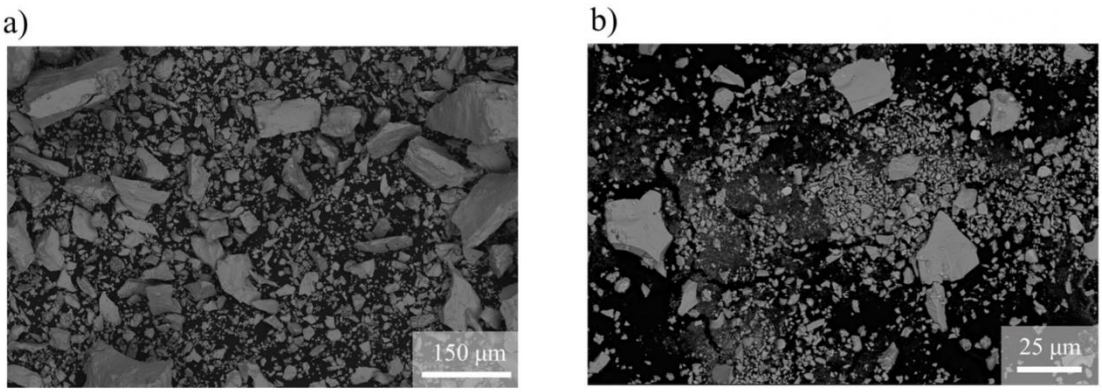


Fig. 2. BS-SEM of as-received LFSC powder at a) 150x and b) 650x magnifications. Notice the broad range of particle sizes.

80 °C for 12 h. For the depositions, N_2 was set as the carrier gas, and the chamber was evacuated to < 0.4 mbar. The number of deposition scans was adjusted in order to achieve ~5 µm-thick samples. Two types of thick films were prepared, namely the PMN–10PT films and PMN–10PT/LFSC composite films. A schematic representation of the prepared structures is shown in Fig. 1. To release internal stresses, the as-deposited samples were post-annealed in argon at 400 °C for 1 h with heating and cooling rates of 2 K min^{-1}.

X-ray diffractograms (XRD; MiniFlex 600-C, Rigaku, Tokyo, Japan) were performed using Cu-Kα, with a 2θ interval of 10°–70°, step size of 0.01° and a scan speed of 10° min^{-1}. To compare the microstrain in the samples before and after annealing, Rietveld refinement was performed on the XRD spectra of as-deposited and annealed samples. The analysis was performed with Topas R package (version 2.1, Bruker AXS GmbH, Germany), using the perovskite structure with the $Pm\bar{3}m$ space group (COD ID: 1532759).

For the microstructural analyses of the films in cross-sectional form, the samples were cut, mounted in epoxy resin, and fine-polished in hexane. Analyses were performed using scanning electron microscopy (SEM) and energy dispersive spectroscopy (EDS) with a field-emission scanning electron microscope (Verios HP 4 G, ThermoFisher, USA) equipped with a backscattered (BS) electron detector and an energy dispersive X-ray spectrometer (Aztec Oxford 350 EDS SSD, Oxford Instruments, Abingdon, UK). Powder SEM images were acquired on the electron microscope Prisma-E (Thermo Fisher, Massachusetts, USA). Prior to the SEM analyses, all samples were coated with a 10-nanometer-thick carbon layer by carbon evaporation (Bal-Tec Sputter-coater SCD 050, Bal-Tec, Pfäffikon, Switzerland).

The influence of annealing in air was investigated with a scanning transmission electron microscope - STEM (a probe Cs-corrected Jeol ARM 200 CF equipped with Centurio EDX system operated at 200 kV). The analysis was performed on cross-sectional lamellae using a Ga^+-source focused ion beam in a Helios Nanolab 650 HP (Thermo Fischer Scientific, Waltham, MA, USA).

Room-temperature permittivity was measured using a Precision LCR meter (HP 4244 A, USA) within the 100 Hz to 1 MHz. For the measurements, Au electrodes with 0.5 mm diameter were sputtered on the samples. The P–E loops were measured by applying a sinusoidal electric field with frequency of 100 Hz (aixACCT TF analyser 2000, aixACCT Systems GmbH, Germany).

The samples were also characterized using conductive atomic force microscopy (CAFM; Asylum Research MFP−3D, Oxford Instruments, Abingdon, UK). The measurements were performed with titanium-iridium-coated silicon tips (Asylec−01-R2, Oxford Instruments, Abingdon, UK). The CAFM measurements were performed in 20 µm x 20 µm areas and DC voltage of 40 V.

For the direct EC measurements, ~0.1-µm thick top electrodes were sputtered on the samples. The measurements were performed in a modified differential scanning calorimeter (DSC, Netzsch DSC 204 F1, Germany), which was used as a temperature-stabilization chamber, limiting thermal fluctuations to ~1 mK. The temperature change was directly measured with a radial glass bead thermistor (GR500KM4261J15, Measurement Specialties, Ohio, USA) glued to the top electrode. The temperature change on the thermistor was monitored through its resistance by a Keithley 2100 digital multimeter (Keithley Instruments, Ohio, USA). The electric field was applied using a Keithley High Voltage Source-Measure Unit 237, connected via copper wires and Epoxy/Ag adhesives. The background temperature linear drift was subtracted and the EC peak was calculated as difference between the cooling peak and the respective baseline, after electric field switch-off. Due to the nature of the setup, the intrinsic electrocaloric effect is reduced by a correction factor, k, defined as:

$$\Delta T_{EC} = k\Delta T, \tag{1}$$

where ΔT is the directly measured caloric response. The correction factor can be promptly calculated from the heat capacities of the materials and components on the device [15,65], mathematically described as:

$$k = \frac{C_p^T}{C_p^{EC}}, \tag{2}$$

where C_p^T is the total heat capacity of the system and C_p^{EC} is the heat capacity of the active material, between the electrodes. In this work the electrocaloric correction factor was ~40.

The room temperature magnetic moment as function of external magnetic field was measured by a vibrating sample magnetometer (LakeShore Series 7400, LakeShore, USA) within the −1 T to 1 T range. The temperature dependence of the magnetic moment was characterized from −25 °C to 75 °C using a Superconductor quantum interferometer device (SQUID; MPMS3 SQUID magnetometer, Quantum Design, California, USA) up to 0.5 T.

The MC response was characterized utilizing a custom-built experimental setup [12]. The applied magnetic field was measured using a Hall sensor near the sample. The room temperature measurements were performed with an infrared (IR) thermographic camera (InfraTec 8300, InfraTec GmbH, Dresden, Germany), with an acquisition rate set to 20 Hz, on an area of ~4 mm^2. Before the acquisitions, the samples were coated with a ~2 µm of black paint using a commercially available airbrush [66].

3. Results

The PMN–10PT ceramic films and PMN–10PT/LFSC composite films were deposited using aerosol deposition on gold-sputtered polyimide substrates. Prior to the deposition, the particle size of the PMN–10PT

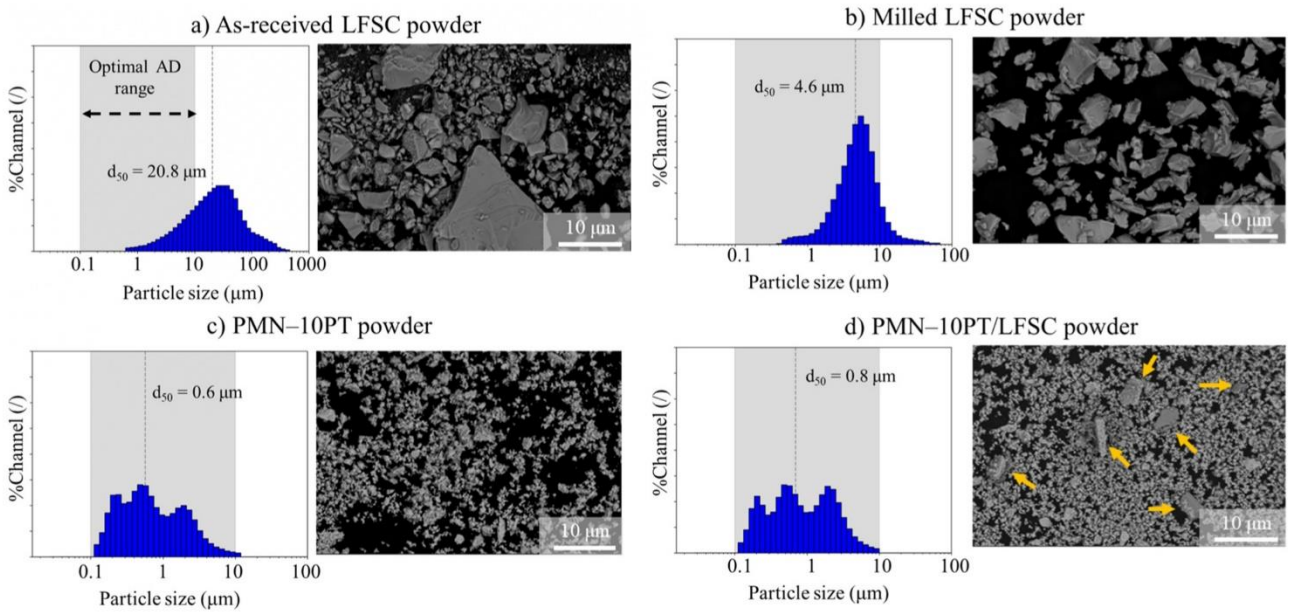


Fig. 3. Particle size distribution and BS-SEM of a) as-received LFSC, b) milled LFSC, c) PMN–10PT and d) PMN–10PT/LFSC composite powders, compared at the same scale. The dashed line indicates the d_{50} values. The grey region highlights the optimal particle size range for successful aerosol deposition. The yellow arrows indicate the largest LFSC particles in the composite powder.

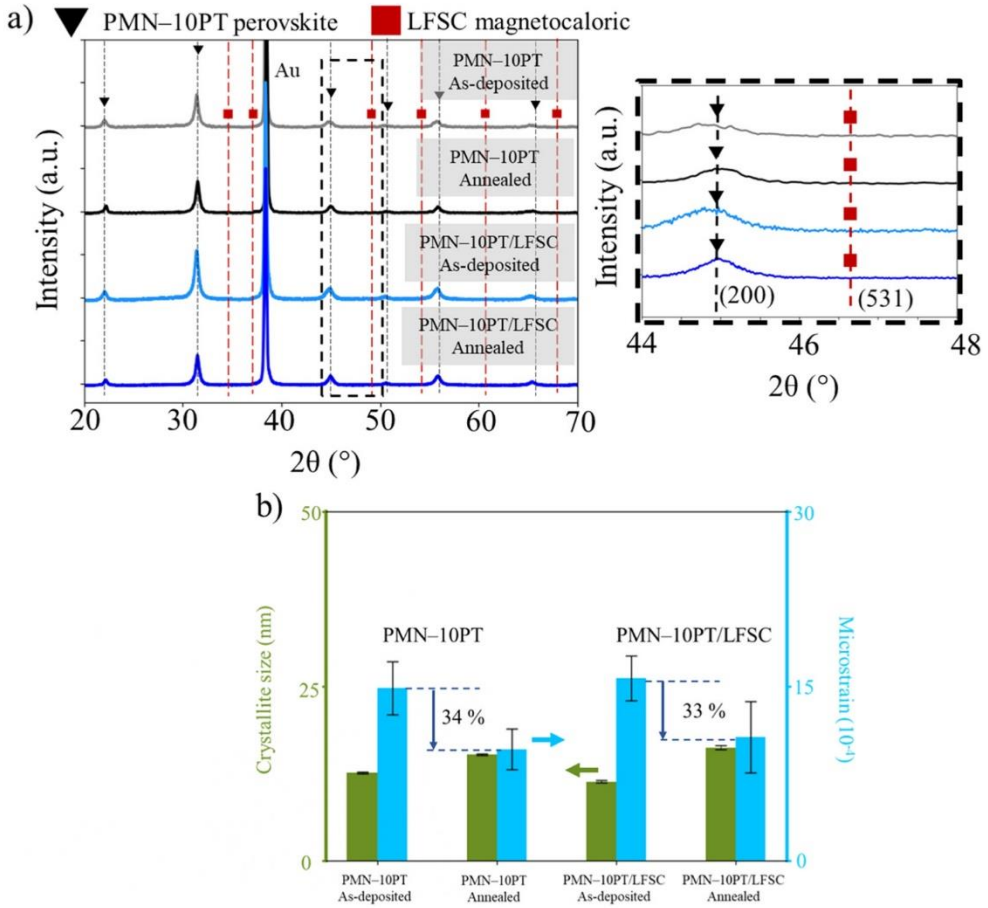


Fig. 4. a) X-ray diffractograms of as-deposited and annealed PMN–10PT and PMN–10PT/LFSC samples. Enlarged view from 44 ° to 48 °, emphasizing the lack of the expected high-intensity LFSC magnetocaloric (531) peak. Notice that only the PMN–10PT (200) peak was detected. b) Crystallite size (green bars) and microstrain (blue bars) of as-deposited and annealed PMN–10PT and PMN–10PT/LFSC samples.

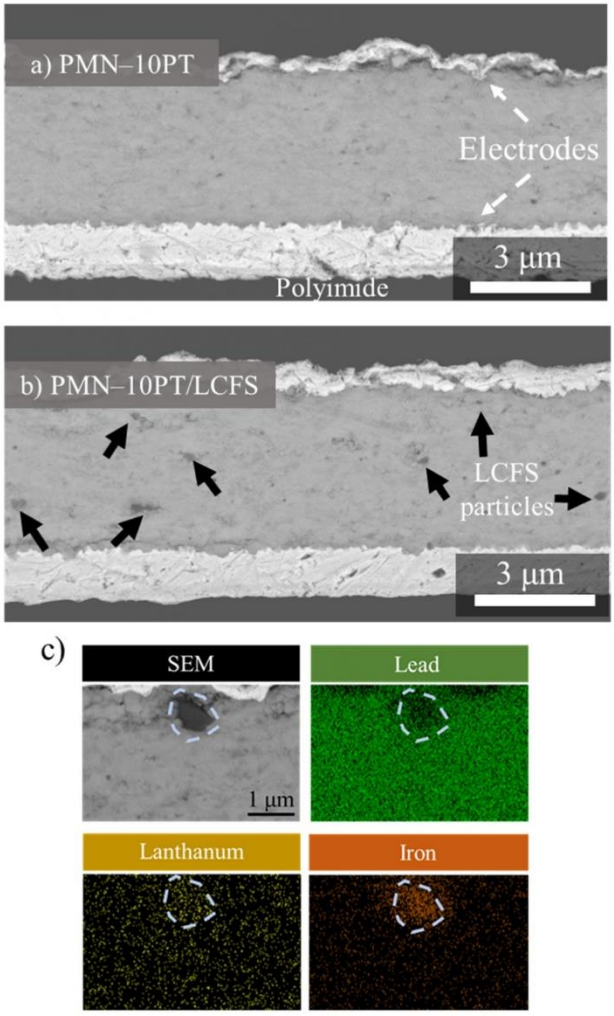


Fig. 5. BS-SEM images of a) PMN–10PT and b) PMN–10PT/LFSC annealed samples in cross-section view. c) EDS analysis of a PMN–10PT/LFSC sample, identifying a large embedded LFSC particle. The detected Pb signal is attributed to the surrounding PMN–10PT ceramic matrix. Notice, in the composite case, that the embedded particles can be either circular or elongated.

and LFSC powders was investigated to ensure a suitable particle size distribution (0.1 µm – 10 µm) for the AD method [54,67]. The as-received LFSC powder exhibited a broad particle size distribution, including particles as large as ~150 µm, as well as particles smaller than 10 µm, as shown in Fig. 2.

The particle size distribution of the as-received LFSC powder was further confirmed via granulometry. The powder exhibited a median particle size (d_{50}) of 20.8 µm, with most particles being outside the optimal particle size range for AD, as indicated by the grey region in Fig. 3a. After the milling, the LFSC powder particle size is significantly reduced down to d_{50} ~4.6 µm, as shown in Fig. 3b, with a significantly narrower distribution, mostly within the desired window for AD. The PMN–10PT powder was prepared for optimal deposition rate, as reported in ref. [67], exhibiting a d_{50} of 0.6 µm. As shown in Fig. 3c, its particle distribution is trimodal as the powder consists of smaller and medium particles ($\leq$ 1 µm), with few larger agglomerates, in agreement with the PMN–10PT powder that resulted in high-quality AD films on stainless steel substrates reported in the literature [67]. The composite powder exhibited a similar behavior to PMN–10PT powder, albeit slightly skewed towards larger particle sizes due to the influence of the LFSC particles, resulting in a d_{50} of 0.8 µm as shown in Fig. 3d. It is worth emphasizing that the as-received and milled LFSC powders exhibit the same XRD peaks, shown in Supplementary Material S1, indicating that the LFSC MC phase is still preserved after milling.

Next, the PMN–10PT and PMN–10PT/LFSC thick films were prepared. In all cases, the deposition rate was approximately 0.3 mm^3 min^{-1}, in excellent agreement with the literature [54,57,67,68]. It is worth emphasizing that due to the particle fracturing caused by the AD method, the prepared samples exhibit significant residual stresses [54, 69]. In light of this, the films were thermally treated at 400 °C in argon atmosphere to release such stresses. The argon atmosphere was chosen to prevent unwanted oxidation of MC phase in PMN–10PT/LFSC samples, as shown in Supplementary Material S2.

The XRD of the prepared films are shown in Fig. 4a. The as-deposited and annealed PMN–10PT samples exhibited only perovskite PMN–10PT peaks, with no detected pyrochlore phase. As conventionally observed in AD samples, the XRD peaks are broader in the films before heat treatment, due to the fracturing of the crystallites during the deposition. To further investigate the influence of annealing, the XRD patterns were analysed via Rietveld refinement. As shown in Fig. 4b, the PMN–10PT samples exhibited a slight crystallite size growth from 12.6 nm ± 0.1 nm before annealing to 14.8 nm ± 0.1 nm after annealing. The microstrain decreased from $15 \bullet 10^{-4} \pm 2 \bullet 10^{-4}$ before annealing to $10 \bullet 10^{-4} \pm 2 \bullet 10^{-4}$ after annealing, which is a ~34% reduction, similarly as observed for the aerosol-deposited PMN–10PT films on stainless steel substrates after annealing as reported in the ref. [67].

The as-deposited PMN–10PT/LFSC samples also exhibited broad XRD peaks that narrowed slightly after annealing. The crystallite size increased from 11.4 nm ± 0.1 nm before annealing to 16.2 nm ± 0.3 nm after annealing, and the stresses reduced from $16 \bullet 10^{-4} \pm 5 \bullet 10^{-4}$ to $11 \bullet 10^{-4} \pm 3 \bullet 10^{-4}$, which is a 33% decrease after annealing. Notice that, due to the large mass difference between the phases, the LFSC MC peaks could not be observed in the diffraction pattern of PMN–10PT/LFSC composite films.

To confirm the presence of the LFSC phase, SEM images were acquired on annealed PMN–10PT and PMN–10PT/LFSC samples in cross-section form, as shown in Figs. 5a and 5b. In both cases, the films were dense and exhibited excellent adhesion to the substrate. In composites, the embedded particles were homogeneously distributed across the PMN–10PT matrix, as shown in Fig. 5b. To further confirm the nature of the embedded phase, the EDS analysis was performed. As shown in Fig. 5c, the embedded phase is rich in lanthanum and iron, as expected for the LFSC particles. The effective mass fraction LFSC material deposited was estimated by calculating the relative volume of embedded LFSC particles within the matrix. By investigating distinct regions from different PMN–10PT/LFSC samples, a mass fraction of 1.7 wt% ± 0.3 wt % of LFSC phase within the PMN–10PT matrix was estimated, in excellent agreement with the nominal value of 2 wt% mixed in the starting powder before the deposition.

The dielectric permittivity of the films was characterized at room temperature, as shown in Fig. 6a. PMN–10PT samples exhibited a permittivity of ~600, while PMN–10PT/LFSC samples showed an enhanced permittivity of ~700. This increase is due to the embedded metallic particles acting as electric dipoles during electric field application and thereby increasing the permittivity, namely, the Maxwell-Wagner effect [61,70]. Notice that due to the low concentration of magnetic particles, no significant increase in the dielectric losses was observed in the composite samples. The insulating behavior of composites was further confirmed via CAFM current measurements, shown in Fig. 6b. With a bias voltage of 40 V, no electrical current was observed, in other words, the current is lower than the detection limit of the device (< 0.5 pA).

The influence of the LFSC phase was also observed in the P–E hysteresis loops (Fig. 6c, d). The PMN–10PT films exhibited a slim hysteresis loop, with a maximum polarization of approximately 30 µC cm^{-2} at 600 kV cm^{-1} and 100 Hz. In comparison, the composite films showed an increased maximum polarization of approximately 40 µC cm^{-2}, although

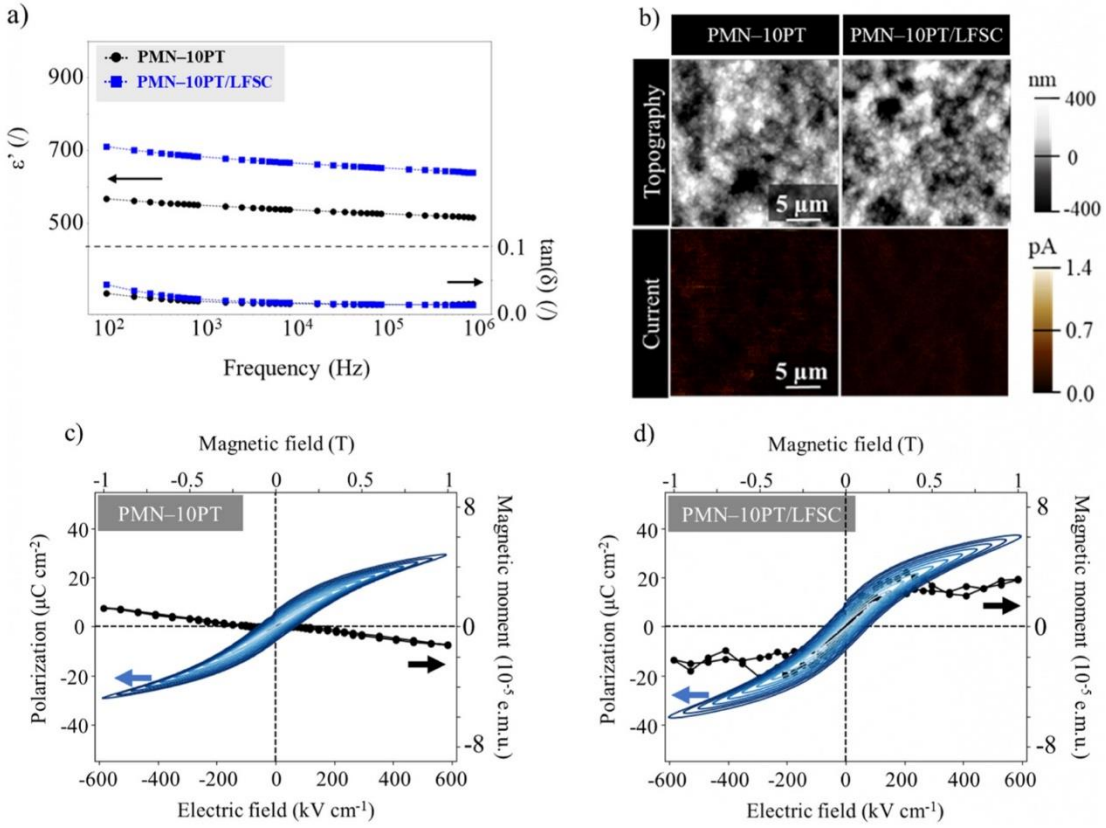


Fig. 6. a) Dielectric permittivity and dielectric losses, b) CAFM topography and current maps of investigated films. P-E (blue curves) and M-H (black dots) loops of c) PMN–10PT and d) PMN–10PT/LFSC samples.

the loops were slightly broader.

To verify that the metallic particles did not introduce a significant contribution from electrical conductivity, the P–E loops of the composite films were also measured at 1 Hz. As shown in Supplementary Material S3, the loop shape and maximum polarization value, approximately 40 µC cm^{-2}, remained similar at 1 Hz, indicating that the electrical conductivity contribution was not significant.

In addition, the magnetic moment of the films up to 1 T was also measured at room temperature. PMN–10PT samples exhibit a clear diamagnetic behavior, with their magnetic moment linearly decreasing with field. Composites, on the other hand, exhibit a ferromagnetic loop, showcasing the magnetic behavior of the LFSC phase. The ferromagnetic behaviour of PMN–10PT/LFSC composite samples annealed in argon was also observed via SQUID measurements (Supplementary Material S4), further confirming that the embedded LFSC phase within the composite films is magnetically active.

The room temperature EC effect was characterized using the thermistor-in-calorimeter method. To accurately determine the intrinsic ΔT_{EC}, a correction factor (k) is necessary which accounts for the experimental heat losses [15]. In this work, for the thermistor-in-calorimeter method, the correction factor in all cases was k ~40. Further details on the measurement method and the calculation of k can be found in Supplementary Material S5. As shown in Fig. 7a, the PMN–10PT films exhibited a room temperature ΔT_{EC} ~0.34 K, at 250 kV cm^{-1}. The composites exhibited a 32% larger value with ΔT_{EC} ~0.45 K, under the same conditions. A similar trend of enhancement was also observed on a different composite sample with a non-magnetic metallic phase, shown in Supplementary Material S6. Therefore, this enhancement in ΔT_{EC} can be attributed to the presence of the metallic particles embedded in the ceramic matrix.

According to the literature [70–76] in dielectric and piezoelectric materials, an enhancement in functional properties has been observed when introducing the metallic particles into the matrix. This enhancement is due to the Maxwell-Wagner-induced polarization contributing to the dielectric and piezoelectric responses of the composite samples. From thermodynamic theory, the EC effect is proportional to the square of the polarization [77,78], which is larger in composites due to the embedded LFSC particles. In other words, the enhancement in EC effect in composites can also be attributed to Maxwell-Wagner contributions.

The room-temperature ΔT_{MC} was directly measured on PMN–10PT/LFSC samples, using the IR camera method, discussed in further detail in Supplementary Material S7. Under a magnetic field of 2 T, a ΔT_{MC} ~0.2 K was obtained, as shown in Fig. 7b. The magnetic cycle was then performed two additional times, with all the magnetocaloric responses exhibiting comparable measured values. However, similar to the previous method, the measured ΔT_{MC} corresponds to a fraction of the intrinsic ΔT_{MC}, as there are heat sink effects from the experimental setup [15]. To address this issue, iterative finite element modelling was performed, as explained in the Supplementary Material S7. The intrinsic room-temperature ΔT_{MC} of ~1.4 K was found to be the best fit for the as-measured data (correction factor of 6.4), as shown in Fig. 7c.

4. Conclusions

For the first time, a room-temperature magneto-electro-caloric composite has been prepared and directly characterized. By combining the EC PMN–10PT with 2 wt% of the MC LFSC alloy, composite thick films were prepared using the aerosol deposition method. Prior to the deposition, the LFSC powder was milled to ensure a suitable particle size for deposition, while preserving its MC phase. The prepared films were 5-µm thick, post-annealed in argon atmosphere to release residual stresses and improve functional properties. The films exhibited dense

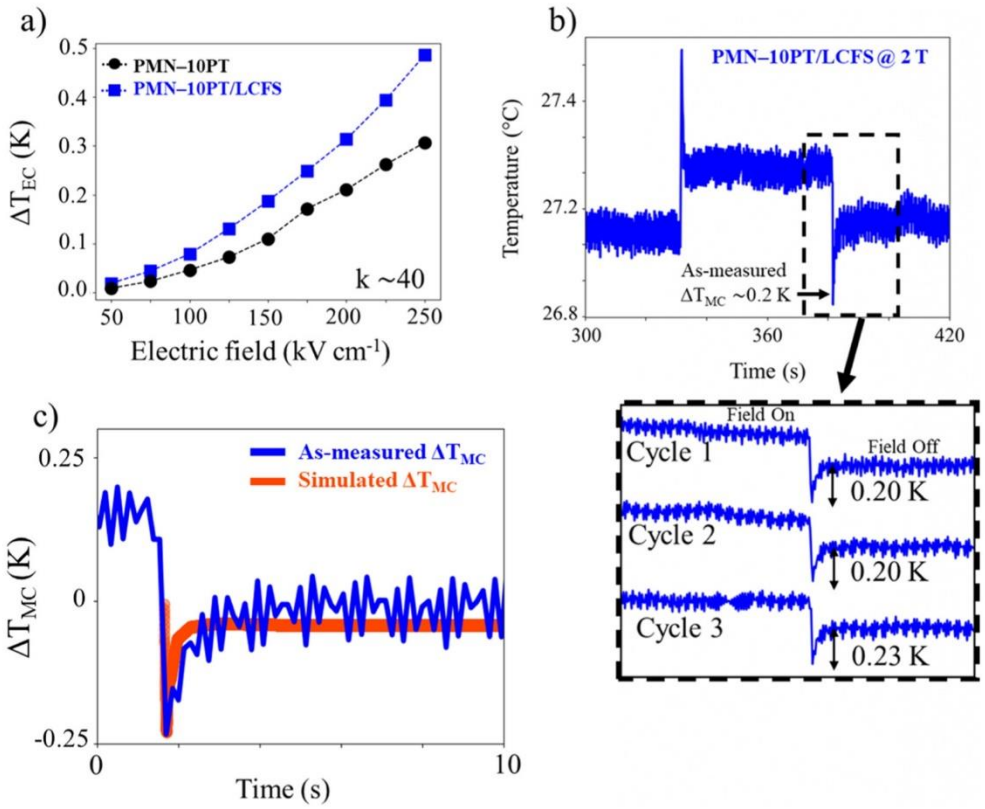


Fig. 7. a) The EC response of PMN–10PT and PMN–10PT/LFSC samples at room temperature up to 250 kV cm^{-1} (correction factor k ~ 40). b) The as-measured MC response of composite films at room temperature and at 2 T. During field switch-on, the operating magnet bores heat up resulting in a slight offset in the ambient temperature. c) The as-measured MC response (blue) and simulated MC response (red).

microstructure and, in PMN–10PT/LFSC composite samples, the magnetic LFSC particles were uniformly distributed across the PMN–10PT thick-film matrix.

The insertion of the magnetic phase enhanced the dielectric permittivity from 600, in PMN–10PT ceramic films, to 700 in composite films with no increase in dielectric losses. Similarly, an enhanced room-temperature EC response was observed in composite films compared to only PMN–10PT ceramic films. While PMN–10PT ceramic films exhibit ΔT_{EC} ~0.34 K at 250 kV cm^{-1}, composite films exhibited ΔT_{EC} ~0.45 K under the same conditions. The ~32% enhancement in ΔT_{EC} is attributed to Maxwell-Wagner type polarization effects, induced by the embedded LFSC alloy particles. In addition, under a magnetic field of 2 T, a corrected value of ΔT_{MC} of ~1.4 K was obtained on PMN–10PT/LFSC composite films, confirming the multicaloric performance of these samples. To conclude, our work offers novel insights into using the aerosol deposition method for multifunctional applications, particularly targeting caloric materials for future micro-cooling technologies.

CRediT authorship contribution statement

Victor Regis: Writing – review & editing, Writing – original draft, Visualization, Software, Methodology, Investigation, Formal analysis, Data curation, Conceptualization. **Ivana Goričan:** Writing – review & editing, Methodology, Investigation. **Matej Šadl:** Writing – review & editing, Methodology, Investigation. **Andreja Benčan:** Writing – review & editing, Methodology, Investigation. **Goran Dražić:** Writing – review & editing, Methodology, Investigation. **Sašo Gyergyek:** Writing – review & editing, Methodology, Investigation. **Urban Tomc**: Writing – review & editing, Methodology, Investigation. **Andrej Kitanovski:** Writing – review & editing, Methodology, Investigation. **Lukas Beyer:** Writing – review & editing, Methodology, Investigation. **Enric Stern-Taulats:** Writing – review & editing, Methodology, Investigation. **Klara Lünser:** Writing – review & editing, Methodology, Investigation. **Lluís Mañosa:** Writing – review & editing, Resources, Methodology, Investigation, Data curation. **Hana Uršič:** Writing – review & editing, Writing – original draft, Supervision, Project administration, Methodology, Investigation, Funding acquisition, Data curation, Conceptualization.

Declaration of Competing Interest

The authors declare that they have no known competing financial interests or personal relationships that could have appeared to influence the work reported in this paper.

Acknowledgements

The authors acknowledge the financial support of the Slovenian Research and Innovation Agency (projects no. N2–0212 and J2–60035, programs no. P2–0105, P2–0089 and young researcher project), the Agencia Estatal de Investigación, Spain (project PID2024–161052NA-I00) and the transnational consortium M-ERA.NET for the project Cool BatMan: Battery Thermal Management System Based on High Power Density Digital Microfluidic Magnetocaloric Cooling (No. 9400, Slovenian part of the project is financed by Ministry of Higher Education, Science and Innovation. Spanish part financed by MCIN/AEI/10.13039/501100011033, project No. PCI2022–132957, German part is co-financed with tax funds on the basis of the budget adopted by the Saxon State Parliament, SAB-Nr: 100632843) and CENN Nanocenter for the use of Vibrating-Sample Magnetometer LakeShore 7400 Series VSM. The Erasmus + program is greatly acknowledged by Victor Regis. The

authors also acknowledge Jena Cilenšek, Alan Selin, Val Fišinger, Maja Koblar and Brigita Kmet for help in the laboratory.

Appendix A. Supporting information

Supplementary data associated with this article can be found in the online version at doi:10.1016/j.jeurceramsoc.2026.118584.

Data Availability

The data that support the findings of this study are available online in Zenodo repository at doi.org/10.5281/zenodo.17650836, reference number [79].

References

[1] T. Correia, Q. Zhang (Eds.), Electrocaloric Materials: New Generation of Coolers, Springer-Verlag, Berlin Heidelberg, Germany, 2014.
[2] A.M. Tishin, Y.I. Spichkin, Taylor francis, oxfordshire, United Kingdom, Magn. Eff. Appl. (2003).
[3] V. Franco, J.S. Blázquez, J.J. Ipus, J.Y. Law, L.M. Moreno-Ramírez, A. Conde, Magnetocaloric effect: from materials research to refrigeration devices, Prog. Mater. Sci. 93 (2018) 112–232.
[4] K. Klinar, J.Y. Law, V. Franco, X. Moya, A. Kitanovski, Perspectives and energy applications of magnetocaloric, pyromagnetic, electrocaloric, and pyroelectric materials, Adv. Energy Mater. 14 (2024) 2401739.
[5] A.L. Kholkin, O.V. Pakhomov, A.A. Semenov, A. Tselev (Eds.), The Electrocaloric Effect: Materials and Applications, Elsevier, Amsterdam, Netherlands, 2023.
[6] L. Mañosa, A. Planes, Materials with giant mechanocaloric effects: cooling by strength, Adv. Mater. 29 (2017) 1603607.
[7] A. Planes, L. Mañosa, M. Acet, Magnetocaloric effect and its relation to shape-memory properties in ferromagnetic Heusler alloys, J. Phys. Condens. Matter 21 (2009) 233201.
[8] E. Bonnot, R. Romero, L. Mañosa, E. Vives, A. Planes, Elastocaloric effect associated with the martensitic transition in shape-memory alloys, Phys. Rev. Lett. 100 (2008) 125901.
[9] L. Mañosa, D. González-Alonso, A. Planes, E. Bonnot, M. Barrio, J.-L. Tamarit, S. Aksoy, M. Acet, Giant solid-state barocaloric effect in the Ni–Mn–In magnetic shape-memory alloy, Nat. Mater. 9 (2010) 478–481.
[10] V.M. Andrade, A. Amirov, D. Yusupov, B. Pimentel, N. Barroca, A.L. Pires, J. H. Belo, A.M. Pereira, M.A. Valente, J.P. Araújo, M.S. Reis, Multicaloric effect in a multiferroic composite of $Gd_5(Si,Ge)_4$ microparticles embedded into a ferroelectric PVDF matrix, Sci. Rep. 9 (2019) 18308.
[11] G. Qian, K. Zhu, X. Li, K. Yan, J. Wang, J. Liu, W. Huang, The electrocaloric effect of PBZ/PVDF flexible composite film near room temperature, J. Mater. Sci. Mater. Electron. 32 (2021) 12001–12016.
[12] Q. Badosa, L. Mañosa, E. Vives, A. Planes, B. Weise, L. Beyer, E. Stern-Taulats, Demagnetizing field-induced magnetocaloric effect in Gd, J. Appl. Phys. 134 (2023) 113902.
[13] M. Vrabelj, H. Uršič, Z. Kutnjak, B. Rožič, S. Drnovšek, A. Benčan, V. Bobnar, L. Fulanović, B. Malič, Large electrocaloric effect in grain-size-engineered $0.9Pb(Mg_{1/3}Nb_{2/3})O_3$-$0.1PbTiO_3$, J. Eur. Ceram. Soc. 36 (2016) 75–80.
[14] H. Uršič, M. Vrabelj, M. Otoničar, L. Fulanović, B. Rožič, Z. Kutnjak, V. Bobnar, B. Malič, Influence of synthesis-related microstructural features on the electrocaloric effect for $0.9Pb(Mg_{1/3}Nb_{2/3})O_3$-$0.1PbTiO_3$ ceramics, Crystals 11 (2021) 372.
[15] U. Prah, M. Sadl, A. Torello, P. Lheritier, V. Kovacova, H. Ursic, E. Defay, Direct Electrocaloric Characterization of Ceramic Films, Small Methods 7 (2023) 2300212.
[16] J. Li, A. Torelló, V. Kovacova, U. Prah, A. Aravindhan, T. Granzow, T. Usui, S. Hirose, E. Defay, High cooling performance in a double-loop electrocaloric heat pump, Science 382 (2023) 801–805.
[17] B. Li, Y. Kawakita, S. Ohira-Kawamura, T. Sugahara, H. Wang, J. Wang, Y. Chen, S. I. Kawaguchi, S. Kawaguchi, K. Ohara, K. Li, D. Yu, R. Mole, T. Hattori, T. Kikuchi, S. Yano, Z. Zhang, Z. Zhang, W. Ren, S. Lin, O. Sakata, K. Nakajima, Z. Zhang, Colossal barocaloric effects in plastic crystals, Nature 567 (2019) 506–510.
[18] P. Lloveras, A. Aznar, M. Barrio, Ph Negrier, C. Popescu, A. Planes, L. Mañosa, E. Stern-Taulats, A. Avramenko, N.D. Mathur, X. Moya, J.-Ll Tamarit, Colossal barocaloric effects near room temperature in plastic crystals of neopentylglycol, Nat. Commun. 10 (2019) 1803.
[19] U. Tomc, G.F. Peixer, C.R.H. Bahl, K.K. Nielsen, J.A. Lozano, J.R. Barbosa, A. Kitanovski, Influence of Layering and Curie Temperature Uncertainty on the Performance of Multilayer Active Magnetic Regenerators, Adv. Funct. Mater. (2025) e24282.
[20] A. Torelló, E. Defay, Electrocaloric coolers: a review, Adv. Electron. Mater. 8 (2022) 2101031.
[21] X. Moya, E. Defay, V. Heine, N.D. Mathur, Too cool to work, Nat. Phys. 11 (2015) 202–205.
[22] K. Engelbrecht, J. Tušek, D. Eriksen, T. Lei, C.-Y. Lee, J. Tušek, N. Pryds, A regenerative elastocaloric device: experimental results, J. Phys. D Appl. Phys. 50 (2017) 424006.
[23] H. Mevada, B. Liu, L. Gao, Y. Hwang, I. Takeuchi, R. Radermacher, Elastocaloric cooling: A pathway towards future cooling technology, Int. J. Refrig. 162 (2024) 86–98.
[24] J. Tušek, K. Engelbrecht, N. Pryds, Elastocaloric effect of a Ni-Ti plate to be applied in a regenerator-based cooling device, Sci. Technol. Built Environ. 22 (2016) 489–499.
[25] J. Tušek, K. Engelbrecht, L.P. Mikkelsen, N. Pryds, Elastocaloric effect of Ni-Ti wire for application in a cooling device, J. Appl. Phys. 117 (2015) 124901.
[26] L. Fulanović, S. Drnovšek, H. Uršič, M. Vrabelj, D. Kuščer, K. Makarovič, V. Bobnar, Z. Kutnjak, B. Malič, Multilayer $0.9Pb(Mg_{1/3}Nb_{2/3})O_3$-$0.1PbTiO_3$ elements for electrocaloric cooling, J. Eur. Ceram. Soc. 37 (2017) 599–603.
[27] A. Kitanovski, J. Tušek, U. Tomc, U. Plaznik, M. Ožbolt, A. Poredoš, Magnetocaloric Energy Conversion: From Theory to Applications, Springer Cham, Switzerland, 2015.
[28] X. Moya, M.H. Phan, H. Srikanth, F. Albertini, Multicalorics, J. Appl. Phys. 128 (2020) 240401.
[29] X. Moya, S. Kar-Narayan, N.D. Mathur, Caloric materials near ferroic phase transitions, Nat. Mater. 13 (2014) 439–450.
[30] A. Amirov, D. Samsonov, Demonstration of the multicaloric effect in a laboratory prototype, J. Appl. Phys. 136 (2024) 053902.
[31] M. Zeng, M. Romanini, I. Gorican, S. Drnovsek, H. Ursic, A. Salvatori, M. Barrio, S. Loehle, N. Obrecht, C. Escorihuela-Sayalero, C. Cazorla, À. Torelló, P. Lloveras, J.-L. Tamarit, Simultaneous shifts in pressure and electric field boost the caloric response in ferroelectrics, Mater. Horiz. 12 (2025) 8460–8471.
[32] U. Prah, M. Wencka, T. Rojac, A. Benčan, H. Uršič, $Pb(Fe_{0.5}Nb_{0.5})O_3$-$BiFeO_3$-based multicalorics with room-temperature ferroic anomalies, J. Mater. Chem. C. 8 (2020) 11282–11291.
[33] U. Prah, T. Rojac, M. Wencka, M. Dragomir, A. Bradeško, A. Benčan, R. Sherbondy, G. Brennecka, Z. Kutnjak, B. Malič, H. Uršič, Improving the multicaloric properties of $Pb(Fe_{0.5}Nb_{0.5})O_3$ by controlling the sintering conditions and doping with manganese, J. Eur. Ceram. Soc. 39 (2019) 4122–4130.
[34] E. Stern-Taulats, T. Castán, A. Planes, L.H. Lewis, R. Barua, S. Pramanick, S. Majumdar, L. Mañosa, Giant multicaloric response of bulk $Fe_{49}Rh_{51}$, Phys. Rev. B 95 (2017) 104424.
[35] E. Stern-Taulats, T. Castán, L. Mañosa, A. Planes, N.D. Mathur, X. Moya, Multicaloric materials and effects, MRS Bull. 43 (2018) 295–299.
[36] A. Gràcia-Condal, T. Gottschall, L. Pfeuffer, O. Gutfleisch, A. Planes, L. Mañosa, Multicaloric effects in metamagnetic Heusler Ni-Mn-In under uniaxial stress and magnetic field, Appl. Phys. Rev. 7 (2020) 041406.
[37] H. Hou, S. Qian, I. Takeuchi, Materials, physics and systems for multicaloric cooling, Nat. Rev. Mater. 7 (2022) 633–652.
[38] A. Abadia-Huguet, E. Mendive-Tapia, E. Stern-Taulats, A. Planes, B. Eggert, H. Wende, M. Acet, M.-I. Sturza, H. Kohlmann, M.V. Costache, L. Mañosa, Multicaloric effects and magnetostructural coupling in the $Cr_2Ge_2Te_6$ van der Waals crystal, Appl. Mater. Today 44 (2025) 102749.
[39] X. Xie, H. Wang, Y. Zhu, G. Lin, R. zhao, H. Zhu, Multicaloric effect and spin-wave excitation in the $YMn_{0.5}Cr_{0.5}O_3$ compound, J. Magn. Magn. Mater. 475 (2019) 184–188.
[40] M.A. Carpenter, M.B. Costa, G.F. Nataf, X. Moya, Strain-coupling and relaxation dynamics in multicaloric ammonium sulphate $(NH_4)_2SO_4$, Phys. Rev. Mat. 7 (2023) 083601.
[41] R. Ramesh, N.A. Spaldin, "Multiferroics: progress and prospects in thin films, Nat. Mater. 6 (2007) 21–26.
[42] N.A. Spaldin, R. Ramesh, Advances in magnetoelectric multiferroics, Nat. Mater. 18 (2019) 203–212.
[43] N.A. Hill, Why are there so few magnetic ferroelectrics? J. Phys. Chem. B 104 (2000) 6694–6709.
[44] Y. Liu, L.C. Phillips, R. Mattana, M. Bibes, A. Barthélémy, B. Dkhil, Large reversible caloric effect in FeRh thin films via a dual-stimulus multicaloric cycle, Nat. Comm. 7 (2016) 11614.
[45] K. Qiao, J. Wang, F. Hu, J. Li, C. Zhang, Y. Liu, Z. Yu, Y. Gao, J. Su, F. Shen, H. Zhou, X. Bai, J. Wang, V. Franco, J. Sun, B. Shen, Regulation of phase transition and magnetocaloric effect by ferroelectric domains in FeRh/PMN-PT heterojunctions, Acta Mater. 191 (2020) 51–59.
[46] E. Mikhaleva, I. Flerov, A. Kartashev, M. Gorev, A. Cherepakhin, K. Sablina, N. Mikhashenok, N. Volkov, A. Shabanov, Caloric effects and phase transitions in ferromagnetic-ferroelectric composites $xLa_{0.7}Pb_{0.3}MnO_3$-$(1-x)PbTiO_3$, J. Mater. Res. 28 (2013) 3322–3331.
[47] M.G. Zavareh, Y. Skourski, K.P. Skokov, D. Yu, L. Karpenkov, A. Zvyagina, D. Waske, M. Haskel, J. Zhernenkov, O. Wosnitza, Gutfleisch, Direct Measurement of the Magnetocaloric Effect in $La(Fe,Si,Co)_{13}$ Compounds in Pulsed Magnetic Fields, Phys. Rev. Appl. 8 (2017) 014037.
[48] K. Löwe, J. Liu, K. Skokov, J.D. Moore, H. Sepehri-Amin, K. Hono, M. Katter, O. Gutfleisch, The effect of the thermal decomposition reaction on the mechanical and magnetocaloric properties of $La(Fe,Si,Co)_{13}$, Acta Mater. 60 (2012) 4268–4276.
[49] J.M. Lommel, J.S. Kouvel, Effects of Mechanical and Thermal Treatment on the Structure and Magnetic Transitions in FeRh, J. Appl. Phys. 38 (1967) 1263–1264.
[50] L.H. Lewis, C.H. Marrows, S. Langridge, Coupled magnetic, structural, and electronic phase transitions in FeRh, J. Phys. D Appl. Phys. 49 (2016) 323002.
[51] S.Yu Dan'kov, A.M. Tishin, V.K. Pecharsky, K.A. Gschneidner, Magnetic phase transitions and the magnetothermal properties of gadolinium, Phys. Rev. B 57 (1998) 3478–3490.
[52] M.E. Gruner, P. Entel, Simulation of the (p,T) phase diagram of the temperature-driven metamagnet α-FeRh, Phase Transit. 78 (2005) 209–217.

[53] P. Carrillo, R. Shi, K. Teeluck, S.D. Senanayake, M.G. White, *In Situ* Formation of FeRh Nanoalloys for Oxygenate Synthesis, ACS Catal. 8 (2018) 7279–7286.
[54] D. Hanft, J. Exner, M. Schubert, T. Stöcker, P. Fuierer, R. Moos, An overview of the Aerosol Deposition method: Process fundamentals and new trends in materials applications, J. Ceram. Sci. Technol. 6 (2015) 147–181.
[55] J. Akedo, M. Lebedev, Microstructure and Electrical Properties of Lead Zirconate Titanate ($Pb(Zr_{52}/Ti_{48})O_3$) Thick Films Deposited by Aerosol Deposition Method, Jpn. J. Appl. Phys. 38 (1999) 5397.
[56] G. Hwang, V. Annapureddy, J.H. Han, D.J. Joe, C. Baek, D.Y. Park, D.H. Kim, J. H. Park, C.K. Jeong, K. Park, J. Choi, D.K. Kim, J. Ryu, K.J. Lee, Self-Powered Wireless Sensor Node Enabled by an Aerosol-Deposited PZT Flexible Energy Harvester, Adv. Energy Mater. 6 (2016) 1600237.
[57] J. Exner, M. Hahn, M. Schubert, D. Hanft, P. Fuierer, R. Moos, Powder requirements for aerosol deposition of alumina films, Adv. Powder Technol. 26 (2015) 1143–1151.
[58] M. Sadl, U. Tomc, U. Prah, H. Ursic, Protective alumina coatings prepared by aerosol deposition on magnetocaloric gadolinium elements, Inf. MIDEM 49 (2019) 177–182.
[59] U. Eckstein, J. Exner, A. Bencan Golob, K. Ziberna, G. Drazic, H. Ursic, H. Wittkämper, C. Papp, J. Kita, R. Moos, K.G. Webber, N.H. Khansur, Temperature-dependent dielectric anomalies in powder aerosol deposited ferroelectric ceramic films, J. Mater. 8 (2022) 1239–1250.
[60] M. Suzuki, J. Akedo, Temperature Dependence of Dielectric Properties of Barium Titanate Ceramic Films Prepared by Aerosol Deposition Method, Jpn. J. Appl. Phys. 49 (2010), 09MA10.
[61] V. Regis, M. Šadl, G. Brennecka, A. Bradeško, U. Tomc, H. Uršič, Investigation of Structural and Electrical Properties of Al_2O_3/Al Composites Prepared by Aerosol Co-Deposition, Crystals 13 (2023) 850.
[62] O.-Y. Kwon, H.-J. Na, H.-J. Kim, D.-W. Lee, S.-M. Nam, Effects of mechanical properties of polymer on ceramic-polymer composite thick films fabricated by aerosol deposition, Nanoscale Res. Lett. 7 (2012) 261.
[63] C. Lee, M.-Y. Cho, M. Kim, J. Jang, Y. Oh, K. Oh, S. Kim, B. Park, B. Kim, S.-M. Koo, J.-M. Oh, D. Lee, Applicability of Aerosol Deposition Process for flexible electronic device and determining the Film Formation Mechanism with Cushioning Effects, Sci. Rep. 9 (2019) 2166.
[64] M. Dragomir, M. Otoničar, M. Vrabelj, L. Fulanović, S. Drnovšek, T. Rojac, B. Malič, Seeding effects on the mechanochemical synthesis of $0.9Pb(Mg_{1/3}Nb_{2/3})O_3$–$0.1PbTiO_3$, J. Eur. Ceram. Soc. 39 (2019) 1837–1845.
[65] Z. Kutnjak, B. Rožič, R. Pirc, Electrocaloric Effect: Theory, Measurements, and Applications, in: J.G. Webster (Ed.), Wiley Encyclopedia of Electrical and Electronics Engineering, 1st ed., Wiley, 2015, pp. 1–19.
[66] V. Regis, G. Brennecka, U. Tomc, A. Kitanovski, J. Cerar, J. Tušek, I. Jerman, E. Stern-Taulats, K. Lünser, L. Mañosa, H. Uršič, Airbrushing: A Novel Method for Preparation of High-Emissivity Black Coating for Infrared Measurements, Adv. Mater. Inter. 21 (2025) e00467.
[67] M. Sadl, O. Condurache, A. Bencan, M. Dragomir, U. Prah, B. Malic, M. Deluca, U. Eckstein, D. Hausmann, N.H. Khansur, K.G. Webber, H. Ursic, Energy-storage-efficient $0.9Pb(Mg_{1/3}Nb_{2/3})O_3$–$0.1PbTiO_3$ thick films integrated directly onto stainless steel, Acta Mater. 221 (2021).
[68] D. Hanft, P. Glosse, S. Denneler, T. Berthold, M. Oomen, S. Kauffmann-Weiss, F. Weis, W. Häßler, B. Holzapfel, R. Moos, The Aerosol Deposition Method: A Modified Aerosol Generation Unit to Improve Coating Quality, Materials 11 (2018) 1572.
[69] S. Merselmiz, I. Goričan, T. Rojac, V. Bobnar, V. Regis, M. Šadl, V. Fišinger, N. Suban, B. Kmet, A. Benčan, A. Bradeško, A. Debevec, B. Malič, H. Uršič, Capacitive energy-storage and electromechanical properties of aerosol-deposited $0.5BaZr_{0.2}Ti_{0.8}O_3$–$0.5Ba_{0.7}Ca_{0.3}TiO_3$ films, Acta Mater. 304 (2026) 121749.
[70] P. Lunkenheimer, V. Bobnar, A.V. Pronin, A.I. Ritus, A.A. Volkov, A. Loidl, Origin of apparent colossal dielectric constants, Phys. Rev. B 66 (2002) 052105.
[71] V. Bobnar, A. Levstik, C. Huang, Q.M. Zhang, Enhanced dielectric response in all-organic polyaniline–poly(vinylidene fluoride-trifluoroethylene-chlorotrifluoroethylene) composite, J. Non-Cryst. Solids 353 (2007) 205–209.
[72] A.V. Turik, G.S. Radchenko, Maxwell-Wagner relaxation in piezoactive media, J. Phys. D Appl. Phys. 35 (2002) 1188–1192.
[73] D. Damjanovic, M. Demartin Maeder, P. Duran Martin, C. Voisard, N. Setter, Maxwell–Wagner piezoelectric relaxation in ferroelectric heterostructures, J. Appl. Phys. 90 (2001) 5708–5712.
[74] V. Bobnar, H. Uršič, G. Casar, S. Drnovšek, Distinctive contributions to dielectric response of relaxor ferroelectric lead scandium niobate ceramic system, Phys. Status Solidi (b 250 (2013) 2232–2236.
[75] V. Bobnar, M. Hrovat, J. Holc, M. Kosec, All-ceramic lead-free percolative composite with a colossal dielectric response, J. Eur. Ceram. Soc. 29 (2009) 725–729.
[76] Z. Yu, C. Ang, Maxwell–Wagner polarization in ceramic composites $BaTiO_3$–$(Ni_{0.3}Zn_{0.7})Fe_{2.1}O_4$, J. Appl. Phys. 91 (2002) 794–797.
[77] A. Planes, T. Castán, A. Saxena, Thermodynamics of multicaloric effects in multiferroics, Philos. Mag. 94 (2014) 1893–1908.
[78] N. Novak, Z. Kutnjak, R. Pirc, High-resolution electrocaloric and heat capacity measurements in barium titanate, EPL 103 (2013) 47001.
[79] V. Regis, H. Uršič, 'Direct observation of room-temperature electrocaloric and magnetocaloric responses in multicaloric composite films, Zenodo (2025), https://doi.org/10.5281/zenodo.17650836.

Supplementary Material

Direct observation of room-temperature electrocaloric and magnetocaloric responses in multicaloric composite films

Victor Regis[1,2], Ivana Goričan[1,2], Matej Šadl[1,2], Andreja Benčan[1,2], Goran Dražić[1,2,3], Sašo Gyergyek[4], Urban Tomc[5], Andrej Kitanovski[5], Lukas Beyer[6,7], Enric Stern-Taulats[8], Klara Lünser[8,9,10], Lluís Mañosa[8] and Hana Uršič[1,2,*]

[1] Electronic Ceramics Department, Jožef Stefan Institute, Jamova cesta 39, 1000 Ljubljana, Slovenia

[2] Jožef Stefan International Postgraduate School, Jamova cesta 39, 1000 Ljubljana, Slovenia

[3] Department of Materials Chemistry, National Institute of Chemistry, Hajdrova ulica 19, 1000 Ljubljana, Slovenia

[4] Department of Synthesis of Materials, Jožef Stefan Institute, Jamova cesta 39, 1000 Ljubljana, Slovenia

[5] Faculty of Mechanical Engineering, University of Ljubljana, Aškerčeva cesta 6, 1000 Ljubljana, Slovenia

[6] Leibniz Institute for Solid State and Materials Research Dresden, Helmholtzstr. 20, 01069 Dresden, Germany

[7] Institute of Materials Science, Technische Universität Bergakademie Freiberg, Gustav-Zeuner-Str. 5, 09599 Freiberg, Germany

[8] Departament de Física de la Matèria Condensada, Facultat de Física, Martí i Franquès 1, Universitat de Barcelona, 08028 Barcelona, Catalonia

[9] Institute for Energy and Materials Processes – Applied Quantum Materials, University Duisburg-Essen, 47057 Duisburg, Germany

[10] Research Center Future Energy Materials and Systems (RC FEMS), Research Alliance Ruhr, Bochum, Germany

*Correspondence: hana.ursic@ijs.si

S1. XRD spectra of the powders

The XRD spectra of the powders are shown in Figure S1. Only perovskite peaks are observed in the XRD spectrum of the PMN–10PT powder. No pyrochlore phase is detected. In the XRD spectra of the as-received and annealed LFSC powders, only the LFSC magnetocaloric phase is observed. In the XRD spectrum of the PMN–10PT/LFSC composite powder, only peaks corresponding to PMN–10PT are observed due to the large mass difference between PMN–10PT and LFSC.

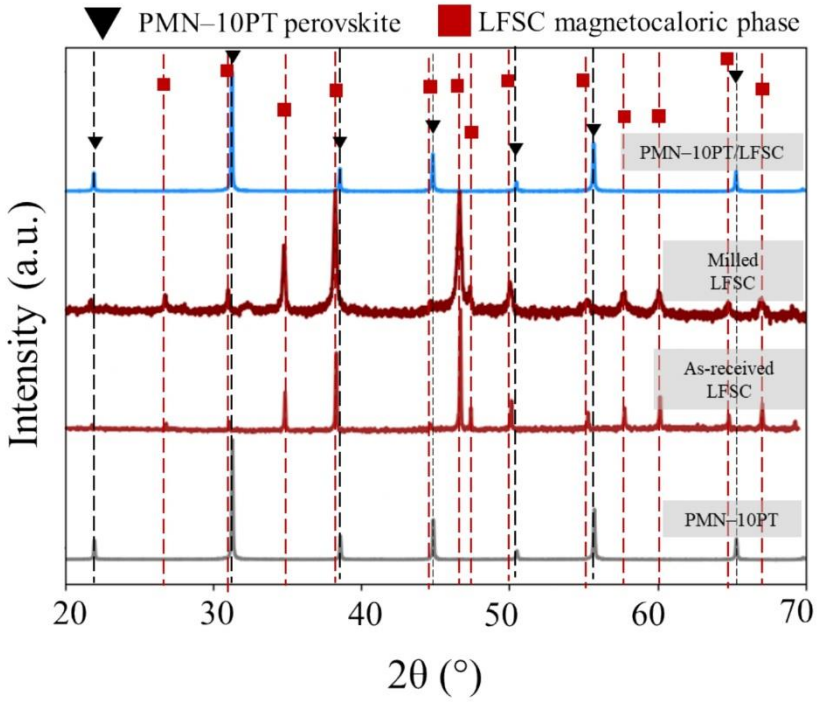


Figure S1: XRD spectra of PMN–10PT powder, LFSC as-received powder, LFSC milled powder, and PMN–10PT/LFSC composite powder.

S2. Scanning transmission electron microscopy analysis of films

To investigate the effects of oxidation of the LFSC phase in PMN–10PT/LFSC composite films when annealed in air, scanning transmission electron microscopy (STEM) analysis was conducted. The STEM images of the as-deposited and air-annealed PMN–10PT/LFSC composite films are shown in Figure S2. In as-deposited composite films, the LFSC phase can be promptly identified by a quasi-circular shape generally elongated along the deposition plane. Notice, however, that after annealing in air atmosphere at 400 °C for 1 h, the magnetic phase is oxidized. Evidently, the

oxidized phase exhibits a core-shell structure with a darker core, rich in La, and a lighter La-poor shell.

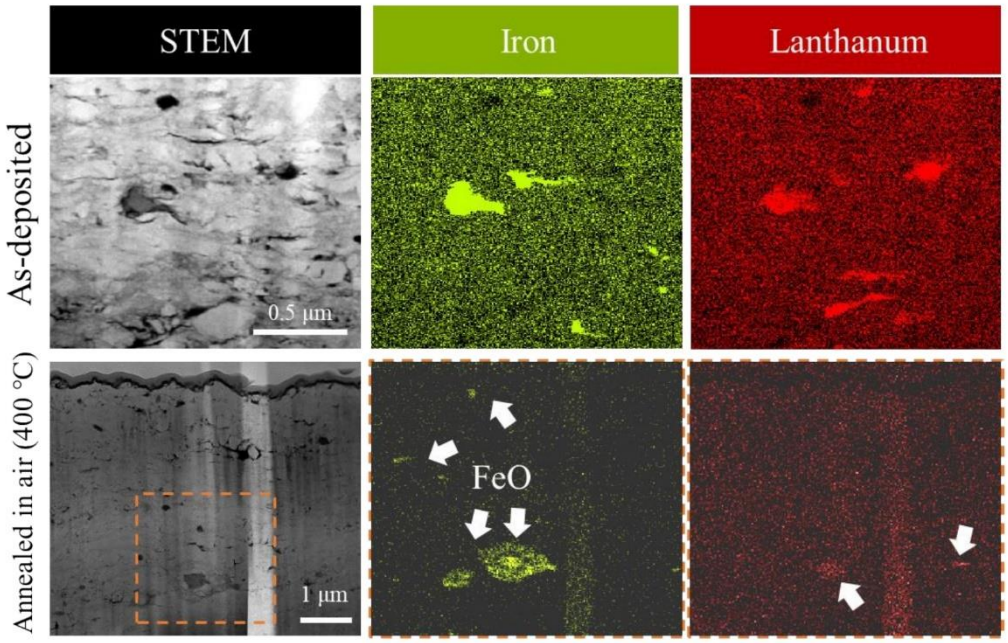


Figure S2: STEM image of a) as-deposited and b) air-annealed PMN–10PT/LFSC composite films.

As shown in Figure 5 in the main text, the PMN–10PT/LFSC composite films annealed in argon do not exhibit core-shell structure in the LFSC embedded particles, confirming the preservation of the LFSC magnetocaloric phase.

S3. P-E measurement of composite thick films at 1 Hz

P-E hysteresis loops were measured at 1 Hz and 100 Hz as shown in Figure S3 below for 600 kV cm^{-1}. The maximum value of ~40 µC cm^{-2} was observed at both frequencies. The result suggests that the Maxwell-Wagner contribution from the embedded particles enhances the polarization values; however, no significant contribution to the electrical conductivity is observed.

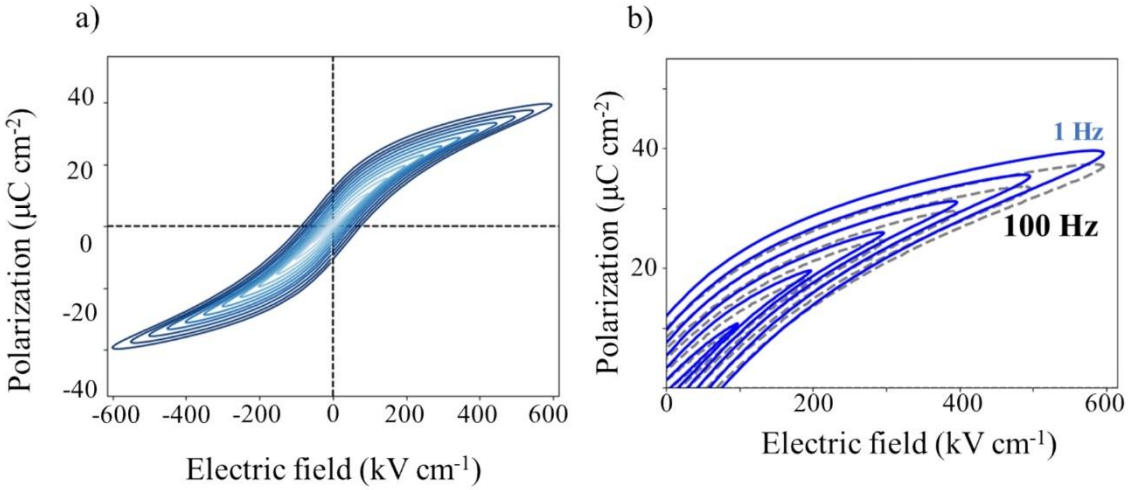


Figure S3: a) Polarization hysteresis loop of composite film measured at 1 Hz. b) Zoomed in comparison between 1 Hz and 100 Hz measurements.

S4. Temperature-dependent magnetic analysis

Superconducting quantum interference device (SQUID) measurements at different fields were performed on PMN–10PT/LFSC composite films annealed in argon atmosphere. The magnetic moment of composites from -25 °C to 75 °C is shown in Figure S4. With increasing magnetic field, the ferromagnetic contribution becomes proportionally larger. In this manner, the magnetic response of the LFSC phase inside the composite films is additionally confirmed.

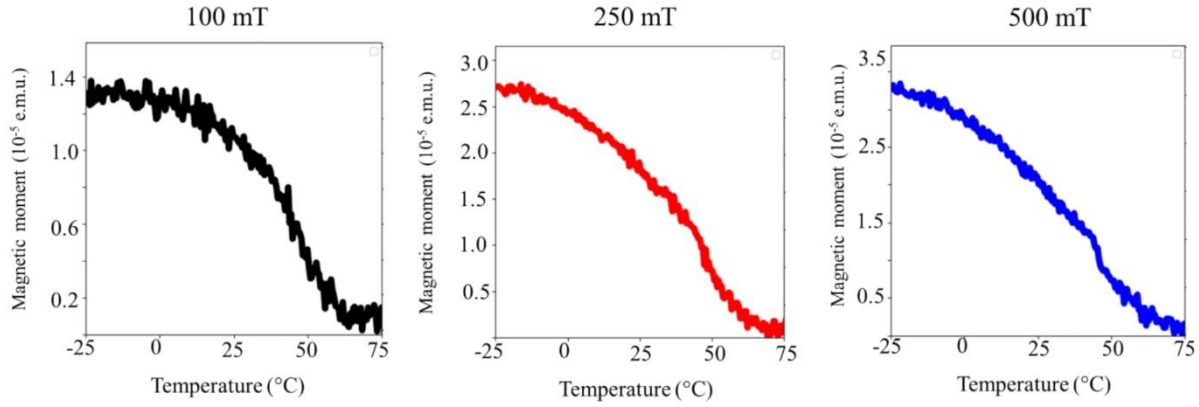


Figure S4: The SQUID response of ferromagnetic LFSC phase in PMN–10PT/LFSC composite films from -25 °C to 75 °C temperature range at different magnetic fields. To emphasize the low-signal ferromagnetic behaviour, non-ferromagnetic contributions from the matrix and substrate were subtracted.

S5. Electrocaloric measurement setup

The electrocaloric measurements were directly obtained using the thermistor-in-calorimeter method. After annealing of the thick films in argon atmosphere, 100-nm-thick Au electrodes were sputtered on the top surface of the samples. The copper wires were glued onto the electrodes with a two-part epoxy-based silver glue. The bead-thermistor was glued near the center of the sample. A schematic representation of the sample after the preparation is shown in Figure S5.

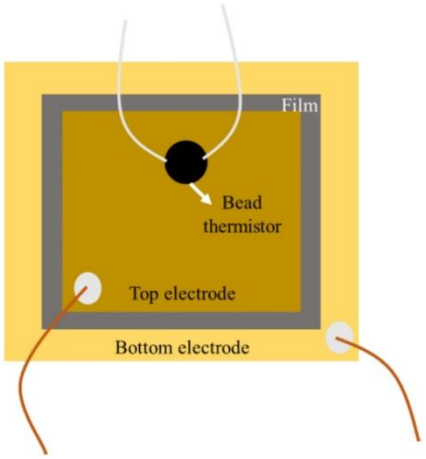


Figure S5: Schematic representation of a sample prepared for the electrocaloric measurement.

Due to the thermalization time of the thermistor (~1 s), the measured ΔT is significantly reduced, in comparison to the intrinsic ΔT_{EC} of the material. To account for this, the geometry of the sample stack and the specific heat capacities of the components of the measurement system need to be considered. The intrinsic ΔT_{EC} can be obtained according to the following equation:

$$\Delta T_{EC} = \frac{\Sigma C_p^{total}}{C_p^{active}} \Delta T = k \Delta T, \qquad (1)$$

Where C_p^{total} is the heat capacity of the entire system (sample, substrate, electrodes, wires and glue), and C_p^{active} is the heat capacity of the films under the top electrode, in other words, the area where the electric field was applied. In this study, the correction factor, k, was ~40. Further details on the measurement setup can be found elsewhere [1].

Albeit the measurements system exhibits excellent thermal stability, to accurately obtain the electrocaloric response corrections must be performed. Figure S6 shows a representative case of a composite sample at room temperature and with an applied electric field of 250 kV cm^{-1}. Notice that the electrocaloric heating and cooling peaks are visible and pronounced, with a small difference between starting and ending points due to temperature drift. To account for this, data from the region after field switch-off is considered and a straight line is extrapolated. By subtracting the linear fit from the data around the electrocaloric temperature change one can obtain the electrocaloric temperature change at cooling. Such value is subsequently multiplied by the

correction factor, detailed above. It is worth mentioning that the switch-off region was considered as the one that most accurately represent the intrinsic ΔT_{EC}.

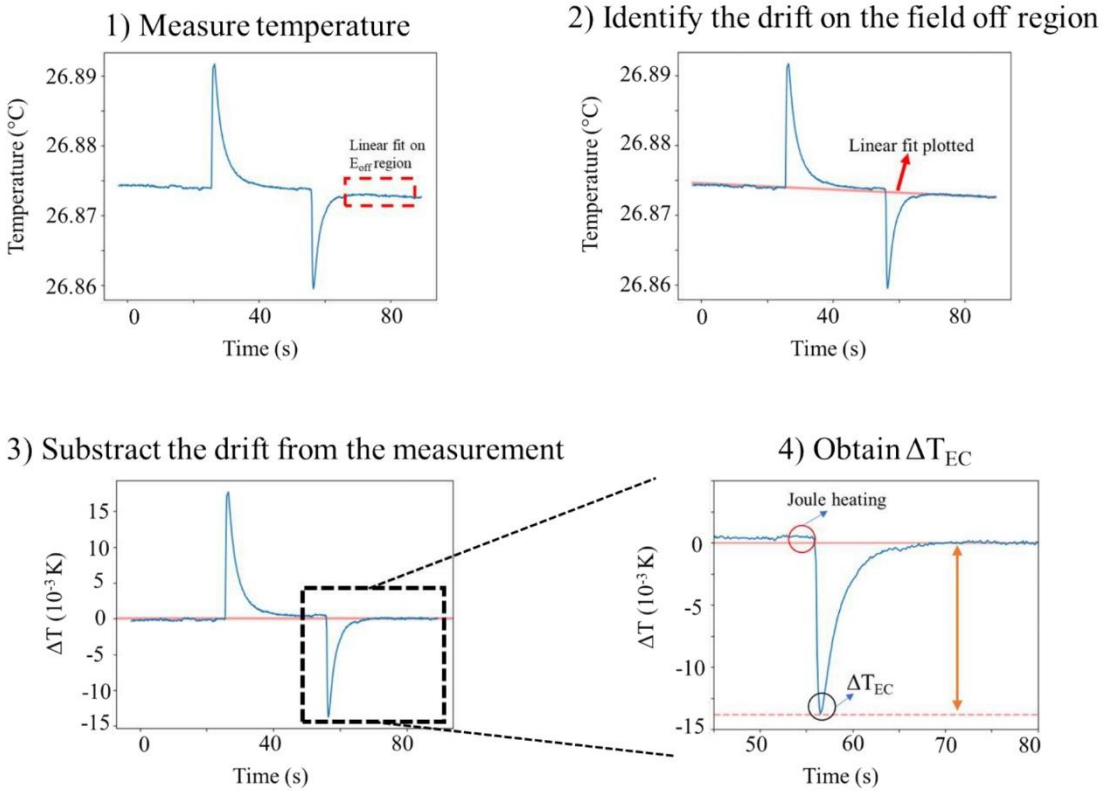


Figure S6: Temperature drift correction of caloric measurements.

S6. Electrocaloric effect on Cu-based composite samples

To better understand the nature of the large enhancement in electrocaloric response in PMN–10PT/LFSC composite films compared to PMN–10PT films, another set of composite samples was prepared, where non-magnetic metal was chosen as a second phase in the composite film. The composites with ~1 wt% of Cu were prepared and annealed under the same conditions as the PMN–10PT/LFSC composite films. In comparison to PMN–10PT films, with ΔT_{EC} ~8.9 mK at 50 kV cm^{-1}, the LFSC and Cu composites exhibited larger ΔT_{EC}, namely ~18.7 mK and ΔT_{EC} ~46.1 mK, respectively. With increasing the electric field to 75 kV cm^{-1}, enhancements of ΔT_{EC} were also observed, as shown in Figure S7. The larger enhancement in Cu composites can be attributed to the two orders of magnitude larger electrical conductivity of Cu than that of LFSC alloys [2], which increases the induced Maxwell-Wagner polarization as explained in the literature [3,4].

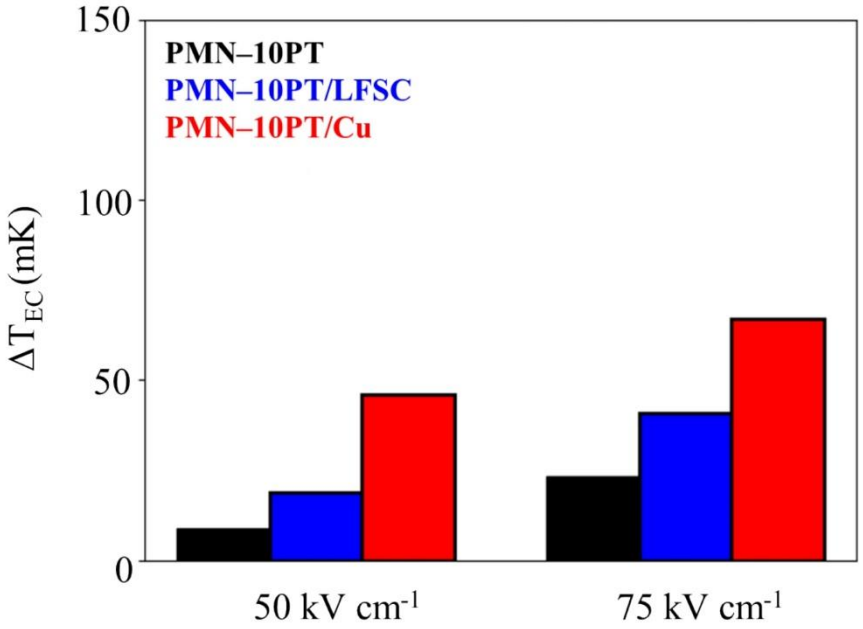


Figure S7: Room temperature electrocaloric response of PMN–10PT film, PMN–10PT/LFSC composite film and PMN–10PT/Cu composite film.

S7. Magnetocaloric measurement setup

The magnetocaloric setup is shown schematically in Figure S8a. The investigated samples were mounted onto a holder by means of a thin thermally insulating polyimide-based tape across an exposed section of the polyimide substrate to fix the sample onto the holder, in this manner ensuring that the surface of interest is perpendicular to the infrared camera while simultaneously preventing heat losses. The magnetic coils were distanced ~10 mm from each other, which resulted in an applied magnetic field of 2 T at the central region of the film.

To obtain accurate infrared measurements, high surface emissivity is required, which was achieved by preparing a black paint coating with thickness of ~2 µm, via an airbrush method [5]. Unlike the thermistor-in-calorimeter method, aside from the sample stack, only the additional paint is necessary and therefore the only external component. In this work, the acquisition rate of the camera was set to 20 Hz. In light of this, to calculate the correction factor for the intrinsic ΔT_{MC}, a two-dimensional heat transfer simulation was performed using COMSOL version 6.2. The iterative simulations were performed as follows:

- Using heat transfer package and having the relevant thermal properties, a heat pulse (P_{MC}) was simulated on the sample. This heat pulse is linearly proportional to the intrinsic temperature change, ΔT_{MC}, as shown in equation 2;

$$P_{MC} = \frac{c_p \rho \Delta T_{MC}}{\tau} = \frac{c_p \rho k \Delta T}{\tau}, \qquad (2)$$

where c_p and ρ are the specific heat capacity and density of the material, k is the correction factor and ΔT is the temperature change at the surface of the black paint, namely the measured temperature change. Due to its larger concentration, the thermal properties used in the simulations were assumed to be those of PMN–10PT. The time interval τ is obtained from the infrared camera parameters. The simulated sample stack is schematically shown in Figure S8b.

- Within a time interval, the heat will propagate through the sample, substrate and black paint;
- From the simulations, one can obtain the temperature change at the surface of the black paint;
- By comparing the simulated ΔT value with the measured ΔT, one can assess the accuracy of the simulations. If the discrepancy is significant, the input ΔT_{MC} on P_{MC} is adjusted and the simulations redone;
- The process is repeated until the simulated ΔT and experimental ΔT are in agreement, and therefore the intrinsic ΔT_{MC} of the material is obtained;

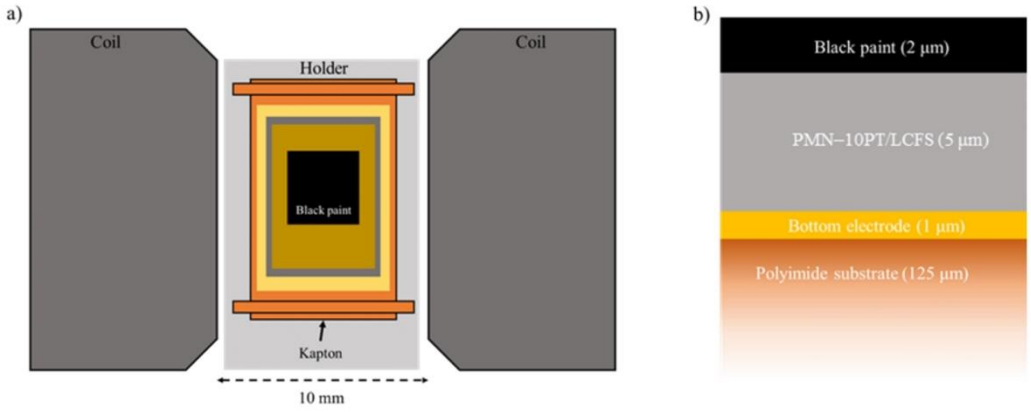


Figure S8: a) Schematic representation of sample and setup for magnetocaloric measurements using an infrared camera and b) Schematic representation of the simulated sample stack.

In this work, the as-measured value on composites was ~0.2 K, originating from the 2 wt% of LFSC MC particles. After considering the heat dissipation to the PMN–10PT matrix and experimental setup, the intrinsic value was corrected to ~1.4 K. This value is lower than the reported value for the bulk material, i.e., $\Delta T_{MC} > 2.5$ K [6], due to the milling and the deposition processes that reduce the crystallite size of the LFSC particles [7].

References

[1] U. Prah, M. Sadl, A. Torello, P. Lheritier, V. Kovacova, H. Ursic, E. Defay, "Direct Electrocaloric Characterization of Ceramic Films," Small Methods, vol. 7, pp. 2300212 1-8, 2023.

[2] R. Huang, Y. Liu, W. Fan, J. Tan, F. Xiao, L. Qian, L. Li, "Giant Negative Thermal Expansion in $NaZn_{13}$ -Type $La(Fe, Si, Co)_{13}$ Compounds," J. Am. Chem. Soc., vol. 135, pp. 11469–11472, 2013.

[3] V. Bobnar, A. Levstik, C. Huang, Q.M. Zhang, "Enhanced dielectric response in all-organic polyaniline–poly(vinylidene fluoride-trifluoroethylene-chlorotrifluoroethylene) composite," J. Non-Cryst. Solids, vol. 353, pp. 205–209, 2007.
[4] P. Lunkenheimer, V. Bobnar, A.V. Pronin, A.I. Ritus, A.A. Volkov, A. Loidl, "Origin of apparent colossal dielectric constants," Phys. Rev. B, vol. 66, pp. 052105 1-4, 2002.
[5] V. Regis, G. Brennecka, U. Tomc, A. Kitanovski, J. Cerar, J. Tušek, I. Jerman, E. Stern-Taulats, K. Lünser, L. Mañosa, H. Uršič, "Airbrushing: A Novel Method for Preparation of High-Emissivity Black Coating for Infrared Measurements," Adv. Mater. Inter., vol. 21, pp. e00494 1-8, 2025.
[6] Vacuumschmelze, Magnetocaloric Materials Calorivac, 2015. vacuumschmelze.com/products/Further-Technologies/Magnetocaloric-Material--CALORIVAC. (Last accessed: 02/02/2026)
[7] J. Exner, M. Hahn, M. Schubert, D. Hanft, P. Fuierer, R. Moos, "Powder requirements for aerosol deposition of alumina films," Adv. Powder Technol., vol. 26, pp. 1143–1151, 2015.

Chapter 6

Summary and Conclusions

In the pursuit for materials with enhanced caloric response, multicaloric materials have received increased attention in recent years. In this thesis, we investigate the preparation and direct characterization of multicaloric PMN–10PT/LFSC composite thick films prepared via the AD method. Although multicaloric materials have been widely studied in the last decades, the literature on the topic is rather limited, and the combination of electrocaloric ceramics with magnetocaloric metals is mostly unaddressed. To establish a starting point, we began our research by investigating the properties of non-caloric ceramic-metal composite films prepared via the AD method. For this, we aerosol-deposited thick films from Al_2O_3 ceramics and Al metallic powders, at different vol % of Al. These materials were chosen as these are low-cost and have been previously successfully prepared via the AD method. In addition, these materials do not exhibit caloric properties, therefore contributing to a better understanding of phenomena inherent to ceramic-metal composites. In agreement with percolation theory, the addition of metallic content results in a non-linear increase in dielectric permittivity, up to 29 vol% of Al where the composite films become electrically conductive. However, at concentrations ≤15 vol% of Al, the permittivity of composite films was also enhanced, and no significant increase in dielectric losses was observed. This investigation supports hypothesis 1 and it indicates that it is possible to achieve enhanced electrical properties even at low concentrations of the metallic phase.

Moreover, since our primary objective is to directly characterize the caloric properties of thick films, it is essential to ensure a maximized response during measurements. In the case of films, the substrate acts as a heat sink, lowering the measured caloric response. However, to which extent remains unaddressed. Within this scope, we have numerically investigated the influence on the thermal properties of the substrate on the measured caloric response of films. Our results show that the substrate material should exhibit an effusivity lower than 3 kW $s^{1/2}$ m^{-2} K^{-1} or a thermal conductivity lower than 1 W m^{-1} K^{-1} to achieve a minimized thermal influence during caloric measurements. These conditions are satisfied by polymers, particularly polyimide, in agreement with hypothesis 2. Thus, polyimide will be used as the substrate for the multicaloric composite films.

Furthermore, for the characterization of caloric properties via the IR camera method, a black paint layer is needed to ensure a high-emissivity surface and accurate measurements. However, most of the literature consists of characterizations of caloric properties of bulk materials, where the thickness of the paint is considered to be negligible. The reports which utilize the technique on films generally only consider case-specific parameters. In light of this, we have numerically investigated the influence of the caloric layer and black paint thicknesses on IR camera measurements. Our results indicate that,

in order to achieve a maximized response, the caloric layer must exhibit a thickness of at least 5 µm, whereas the black paint coating should be thinner than the caloric layer, with a thickness of only a few µm. For this reason, we have developed and optimized the airbrush method, which can prepare black-paint coatings down to ~3 µm, satisfying the aforementioned requirements and supporting hypothesis 3.

With these understandings, we have established the necessary groundwork for the primary goal of the thesis. By joining the electrocaloric PMN–10PT ceramic with 2 wt% of the magnetocaloric LFSC alloy, multicaloric thick films were successfully prepared onto gold-sputtered polyimide substrates via AD. Prior to the deposition, the as-received LFSC powder was further milled, and the MC phase was preserved. The prepared films exhibit a homogeneous distribution of the embedded metallic phase, confirming hypothesis 4. To release the residual stresses from the deposition process, the samples were annealed at 400 °C in argon atmosphere. After the heat treatment, no oxidation of the LFSC phase was observed. In addition, enhancements in the electrical properties were observed in composites, as shown in Table 6.1. When compared to PMN–10PT samples, the composite thick films exhibited larger dielectric permittivity and larger maximum polarization. Furthermore, the room-temperature ΔT_{EC} of composite films exhibited a 32% larger value than PMN–10PT films at 250 kV cm^{-1}. This enhancement is attributed to the embedded metallic particles, contributing with Maxwell-Wagner type polarization effect. Composites also exhibited a room-temperature MC response, with ΔT_{MC} ~1.4 K, after corrections. These results fully confirm hypotheses 5 and 6.

Table 6.1 Comparison between the properties of PMN–10PT and PMN–10PT/LFSC composite thick films.

Property	PMN–10PT	PMN–10PT/LFSC	Relative enhancement
Permittivity (/)	600	700	17 %
Maximum polarization (µC cm^{-2})	30	40	28 %
ΔT_{EC} (K)	0.35	0.45	32 %
ΔT_{MC} (K)	—	1.4	—

As summarized in Table 6.2, we measured both caloric effects via direct methods, whereas the previous literature reports at most one directly characterized caloric response of the multicaloric samples. In addition, this work offers another major contribution to the research of multicalorics: the measurements of the different caloric responses were both performed at near room temperature conditions. In contrast, previous studies had only directly measured one of the caloric responses of multicaloric EC-MC samples, while the other caloric effect was obtained indirectly from data acquired over 200 °C apart.

Table 6.2 Comparison of caloric measurement conditions from the previous literature and from this work.

Material	Multicaloric type	Caloric effect	Method	ΔT_{AD} (K)	Measured at (°C)
PFN-based [43]	Single-phase bulk	EC	Direct	1.1	20
		MC	Indirect	3.6	-268
PT-LPM [50]	Composite bulk	EC	Indirect	2.1	493
		MC	Direct	0.06	60
This work	Composite film	EC	Direct	0.45	27
		MC	Direct	1.4	27

In conclusion, the work elaborated in this thesis demonstrates that, albeit challenging, room-temperature EC-MC composites are possible to prepare, and reveals novel mechanisms for enhanced caloric responses. However, the literature of EC-MC multicaloric composites remains underexplored, and further investigations are still necessary, with our work as a starting point. We expect our work to expand the possibilities for multicaloric materials, and contribute to the research of novel refrigeration technologies for a greener future.

References

[1] A. L. Kholkin, O. V. Pakhomov, A. A. Semenov, and A. Tselev, Eds., The Electrocaloric Effect: Materials and Applications. Cambridge, U.K.: Woodhead Publishing, 2023.

[2] T. Correia and Q. Zhang, Eds., Electrocaloric Materials: New Generation of Coolers, vol. 34, Engineering Materials Series. Berlin, Germany: Springer-Verlag, 2014.

[3] J. Shi, D. Han, Z. Li, L. Yang, S. Lu, Z. Zhong, J. Chen, Q. Zhang, X. Qian, "Electrocaloric Cooling Materials and Devices for Zero-Global-Warming-Potential, High-Efficiency Refrigeration," *Joule*, vol. 3, no. 5, pp. 1200–1225, 2019.

[4] A. Kitanovski, J. Tušek, U. Tomc, U. Plaznik, M. Ožbolt, and A. Poredoš, Magnetocaloric Energy Conversion: From Theory to Applications. in Green Energy and Technology. Cham, Switzerland: Springer International Publishing, 2015.

[5] M. M. Vopson, "Fundamentals of multiferroic materials and their possible applications," *Crit. Rev. Solid State Mater. Sci.*, vol. 40, no. 4, pp. 223–250, 2012.

[6] E. Stern-Taulats, T. Castán, L. Mañosa, A. Planes, N. D. Mathur, and X. Moya, "Multicaloric materials and effects," *MRS Bull.*, vol. 43, no. 4, pp. 295–299, 2018.

[7] H. Hou, S. Qian, and I. Takeuchi, "Materials, physics and systems for multicaloric cooling," *Nat. Rev. Mater.*, vol. 7, no. 8, pp. 633–652, 2022.

[8] H. Ursic V. Bobnar, B. Malic, C. Filipic, M. Vrabelj, S. Drnovsek, Y. Jo, M. Wencka, Z. Kutnjak, "A multicaloric material as a link between electrocaloric and magnetocaloric refrigeration," *Sci. Rep.*, vol. 6, p. 26629, 2016.

[9] A. Chirkova, K. P. Skokov, L. Schultz, N. V. Baranov, O. Gutfleisch, and T. G. Woodcock, "Giant adiabatic temperature change in FeRh alloys evidenced by direct measurements under cyclic conditions," *Acta Mater.*, vol. 106, pp. 15–21, 2016.

[10] E. Bonnot, R. Romero, L. Mañosa, E. Vives, and A. Planes, "Elastocaloric Effect Associated with the Martensitic Transition in Shape-Memory Alloys," *Phys. Rev. Lett.*, vol. 100, no. 12, p. 125901, 2008.

[11] J. Chen, L. Lei, and G. Fang, "Elastocaloric cooling of shape memory alloys: A review," *Mater. Today Commun.*, vol. 28, p. 102706, 2021.

[12] H. Mevada, B. Liu, L. Gao, Y. Hwang, I. Takeuchi, and R. Radermacher, "Elastocaloric cooling: A pathway towards future cooling technology," *Int. J. Refrig.*, vol. 162, pp. 86–98, 2024.

[13] L. Mañosa and A. Planes, "Elastocaloric Effect in Shape-Memory Alloys," *Shap. Mem. Superelasticity*, vol. 10, no. 2, pp. 89–98, 2024.

[14] A. Aravindhan, P. Lheritier, A. Torelló, U. Prah, Y. Nouchokgwe, A. El Moul, X. Chevalier, F. Domingues dos Santos, E. Defay, V. Kovacova., "Direct measurement of electrocaloric effect in P(VDF-TrFE-CFE) film using infrared imaging," *J. Materiomics*, vol. 9, no. 2, pp. 256–260, 2023.

[15] B. Li, Y. Kawakita, S. Ohira-Kawamura, T. Sugahara, H. Wang, J. Wang, Y. Chen, S. Kawaguchi, S. Kawaguchi, K. Li, D. Yu, R. Mole, T. Hattori, T. Kikuchi, S. Yano, Z. Zhang, Z. Zhang, W. Ren, S. Lin, O. Sakata, K. Nakajima, Z. Zhang, "Colossal barocaloric effects in plastic crystals," *Nature*, vol. 567, no. 7749, pp. 506–510, 2019.

[16] K. Lünser, E. Kavak, K. Gurpinar, B. Emre, O. Atakol, E. Stern-Taulats, M. Porta, A. Planes, P. Lloveras, J. Tamarit, L. Mañosa, "Elastocaloric, barocaloric and magnetocaloric effects in spin crossover polymer composite films," *Nat. Commun.*, vol. 15, no. 1, p. 6171, 2024.

[17] P. Lloveras, A. Aznar, M. Barrio, P. Negrier, C. Popescu, A. Planes, L. Mañosa, E. Stern-Taulats, A. Avramenko, N. Mathur, X. Moya, J. Tamarit, "Colossal barocaloric effects near room temperature in plastic crystals of neopentylglycol," *Nat Commun*, vol. 10, no. 1, p. 1803, 2019.

[18] A. Torelló, E. Defay, "Electrocaloric Coolers: A Review," *Adv. Elect. Mater.*, vol. 8, no. 6, p. 2101031, 2022.

[19] J. Wang, R. Ji, J. Xu, Z. Li, Y. Zhang, and L. Li, "Magnetic properties and magnetocaloric effect in Tb_2CoCrO_6 oxide," *J. Magn. Magn. Mater.*, vol. 619, p. 172897, 2025.

[20] M. Zeng, M. Romanini, I. Gorican, S. Drnovsek, H. Ursic, A. Salvatori, M. Barrio, S. Loehle, N. Obrecht, C. Escorihuela-Sayalero, C. Cazorla, A. Torelló, P. Lloveras, J. Tamarit, "Simultaneous shifts in pressure and electric field boost the caloric response in ferroelectrics," *Mater. Horiz.*, vol. 12, no. 20, pp. 8460–8471, 2025.

[21] T. M. Correia, S. Kar-Narayan, J. Young, J. Scott, N. Mathur, R. Whatmore, Q. Zhang, "PST thin films for electrocaloric coolers," *J. Phys. D: Appl. Phys.*, vol. 44, no. 16, p. 165407, 2011.

[22] J. Li, A. Torelló, V. Kovacova, U. Prah, A. Aravindhan, T. Granzow, T. Usui, S. Hirose, E. Defay, "High cooling performance in a double-loop electrocaloric heat pump," *Science*, vol. 382, no. 6672, pp. 801–805, 2023.

[23] U. Prah M. Sadl, A. Torelló, P. Lheritier, V. Kovacova H, Ursic, E. Defay, "Direct Electrocaloric Characterization of Ceramic Films," *Small Methods*, vol. 7, no. 9, 2023.

[24] D. Damjanovic, "Ferroelectric, dielectric and piezoelectric properties of ferroelectric thin films and ceramics," Rep. Prog. Phys., vol. 61, no. 9, pp. 1267–1324, 1998.

[25] M. S. Dresselhaus, G. Dresselhaus, and A. Jorio, Group Theory: Application to the Physics of Condensed Matter. Berlin, Germany: Springer-Verlag, 2008.

[26] R. Pirc, R. Blinc, and V. Bobnar, "Dynamics of relaxor ferroelectrics," *Phys. Rev. B*, vol. 63, no. 5, p. 054203, 2001.

[27] L. Cross, "Relaxor Ferroelectrics," *Ferroelectrics*, vol. 76, no. 1, pp. 241–267, 1987.

[28] A. Peláiz-Barranco, Ed., Advances in Ferroelectrics. London,UK: InTech, 2012.

[29] M. Vrabelj, H. Ursic, Z. Kutnjak, B. Rozic, S. Drnovsek, A. Bencan, V. Bobnar, L. Fulanovic, B. Malic, "Large electrocaloric effect in grain-size-engineered $0.9Pb(Mg_{1/3}Nb_{2/3})O_3$–$0.1PbTiO_3$," *J. Eur. Ceram. Soc.*, vol. 36, no. 1, pp. 75–80, 2016.

[30] A. Sarkar, M. Sadl, A. Jazbec, L. Snoj, S. Drovsek, T. Rojac, G. Brennecka, H. Ursic, B. Malic, "Influence of neutron and gamma irradiation on the electrocaloric properties of Mn-doped $0.9Pb(Mg_{1/3}\ Nb_{2/3}\ )O_3$ –$0.1PbTiO_3$ ceramics," *J. Phys. Energy*, vol. 5, no. 4, p. 045006, 2023.

[31] M. Dragomir, M. Otonicar, M. Vrabelj, L. Fulanovic, S. Drnovsek, T. Rojac, B. Malic,"Seeding effects on the mechanochemical synthesis of $0.9Pb(Mg_{1/3}Nb_{2/3})O_3$–$0.1PbTiO_3$," *J. Eur. Ceram. Soc.*, vol. 39, no. 5, pp. 1837–1845, May 2019.

[32] R. E. Newnham, Properties of Materials: Anisotropy, Symmetry, Structure. Oxford, U.K.: Oxford University Press, 2004.

[33] Q. Badosa, L. Mañosa, E. Vives, A. Planes, B. Weise, L. Beyer, E. Stern-Taulats, "Demagnetizing field-induced magnetocaloric effect in Gd," *J. Appl. Phys.*, vol. 134, no. 11, p. 113902, 2023.

[34] S. Yu. Dan'kov, A. M. Tishin, V. K. Pecharsky, and K. A. Gschneidner, "Magnetic phase transitions and the magnetothermal properties of gadolinium," *Phys. Rev. B*, vol. 57, no. 6, pp. 3478–3490, 1998.

[35] M. G. Zavareh, Y. Skourski, K. P. Skokov, D. Karpenkov, L. Zvyagina, A. Waske, D. Haskel, M. Zhernenkov, J. Wosnitza, O. Gutfleisch, "Direct Measurement of the Magnetocaloric Effect in $La(Fe,Si,Co)_{13}$ Compounds in Pulsed Magnetic Fields," *Phys. Rev. Appl.*, vol. 8, no. 1, p. 014037, 2017.

[36] K. Löwe, J. Liu, K. Skokov, J. Moore, H. Sepehri-Amin, K. Hono, M. Katter, O. Gutfleisch., "The effect of the thermal decomposition reaction on the mechanical and magnetocaloric properties of $La(Fe,Si,Co)_{13}$," *Acta Mater.*, vol. 60, no. 10, pp. 4268–4276, 2012.

[37] J. M. Lommel and J. S. Kouvel, "Effects of Mechanical and Thermal Treatment on the Structure and Magnetic Transitions in FeRh," *J. Appl. Phys.*, vol. 38, no. 3, pp. 1263–1264, 1967.

[38] L. H. Lewis, C. H. Marrows, and S. Langridge, "Coupled magnetic, structural, and electronic phase transitions in FeRh," *J. Phys. D: Appl. Phys.*, vol. 49, no. 32, p. 323002, 2016.

[39] A. Planes, T. Castán, and A. Saxena, "Thermodynamics of multicaloric effects in multiferroics," *Philos. Mag.*, vol. 94, no. 17, pp. 1893–1908, 2014.

[40] A. Planes, L. Mañosa, and M. Acet, "Magnetocaloric effect and its relation to shape-memory properties in ferromagnetic Heusler alloys," *J. Phys.: Condens. Matter*, vol. 21, no. 23, p. 233201, 2009.

[41] E. Vives, S. Burrows, R. Edwards, S. Dixon, L. Mañosa, A. Planes, R. Romero, "Temperature contour maps at the strain-induced martensitic transition of a Cu–Zn–Al shape-memory single crystal," *Appl. Phys. Lett.*, vol. 98, no. 1, p. 011902, 2011.

[42] A. Amirov and D. Samsonov, "Demonstration of the multicaloric effect in a laboratory prototype," *J. Appl. Phys.*, vol. 136, no. 5, p. 053902, 2024.

[43] U. Prah, M. Wencka, T. Rojac, A. Benčan, and H. Uršič, "$Pb(Fe_{0.5}\ Nb_{0.5}\ )O_3$ –$BiFeO_3$ -based multicalorics with room-temperature ferroic anomalies," *J. Mater. Chem. C*, vol. 8, no. 32, pp. 11282–11291, 2020.

[44] N. A. Hill, "Why are there so few magnetic ferroelectrics?," *J. Phys. Chem. B*, vol. 104, no. 29, pp. 6694–6709, 2000.

[45] Y. Hadouch, D. Mezzane, M. Amjoud, H. Ursic, A. Lahmar, B. Rozic, I. Lukyanchuk, Z. Kutnjak, M. El Marssi, "Current advances in magnetoelectric composites with various interphase connectivity types," *Sustainable Energy Fuels*, vol. 9, no. 8, pp. 1957–1992, 2025.

[46] Y. Liu, L. C. Phillips, R. Mattana, M. Bibes, A. Barthélémy, and B. Dkhil, "Large reversible caloric effect in FeRh thin films via a dual-stimulus multicaloric cycle," *Nat. Commun.*, vol. 7, 2016.

[47] Z. Yu and C. Ang, "Maxwell–Wagner polarization in ceramic composites $BaTiO_3$–$(Ni_{0.3}Zn_{0.7})Fe_{2.1}O_4$," *J. Appl. Phys.*, vol. 91, no. 2, pp. 794–797, 2002.

[48] D. Damjanovic, M. Demartin Maeder, P. Duran Martin, C. Voisard, and N. Setter, "Maxwell–Wagner piezoelectric relaxation in ferroelectric heterostructures," *J. Appl. Phys.*, vol. 90, no. 11, pp. 5708–5712, 2001.

[49] V. Bobnar, M. Hrovat, J. Holc, and M. Kosec, "All-ceramic lead-free percolative composite with a colossal dielectric response," *J. Eur. Ceram. Soc.*, vol. 29, no. 4, pp. 725–729, 2009.

[50] E. Mikhaleva, I. Flerov, A. Kartashev, M. Gorev, A. Chrepakhin, K. Sablina, N. Mikhashenok, N. Volkov, A. Shabanov, "Caloric effects and phase transitions in ferromagnetic-ferroelectric composites $xLa_{0.7}Pb_{0.3}MnO_3$–$(1\text{-}x)PbTiO_3$," *J. Mater. Res.*, vol. 28, no. 24, pp. 3322–3331, 2013.

[51] D. Hanft, J. Exner, M. Schubert, T. Stöcker, P. Fuierer, and R. Moos, "An overview of the Aerosol Deposition method: Process fundamentals and new trends in materials applications," *J. Ceram. Sci. Technol.*, vol. 6, no. 3, pp. 147–181, 2015.

[52] J. Akedo, "Aerosol deposition of ceramic thick films at room temperature: Densification mechanism of ceramic layers," presented at the *J. Am. Ceram. Soc.*, pp. 1834–1839, 2006.

[53] M. Sadl, U. Tomc, U. Prah, and H. Ursic, "Protective alumina coatings prepared by aerosol deposition on magnetocaloric gadolinium elements," *Informacije MIDEM*, vol. 49, no. 3, pp. 177–182, 2019.

[54] M. K. Kumar, Z. Yang, M. Jadidi, T. W. Coyle, and A. Dolatabadi, "Numerical simulation and experimental analysis of aerosol deposition: Investigating nozzle effects on particle dynamics and deposition," *J. Aerosol Sci.*, vol. 183, p. 106488, 2025.

[55] A. Zabihi Yeganeh, M. Jadidi, C. Moreau, and A. Dolatabadi, "Numerical modeling of aerosol deposition process," *Surf. Coat. Technol.*, vol. 370, pp. 269–287, 2019.

[56] M. Sadl, O. Condurache, A. Bencan, M. Dragomir, U. Prah, B. Malic, M. Deluca, U. Eckstein, D. Hausmann, N. Khansur, K. Webber, H. Ursic, "Energy-storage-efficient $0.9Pb(Mg_{1/3}Nb_{2/3})O_3$–$0.1PbTiO_3$ thick films integrated directly onto stainless steel," *Acta Mater.*, vol. 221, p. 117403, 2021.

[57] J. Exner, M. Hahn, M. Schubert, D. Hanft, P. Fuierer, and R. Moos, "Powder requirements for aerosol deposition of alumina films," *Adv. Powder Technol.*, vol. 26, no. 4, pp. 1143–1151, 2015.

[58] V. Regis, M. Šadl, G. Brennecka, A. Bradeško, U. Tomc, and H. Uršič, "Investigation of Structural and Electrical Properties of Al_2O_3/Al Composites Prepared by Aerosol Co-Deposition," *Crystals*, vol. 13, no. 5, p. 850, 2023.

[59] N. H. Khansur, U. Eckstein, K. Riess, A. Martin, J. Drnec, U. Deisinger, K. Webber, "Synchrotron x-ray microdiffraction study of residual stresses in $BaTiO_3$ films deposited at room temperature by aerosol deposition," *Scr. Mater.*, vol. 157, pp. 86–89, 2018.

[60] M. Schubert, J. Exner, and R. Moos, "Influence of Carrier Gas Composition on the Stress of Al_2O_3 Coatings Prepared by the Aerosol Deposition Method," *Materials*, vol. 7, no. 8, pp. 5633–5642, 2014.

[61] S. Merselmiz, I. Gorican, T. Rojac, V. Bobnar, V. Regis, M. Sadl, V. Fisinger, N. Suban, B. Kmet, A. Bencan, A. Bradesko, A. Debevec, B. Malic, H. Ursic, "Capacitive energy-storage and electromechanical properties of aerosol-deposited $0.5BaZr_{0.2}Ti_{0.8}O_3$–$0.5Ba_{0.7}Ca_{0.3}TiO_3$ films," *Acta Mater.*, vol. 304, p. 121749, 2026.

[62] U. Eckstein, J. Exner, A. Bencan, K. Ziberna, G. Drazic, H. Ursic, H. Wittkamper, C. Papp, J. Kita, R. Moos, K. Webber, N. Khansur, "Temperature-dependent dielectric anomalies in powder aerosol deposited ferroelectric ceramic films," *J. Materiomics*, vol. 8, no. 6, pp. 1239–1250, 2022.

[63] A. Chrir, O. Rojas, L. Boyer, O. Durand-Panteix, and P. Marchet, "Effect of post-annealing on microstructure and electrical properties of $BaTiO_3$ thick films grown by aerosol deposition (AD)," *J. Eur. Ceram. Soc.*, vol. 44, no. 6, pp. 3965–3984, 2024.

[64] G. Han, J. Ryu, W. Yoon, J. Choi, B. Hahn, and D. Park, "Effect of Film Thickness on the Piezoelectric Properties of Lead Zirconate Titanate Thick Films Fabricated by Aerosol Deposition," *J. Am. Ceram. Soc.*, vol. 94, no. 5, pp. 1509–1513, 2011.

[65] J. Akedo and M. Lebedev, "Microstructure and Electrical Properties of Lead Zirconate Titanate ($Pb(Zr_{52}/Ti_{48})O_3$) Thick Films Deposited by Aerosol Deposition Method," *Jpn. J. Appl. Phys.*, vol. 38, no. 9S, p. 5397, 1999.

[66] Y.-H. Kim, J.-W. Lee, H.-J. Kim, Y.-H. Yun, and S.-M. Nam, "Silver metallization for microwave device using aerosol deposition," *Ceram. Int.,* vol. 38, pp. S201–S204, 2012.

[67] H.-J. Kim and S.-M. Nam, "Powder preparation in aerosol deposition for Al_2O_3-polyimide composite thick films," *Electron. Mater. Lett.*, vol. 8, no. 1, pp. 65–70, 2012.

[68] O.-Y. Kwon, H.-J. Na, H.-J. Kim, D.-W. Lee, and S.-M. Nam, "Effects of mechanical properties of polymer on ceramic-polymer composite thick films fabricated by aerosol deposition," *Nanoscale Res. Lett.*, vol. 7, no. 1, p. 261, 2012.

[69] Z. Kutnjak, B. Rožič, and R. Pirc, "Electrocaloric effect: Theory, measurements, and applications," in Wiley Encyclopedia of Electrical and Electronics Engineering, 1st ed., J. G. Webster, Ed. Hoboken, New Jersey, USA: Wiley, 2015.

[70] Y. Liu, J. F. Scott, and B. Dkhil, "Direct and indirect measurements on electrocaloric effect: Recent developments and perspectives," *Appl. Phys. Rev.*, vol. 3, no. 3, p. 031102, 2016.

[71] M. Sadl, U. Prah, V. Kovacova, E. Defay, T. Rojac, A. Lebar, J. Valenticic, H. Ursic, "Multifunctional flexible ferroelectric thick-film structures with energy storage, piezoelectric and electrocaloric performance," *J. Mater. Chem. C*, vol. 11, no. 29, pp. 10058–10068, 2023.

[72] K. Engelbrecht, J. Tusek, D. Eriksen, T. Lei, C. Lee, J. Tusek, N. Pryds, "A regenerative elastocaloric device: experimental results," *J. Phys. D: Appl. Phys.*, vol. 50, no. 42, p. 424006, 2017.

[73] L. Ianniciello, M. Romanini, L. Mañosa, A. Planes, K. Engelbrecht, and E. Vives, "Tracking the dynamics of power sources and sinks during the martensitic

transformation of a Cu–Al–Ni single crystal," *Appl. Phys. Lett.*, vol. 116, no. 18, p. 183901, 2020.

[74] M. J. Pereira, T. Santos, R. Correia, J. Amaral, V. Amaral, S. Fabbrici, F. Albertini, "Mapping the magnetocaloric effect at the microscale on a ferromagnetic shape memory alloy with infrared thermography," *J. Phys. Mater.*, vol. 6, no. 2, p. 024002, 2023.

[75] K. Wang, Y. Ouyang, Y. Shen, Y. Zhang, M. Zhang, and J. Liu, "High-throughput characterization of the adiabatic temperature change for magnetocaloric materials," *J. Mater. Sci.*, vol. 56, no. 3, pp. 2332–2340, 2021.

[76] H. Ossmer, F. Lambrecht, M. Gültig, C. Chluba, E. Quandt, and M. Kohl, "Evolution of temperature profiles in TiNi films for elastocaloric cooling," *Acta Mater.*, vol. 81, pp. 9–20, 2014.

[77] T. Hirai, R. Iguchi, A. Miura, and K. Uchida, "Elastocaloric Kirigami Temperature Modulator," *Adv. Funct. Mater.*, vol. 32, no. 28, p. 2201116, 2022.

[78] M. A. S. Arikan and T. Balkan, "Process Simulation and Paint Thickness Measurement for Robotic Spray Painting," *CIRP Annals*, vol. 50, no. 1, pp. 291–294, 2001.

[79] S. Krimi, J. Klier, J. Jonuscheit, G. Von Freymann, R. Urbansky, and R. Beigang, "Highly accurate thickness measurement of multi-layered automotive paints using terahertz technology," *Appl. Phys. Lett.*, vol. 109, no. 2, p. 021105, 2016.

[80] J. Lim, Y. Kim, J. Akedo, H. K. Yu, J.-Y. Choi, and J.-H. Park, "Fabrication of PZT-Au composite films via Aerosol Deposition for real-time tunable optical modulators," *Opt. Mater.*, vol. 164, p. 117041, 2025.

Bibliography

Scientific articles related to the thesis

V. Regis de Moraes, M. Šadl, G. Brennecka, A. Bradeško, U. Tomc, H. Uršič Nemevšek, "Investigation of structural and electrical properties of Al_2O_3/Al composites prepared by aerosol co-deposition," *Crystals*, vol. 13, p. 850, 2023.

V. Regis de Moraes, G. Brennecka, U. Tomc, A. Kitanovski, J. Cerar, J. Tušek, I. Jerman, E. Stern-Taulats, K. Lünser, L. Mañosa, H. Uršič Nemevšek, "Airbrushing: a novel method for preparation of high-emissivity black coating for infrared measurement," *Adv. Mater. Interfaces*, vol. 12, no. 21, p. e00467, 2025.

V. Regis de Moraes, U. Tomc, A. Kitanovski, H. Uršič Nemevšek, "Roadmap for electrocaloric characterization," *iScience*, vol. 29, p. 115965, 2026.

V. Regis de Moraes, I. Goričan, M. Šadl, A. Benčan, G. Dražić, S. Gyergyek, U. Tomc, A. Kitanovski, L. Beyer, E. Stern-Taulats, K. Lünser, L. Mañosa, H. Uršič, "Direct observation of room-temperature electrocaloric and magnetocaloric responses in multicaloric composite films," *J. Eur. Ceram. Soc.*, vol. 46, p. 118584, 2026.

Other scientific articles

B. Velkavrh, U. Tomc, M. Šadl, V. Regis de Moraes, M. Koblar, B. Colarič, A. Kitanovski, H. Uršič Nemevšek, "Preparation of dielectric layers for applications in digital microfluidic thermal switches," Informacije MIDEM, vol. 54, no. 3, p. 215-223, 2024.

S. Merselmiz, Ivana Goričan, T. Rojac, V. Bobnar, V. Regis de Moraes, M. Šadl, V. Fišinger, N. Suban, B. Kmet, A. Benčan, A. Bradeško, A. Debevec, B. Malič, H. Uršič Nemevšek, "Capacitive energy-storage and electromechanical properties of aerosol-deposited $0.5BaZr_{0.2}Ti_{0.8}O_3$–$0.5Ba_{0.7}Ca_{0.3}TiO_3$ films," *Acta materialia*, vol. 304, no. 121749, p. 1-12, 2026.

A. Lakouader, V. Jurečič, Š. Kunej, D. Mezzane, H. Uršič Nemevšek, V. Regis de Moraes, N. Suban, A. Matavž, Z. Kutnjak, M. El Marssi, et al., "Thermally stable electrostatic energy storage in X9R-type $BaTiO_3$-based thin films elaborated by chemical solution deposition", J. Energy Storage, vol. 141, no. 119421, p. 1-13, 2026.

Published Scientific Conference Contributions – Abstracts (Invited Lecture)

H. Uršič Nemevšek, M. Šadl, I. Goričan, V. Regis de Moraes, "$Pb(Mg_{1/3}Nb_{2/3})O_3$-based thick-film elements prepared by the aerosol deposition method", in *ECAPD 2024: European Conference on Applications of Polar Dielectrics*, Trondheim, Norway, 2024.

H. Uršič Nemevšek, M. Šadl, V. Regis de Moraes, "Aerosol deposition of functional thick films on metal and polymer substrates", in *International Conference on Advanced Functional Materials and Devices (AFMD-2024)*,Tamil Nadu, India, 2024.

Published Scientific Conference Contributions – Abstracts

V. Regis de Moraes, M. Šadl, H. Uršič Nemevšek, "Preparation of multicaloric composites by aerosol deposition method", in *2022 UFFC Ferroelectrics School:* Lyon, France, 2022.

V. Regis de Moraes, M. Šadl, H. Uršič Nemevšek, "Aerosol-deposited multicaloric composites", in *57th International Conference on Microelectronics, Devices and Materials & The Workshop on Energy Harvesting: Materials and Applications: conference 2022*: Maribor, Slovenia, 2022.

V. Regis de Moraes, M. Šadl, H. Uršič Nemevšek, et al., "Preparation of multicaloric composites using aerosol deposition method", in *ISAF 2022: ISAF-PFM-ECAPD joint conference*, Tours, France: Institute of Electrical and Electronics Engineers (IEEE), 2022.

V. Regis de Moraes, M. Šadl, G. Brennecka, A. Bradeško, U. Tomc, H. Uršič Nemevšek, "Preparation of Al_2O_3/Al composite thick films via aerosol deposition", in *15th Jožef Stefan International Postgraduate School Students' Conference*, Kamnik, Slovenia 2023.

B. Velkavrh, U. Tomc, V. Regis de Moraes, M. Šadl, A. Kitanovski, H. Uršič Nemevšek, "Preparation of dielectric thick films for use in fluidic thermal switches", in *15th Jožef Stefan International Postgraduate School Students' Conference*, Kamnik, Slovenia 2023.

U. Tomc, H. Uršič Nemevšek, V. Regis de Moraes, B. Velkavrh, L. Mañosa, J. Freudenberger, Bruno Weise, A. Kitanovski, "Digital microfluidic thermal switch in magnetocaloric cooling", in *2023 MRS Spring Meeting & Exhibition*, San Francisco, California USA, 2023.

S. Merselmiz, V. Regis de Moraes, M. Šadl, B. Malič, A. Debevec, S. Drnovšek, H. Uršič Nemevšek, "Lead-free $Ba(Zr,Ti)O_3$–$(Ba,Ca)TiO_3$ thick films prepared by aerosol deposition and screen-printing techniques", in *58th International Conference on Microelectronics, Devices and Materials & The Workshop on Chemical sensors: Materials and Applications*, Lipica, Slovenia, 2023.

B. Velkavrh, U. Tomc, V. Regis de Moraes, M. Šadl, A. Kitanovski, H. Uršič Nemevšek, "Preparation of dielectric thick films for fluidic thermal switches in magnetocaloric cooling device", in *58th International Conference on Microelectronics, Devices and Materials & The Workshop on Chemical sensors: Materials and Applications*, Lipica, Slovenia, 2023.

V. Regis de Moraes, M. Šadl, A. Benčan, G. Dražić, H. Uršič Nemevšek, "Preparation of lead magnesium niobate-based multicaloric composites using the aerosol deposition method", in *Conference and exibition of the European Ceramic Society: When ceramists meet in the city of lights : 18th ECERS*, Lyon, France, 2023

B. Velkavrh, U. Tomc, V. Regis de Moraes, M. Šadl, B. Colarič, A. Kitanovski, H. Uršič Nemevšek, "Dielectric thick films for fluidic thermal switches in magnetocaloric cooling device", in *Dresden Days on Magnetocalorics 2023*, Helmholtz-Zentrum Dresden-Rossendorf, Dresden, Germany, 2023

B. Velkavrh, U. Tomc, V. Regis de Moraes, M. Šadl, B. Colarič, A. Kitanovski, H. Uršič Nemevšek, "Dielectric thick films for use in fluidic thermal switches", in *E-MRS 2023 Fall Meeting*, Warsaw, Poland, 2023.

H. Uršič Nemevšek, M. Šadl, U. Prah, V. Regis de Moraes, A. Sarkar, T. Rojac, A. Jazbec, L. Snoj, M. Otoničar, B. Malič, "0.9Pb($Mg_{1/3}Nb_{2/3}$)O_3–0.1$PbTiO_3$ for various cooling applications", in *EMA 2023: Basic Science and Electronic Materials Meeting*, Florida, USA, 2023.

B. Velkavrh, U. Tomc, M. Šadl, V. Regis de Moraes, U. Erjavec Nagode, B. Colarič, A. Kitanovski, H. Uršič Nemevšek, "Dielectric thick films for use in digital microfluidic thermal switches", in *16th Jožef Stefan International Postgraduate School Students' Conference*, Piran, Slovenia, 2024.

V. Regis de Moraes, M. Šadl, I. Goričan, A. Benčan, G. Dražić, U. Tomc, A. Kitanovski, H. Uršič Nemevšek, et al., "Lead magnesium niobate-based multicaloric thick-film composites", in *16th Jožef Stefan International Postgraduate School Students' Conference*, Piran, Slovenia, 2024.

V. Regis de Moraes, M. Šadl, I. Goričan, A. Benčan, G. Dražić, S. Gyergyek, J. Cerar, J. Tušek, U. Tomc, A. Kitanovski, H. Uršič Nemevšek, et al., "Characterization of multicaloric composites prepared via the aerosol deposition method", in *59th International Conference on Microelectronics, Devices and Materials & Workshop on Electromagnetic Compatibility: From Theory to Practice*, Rimske Toplice, Slovenia, 2024.

B. Velkavrh, U. Tomc, M. Šadl, V. Regis de Moraes, M. Koblar, U. Erjavec Nagode, B. Colarič, A. Kitanovski, H. Uršič Nemevšek, "Preparation of multilayer structures for digital microfluidic thermal switches", in *59th International Conference on Microelectronics, Devices and Materials & Workshop on Electromagnetic Compatibility: From Theory to Practice*, Rimske Toplice, Slovenia, 2024.

S. Merselmiz, V. Regis de Moraes, M. Šadl, B. Malič, A. Debevec, S. Drnovšek, T. Rojac, H. Uršič Nemevšek, "Lead-free Ba(Zr,Ti)O_3–(Ba,Ca)TiO_3 thick films prepared by aerosol deposition", in *ECAPD 2024 : European Conference on Applications of Polar Dielectrics*, Trondheim, Norway, 2024.

H. Uršič Nemevšek, V. Regis de Moraes, "Preparation of functional composite films using the aerosol deposition method", in *EMA 2024: Basic Science and Electronics Division Meeting*, Denver, Colorado, USA.

B. Velkavrh, H. Uršič Nemevšek, V. Regis de Moraes, M. Šadl, B. Colarič, A. Kitanovski, U. Tomc, "Fabrication of microfluidic thermal switches for magnetocaloric cooling applications", in *Eurotherm 2024: 9th European Thermal Sciences Conference*, Bled, Slovenia, 2024.

V. Regis de Moraes, M. Šadl, A. Benčan, G. Dražić, Sašo Gyergyek, J. Cerar, J. Tušek, U. Tomc, A. Kitanovski, H. Uršič Nemevšek, et al., "Multicaloric composites prepared via the powder aerosol deposition method", in *FerroSchool 2024: Jožef Stefan Institute*, Ljubljana, Slovenia, 2024.

S. Merselmiz, I. Goričan, V. Regis de Moraes, B. Kmet, A. Benčan, T. Rojac, A. Debevec, B. Malič, H. Uršič Nemevšek, "Piezoelectric and energy-storage properties of 0.5$BaZr_{0.2}Ti_{0.8}O_3$–0.5$Ba_{0.7}Ca_{0.3}TiO_3$ films prepared by the aerosol deposition", in *2025 Conference on Electronic Materials and Applications*, Denver, Colorado, 2025.

M. D'Angelo, V. Regis de Moraes, I. Goričan, S. Drnovšek, H. Uršič Nemevšek, "Powder aerosol deposition of Pb($Sc_{0.5}Ta_{0.5}$)O_3 thick films", in *60th International Conference on Microelectronics, Devices and Materials & The Workshop on Energy Management and Renewable Energy Sources*, Ljubljana, Slovenia, 2025.

B. Velkavrh, U. Tomc, M. Šadl, V. Regis de Moraes, M. Koblar, Urška Erjavec Nagode, B. Colarič, A. Kitanovski, H. Uršič Nemevšek, "Fabrication of digital microfluidic thermal switches for caloric cooling applications", in *IEEE ISAF 2025: 2025 IEEE International Symposium on Applications of Ferroelectrics*, Graz, Austria, 2025.

I. Goričan, S. Merselmiz, V. Regis de Moraes, M. Šadl, V. Fišinger, B. Kmet, A. Benčan, T. Rojac, Vid Bobnar, A. Debevec, B. Malič, H. Uršič Nemevšek, "Functional properties of $0.5BaZr_{0.2}Ti_{0.8}O_3$–$0.5Ba_{0.7}Ca_{0.3}TiO_3$ thick films prepared by aerosol deposition", in *IEEE ISAF 2025: 2025 IEEE International Symposium on Applications of Ferroelectrics*, Graz, Austria, 2025.

V. Regis de Moraes, M. Šadl, I. Goričan, A. Benčan, G. Dražić, S. Gyergyek, H. Uršič Nemevšek, et al., "Room-temperature multicaloric composite thick films prepared via the powder aerosol deposition method", in *IEEE ISAF 2025: 2025 IEEE International Symposium on Applications of Ferroelectrics*, Graz, Austria, 2025.

M. Lachhab, V. Regis de Moraes, Vinko Sršan, M. Vallet, C. Paillard, A. Benčan, G. Dražić, M. Otoničar, "Studying perovskites at the atomic scale by 4DSTEM", in *2026 Workshop on the Fundamental Physics of Ferroelectrics and Related Materials: The 37th Annual Workshop: Fundamental Physics of Ferroelectrics*, Tours, France, 2026.

H. Uršič Nemevšek, M. D'Angelo, V. Regis de Moraes, I. Goričan, "Aerosol deposition of functional $Pb(Mg_{1/3}Nb_{2/3})O_3$–$PbTiO_3$ and $PbSc_{0.5}Ta_{0.5}O_3$ films", in *The American Ceramic Society: Spring Meeting 2026*, Bellevue, Washington, USA, 2026.

Unpublished Scientific Conference Contributions

V. Regis de Moraes, "Aerosol-deposited composite films," in *Japan-Slovenia Workshop on Piezoelectric thin films*, Online event, 2022.

H. Uršič Nemevšek, M. Šadl, V. Regis de Moraes, I. Goričan, U. Prah, E. Defay, A. Lebar, J. Valentinčič, "Energy storage and caloric ceramic thick films on flexible polymer substrates," *IEEE 2023 ISAF-ISIF-PFM Joint Conference (Hybrid Format)*, 2023.

B. Velkavrh, H. Uršič Nemevšek, U. Tomc, V. Regis de Moraes, "Fluidic thermal switches based on electrowetting effects," *in Cool Batman Meeting*, Barcelona, Spain, 2023.

V. Regis de Moraes, M. Šadl, G. Brennecka, A. Bradeško, U. Tomc, H. Uršič Nemevšek, "Investigation of structural and electrical properties of Al_2O_3/Al composites prepared by aerosol co-deposition," in *Cool Batman Meeting*, Online event, 2023.

B. Velkavrh, U. Tomc, V. Regis de Moraes, M. Šadl, B. Colarič, A. Kitanovski, H. Uršič Nemevšek, "Processing of dielectric thick films for use in fluidic thermal switches," Ankaran Meeting, Ankaran, Slovenia, 2023.

Biography

I was born on 12th of September 1996, in Rio de Janeiro, Brazil. After finishing high school, I started my BSc in Physics at the Federal University of Rio de Janeiro (UFRJ) where I focused on condensed matter physics, and graduated in 2019. For my master, I continued my studies in the same institution, now doing computational physics in the topic of non-crystalline topological insulators.

In 2021, looking to become a more hands-on researcher with stronger experimental skills, I enrolled in the Sensors Technologies PhD programme at the Jožef Stefan International Postgraduate School and took up the position of Young researcher in the Electronic Ceramics Department under the supervision of Prof. Dr. Hana Uršič. My research focuses on the preparation and characterization of multicaloric composites prepared via the powder aerosol deposition method, targeting alternative room-temperature cooling technologies.

During my PhD, I was awarded an Erasmus+ grant for a 3-month mobility to the University of Barcelona, in 2023, where I performed a crucial experiment relevant to my thesis. In 2025, I was awarded for the best scientific communication video for the Jožef Stefan International Postgraduate School. At the ISAF 2025 conference in Austria, I also won the first place at the student pitch competition for the contribution entitled: “Preparation and characterization of multicaloric composites.”